


Doctoral Dissertation
Doctoral Program in Material Science and Technology (31th Cycle)

Feasibility studies on Laser Powder Bed Fusion of powders mixtures based on Aluminium Alloys or High Entropy Alloys

Giulio Cattano
* * * * * *

Supervisors
Prof. P. Fino, Supervisor
Dott. D. Manfredi, Co-Supervisor

Doctoral Examination Committee:
Prof. L. Battezzati, Referee, University of Turin
Prof. R. Lupoi, Referee, Trinity College Dublin

Politecnico di Torino
April 2019

I hereby declare that, the contents and organisation of this dissertation constitute my own original work and does not compromise in any way the rights of third parties, including those relating to the security of personal data.

…….....

Giulio Cattano

Turin, April 2019

Ai miei genitori

Acknowledgment

Firstly, I express my gratitude to my Supervisor, Prof. Paolo Fino, for having financially supported the many training experiences along my research studies.

I would like to express my heartfelt gratitude to Dr. Diego Manfredi for his work as Co-Supervisor, for his continuous support and encouragement, patience and empathy. I could not ask for a better mentor. His enthusiasm and passion in doing research is something I always seek and hope to constantly follow in my life. My sincere gratitude goes to Prof. Mariangela Lombardi for her precious contribute to the drafting of this thesis, her valuable suggestions during my research studies, her expertise and outstanding patience. I would like also to acknowledge Prof. Marco Actis Grande for its scientific support and Prof. Matteo Pavese for the time dedicated to the training on the XRD.

My deep gratitude goes to Dr. Flaviana Calignano for her expertise during the training of the LPBF machine system and for having shared her knowledge of the process. I learnt a lot and it has been truly an honour to work closely with her. I am grateful to Dr. Massimo Lorusso for its ongoing support along my research activities and in the testing and characterization of samples and to Dr. Sergio Bocchini for his support in setting up the experimental part on mechanical alloying.

I am grateful to Politecnico di Torino, to the Doctoral School and the Department of Applied Science and Technology for the third level PhD courses, seminars and activities, to the Italian Institute of Technology (IIT) for my PhD scholarship and to the Material Science and Engineering department of the Monash University for the scientific collaboration. I would like also to thanks all the technicians and administrative staff in Politecnico, IIT and Monash University for their expertise, time and assistance.

Special thanks goes to my tutor at Monash University, Prof. Nick Birbilis, for having given to me the opportunity to spent six incredible months with his research group, for having me engaged into stimulating 3D printing activities within the

Woodside FutureLab and for having extended my research topic to the use of Pandat and Thermo-calc software. Mostly, I am grateful to Nick for its support, enthusiasm, passion and for having nicely stressed my research activity at Monash to the sound of “Go crazy!”. I will certainly keep it in mind along my career.

I would like to thanks all the people who with I shared even just a part of my PhD path, particularly: Patty, Trevi and Luisa for the support, coffee-breaks and laughs in IIT, Luca, Alessandro and Daniel for the friendly support during the draft of my thesis, Emilio for having shared its metallurgy knowledge, for its expertise and sincere availability in helping me in interpreting results, Alberta for the fruitful discussion on my research topic, Elisa for her patience during the training on thermal characterization equipment and then Giulio, Hamed, Federico, Mario, Eleonora and Oxana. Special thanks to Enrico, Bartolo, Alberto, Barbara and Simone who warmly welcomed in theirs office along the very last weeks of my period in Politecnico.

Finally, I want to thanks my friends Giorgia, Isabel, Laura, Viola, Angelo, Paola, Dario, Dado, Bea and Alessio for their support. It meant a lot for me. Ugo and Cheryl, who have always believed in me, welcomed like their son when I first moved to Turin, helping me settle down and feel like home. My father and my mother, my brother Andrea and my sisters Bruna and Costanza for their daily encourage and unconditioned love.

Thank you all. I look forward to a new beginning of my career.

Abstract

Laser Powder Bed Fusion (LPBF) is an advanced metal additive manufacturing process, which allows to fabricate components with sophisticated shapes by locally melting subsequent layers of powders with a computer-controlled laser beam. Over the last years, LPBF has gained much interest not only for its inherent advantages related to the high design freedom but also for its opportunities from a material point of view. During LPBF process, in fact, the highly focused laser beam creates a small and highly dynamic melt pool in which the alloy rapidly solidifies and undergoes complex thermal cycles with kinetics significantly different from that occurring in conventional manufacturing processes. This contributes in creating new materials with different microstructures and unique properties. Recently, broad material research opportunities for LPBF have been perceived in the exploitation of the metallurgical effects associated to the rapid solidification conditions during the process, namely the refinement of the segregation scale, the formation of supersatured solid solutions and metastable phases as well as the retention of disordered crystalline phases. These effects have been considered promising for heading *ad-hoc* alloying strategies aimed to develop novel Aluminium alloys with high strength and for boosting maturity of recently discovered High Entropy Alloys (HEAs). Nevertheless, to date, major obstacles to the development of novel alloys by LPBF come from the high-cost, poor availability and large size of purchased batches of the gas-atomized powders. Novel, economically affordable as well as stimulating material research opportunities for LPBF could come both from the *in-situ* synthesis of alloys from mixtures of different powders and from the use of alloy powders synthesized by other alloying techniques than atomization, i.e. mechanical alloying. The present thesis investigated both the scenarios, according also to the compositional complexity of the alloy system. Novel Al-Si-Ni and Al-Si-Ni-Cr-Fe aluminium alloys and two HEA systems were studied in the present thesis.

The first study investigated the consolidation, the alloying behavior as well as the microstructure and the mechanical properties of an Al-Si-Ni alloy *in-situ* synthesized from a powder mixture constituted by AlSi10Mg and pure Ni powders. By properly tailoring the alloy composition, it was possible to manufacture nearly full dense and crack free samples. The physical phenomena occurring within the melt pool during LPBF together with the continuous heating/melting of the material during the building were effective in mixing the starting powders. The material microstructure consisted of wide regions with composition close to that of the powder mixture alternated to coarse and randomly distributed Ni-rich precipitates, globally designating a heterogeneous microstructure. Notwithstanding this, the addition of Ni was effective in producing an alloy with high hardness due to the precipitation of sub-micrometric strengthening Al_3Ni phase.

The second study investigated an Al-Si-Ni-Cr-Fe aluminium alloy synthesized starting from a powders system by far more complex than the previous one, constituted by a mixture of AlSi10Mg and Hastelloy X nickel-base superalloy powders. The consolidated samples were porous due to adoption of a powder layer thickness not appropriated with respect to the other processing parameters. Nevertheless, the alloy composition synthesized was promising due to the absence of composition-related defects, such as cracks. The scanning speed during LPBF controlled the extent of the reaction between the starting powders, the alloying process and the fraction of product phases formed as well as the mechanical properties of the synthesized alloy. Alloying with Hastelloy X resulted into an enhancement of the microhardness up to 50% with respect to AlSi10Mg. Major concerns were found in the capability of LPBF of effectively *in-situ* mixing a powder system constituted by many species from different alloy powders.

The third study adopted a Single Scan Track (SST) technique for preliminarily investigating the processability and the alloying behaviour of compositionally complex AlTiCuNb and AlTiVNb HEAs powder compositions by using both mixture of the constitutive elemental powders and alloy powder synthesized by mechanical alloying. The characterization of the SSTs revealed that the microstructure homogeneity as well as the chemical composition accuracy within the melt pool were enhanced by using alloy powders synthesized by mechanical alloying rather than elemental powders mixtures. The broad ranges into the physical as well as powder properties of the elemental powders mixtures contributed in creating inhomogeneous distribution of the elements and unmelted powder particles. SSTs on compositionally complex HEAs powders synthesized by mechanical alloying can represent a fast and cost-effective technique for preliminarily assessing the behaviour of novel HEAs powders during LPBF.

Contents

List of Tables

List of Figures

Preface

Introduction

I. Additive manufacturing

Over the last decades, additive manufacturing has been heading a fundamental revolution in the manufacturing industry for its capability of both fabricating objects with an unprecedented design freedom and innovating materials with unique microstructure and properties.

In its broader definition, the term Additive Manufacturing (AM) refers to processes that make 'object' from a digital 'model' by depositing in a layer-by-layer manner the material in its smallest possible form (powder, wire, droplets, etc.) [1]. A rigorous definition of AM is given in the ASTM F2792-10 standard [2], which defines AM as the "process of joining materials to make objects from 3Dimensional (3D) model data, usually layer upon layer, as opposed to subtractive manufacturing methodologies". In the industry, AM is a commonly used term but the processes are also known as 3D printing, rapid prototyping, free-form fabrication or additive layer manufacturing. The fabrication of an object by AM starts from a 3D software model and it proceeds with the conversion of this latter in a STereoLitography (STL) file [3], which represents the *de facto* standard file format interfacing with nearly every AM system. Once the .stl file has been generated, the file is modified assessing the correct size, position and orientation of the 3D model in the building envelope, along with the geometry and density of the support structures [4]. The 3D model of the object as well as the support structures are thus sliced into a given number of layers and the definitive sliced file is sent to the AM machine software for built preparation. The subsequent operations (building, removal and post-processing) are mostly depended on the peculiar AM system adopted [3].

Modern layered-manufacturing dates back to the mid-1980s with the advent of stereolithography but it is in the late 1980s and early 1990s that AM processes started to flourish [5] and only recently they have been considered as part of a revolutionary paradigm of industry [6]. Among all, AM has yielded an

unprecedented freedom in fabricating complex structures with high degree of precision thanks to the direct translation of design to component, without the need for creation of part-specific tooling. The use of lattice design and hollow structures have made possible to manufacture flexible and lightweight components and new functions such as complex internal channels can be included to the part design. AM has the capability of manufacturing the component to its final (net) or near final (near net) shape, reducing the excessive consumption of raw material and cutting down the number of subsequent processing steps. In addition, it has the potential of reducing the cost and the time of the overall product development, from design to manufacturing, leading to quicker transfer of products to the market [7].

Historically, the first generation of AM machines worked almost exclusively with polymers and they were specifically addressed to the rapid fabrication of prototypes [8]. The EOS German Company did the first step in AM of metals in the early 90s, fabricating the first prototype of a Direct Metal Laser Sintering (DMLS) machine working with a metal powder-bed fused by a laser beam. Over the last 25 years, intensive research into processes, software, equipment and materials has allowed to apply AM processes to face a broad variety of research problems into different technical fields, spanning from aerospace to automotive, energy, medical and tooling going through the production of consumer goods [9]. The incentive from industry has stimulated the change of AM techniques from the rapid prototyping to the rapid manufacturing of small or medium quantities of end-use products and nowadays this latter represents the main market field for AM technologies [10]. Although the significant benefits brought by AM to the manufacturing industry in terms of design freedom in the manufacturing of complex-shaped products and virtually resource saving, care must be paid in generalizing that AM would be suitable for business regardless of their needs and sizes. In 2014, Conner *et al.* [11] developed a map as reference system for evaluating the suitability of a product to be produced by AM. By means of this map, the manufacturer can assess, based on the complexity, customization and production volume, whether AM provides an advantage over traditional manufacturing routes.

One of the most important consequences of the transformation of AM from rapid prototyping to rapid manufacturing has been the flourishing of many different processes and companies. In the field of Metal Additive Manufacturing (MAM), the industrially most relevant processes are categorized according to the type of feedstock material, namely wires, blown-powders and powder-bed [12]. Both wire- and blown-powder systems are generally referred as Direct Energy Deposition (DED) technologies, since they are based on the same principle of melting and depositing the material using a concentrated energy source. Wire-feed systems are versatile technologies for manufacturing large metal components with medium-to-low complexity, while blown-powder systems allow the direct fabrication of near-net shape components at high building rates [12]. On the contrary, beam powder-bed systems, namely Laser Powder Bed Fusion (LPBF) and Electron Beam Melting (EBM), use a focused energy source, either a laser or an electron beam, for selectively melting a loose powder bed, which rapidly consolidate to create the 3D

object. Nowadays, beam powder-bed based systems represent the most mature and researched MAM processes and - differently to generic DED systems - allow manufacturing parts with a high resolution of features, a high dimensional control and nearly unlimited part complexity [13]. In medical sector, LPBF and EBM have already achieved manufacturing readiness (MRL 9-10) in the series production of standard orthopaedic prosthesis, patient-specific implants for cranial or facial reconstruction but also surgical instruments and medical devices adopting Ti, Ti6Al4V and CoCr alloys [14]. In the aerospace and automotive field, process development and complex operational environment testing are ongoing (MRL 4-7) but the intended applications span from turbine parts and fuel injection nozzles to special components for motorsport vehicles, i.e. cooling ducts [13], with the great potential of improving the performance of the components and to save resources. In particular, LPBF, which is the technology of interest in the present thesis, is leader for the manufacturing of high quality objects with sophisticated shapes. As the scheme reported in Figure 1 visualizes, LPBF dominates in terms of number of companies on the market. The market size for LPBF has been expanding, boosted by the high number of system producers, the constant growth of the machines sold as well as the ongoing improvements in machine accuracy, laser technology and costs [15].

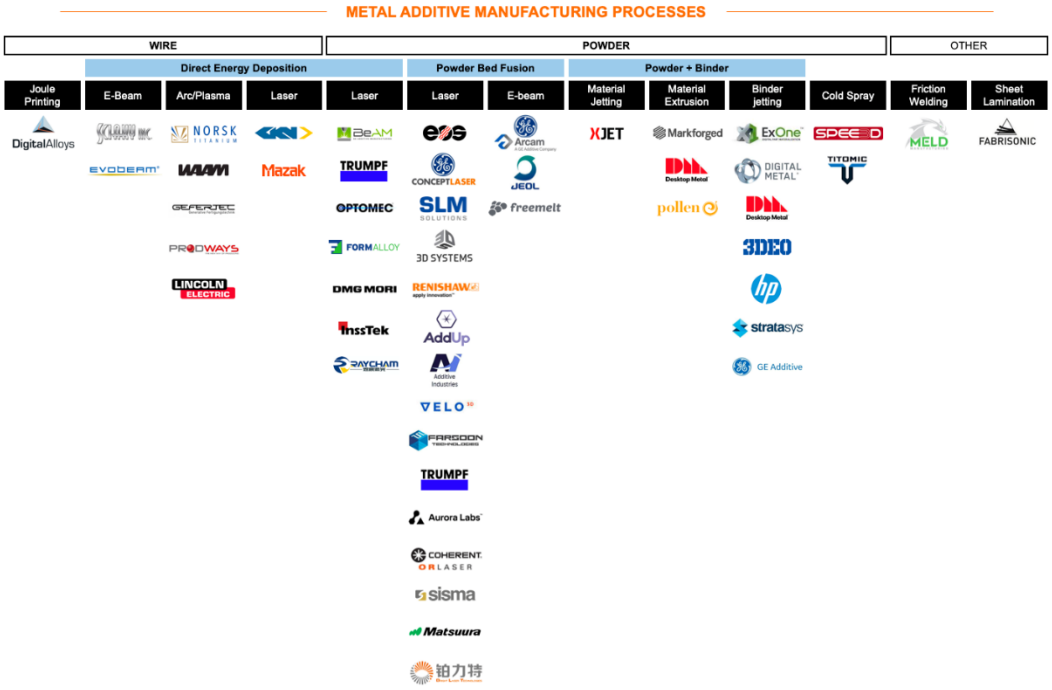

Figure 1. MAM processes available today and companies. LPBF process plays a leading role in the market [16].

II. The development of materials for LPBF

Over the last years, many studies and reviews have pointed out that vast market and research opportunities for AM not only stay in design but also in materials [17]. As it will be further discussed along this thesis, to date, the number of alloys

commercially available for LPBF is rather limited and the research and development of new alloys for LPBF is industrially of current interest.

On the one hand, the research of new materials for LPBF has addressed to extend the portfolio of conventional alloys able to be processed by LPBF, so to fully catch the market opportunities opened up by MAM in many industrial fields. This is the case, for instance, of Aluminium alloys, whose low density and outstanding properties make them ideal candidate for the manufacturing of high strength-to-weight structural components for the automotive, transportation, defence and aerospace industry [18]. Although the promising properties, to date, the most processed as well as almost the unique Aluminium alloy commercially available for LPBF is AlSi10Mg [19], a cast Al-Si-Mg alloy with good processability by AM, intermediate mechanical properties but low thermal resistance, which makes this alloy not suitable for aeronautical structural applications. A key research challenge is thus the development of new Aluminium alloys with superior performances and able to be processed by LPBF.

On the other hand, the research of new materials for LPBF has addressed to unconventional and less common alloys systems, such as recently discovered High Entropy Alloys (HEAs), whose processing by LPBF has been substantially perceived promising for boosting their development. In their broader definition, the so-called HEAs are compositionally complex metallic alloys composed by more than four elements in equi- or near equi-atomic concentration, preferably forming single-phase solid solutions. Their characteristic "multiple-element" composition, radically different from the 'base-element' composition of conventional alloys, have opened up research community to the exploration of a vast compositional space and new possibilities of designing materials with combinations of properties promising for many industrial fields, i.e. automotive and aerospace, have been perceived. However, due to their inherent compositional complexity, the melting and casting route traditionally adopted for processing HEAs require lots of process control, aside with strongly limiting the final shape and size of manufactured objects, potentially hindering their development as engineering materials. For these reasons, recently, MAM technologies have been explored for the fabrication of HEAs parts. From an industrial point of view, MAM technologies allow higher degree of process control than casting, thanks the localized energy source. In addition, they virtually allow the manufacturing of parts with more complex shapes and larger sizes. This research field has gained much interest over the very last years and it is expected will grow significantly in the future.

Generally, the development of new materials requires the alloy compositions be optimized for the particular manufacturing technology, so to develop materials that exploit the advantages of the process to the best. The materials processed by LPBF experience directional heat extraction, extremely high cooling rates and repeated heating and/or melting cycles, which results in material microstructures and properties significantly different from their cast and/or wrought counterpart. On the one hand, materials able to be processed by LPBF should have high tolerance to such thermal conditions, i.e. low solidification range and low tendency to segregation, in order to manufacture defects free objects. On the other hand, the

alloy compositions should take advantage of the thermal conditions during LPBF, in order to provide materials with optimal microstructure and properties.

Exciting material research opportunities can be perceived in taking advantage of the metallurgical effects of the high cooling rate during LPBF, namely the refinement of the microstructural features and of segregation scale, the precipitation of metastable phases, the formation of supersatured solid solutions and the stabilization of disordered crystalline phases in place of multiple brittle intermetallics. These effects generally increase material strength, also by enhancing their compositional homogeneity and can be promising for heading *ad-hoc* alloying strategies aimed to develop new high-strength Aluminium alloys or for producing homogenous HEAs with simple microstructures.

II.I Challenges in the development of new materials for LPBF

As it will be extensively discussed in the first chapter of this thesis, the materials commercially available for LPBF are in the form of alloy powders mainly produced by gas-atomization, with tight compositional tolerances as well as well-defined powder-related properties. These features ensure good chemical homogeneity and stability during the process and allow to manufacture defect-free parts.

Nevertheless, when developing new materials for LPBF at least two aspects need to be considered:

1. The capability of the market of effectively providing gas-atomized powders with customized compositions
2. The financial resources invested in the purchase, use and consumption of material in the powder form

As regard the first point, gas-atomized alloy powders with customized composition can be actually rather difficult and/or expensive to readily source commercially, because of the limited number of powder producers available on the market and/or the requirement of purchasing a minimum batch od powders (generally large), respectively. In addition, some alloy compositions can be intrinsically difficult to obtain in the form of gas-atomized powders. The possibility of *in-situ* alloying different powders during LPBF would allow to overcome the issues related to the poor availability and/or high costs of gas-atomized alloy powders with customized compositions, providing high flexibility for experimenting novel compositions at the same time.

As regard the second point, the financial resources invested in powder material sensibly increase with the vastness – and complexity - of the compositional space to investigate. The alloy concept introduced with HEAs has opened up research community to the investigation of a broad composition space and one of the main challenges that the research is facing is how to investigate such vast compositional space with the aim of identifying promising systems, without wasting resources and with high compositional flexibility. The use of the Single Scan Track (SST)

technique can accelerate the development of new materials for LPBF, limiting the material consumption. In SST, in fact, only a thin layer of powder is laser scanned, providing preliminarily information into the processability and/or alloying behaviour of the selected material when irradiated by the laser beam during LPBF. Then, the use of powders mixtures or alloy powders synthesized by other alloying technique than gas-atomization, i.e. mechanical alloying, would allow the required compositional flexibility for experimenting several HEA compositions, by providing few amounts of customized powder compositions to investigate through SST experiments.

III. The aim and the objectives of the thesis

Within this broad research field, this thesis will investigate the alloying behaviour of different powders during LPBF with the major aim of assessing the feasibility of adopting the mixing approach for developing Aluminium alloys or HEAs for LPBF.

To achieve this aim, the research is divided into two sections: the first section focuses on Aluminium alloys and the second one on HEAs. The choice of dividing the thesis in two sections is a requirement arising from the difference in which the same topic, that is the use of the powder mixing approach for developing new materials for LPBF, has been developed. In addition, the alloy families investigated in this thesis are significantly different. Aluminium alloys are commercially available for LPBF, well-researched both in academia and industry and with well-established criteria for designing compositions with desired microstructures and/or properties, within a relatively narrow compositional space. On the contrary, HEAs are recently discovered, currently of academic interest only and with complex and sometimes bias criteria for designing compositions with targeted microstructures and properties, mainly established for conventional casting route.

III.I Specific aim and objectives of the first section

The specific aim of the first section is that of improving the mechanical properties of AlSi10Mg, the most processed Aluminium alloy by LPBF, adopting an alloying strategy based on the addition of transition metals (TM) in the form of commercially available pure Ni or Ni-, Cr- and Fe-rich nickel-base superalloy Hastelloy X powders.

The objectives of this section are:

1. Designing the compositions of two Aluminium alloys suitable to be processed by LPBF.

2. Evaluating the densification and alloying behaviours as well as the phases and the mechanical properties of the *in-situ* synthesized bulk alloy samples. This includes the characterization of the microstructures of the samples in the as-built condition.

It is worth to mention here that the two alloys experimentally investigated in the first section were synthesized using different source materials and equipment because the studies were carried out at Istituto Italiano di Tecnologia - IIT (Turin, Italy) or at the Department of Material Science and Engineering of the Monash University (Melbourne, Australia), as part of a scientific collaboration between Politecnico di Torino and Monash University.

III.II Specific aim and objectives of the second section

The specific aim of the second section is that of investigating the feasibility of producing compositionally homogenous SSTs of two selected HEAs based on refractory species without resorting to gas-atomized alloy powders but using different powders systems, namely elemental powders mixtures corresponding to the HEA compositions or alloy powders synthesized by mechanical alloying.

The objectives of the second section are:

1. Designing, screening and selecting the HEAs compositions.

2. Optimizing the milling time for producing chemically and morphologically homogenous HEAs alloy powders from the elemental powders mixtures.

3. Conducting a comparative analysis on the alloying behaviour of the elemental powders mixtures and the milled HEAs powders when irradiated with the laser beam during the formation of the SSTs.

IV. The structure of the thesis

This thesis will consists of seven chapters and two distinct sections, as previously anticipated.

The current preface is basically an introduction to AM, to the interest in this topic and to the opportunities of LPBF. It provides background information and clarifies the context of the investigated research field. This section identifies also the main challenges in the development of materials for LPBF and motivates the significance of the present research. In conclusion, it contains the aims and the objectives of the studies.

Chapter 1 provides a comprehensive description of the LPBF process, from the main physical phenomena controlling the melting and solidification of the powder bed to the variables mostly affecting its densification behaviour and passing through the thermal regimes determining the microstructure development of materials. Capturing the main features of these phenomena is crucial not only for the industrial aspects of LPBF, aimed to manufacture high-quality, dense and defects-free objects, but also for its material science and engineering ones, aimed to develop materials with optimized processability, microstructure and properties.

The first section of the thesis, which includes Chapter 2 and Chapter 3, addresses to Aluminium alloys and it consists of the literature review on Aluminium

alloys and of the experimental part on the *in-situ* synthesis of Al-Si-Ni and Al-Si-Ni-Cr-Fe alloys from powders mixtures, respectively.

In particular, Chapter 2 begins with the description of the strengthening mechanism for Aluminium alloys. Then, it focuses on reviewing the efforts did in the past for developing new generations of Aluminium alloys using rapid solidification techniques, i.e. melt spinning. Such techniques were extensively studied in the past since they offered new opportunities for developing new compositions, which exploited several strengthening mechanisms in an effective way. In conclusion, the literature review goes through the microstructure and properties of AlSi10Mg - the base alloy used within this thesis in the experimental part - and the most significant trials already done for the development of Aluminium alloys by LPBF.

Chapter 3 provides details of the experimental work carried out and shows the results achieved over the investigation of the feasibility of improving the mechanical properties of commercial AlSi10Mg by mixing this latter with small quantities of commercially available pure Ni or Hastelloy X powders.

The second section of the thesis, which includes Chapter 4 and Chapter 5, addresses to High Entropy Alloys and - again - it consists of the literature review on HEAs and of the experimental part on the development of HEAs by SSTs technique on different powder systems, respectively.

In particular, Chapter 4 provides a comprehensive analysis of the material development opportunities opened up by the discovery of HEAs Theoretically, in HEAs, the composition can be designed as for exhibiting desired microstructures and targeted sets of properties, often unusual for conventional alloys. Nevertheless, the relationship between composition, microstructure and properties, which is fundamental for designing materials, is still weak established for this young class of alloys. For this reason, the scope of this chapter will be that of providing a critical summary of the relationship between composition, microstructure and properties up to know established for the most studied HEA families produced by casting route, where most of the efforts has concentrated up to now. Great attention is given also to the description of the thermodynamic parameters that affect phase selection in HEAs and to review the efforts did in the past for designing empirical parameters to use as alloy design criteria for predicting the formation of HEAs. A crucial point concerning the development of HEAs, in fact, is that of having methods able to predict which type of phases (solid solutions, intermetallic, amorphous phase or multiple phases) would form for a given composition (type, number and concentration of the constitutive elements). This point is of great for searching and/or designing HEAs with selected microstructures/properties. In addition, a detailed summary of the pros and cons of main HEAs manufacturing techniques (casting, mechanical alloying, AM) is provided, emphasizing the role played by the cooling rate on the final phase constitution in HEAs. In conclusion, the literature review goes through the trials already done for the *in-situ* synthesis of HEAs from mixtures of different powders by AM technologies.

Chapter 5 provides details of the experimental work carried out. It describes the methodology used for selecting the HEAs systems here investigated and the

experimental equipment used during mechanical alloying and it presents the results achieved over the investigation of the feasibility of producing SSTs of HEA by using different powders systems, namely mixtures of the elemental constitutive species or alloy powders synthesized by mechanical alloying.

Chapter 6 summarizes the key findings for both the sections, followed by some closing remarks.

Finally, Chapter 7 provides details on the experimental equipment and characterization methods used to study the materials and samples produced within this thesis.

In favour of the reader, the overall thesis structure is summarized in Figure 2.

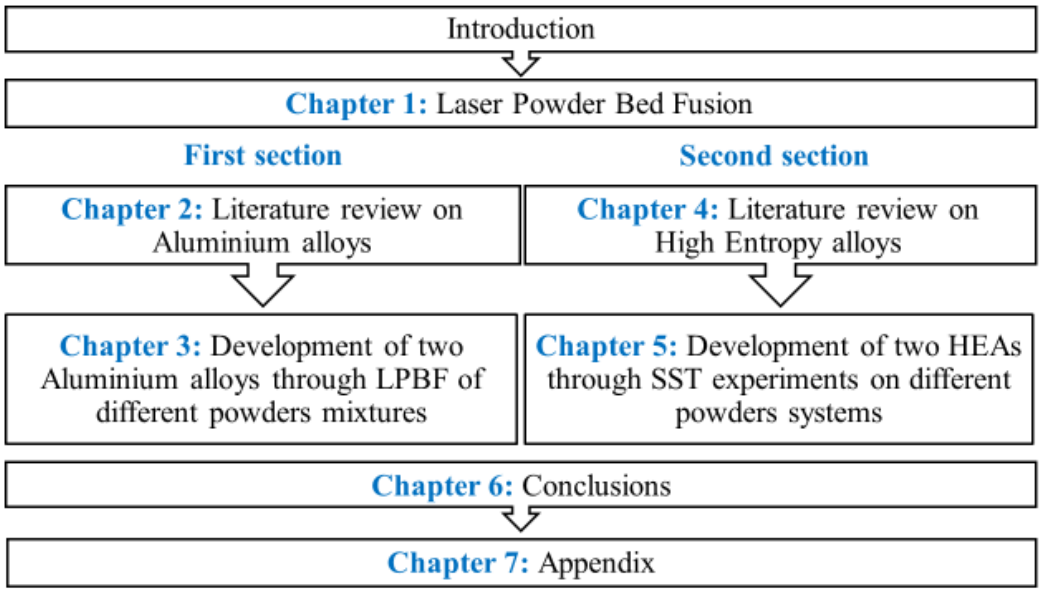

Figure 2. Thesis structure

Chapter 1

Laser Powder Bed Fusion

Laser Powder Bed Fusion (LPBF) is a breakthrough AM technology for the manufacturing of net-shape metal objects with high design freedom and high resolution of features for the automotive, aerospace, medical, tooling and energy industrial fields. From a material engineering perspective, the growing interest in LPBF motivates the development of new alloys, whose compositions are specifically tailored for exploiting to the best the unique manufacturing features of LPBF and the properties are optimized for catching the broad opportunities opened by MAM in several industrial fields.

The comprehension of the physical phenomena taking place during LPBF, which lead to the melting and subsequent rapid consolidation of the powder material, are crucial for gaining confidence with the process, for defining those conditions rendering a material suitable to be processed by LPBF and for developing new materials.

In the present chapter, the LPBF manufacturing process will be described and the physical phenomena occurring within the time-scale governing the interaction between the laser and the powder material will be summarized, aside with the main LPBF process parameters and powders properties, which control the manufacturing of high-quality dense and defect-free objects. In conclusion, an overview of materials commercially available for LPBF will be provided and some material development opportunities will be outlined.

1.1 The manufacturing process

A generic representation of a LPBF system is shown in Figure 3. For this kind of MAM systems, a powder bed lays on a building platform. A laser energy source is focused on the powder bed and selectively melts the upper layer of this latter that rapidly consolidates. After the powder material representing the 2D layer of the final object has been melted and it has consolidated into the desired shape, the platform is lowered, an additional layer of powder is spread across the work area and the cycle is repeated until the 3D solid object is fully built, embedded in the unprocessed powder [12]. During the process, the 3D object grows along the vertical axis, fixed to the building platform by means of support structures, whose main function is that of supporting overhanging or horizontally aligned surfaces and of dissipating process heat [20]. At the end of the process, the as-built object

undergoes post-processing operations, such as unprocessed powders and support structures removals and heat treatments.

The entire LPBF process takes place inside a closed chamber where an inert gas atmosphere, with the twofold function of protecting the melt from undesired reactions with the environment and of clearing the by-products of the process, is maintained. In addition, the building platform can be pre-heated at a temperature specifically set depending on the material, allowing to conduct the building process at temperature higher than the room one [21]. The largest part of the LPBF systems adopts continuous-wave Yb and Nd:YAG fiber laser operating at 1075 nm wavelength and with power up to 1 kW [22]. The scanner system with optics allows to deliver the focused laser spot on the working area, whose dimensions may vary from a circular zone of Ø 70 mm (Realizer SLM 50 machine) to rectangular one of 800 mm × 400 mm (Concept X Line 2000R machine). The powder delivery system consists of a piston that supplies the powder and a coater (or roller) to deposit on the working plane a controlled amount of material, which generally varies between a thickness of 15 μm and 100 μm.

LPBF is the accepted term for referring to this manufacturing technology, in accordance with information provided in ASTM standard F2792-12a. Nevertheless, the process is commercially known with the trademark as Direct Metal Laser Sintering (DMLS) by EOS GmbH, LaserCUSING® by Concept Laser GmbH, Selective Laser Melting (SLM) by Realizer and SLM Solutions GmbH, Laser Metal Fusion (LMF) by Sisma Industry and Trunpf.

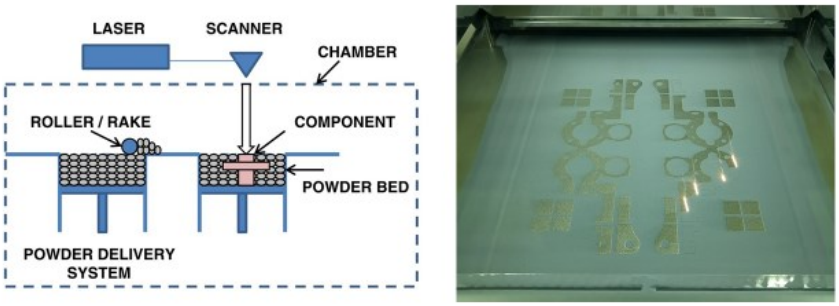

Figure 3. Schematic representation of a LPBF system and the working process chamber during the process [12,23].

In a single layer, during the manufacturing process, the laser exposures the interested area according to a scanning pattern or strategy. A schematic representation of the powder layer as well as a characteristic local scan pattern are shown in Figure 4. Depending on the LPBF system adopted, the scanning pattern may change. Nevertheless, they all are based on the same main features that is the segmentation of the building surface into stripes (or square islands) in which the laser beam moves line after line (infill hatching) at a selected scan speed (v) and laser power (P). The distance between the lines during infilling hatching is the hatching distance (h_d) and it is set to provide an adequate overlap between adjacent laser scans [24]. The melting of the powder bed occurs thus by parallel laser scans

called tracks, which are combined to form the 2D layer of the final object. During its passage, the laser beam locally melts the powder particles producing a melt track (or melt pool), which rapidly solidifies.

In LPBF, the quality and properties of the objects strongly depend on the quality of each single melt track and then of each layer [25]. For this reason, modelling, simulations [26] as well as experimental studies [27] on the formation of single laser scan tracks have been extensively conducted for capturing the main aspects of the interaction between the laser and the powder material and the physical phenomena taking place, which control the stability of the melt pool and the consolidation behaviour of the material.

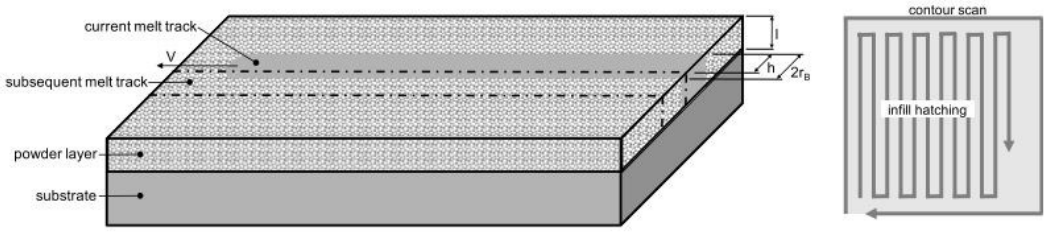

Figure 4. Schematic representation of a single powder layer exposed by the laser beam (left) and a typical local scan pattern adopted in LPBF (right) [28].

1.2 Physical phenomena to consolidation

In LPBF, the interaction between laser and powder bed can be divided into three steps: heating, melting and solidification [29]. In the heating stage, the material absorbs the energy to bring the temperature of the powder bed up to the melting point. The melting stage starts as soon as the particles surface reaches the melting temperature. During this period, the powder rapidly melts (1-4 μs) [30] and it forms a melt pool, which rapidly consolidates (0.3-2.5 ms) [31]. Solidification into a solid layer occurs when the heat transfer phenomena within the melt pool allow the liquid to cool down.

The physical phenomena occurring in the single melt track are many and they include laser beam absorption and scattering, phase transformations, melt pool hydrodynamics controlled by surface tension, evaporation and emission of material, formation of spatter and chemical reactions [32]. In addition, these phenomena depend on many factors related to the laser (i.e. laser type, laser power, scan speed, spot size, etc.), the powder bed (particle morphology, mean dimension and size distribution, layer thickness, etc.) and the material properties (thermal conductivity, absorptivity, melting temperature, chemical composition, etc.) [33].

The understanding of these phenomena and of their main controlling parameters is important for the development of alloys for LPBF. The following sub-sections will go through their description.

1.2.1 Laser absorption and scattering

In the powder-bed, across the time-window in which the laser irradiates the powder bed, the material changes from powder to liquid, and then to solid. Absorption and scattering of the incident radiation are the main physical phenomena. The reflectivity of metals is generally very high at the laser wavelength used commonly nowadays during LPBF (i.e. 0.91 and 0.98 for Al and Cu, respectively at 1.076 μm) and most of metals best absorbs at wavelength lower than 1 μm.

When the laser beam irradiates a metallic flat surface, the overall absorbance is controlled by intrinsic physical properties of the material and extrinsic factors, i.e. laser power and wavelength. Differently, the net absorption of the incident radiation from powder particles is influenced by many other parameters, including the wavelength, the laser power, the powder bed temperature, the angle of incidence, the polarization, the surface roughness, the powder-surface chemistry (i.e. oxidation) and contaminants [30,34]. In addition, the particle shape, the size distribution and packing density, influencing the powder bed morphology, also affect the radiative heat transfer according to the mechanism represented in Figure 5.

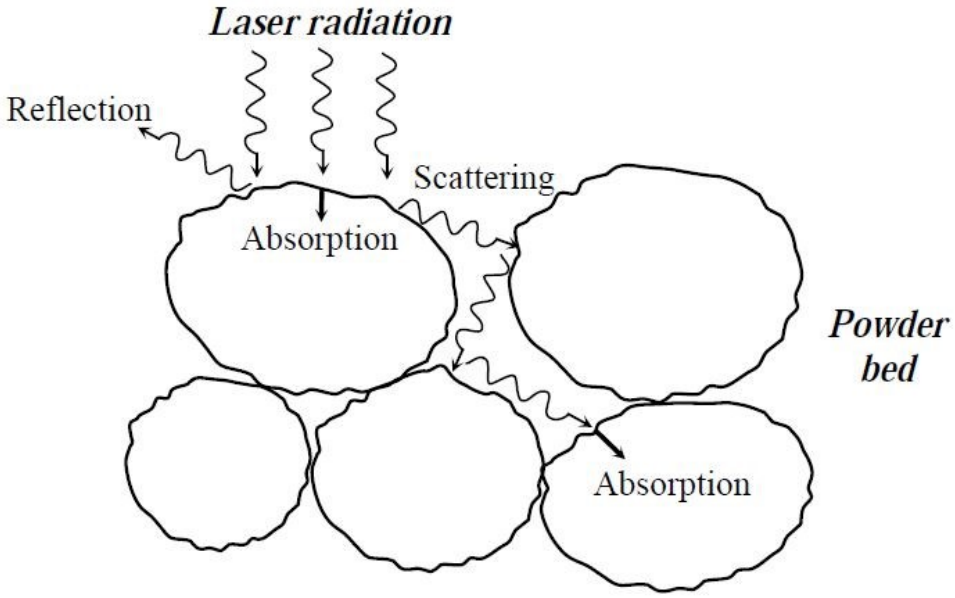

Figure 5. The mechanism of laser-powder interaction within the powder bed [29].

Boley *et al.* [30] used a ray-trace model to simulate the absorption of laser radiation by metal powder during LPBF. The simulation of the interaction between the laser beam and the powder-bed revealed that the multiple scattering of the incident laser beam occurring within the open-pores of the powder bed actually governs the laser beam absorption, as highlighted in Figure 6(a,b). As a result, the amount of energy lost away from reflection phenomena is lower than for a flat metal surface: more rays are trapped within the powder bed and more energy is available for heat transfer. The effective absorptivity of the powder bed is thus significantly higher as compared to the value for flat surfaces and the laser beam can penetrate

at depths comparable to the thickness of the powder layer [35]. Rigorously, rather than a surface heat source, in LPBF the incident laser beam energy must be considered as a volumetric heat source interacting with nearly the entire powder bed thickness.

In this stage, a critical issue is related to the heat transfer phenomena within the powder bed. Due to the granularity of the system, the contact surfaces among the particle (inter-particle) are negligible and the effective thermal conductivity within the open pores of the powder is basically that of the filling gas, which is order of magnitude lower than the conductivity of the solid material [36]. Moreover, the time scales governing the heat conduction within powder particles (intra-particle) are significantly larger than the time scales controlling the powder melting. Boley *et al.* [30] estimated that during LPBF of steel the melting time of powder is around 2.5 μs and the thermal diffusion time is higher by nearly a factor of 10. Therefore, in the typical LPBF process conditions, phenomena of conductive homogenization of non-uniform temperature and/or energy distribution among the powder particles but also across individual particles do not have enough time to occur. If the amount of heat deposited to the particles is insufficient, partially molten particles can form and the formation of defects such as voids or inclusions may be induced [30].

The direct absorption of the laser radiation is thus the dominant mechanism inducing the phase transition from solid to liquid in LPBF. Adopting a realistic laser ray-trace model, Khairallah *et al.* [26] showed that melting of a powder particle is not uniform but it firstly occurs at the powder particle surface, where radiation is firstly absorbed and the heat is transferred (Figure 6c).

Before moving to the physical phenomena occurring within the melt pool, it might be worth to remark that since LPBF is a layer-by-layer process, the quality of deposited layer is a matter of prime importance in controlling the melting behaviour, the melt pool hydrodynamics and subsequent consolidation.

The existence of individual particle with large size as compared to the layer thickness and/or the laser beam spot size can indeed lead to non-uniform energy distribution across the powder bed but even across individual particles, as it has been discussed above [30]. The presence of thicker regions in the powder layer, not well attached to the substrate, can disconnect during the deposition and can damage other region of the powder bed. In addition, the first layer of powder should be spread on a rough substrate that provides an efficient anchor for the particles. Smooth substrates are indeed unfavourable for the first layer because particle can roll and move during powder deposition, leading to regions with low density [29].

These large heterogeneities create differences in the resulting temperature fields and in the shape of the melt track, layer upon layer, which produce a broad variance in the consolidation phenomena, hindering the production of dense parts.

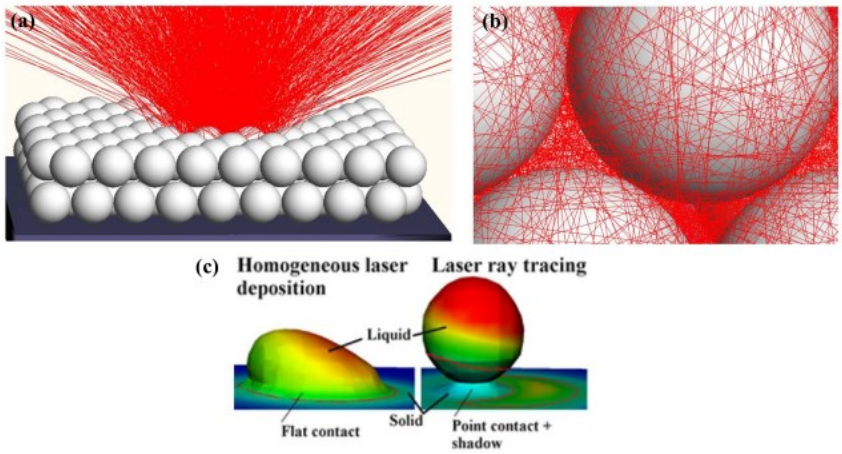

Figure 6. (a) Characteristic irradiation by a laser beam of an ideal array of metal powders adopting a realistic ray-trace model [30], (b) detail of (a) revealing the important role played by multiple reflection in the overall radiation absorption by particle surface [30] and (c) temperature field of a powder particle under laser irradiation adopting an unrealistic volumetric energy deposition (left) and a realistic ray-trace model (right), which shows melting firstly occurs at powder particle surface in LPBF [26].

Once the melting temperature is locally achieved at the powder particle surface, the major interaction occurs between the laser beam and the molten material.

Under the laser beam, the formation of a highly dynamic melt pool and, ideally, of a continuous melt track are induced. Capillary and surface tension forces drive the dynamic of the low viscosity liquid and the heat transfer phenomena within the melt pool [37].

1.2.2 Marangoni flow (thermocapillary effect)

Marangoni flow is one of the most important phenomenon dominating the fluid behaviour and heat transfer within the melt pool. It is generated by the presence of surface tension gradients and it consists in the movement of the molten metal from a region of lower surface tension to a region of higher surface tension [38].

In LPBF, the incident radiation usually has a spatial energy density following a Gaussian distribution, with the 2σ value (where 68.2% of the incident radiation is transferred) generally taken coincident with the laser beam diameter. For this reason, a temperature gradient exists within the melt pool. The melt pool temperature reaches a maximum in the center and a minimum in the melt pool borders. Surface tension gradients are thus generated by temperature differences within the melt pool, even if surface tension is also sensitive to composition, i.e. impurities or minor alloy addition.

The temperature dependence of surface tension for pure metals and alloys is negative. That is, the surface tension (γ) will be lowest at the center and higher at the peripheral regions of the melt pool, inducing an outward flow, as schematized in Figure 7a. On the other hand, surface-active elements, such as oxygen, can induce

the formation of an oxide layer at the melt pool border with lower γ than the molten alloy, causing an inward flow, as indicated in Figure 7b [39].

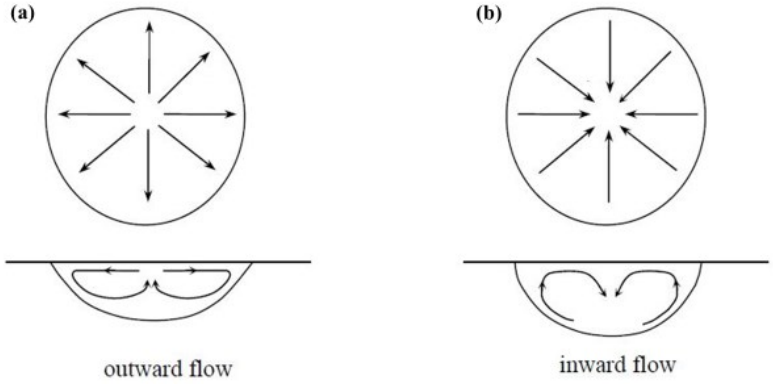

Figure 7. Schematic representation of the mechanism of surface tension gradient induced flow for an (a) outward and (b) inward convection within the melt pool [39].

The surface-tension driven convection induced by temperature gradient is known as Marangoni flow or thermocapillary effect. This phenomenon influences the melt pool shape, which may be spherical (outward flow) or shallow and wide (inward flow), it is responsible for the mixing, thus influencing the composition of the melt pool, and it enhances the rapid cooling and consolidation of the melt pool [40].

The importance of the temperature dependence of the surface tension in driving the heat transfer, the melt pool morphology and flow within the melt pool during LPBF has been captured by Khairallah *et al.* [26], who simulated the melt pool behaviour without and with considering Marangoni flow. With respect to the unrealistic case of constant surface tension (Figure 8a), where more heat is retained within the melt pool, the melt-flow generated by Marangoni flow induces the formation of a less shallow melt pool, it increases the melt-pool depth and enhances melt pool recirculation, thus the melt pool cooling (Figure 8b).

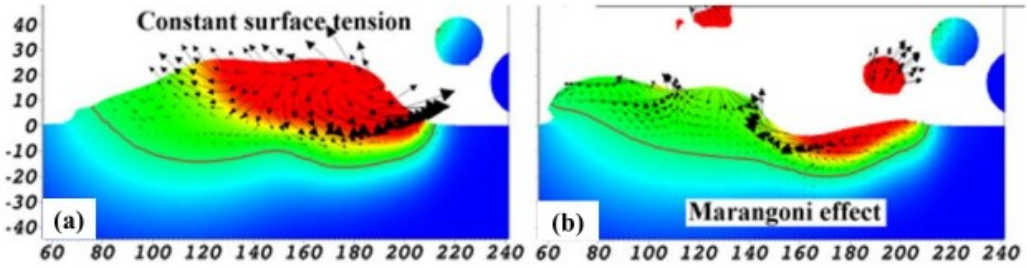

Figure 8. Mesoscopic simulation showing the heat transfer and characteristic of the melt pool without (a) and with (b) considering into the model the temperature-induced surface tension gradient. The red contour line is the melt line [26].

1.2.3 Evaporation

During LPBF, the intense laser beam irradiation inducing the melting of the material can bring the surface temperature below the laser spot to boiling points and considerable liquid vaporization may take place [41].

The evaporation of material is thus a dominant phenomenon occurring within the melt pool, which causes:

1. Modification of the melt pool thermo-hydrodynamic as consequence of the mass and heat loss due to the evaporation.
2. A vapour recoil pressure acting on the melt pool surface, which can considerably distort it.
3. Spattering out of the melt pool of melt drops and even powder particles from the powder bed.

As concern the first point, the laser-induced vaporization of some alloying elements and the Marangoni flow go in the opposite direction to the maximum melt pool surface temperature induced by laser absorption.

Lei *et al.* [42] numerically simulated the phase transformation occurring in laser surface remelting process of stainless steel. They found that heat loss for Langmuir-type vaporization of Fe, Mn, Cr and Ni elements drastically reduced the peak temperature of the heating surface. During LPBF, King *et al.* [40] estimated a peak temperature reduction of stainless steel under the laser beam as consequence of evaporative energy loss from more than 5000 K to about 2700-3000 K, the boiling temperature of steel. Moreover, the laser-induced evaporation of most volatile elements can induce significant variation in the nominal alloy composition while processing and in the resulting microstructure development, as occurs in AlSi10Mg alloy as consequence of the likely evaporation of Mg ($T_{boiling}$ = 1091 °C) [43].

As concern the second point related to evaporation, a recoil pressure acting over the melt pool surface can affect the overall dynamics close to the laser beam, inducing a considerable distortion of the melt pool (Figure 9). Recoil pressure, indeed, together with Marangoni flow, is one of the most important physical phenomena assessing the melt pool shape. The recoil pressure scales exponentially with temperature, as [26]:

$$P(T) \quad \propto P_a e^{\frac{\lambda}{K_B}\left(\frac{1}{T}-\frac{1}{T_b}\right)} \tag{1.1}$$

Where P_a is the ambient pressure, λ is the evaporation energy per particle, K_b is the Boltzmann constant, T is the surface temperature and T_b is the boiling temperature of the material.

The extra force added by the vapour recoil pressure to the liquid surface creates a depression below the laser beam that allows the melt to penetrate well into the substrate. The melt pool depth increases as well as the surface area of the melt pool and the evaporative and radiative surface cooling are further enhanced [26].

It could be assumed that the drop of the peak surface temperature of the melt pool as consequence of the evaporative energy loss could mitigate the magnitude of the recoil pressure, which scales exponentially with temperature according to equation 1.1. However, referring to a simplified model for the vaporization rate from liquid pool surfaces, developed by Anisimov *et al.* [44] and commonly used for modelling the laser-matter interaction, more than 18% of all the vaporized particles condenses back to the surface, reducing thus the cooling effect and the drop of temperature [44].

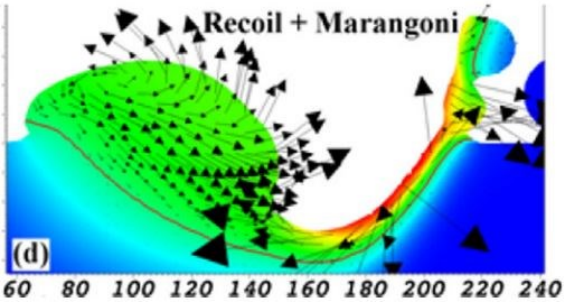

Figure 9. Mesoscopic simulation of the united effect of Marangoni flow and recoil pressure in distorting the melt pool shape. The formation of a depression, which enhances cooling of the material, is induced [26].

Still related to the second point, the recoil pressure acting on the melt pool can cause the formation of defects, i.e. pores, when excessive evaporation of material from the melt pool surface takes place.

A close control of the laser beam is always necessary. High values of laser power are considered to increase the depth of the depression produced by the recoil pressure, according to an effect closely related the so-called keyhole mechanism commonly observed in laser welding [45]. Excessive heating and evaporation within the melt pool are able to produce a deep depression below the laser beam under the effect of the recoil pressure. The incident laser beam is “trapped” within the depression and rays are reflected on the internal surfaces of the depression. At the bottom of the depression, the energy is more concentrated and the temperatures are higher so that further evaporation takes place. The development of a vapour cavity deep into the substrate, with enhanced laser absorption, allows the laser beam to further penetrate, creating a deep and narrow corridor (Figure 10) [46]. This phenomenon is known as keyholing.

As soon as the laser beam moves on, the severe action of the recoil pressure diminishes and, at some point, the keyhole collapses under the effect of the surface tension, which pull the melt back into the depression. However, the incomplete filling of the vapour cavity with melt may result in the formation of residual pores and defects in the wake of the laser track at the bottom of the keyhole (Figure 10) [47]. Cavitation driven by keyholing mechanism contributes thus to the overall porosity of the material.

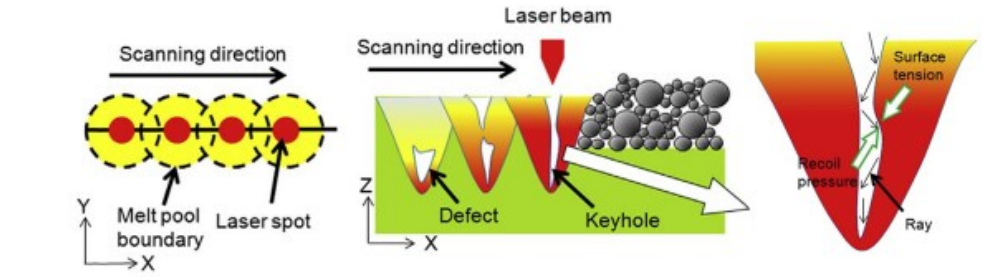

Figure 10. Schematic representation of the physical mechanism associated with keyhole formation [46].

As regard the third point related to evaporation, a common phenomenon occurring during LPBF is the ejection of melt drops from the melt pool and even powder particles from the powder bed into the surrounding.

The ejection of melt drops is very common in laser manufacturing and it is known as spattering. The current accepted explanation for spatter formation during LPBF is that the recoil pressure exerted by metal vapours evaporating from the melt pool surface pushes the liquid alloy towards the melt pool borders. When the recoil pressure exceeds a threshold, which depends on the surface tension of the alloy, small droplets of liquid can be ejected from the melt pool [48].

Recently, Wang *et al.* [49] investigated the mechanism of spatters formation during LPBF and spatters features, indicating the existence of three main types of spatters (Figure 11), namely (i) spherical metallic jet, directly ejected by the molten metal under the effect of the recoil pressure. The long ejection distance and rapid cooling of these particles allow them to exhibit a smooth spherical morphology; (ii) coarse spherical droplet spatter with a large amount of unmolten particles adhered onto the surface; (iii) irregular coarse powder spatter highly deformed and with many unmolten particles adhered onto the surface [49].

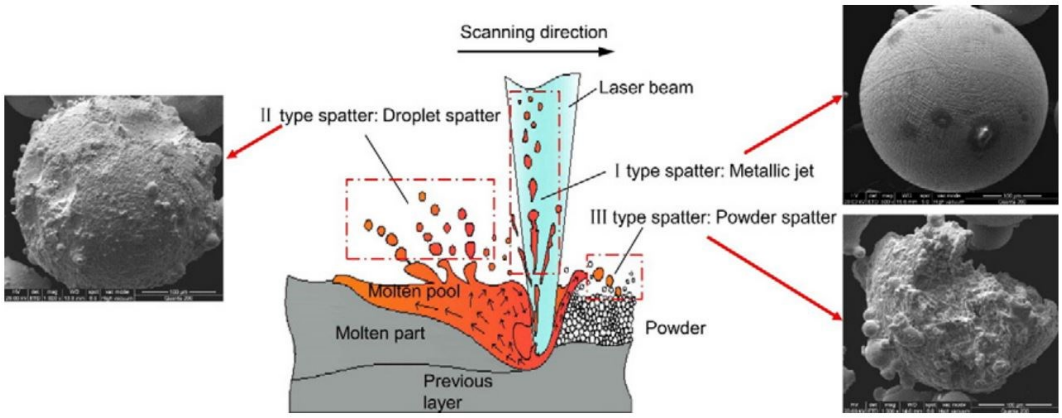

Figure 11. The formation mechanism of three different types of spatter [49].

The formation of spatter during LPBF process is detrimental for the quality of the part. In fact, spatter represent inclusion that can negatively affect the final properties of the material, including the density, microstructure and mechanical properties. When a spatter is ejected from the melt pool, it may redistribute over the manufacturing surface (Figure 12a) [50]. If the deposited spatter is large enough, it

will not melt and contribute to the part porosity according to the mechanism reported in Figure 12b. An example of relocated particles contributing to the part porosity can be observed in Figure 12c. Liu *et al.* [51] performed microstructure analysis and tensile strength tests on 316L stainless steel produced by LPBF, assessing the degradation of the quality of the part as consequence of spattering. Simonelli *et al.* [48] compared the influence of spattering in three different materials, namely AlSi10Mg, Ti-6Al-4V and 316L stainless steel. With the exception of Ti-6Al-4V, surfaces of spatter were constituted of oxides enriched in the most volatile elements of the materials, that is Mg in AlSi10Mg and Mn and Si in 316L stainless steel. In addition, the formation of large spatter particles ejected either in regions already consolidated or in regions not still scanned affects the stability of powder recoating, leading to irregular powder bed that may hinder the movement of the recoater and the formation of a smooth melt track [49].

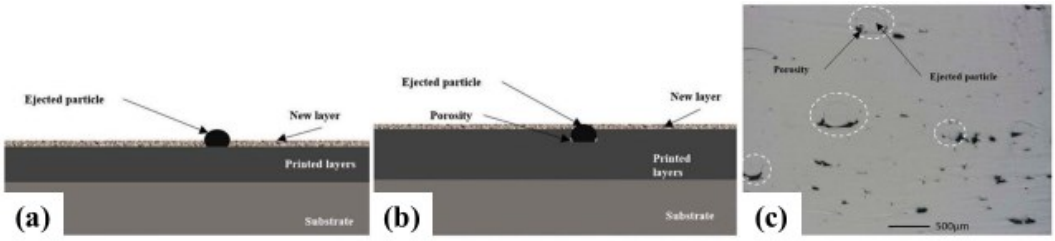

Figure 12. Porosity formation mechanism due to spattering: (a) schematic of an ejected particle, (b) schematic of porosity formation after printing and (c) spherical entrapped particles and porosity in a printed part [50].

1.2.4 Balling

As already anticipated, in addition to the melt pool shape, the surface tension and capillary forces also drive the dynamic of the low viscosity liquid during the formation of the melt track.

On the effect of surface tension on the melt track formation, mesoscopic simulations conducted by Khairallah *et al.* [33] have shown that surface tension acts to minimize surface energy. In other word, during LPBF the effect of surface tension is to bring to coalescence almost immediately the individual melt drops formed during laser scan, producing a smooth surface and lowering the total surface energy. Figure 13(a,b) illustrates the differences in mesoscopic simulation of a melt track formation omitting or including into the model the effect of surface tension. Minimization of the surface tension allows to have a higher contact with the bearing substrate, which accelerates the heat transfer and the melt track cooling. Nevertheless, at high laser scan speed, the melt track might break up into pieces. This phenomenon is known as balling and it is a typical defect observed experimentally in LPBF yielding rough build surfaces [52]. It is ascribed to a variant of Plateau-Rayleight instability of a fluid cylinder and the physics governing this phenomenon is still related to surface energy minimization issues [53]. When the wavelength of the perturbations of a liquid cylinder is bigger than the

circumference of the cylinder, then the cylindrical shape becomes unstable and it breaks into droplet of spherical shape so that the surface energy lowers (Figure 13c).

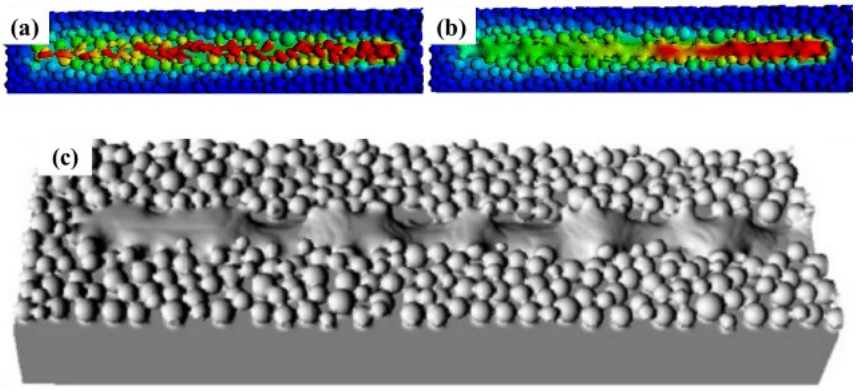

Figure 13. Mesoscopic simulation showing the morphology of a single track (a) without and (b) with including into the model the surface tension effect. In the simulation the laser moves from left to right, the melt temperature is shown in red and the room temperature in blue [33], (c) balling effect attributed to the Plateau-Rayleigh instability of a cylinder liquid at high scan speed [33].

1.2.5 Wetting

The wetting behaviour of the low-viscosity melt towards the bearing substrate, i.e. the solidified material of the previous layers and/or the surrounding powder particles, also contributes in determining the adhesion and continuity of the melt to the previous layer [32]. Together with the surface energy, indeed, wetting is an important factor in assessing the shape of the re-solidified melt pool [37]. With respect to the LPBF process, wetting implies that the melt alloys will spread on the substrate, instead of balling on its surface. In other words, the force of adhesion between the solid and the liquid material must overcome the cohesive force of the liquid [29]. The wetting phenomena are thus very important during the formation of single melt tracks and layers in LPBF process. The wetting behaviour is significantly affected by surface chemistry, material, temperature and roughness of the bearing substrate.

1.2.6 Oxidation

Chemical reactions at high temperatures with the atmospheric gases, such as oxidation, can give problems during LPBF, in particular when the dissociation temperature of the oxide products are by far higher than the melting point of the material. The presence of an oxide layer onto the surface of powder particle or substrate – either due to the contamination of the primary material or to the thermally induced oxidation during the process – significantly decreases the wetting ability of the liquid material, because of the ionic nature in the bond of the oxides. Instable, balled melt tracks with rough surfaces, pores and delamination due to poor layer-to-layer adhesion might form [32].

The formation of an oxide layer, both in the solid and liquid surfaces, is particularly critic for aluminium alloys [54]. High values of laser power are indeed

necessary to break up and disperse in the melt pool or to vaporize the tough α-Al_2O_3 oxide films.

The above discussion has provided evidence of the numerous and complex physical phenomena occurring during the heating and melting of the powder bed in LPBF. These phenomena, which are schematically represented in Figure 14, include laser beam absorption and scattering, melt pool hydrodynamics driven by Maranagoni flow and recoil pressure, evaporation of material, formation of spatter and wetting issues mainly due to the existence of oxide layers onto the surface of powder particles and/or chemical reactions during the process.

Moreover, with heating and melting, the development of many defects such as keyholes, spatter inside the consolidated material, lack-of-fusion or incomplete melting, balling and bonding faults is also established.

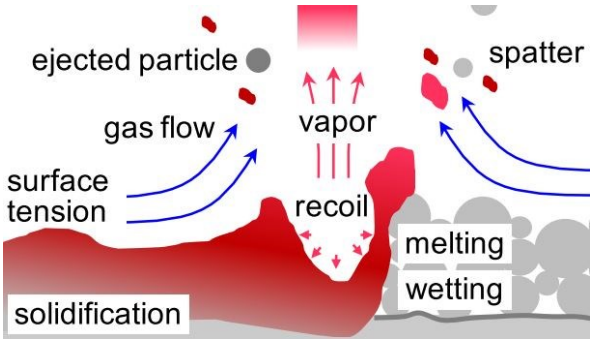

Figure 14. Schematic representation of the main physical phenomena occurring during heating and melting of the powder bed [28]

As soon as the melt pool cools down and the solidification begins, the formation of the metallurgical microstructure, which strongly determines the macroscopic properties of the material, starts.

The development of the solid-phase microstructure, consisting of the grain shape, size and orientation (texture), is ruled by the thermal regimes obtained during the process [55]. In addition, the distortion of the manufactured 3D component and the presence of defects such as hot tearing and cracking inside the material can appear and develop as consequence of the thermal residual stresses and liquation cracking phenomenon, due to the high temperature gradients and non-equilibrium solidification.

1.2.7 Thermal regimes and metallurgical effects

In LPBF, the material experiences two main thermal regimes: the first in proximity of the laser beam and the second in previously consolidated regions, in the adjacent melt tracks or below the current layer, distant from the heat source.

The first thermal regime is controlled by the local complex physical phenomena above discussed, including the absorption of the laser radiation, heat conduction within the powder bed and the convective heat transfer in the melt pool. Close to the laser beam, the material experiences a fast heating above the melting point due

to the laser energy absorption, a high velocity of the front of the melt pool produced by the high velocity of the laser beam and a rapid solidification of the molten material as soon as the laser beam has moved on. The resulting microstructure development depends on the spatial temperature gradient G and the solidification rate R (or solidification front velocity *v*), according to the scheme of Figure 15. The type of microstructure (planar, cellular, columnar dendritic or equiaxed dendritic) depends on the ratio G/*v*, while the scale of the solidification microstructure (grains size or dendrite arm spacing) depends on the cooling rate expressed by the product G×*v* [56].

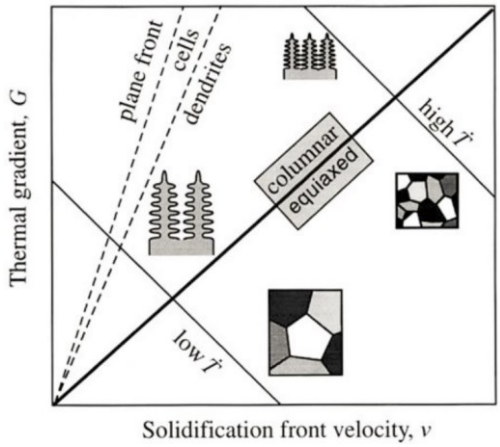

Figure 15. Schematic of the solidification map showing the effect of temperature gradient G and solidification front velocity *v* on the morphology and size of the solidification microstructure [28].

During LPBF, the material within the melt track is subjected to severe temperature gradients, which for laser melting processing have been estimated spanning over the range 10^3-10^8 K m^{-1}, and to high solidification front velocities *v*, spanning across the range 0.1-30 m s^{-1} [57]. Under these non-equilibrium solidification conditions, materials processed by LPBF generally exhibit metastable cellular or columnar-dendritic microstructures [58]. The microstructure grows from the melt pool border – where the G/*v* ratio is maximum and the temperature gradient is high - towards the melt pool centre – where the temperature gradient is lower - and along the direction of the maximum temperature gradient, which is perpendicular to the solidifying surface of the melt pool. Long grains closely aligned with the <001> build direction typically form, producing materials with strong {001} fibre texture and anisotropic behaviour and properties [22,58]. A schematic of the microstructure development mechanism for AlSi10Mg is illustrated in Figure 16 [59]. In AlSi10Mg processed by LPBF, Thijs *et al.* [60] reported the formation of a cellular-dendritic microstructure developing towards the melt pool centre and following the heat extraction direction, with long columnar grains spanning several layers along the building direction. A commonly adopted explanation for the development of the cellular-dendritic microstructure observed in many LPBFed materials is derived from the theory of weld solidification [56]. When the thermal gradients G is high and it dominates over the solidification front

velocity *v* (as it occurs in most of the polycrystalline LPBF materials), the forming solid-liquid interface becomes unstable and breaks into branches that grow faster along preferred orientation, forming cellular or columnar-dendritic structures [56]. K.G. Prashanth and J. Eckert [61] deeply investigated this phenomenon in LPBF materials, particularly for AlSi10Mg, AlSi12, CoCrMo and 316L stainless steel alloys. They found that the cellular-like solidification mechanism during LPBF is kinetically promoted - rather than thermodynamically - by the high solidification front velocity during the process and solute trapping at the solid liquid interface. Moreover, the peculiar accumulation of solutes along the cell boundaries observed in AlSi10Mg, CoCrMo and 316L stainless steel alloys is ascribed to the surface tension-driven convection within the melt pool (Marangoni convection), according to the particle accumulated structure formation mechanism (also known as PAS) [61].

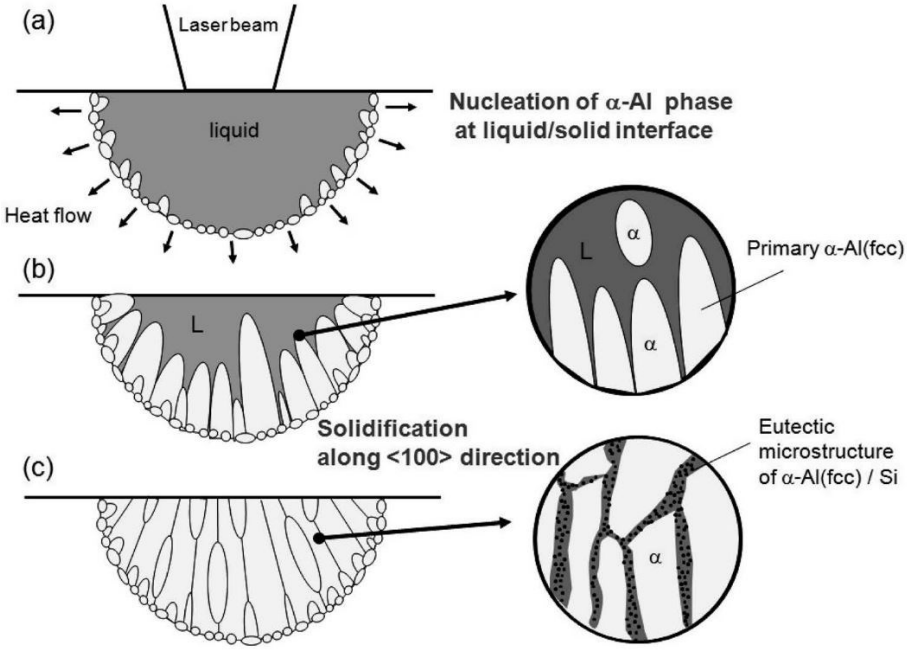

Figure 16. Schematic representation of the microstructure development of AlSi10Mg during LPBF. (a) The primary solid phase (α-Al) forms at the interface between the solid and the liquid phases, where the temperature gradient is higher, (b) the primary α-Al grains grow towards the centre of the melt pool, at higher temperature and they solidify along the preferential <001> direction, (c) at the cooling, the material is constituted by columnar α-Al grains separated by fine eutectic Si particles. [62].

In addition to the high temperature gradients and solidification front velocities, the materials processed by LPBF are subjected to cooling rates that significantly differ from those achieved in conventional manufacturing techniques for material processing, i.e. casting, further contributing in influencing the microstructure development during LPBF and in producing characteristic metallurgical effects in the materials.

In general, for laser melting processes, the cooling rates spread over the range 10^3-10^8 K s^{-1} [57], because of the small size of the melt pool and the high solid-to-

liquid ratio. In particular, cooling rates of around 10^5 K s^{-1} for Ti-6Al-4V [63] and up to 10^6 K s^{-1} for Al alloys [64] have been calculated, values significantly higher than those achieved in conventional casting (10^{-3}-10^0 K s^{-1}) [65]. For this reason, the kinetics of LPBF process gets close to that of other rapid solidification processes (RSPs) such as melt spinning, atomization, splat quenching and laser surface melting [65]. The resulting metallurgical development of the microstructure in terms of size, number and composition of phases as well as the resulting mechanical properties are thus affected by the severe thermal regime experienced by the material.

The high cooling rate and the rapid extraction of the heat allow deviations from the equilibrium and the occurrence of different metastable metallurgical effects, which can be summarized as follow [65]:

- The changes in microstructure development resulting in different morphology, location and sizes of microstructural features, such as grains and phases
- The extension of the solid solubility, orders of magnitude above the equilibrium limit
- The reduction of the number and size of segregated phases
- The formation of non-equilibrium or metastable phases
- Retention of disordered crystalline phases in place of ordered and often brittle intermetallic compounds.

For instance, Jagle *et al.* [66] observed the formation of a metastable martensitic bcc structure in 18Ni300 maranging steel produced by LPBF. The rapid cooling suppressed any precipitation reaction in the as-built material and the microstructure consisted of fine supersatured cells. Thijs *et al.* [67,68] reported the formation of a metastable acicular martensitic α' phase for Ti-6Al-4V under the high temperature gradients and rapid cooling during LPBF, in place of the α + β phases observed in the traditional cast or wrought material [67,68].

Generally, the metallurgical effects of the rapid solidification during LPBF above listed typically result in materials with superior mechanical properties as compared to the same materials processed with traditional melt-base manufacturing routes, such as casting [22]. For instance, Thijs *et al.* [60] measured a hardness value for the as-built AlSi10Mg sample of 127 $HV_{0.5}$, almost twice the hardness value reported for die cast alloy [69], which they ascribed to the refined microstructure and the formation of a supersatured solid solution. Manfredi *et al.* [70] also reported an increase in the Yielding Strength (YS) of more than 30% as compared to the as-cast material, at expenses, however, of a small reduction of the elongation at break along the build direction.

Within this thermal regime, the temperature gradients and cooling rates, crucially affecting the overall microstructure, are controlled by many process

parameters, including the laser beam velocity, the energy density, the layer thickness and temperature of the building platform (pre-heating temperature) [71]. In addition, material properties, namely the thermal conductivity of the solid phase, also control the cooling rate. Local discontinuities in the heat conduction properties of the surrounding material, i.e. due to pores, may also affect the temperature gradients and the resulting microstructure development [60]. For instance, the thermal conductivity of an Al-Si alloy is around 100 W m^{-1} K^{-1} and that of the powder bed or a pore can be as two order of magnitude as lower [72].

On the other hand, the second thermal regime during LPBF consists in the repeated heating and cooling cycles of gradually lower amplitude as the laser beam melts adjacent scan tracks and consecutive layers, resulting in the characteristic temperature-time history for a LPBF material reported in Figure 17. Due to the overlap between adjacent tracks, which depends on the hatching distance value, some sections of the powder layer are exposed to multiple irradiation. The temperature in half portion of the generic track 1 quickly raises again above the melting point while scanning the track 2 and it approaches the melting temperature while processing the track 3, track 4 and so on (Figure 17a) [73]. Similarly, due to the overlap between consecutive layers, which depends on the energy input and the layer thickness, the generic layer *n* undergoes both multiple remelting and multiple solid-state transformations at gradually lower cooling rates, even after several layers (Figure 17b). The extent of these solid-state transformations as well as the resulting cooling rates can be important for understanding the microstructure of materials such as steels and Ti-6Al-4V, which are sensitive to solid-state martensitic transformations within well-known temperature ranges.

During the LPBF process, the material is thus exposed to a sort of process-inherent heat-treatment [74] for long times and the microstructure evolution can be therefore influenced by the overall thermal history [75]. Solid phase transformation nearby the remelting zones – the so-called heat-affected zones (HAZs) - leading to the formation of stable phases or to the coarsening of the microstructural features can occur as consequence of the heat conducted upon thermal cycles. For instance, Zheng *et al.* [76] observed precipitation of $Al_{12}(Fe,V)_3Si$ particles while processing Al-8.5Fe-1.3V-1.7Si alloy and Thijs *et al.* [60] observed coarsening of the eutectic Si network while processing AlSi10Mg.

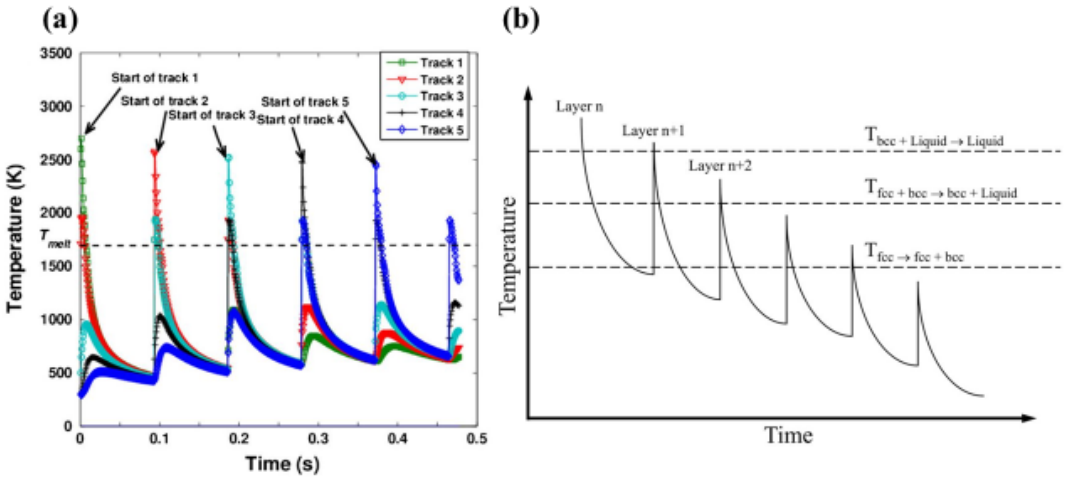

Figure 17. (a) Simulation of the cyclic melting/heating and cooling of 5 consecutive tracks in a layer during LPBF of 316L stainless steel. Due to the tracks overlap, depending on the hatching distance, previously processed sections experience repeated heating and cooling cycles of gradually lower intensity [73]; (b) schematic representation of the cyclic melting/heating and cooling history during BPF of CrMnNi steel of an arbitrary layer *n* undergoing remelting and phase transformations due to the processing of subsequent layers *n* + 1, *n* + 2, etc [74].

Within this second thermal regime, the temperature gradients and cooling rates are rather controlled by the overall part properties, such as the thermal conductivity of the solidified material, the scanning strategy, the building direction and the presence of support structures [71,77].

1.2.8 Residual stresses

As previously anticipated, together with the microstructure development, the two thermal regimes above discussed are responsible for the formation of thermal stresses into the bulk LPBFed part. Generally, thermal stresses rise as consequence of the thermal strains induced by the cyclic thermal expansion and shrinkage of the material due to the rapid phase transformation, high temperature gradients and high cooling rate but also as consequence of the thermal cycles occurring in processed layers at large distance from the laser beam.

According to the temperature gradients mechanism (TGM) model [78], the irradiated portion of material within the irradiated zone tends to expand as a consequence of the phase transition. Being the thermal expansion (ε_{th}) somewhat inhibited by the surrounding material, which is at lower temperature, the irradiated zone exists in a compressive stress-strain condition (Figure 18a). The material will retain a permanent plastic deformation if the compressive stress induced is higher than the compressive yielding strength (σ_{yield}). As soon as the laser beam has moved in another area, the previously irradiated region cools down and tends to shrink. However, the shrinkage is partially hampered by the permanent plastic deformation formed during heating and thus a residual tensile stress (σ_{tens}) condition forms in the irradiated zone (Figure 18b). The overall forces and momentum must be in

equilibrium and thus a compressive stress (σ_{comp}) forms around the previously irradiated zone.

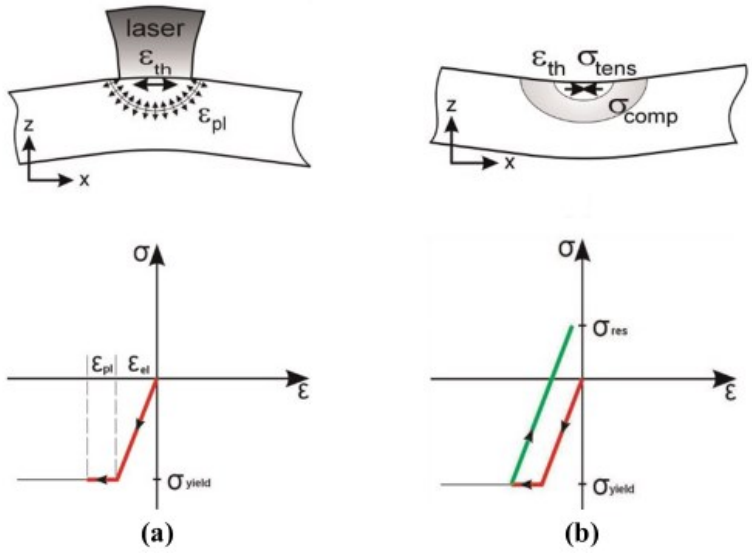

Figure 18. Induced stresses and strain in the irradiated zone (above) and schematic representation of the formation of residual stresses and strain (below) (a) during laser beam heating and (b) during cooling of the part [78].

According to the cool-down phase model, the residual stresses form when previously melted material re-solidifies and shrinks. Being the shrinkage partially hampered by the underlying consolidated material, tensile stresses form in the top layer [78].

Residual stresses need to be limited so to fully take advantage of the mechanical strength of the part when subjected to an external load, to avoid warping and eventually the formation of cracks at locations where residual stresses accumulate, such as pores or inclusions. Residual stresses depend on numerous factors, including building parameters, scanning strategy, materials properties (coefficient of thermal expansion, Young's modulus), part geometry and support structures and they can be reduced by acting on each factor which can decrease the temperature gradients during processing.

Kruth *et al.* [78] investigated the effect of the scan vector length and scanning speed on residual stresses of Ti-6Al-4V and they assessed a reduction of the residual stresses by shortening the scan vector and lowering the scan speed [78]. Shorter scan vectors result in lower temperature gradients due to the remaining heat from the previous laser track. On large surface areas, another option to reduce residual stresses can be the adoption of an island scanning strategy, patented by Concept Laser GmbH, consisting in the stochastic exposure of the powder layer with many small islands (contour + infill hatching) formed by short laser tracks [79]. Kempen *et al.* [80] investigated the effect of the building platform temperature and they found that higher preheating temperatures up to 200 °C - lowering the thermal gradients during processing - reduced thermal stresses and crack-density in M2 high-speed steel parts [80]. Mercelis and Kruth found same outcomes on 316L stainless steel [79]. They also demonstrated that residual stresses depend on part

geometry, specifically residual stresses increase with the part height. Moreover, as long as the component remains attached to the building platform, high stress values in the range of the material yielding strength may be observed. The detachment of the part from the baseplate relieves around 50% of the residual stress but critically affects the dimensional accuracy of the part, which might warp [79]. Annealing treatment is thus generally applied after processing and before support structure removal.

Residual stresses can be experimentally measured using different techniques namely microhardness [81], the contour method [82], the X-ray and neutron diffraction [83] and the hole drilling method [84]. The formation of residual stresses in LPBF can be also modelled through finite element analysis [85].

1.2.9 Liquation cracking

The rapid solidification during LPBF may also cause the formation of hot tearing and cracking defects.

For some alloy compositions, the extremely high cooling rates during LPBF are considered to modify the diffusion processes at the liquid-solid interface and to produce hot tearing cracks at the grain boundaries, according to an effect closely related to the so-called liquation cracking mechanism, commonly observed in laser welding of 'unweldable' alloys [86].

As consequence of the rapid solidification, the time for diffusion processes homogenizing the alloying composition at the liquid/solid interface is suppressed. The primary equilibrium phase that forms, which solidifies at a different composition from the liquid, causes the salute enrichment of the liquid phase near the growing solid interface. The compositional gradient alters the local equilibrium liquidus temperature and produces an undercooled liquid. As consequence of this unstable condition, the solid-liquid interface breaks yielding the formation of a thin interdendritic liquid film trapped between the solidifying regions (Figure 19) [87]. As soon as the liquid volume fraction and temperature decrease, due to the thermal contraction and volumetric shrinkage of the material, cavities and hot tearing cracks form. Cracks can span the whole length of the columnar grains and may propagate through intergranular regions [88]. According to this mechanism, materials exhibiting high fluidity at the molten stage, narrow solidification range and low coefficient of thermal expansion (CTE) as well as low solidification shrinkage are less susceptible to hot tearing.

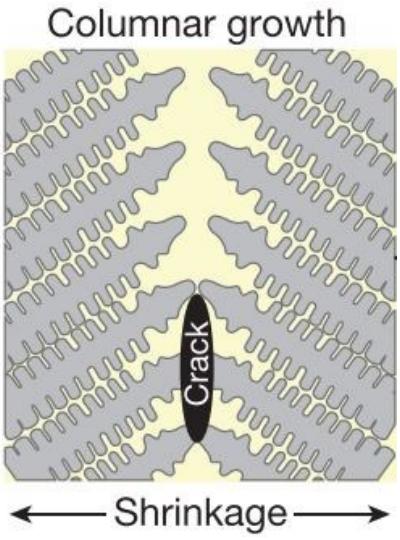

Figure 19. Schematic of the formation mechanism of hot tearing and cracks in alloys solidifying by columnar growth of dendrites and susceptible of liquation cracking [88].

Liquation cracking phenomenon is commonly observed in 'unweldable' alloys processed by LPBF, such as high strength age-hardenable aluminium alloys (i.e. 2xxx, 6xxx or 7xxx series). The presence in these alloys of Cu, Mg, Zn and Si low-cost alloying elements, carefully selected to induce the precipitation of complex strengthening phases upon ageing, promotes also large solidification range [89–91]. Also some nickel-based superalloys, such as Hastelloy X, are susceptible of liquation cracking, probably due to the Si and Mn microsegregation along the grain boundaries [92,93].

Liquation cracking need to be avoided because it suppresses the ductility of the part. One method to limit crack formation in high strength aluminium alloys processed by LPBF is to modify the composition of the alloy in order to increase the fraction of low melting eutectic phases. For instance, Montero *et al.* [94] added silicon to the Al7075 wrought aluminium alloy processed by LPBF, reporting the increase in the density and the reduction of microcracks. Zhang *et al.* [89] reported the elimination of cracks formation during LPBF of AlCu4Mg1 alloy (2xxx series) by adding Zr. Before, Martin *et al.* [88] demonstrated the possibility of producing crack-free Al7075 and Al6061 alloys by decorating the surfaces of powder particles with Zr-based nucleants at the nanoscale.

Another way to limit liquation cracking can be tailoring the process parameters. For instance, Uddin *et al.* [90] managed to produce crack-free Al6061 parts by pre-heating the building platform to 500 °C. The adoption of powder bed heating during processing, indeed, changed the thermodynamics by reducing the solidification undercooling and cracking was prevented.

1.3 Powder properties

LPBF process involves a large number of variables that affect the consolidation and thus the final properties of the part. In previous section, an extensive analysis

on the physical phenomena yielding the consolidation of the powder bed into a bulk object has been given. In addition, the mechanism of most common defects which may form during LPBF has been provided. These defects include:

- Keyhole porosities
- Rough surfaces due to balling
- Spattering
- Residual stresses
- Hot tearing and cracking

In addition, gas porosities in the melt pool and incomplete melting or lack of fusion defects may form during incorrect consolidation.

Together with the physical phenomena yielding consolidation and defects formation, it is important to know the most important factors and variable that influence and that may control the consolidation behaviour of the material and the final properties of the part. These factors can be divided into two main groups, namely powder properties and process parameters.

Powder properties affecting the consolidation behaviour during LPBF are listed in Table 1. The quality of an object produced by LPBF strongly depends on the quality of each track and each layer [25]. Since LPBF is based on the successive processing of tracks and on the successive deposition of uniform powder layers, the starting powder must have well defined physical (absorptivity/reflectivity), chemical (chemical composition) and morphological (particle shape, size and distribution) properties in order to properly be spread, flow and melt over the building platform.

Table 1. Powder properties affecting LPBF [19].

Powder properties
Particle shape
Particle size and distribution
Chemical composition
Absorptivity/reflectivity
Melting temperature
Thermal conductivity

1.3.1 Main powder production techniques

Metal powders for LPBF are mainly produced by water, gas or plasma atomization [95]. The powder production route has an impact on some powder properties, such as the particle morphology, size and chemical composition but also on the powder cost and the production rate [22].

Water atomization is generally used for the production of non-reactive powder materials, principally steels. It allows low costs and high production rates but the powder quality is poor for LPBF application. Powder particles, indeed, have an irregular shape due to the high cooling rate and thus poor flowing and packing behaviour, which negatively affect the densification. Moreover, due to the presence of oxygen in the atomization medium, the oxygen content in the material is very high and the powder particles are covered of a thick oxide layer [95]. The formation of oxide layers is undesired because they worsen the flow behaviour and the wetting ability [96]. Moreover, the presence of an oxide layer unto particle surfaces - acting as a thin ceramic coating - alters the laser absorption and modifies the melting behaviour, leading to the formation of inner defects, such as pores and inclusions [97]. Nevertheless, recently Hoeges *et al*. [98] demonstrated that water atomized 316 stainless steel particles with irregular morphology can lead to full dense parts while processed by LPBF through the optimization of the process parameters (laser power, scanning speed and spreading speed), leading to mechanical properties close to that of the same part produced from gas atomized powders. However, chemical composition differences between the water-atomized and gas-atomized 316L stainless steel powders were critically significant, deeply influencing some properties, such as the corrosion resistance of the material.

Inert gas-atomization is the most common process to produce high-purity powders for LBPF of a wide range of materials - including reactive alloys - in particular aluminium and titanium alloys but also special steels (i.e. stainless steel), superalloys and precious metals. The use of high-purity inert gases (Ar or N_2) allows to reduce the oxygen content in the powder. Moreover, due to the lower heat capacity of the gas as compared to water, the solidification time is higher and the particles are more spherical [95]. Nevertheless, for aluminium alloys, the formation of spherical particles is challenging even when produced by inert gas-atomization, because the formation of small oxide regions over particles surface induces constraints of the surface tension forces, which hinder the spheroidization of the molten alloy [72].

Plasma atomization and spheroidization process allow to produce highly spherical particles using a plasma torch that rapidly heats, melts and solidifies the material. Differently from water and gas-atomization, which use the melt alloy as feed material, plasma atomization can use bars or wires as well as particles. Plasma atomization is used to spheroidise refractory metals such as Mo and W as well as for producing extremely spherical Ti-6Al-4V particles [95].

It is worth to mention here that mechanical alloying is also commonly used to produce the feedstock powder for special alloys to process by LPBF, such as Metal Matrix Composites (MMCs) [99–102]. Mechanical alloying is a solid-state powder

processing technique consisting in the repeated deformation, cold welding, fracturing and rewelding of powder particles in a high-energy ball mill [103]. It allows to synthesize equilibrium and non-equilibrium phases, including supersatured solid solutions, metastable crystalline phases, amorphous alloys and in-situ particle reinforced composite powders [99]. Differently from gas-atomization process, which leads to spherically shaped particles, mechanical alloying generally leads to particles with irregular shapes - ideally not suitable for LPBF – similarly to water atomization. Nevertheless, Attar *et al.* [102] demonstrated that the optimization of milling parameters (i.e. milling time) while synthesizing Ti-TiB_2 MMC can lead to the production of spherical particles with good flowing and packing behaviour, which yielded the manufacturing of nearly full dense samples by LPBF. Examples of metallic powders produced for LPBF process are presented in Figure 20.

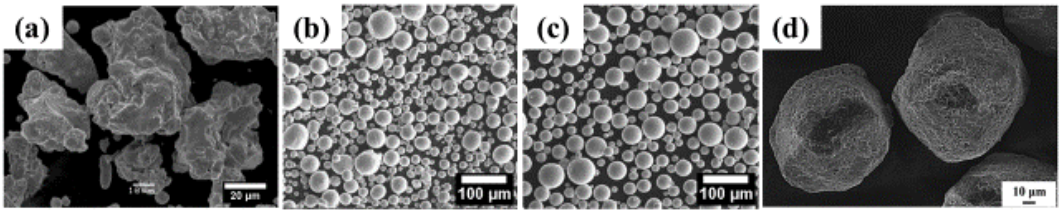

Figure 20. Examples of metallic powders produced by different processing methods: (a) 316L stainless steel produced by water atomization [98], (b) and (c) Ti-6Al-4V powders produced by gas atomization and plasma atomization, respectively [104] and (d) MMC Ti-TiB_2 MMC produced by mechanical alloying under optimized milling time [102].

1.3.2 Particle shape, size and size distribution

LPBF process requires powders with good flow properties and good packing density in order to have a homogenous spreading of the powder over the building platform and powder layers with high relative density. The particle morphology, size and size distribution control the flowing and the packing density behaviour.

Spherical and smooth particles favour good flowability on the build plate and good packing density as compared to irregular particles with satellites [96]. The particle size distribution influences the surface quality of the layer and thus the consolidation itself and the density of the part [105]. Generally, small particles easily melt over the laser radiation due to their high surface area, enhancing the overall melting of the powder bed and the consolidation/densification of the part. Moreover, fine particles enhance the packing density by filling the voids between large particles. Liu *et al.* [106] compared two 316L stainless steel powders with different size distribution and they found that the powders with more ‘fines’ and wider particle size distribution densified over a broader range of process parameters than powders with a narrow size distribution. However, due to the high cohesive forces among small particles, the excessive amount of fines suppresses the flowability [107]. On the other hand, large particles improve the flowability because of the weaker interparticle forces whilst excessive coarse particles might cause

micro grooves during the spreading of the powder, which negatively affects the powder bed homogeneity and density [107].

The optimal size distribution is related to the powder layer thickness adopted during LPBF - thus to the productivity - and to the surface finishing. Many machines use a layer thickness of 30 μm so that the nominal size distribution of gas-atomized particles usually spreads between 20 μm and 63 μm [108]. Moreover, small particles with few satellites improve surface finishing [105].

1.3.3 Chemical composition

The chemical composition of the powder particles also influences the flowing and packing behaviour as well as the densification during LPBF process.

Li *et al.* [96] showed the better densification behaviour of gas-atomized 316L stainless steel than the water atomized powder due to the lower oxygen content and higher packing density. The same alloy can exhibit different morphological properties or chemical composition also in relation to the powder suppliers. The process may be thus affected on how well the supplier adheres to the standard. Kempen *et al.* [109] studied the role of powder specifications testing AlSi10Mg powders with differences in particle morphology and size distribution and chemical composition. Their study confirmed that the quality of the final part in terms of porosity is affected by the choice of the powder batch and thus to the powder properties.

Humidity and moisture adsorbed over particles surfaces might change the chemical composition of powders, favouring the formation of hydrogen bonds upon the surface of the particles, which depress the flowability and affect the densification of the part [110]. Weingarten *et al*. [110] ascribed the existence of spherical gas pores in AlSi10Mg LPBF parts due to the desorption/dissociation of the hydrogen upon particles surfaces and to its release into the melt pool, which rapidly cools down and freezes the hydrogen bubbles. This type of porosity, however, can be reduced by removing the moisture layer from particles surfaces, i.e. by a pre-drying treatment of powder. Weingarten *et al*. [110] showed that the pre-drying of the powder at 200 °C can reduced the porosity by 50%. Similarly, Li *et al.* [111] assessed the enhancement of the densification behaviour of AlSi12 powders when pre-dried at 100 °C for 1h. X-ray Photoelectron Spectroscopy (XPS) analysis conducted on as-received AlSi12 powders, beside Al_2O_3 oxide, revealed the existence of carbonated hydroxide (Al-O-CH_xO) and moisture (H_2O) on the particles surfaces, whose subsequent drying treatment removed in favour of metal Al [111]. Yadroitsev *et al.* [112] also prescribed pre-heating of the powders before processing, in order to improve laser absorptivity.

1.4 Process parameters

The second group of variables affecting the consolidation during LPBF is related to the process parameters, whose main ones are listed in Table 2 [19].

Table 2. Main process parameters affecting LPBF [19].

Process Parameters
Laser power
Scanning speed
Hatching distance
Layer thickness
Scanning strategy
Laser beam diameter
Laser type
Protective atmosphere
Gas flow
Powder bed temperature

The most important parameters involved during the process are the laser related parameters (laser power, type and spot size), the scanning speed, the hatching distance and the layer thickness. The scanning strategy also provides a significant degree of freedom to the LPBF process. Parameters values need to be selected in order to guarantee the full melting of the layer and its proper consolidation without introducing defects due to their inappropriate combination, such as voids, pores, balling and cracks [113]. The optimization of these process parameters to obtain a full-dense part with high quality represents thus the best compromise resulting from their combination. Process parameters can also be varied in order to tailor the microstructure, mechanical properties, surface finishing as well as the production rate and cost.

1.4.1 Laser type, power and beam size

As regard the laser-related parameters, LPBF systems usually adopt Nd:YAG or Yb:YAG fiber lasers with 1.06 μm wavelength. Previous machines mounted CO_2 laser systems with a laser wavelength of 10 μm [114].

The choice of laser wavelength influences the radiation absorptivity by the material and thus the amount of energy provided to the material for melting. Most of metals best absorb at wavelength lower than 1 μm [114], as discussed in previously. Steels and titanium possess absorptivity to YAG fiber lasers between 40% and 47%, respectively, while aluminium and aluminium alloys absorb roughly

9% of the incident radiation, limiting and making more challenging their processability by LPBF [43]. Higher energy for melting can be provided to the material by increasing the laser power, resulting in better densification (Figure 21a) [115]. The first LPBF machines worked with relatively low laser powers, ranging between 100 W and 200 W (i.e. Concept Mlab cusing R [116] and EOS M270 [117], respectively) while nowadays machines has become available with laser power up to 1 KW, which has improved also the overall productivity. Kamath *et al.* [113] demonstrated that high value of laser power increases the range of scan speeds over which 316L stainless steel can reach relative densities > 99%. Same outcomes were found by Buchbinder *et al.* [118] while processing aluminium alloys. However, care must be payed when increasing excessively the laser power. The melting behaviour, indeed, can change from conduction-mode to keyhole-mode, causing the formation of long and tight molten pools, which englobe voids and defects according to the kehyhole mechanisms described before (Figure 21b). Balancing with other process parameters, namely laser beam size, velocity and layer thickness are thus fundamental.

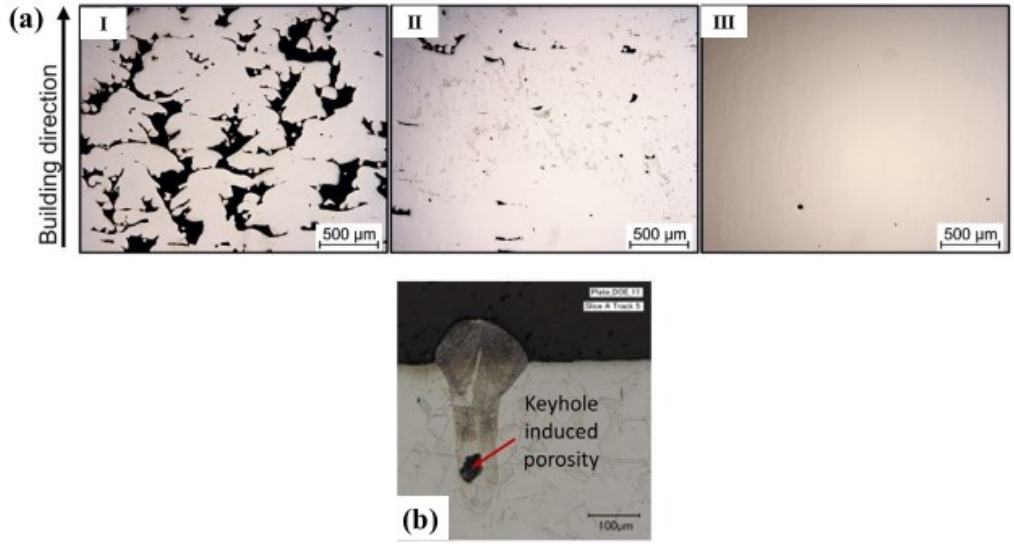

Figure 21. Effect of the laser power on densification of Ti-6Al-4V (I) 90 W (II) 120 W and (III) 180 W. Higher laser powers can reduce the porosity by increasing the size of the melt pool and thus the penetration depth [115] and (b) keyhole porosity on 316 stainless steel induced by excessive power density [47].

Among the laser-related parameters, the laser beam diameter, or spot size, plays also a key role during the densification.

The spot size defines the surface area subjected to the laser beam radiation. In YAG laser-systems, it is usually around 100 µm but it can spread between 35 and 180 µm, approximately. Together with the laser power, scan speed and hatching distance, the spot size influences the width of the melt pool [119]. Currently, the lasers used in LPBF systems have a Gaussian distribution of the energy according to which the energy intensity decreases with further distance from the laser centre.

The first consequence of having a Gaussian energy profile is that the material is primarily melted at the centre of the laser beam [119].

The second consequence of having a Gaussian energy profile is that exists a difference between the nominal laser spot size and the effective size of the scanned area (Figure 22), which creates dimensional error in the geometrical accuracy of the part contour. This error is corrected by shifting the position of the contour line to the inside of the part, making sure the contour will correspond to the 3D model [120].

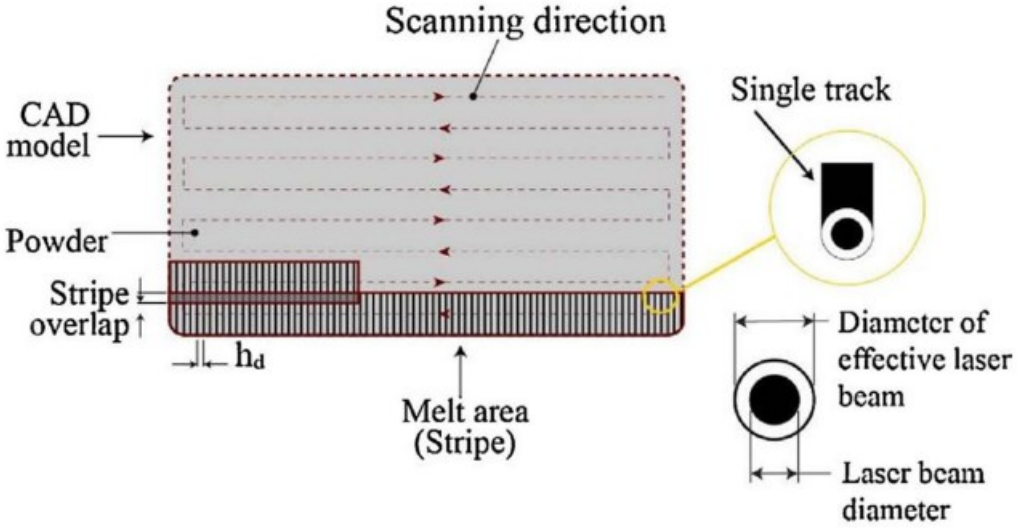

Figure 22. Schematic representation of the effective diameter of the laser beam (right side of the image), which affects the width of melt track, and of the infill hatching scheme. The melt region is divided into stripes that are filled by consecutive hatch lines (single tracks) separated by the hatching distance (h_d) [24].

1.4.2 Hatching distance

The hatching distance defines the distance between two consecutive tracks and its value is selected according to the laser beam spot size and to the laser-powder interaction [24].

The optimal degree of overlapping between adjacent tracks yielding a consolidated part is indeed affected by the extension of the cured zone induced by the laser beam profile and by the melt pool width, which is affected by many factors, including the material properties, the laser power and the scan speed. Due to this interdependence with other parameters, hatching distance must be thus optimized for the production.

Small values of hatching distance (high degree of intra-layer overlapping) lead to a high number of laser tracks and thus a low production rate. Nevertheless, Read *et al.* [121] found that small hatching distances increase the range of scan speeds over which the material can be optimally processed. However, excessive low hatching distance can be deleterious for density. Louvis *et al.* [54] found that while processing Al6061 the increased intra-layer overlapping reduced the amount of energy transferred to the material due to the higher reflectivity of the already solidified material in respect to the powder bed, causing a decrease in the density of the parts. On the contrary, high values of hatching distance (low degree of intra-

layer overlapping) will increase the production rate but extremely high values will yield poor intra-layer bonding and to the formation of gaps between the tracks. Moreover, large values of hatching distance will limit the maximum layer thickness during LPBF [122].

1.4.3 Scanning speed

The scanning speed is the velocity at which the laser beam moves over the powder bed and it generally spreads between 100 mm s^{-1} and 3000 mm s^{-1}. The scanning speed affects the time of exposition of the material to the laser beam and thus influences the maximum melt pool temperature, the cooling rate and the overall consolidation mechanism. Li *et al.* [64] found that when scanning speed increased from 100 mm s^{-1} to 400 mm s^{-1} the maximum temperature at the centre of the melt pool decreased from 1354 °C to 1032 °C during processing of AlSi10Mg, while the maximum cooling rate increased considerably. Broadly speaking, it is suggested to process the material with low scan speed and high laser power for better densification even if a compromise with fast building rates must be found. Read *et al.* [123] found that while processing AlSi10Mg, increasing scanning speed with decreasing laser power induced porosity due to incomplete melting. When excessive low scanning speeds are used, the melt pool might overheat and the track become irregular and unstable under the low viscosity of the melt [124]. Under this circumstance, the material can form so-called metallurgical pores, consisting of small (< 100 μm) and spherical pores. These defects can arise from residual gas bubbles within powder particle due the atomization process or shielding gas or alloy gases formed during the process entrapped within the melt pool (Figure 23a) [125]. On the contrary, at excessive high scanning speed, the amount of energy absorbed by material might be insufficient for complete melting of the powder bed and the solidification too rapid for the liquid alloy to fill the cavities. Lack of fusion defects – so-called keyhole pores – can form (Figure 23a) [43,54]. Moreover, at excessive high scanning speeds, the melt pool size decreases and the amount of lack of fusion defects may increase (Figure 23b) [43].

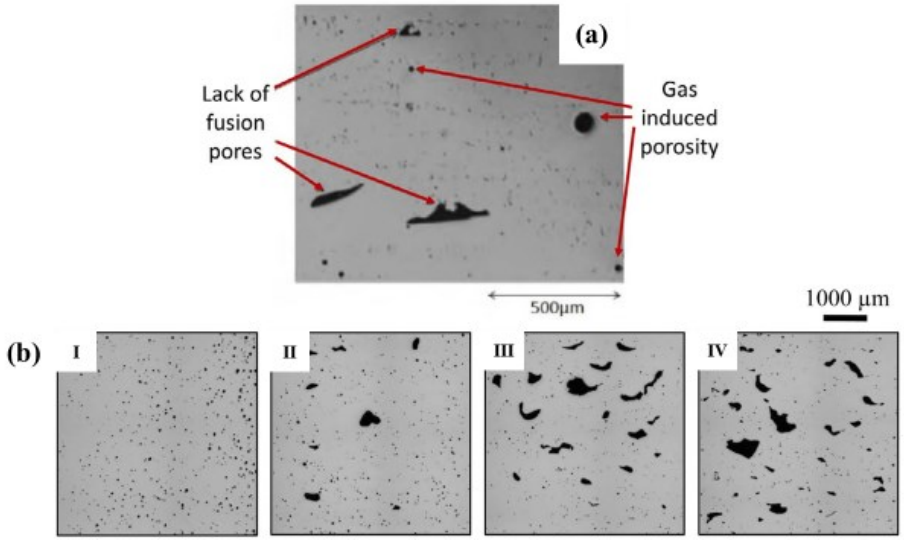

Figure 23. (a) Gas induced pores (metallurgical pores) and lack of fusion porosity (keyhole pores) on Inconel 718 [125], (b) evolution of pores in AlSi10Mg with scanning speed: (I) 250 mm s^{-1}, (II) 500 mm s^{-1}, (III) 750 mm s^{-1}, (IV) 1000 mm s^{-1}. Small and spherical metallurgical pores form at low scan speeds while large and irregular keyhole pores with enclosed non-molten powders form at high scan speeds due to insufficient melting [43].

1.4.4 Layer thickness

Due to the layer-based nature of LPBF process, layer thickness is an important process parameter affecting the overall production rate, the consolidation behaviour of the material and the surface finishing.

The appropriate value of layer thickness should be selected according to the maximum particle size and to the shrinkage underwent by the powder bed during consolidation [124] and it should guarantee sufficient remelting of the underlying layer in order to reach a high degree of inter-layer bonding. Excessive layer thickness, indeed, generates defects between consecutive layers, incomplete wetting and eventually delamination (Figure 24) while excessive low layer thickness, together with a decrease in the production rate, may imply to a decline of the quality of the part due to the interaction between the previously consolidated layer and the recoater [126]. Olakanmi *et al.* [126] found that increasing values of layer thickness imply an increase in the porosity of AlSi12. Very high layer thickness, indeed, produced large and interconnected pores. Layer thickness must be appropriate to the other processing parameters, such as laser power, scan speed and hatching distance. Yadroitsev *et al.* [124] found that higher laser power increases the range of layer thickness for obtaining continuous tracks while processing 316L stainless steel.

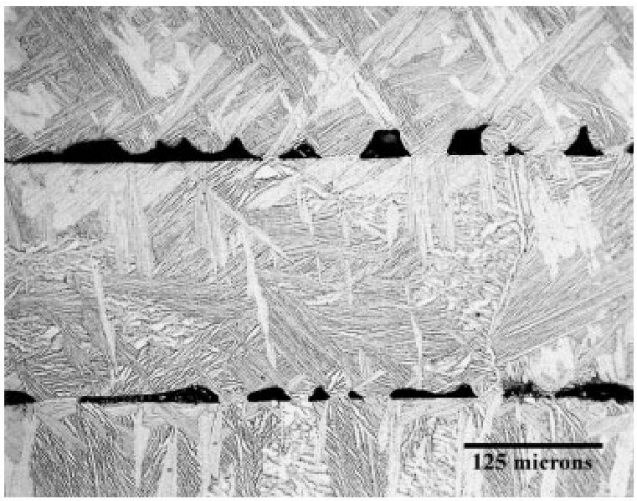

Figure 24. Microstructure of LPBFed Ti-6Al-4V exhibiting insufficient substrate remelt and poor interlayer bonding due to inappropriate laser energy intensity for the given layer thickness [32].

1.4.5 Energy density

Beyond the effect of single process parameters, the densification of the powder bed depends on the overall energy transferred by the laser beam. Indeed, if a sufficient amount of energy is transferred to the particles, the laser energy heats up the powder beyond the melting point and allows to the alloy to melt and to consolidate.

A. Simchi [127] was the first who tried to define the correct amount of energy to be transferred to the powder bed in order to achieve the densification of the metal powders. His approach considered the laser power (P), scanning speed (v), hatching distance (h_d) and layer thickness (t) as the process parameters controlling the energy input during LPBF and combined the above-mentioned parameters to define the volumetric energy density factor Ψ as [127]:

$$\Psi \left[\frac{J}{mm^3}\right] = \frac{P}{v \times h \times t} \tag{1.2}$$

According to this definition, the energy is a measure of the average energy applied to a volume of material during the laser scanning of a layer [67].

Many authors have used this concept to assess the effect that different energy density values had on material densification [123,128] and it has been often used as a tool to compare parts manufactured adopting different combinations of deposition parameters. Simchi *et al.* [127] found that a high energy input (high laser power, low scanning speed, low hatching distance, low layer thickness) favoured better densification while processing different metals powders, whilst a saturation level existed above which further enhancement could not be achieved. Gong *et al.* [129] correlated the energy density to the internal porosity of Ti-6Al-4V parts, showing that residual porosity was lower when the deposited energy density fallen within a window of values. Low values of energy density caused the retention of many

macroscopic pores due to insufficient melting while excessive high values of energy density induced "keyhole mode" melting and increased part porosity. Meier *et al.* [130] found the best densification of 316 stainless steel when energy density values varied between 40 J mm^{-3} and 90 J mm^{-3}. For Al, Al-Mg and Al-Si alloys Olakanmi *et al.* [131] found a narrower range and optimum densification between 60 J mm^{-3} and 75 J mm^{-3}.

In other studies, the main process parameters were combined into surface energy density $\Psi = P/(v \times h)$ [131] and linear energy density $\Psi = P/v$ [132,133] and many process windows were suggested. For instance, by varying the laser power (20-240 W) and the scanning speed (20-250 mm s^{-1}) by keeping constant the hatching distance (h_d = 0.1 mm), Olakanmi *et al.* [131] identified four different consolidation regions for Al, Al-Mg and Al-Si alloys, namely:

1. "No marking" region, where the energy density was not sufficient to melt and bond particles together (energy density < 3.2 J mm^{-2}).

2. "Partial marking" region, where the liquid phase produced was not sufficient to effectively fill the voids between particles due to the low energy input and the material surface exhibited a network of small, open and deep pores (energy density 3.3-10 J mm^{-2}).

3. "Good consolidation" region, where the energy provided to the powder bed was able to promote the full melting of the powder bed and to reach high densification levels. Lower viscosity of the molten alloy, indeed, enhanced the densification by facilitating liquid infiltration (energy density 12-30 J mm^{-2}).

4. "Excessive balling" region, where the synergic effect of high laser power and low scan speed produced an excessive amount of liquid phase, which induces melt pool instability and generated balling (energy density > 30 J mm^{-2}).

Nevertheless, recent studies have pointed out on the limitation of energy density to capture the complex physical phenomena occurring within the melt pool, which lead to consolidation or defects formation, such as Marangoni flow, recoil pressure inducing keyholing, Plateau-Rayleigh instability inducing balling, etc. [24,134]. Energy density is a derived process parameter and a thermodynamic quantity and different authors have advised on exerting caution when using it as design parameter for LPBF process [134]. F. Calignano *et al.* [24] compared AlSi10Mg thin walls manufactured at different laser powers and scanning speeds and they reported differences in the walls morphology whilst the combination of the process parameters yielded the same energy density. Similarly, Bertoli *et al.* [134] demonstrated that the energy density was not able to capture the transition from conduction-mode to keyhole-mode melting when processing single scan tracks of 316L stainless steel at same energy densities but with different process parameters.

1.4.6 Scanning strategy

The scanning strategy is another process parameter offering a high degree of freedom during LPBF. The scanning strategy includes the scan pattern, which refers to the direction of the tracks within a layer, and the scan orientation, which refers to the alignment of the tracks among consecutive layers. The combination of scan pattern and scan orientation produces different scanning strategies, whose most common are illustrated below in Figure 25.

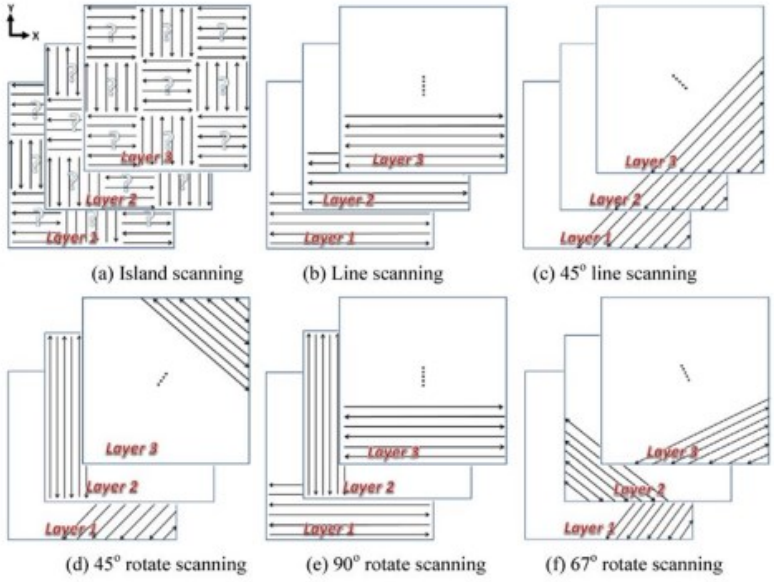

Figure 25. Representation of the most common scanning strategies adopted in LBPF [135].

The main purpose of scanning strategy is to minimize the residual stresses, which develop during LPBF as consequence of thermal gradients, as discussed in 1.2.8 Residual stresses paragraph [136,137]. Nevertheless, consolidation behaviour [43,122], microstructure development [60] and mechanical and functional properties [136,138] are also affected by the scanning strategy and for this reason many studies have been dedicated to the relationship between scanning strategies and properties of the LPBFed parts.

Comparing different scanning strategies, processing Ti-6Al-4V with island scanning strategy Ali *et al.* [136] found that increasing the island size from 2×2 mm^2 to 3×3 mm^2 and 5×5 mm^2 led to higher residual stresses due to the more severe cooling rate at higher scan vector length and that the 90° rotate scan strategy yielded the lowest residual stresses. Traditionally, island scanning strategy has been considered more effective that other strategies in reducing residual stresses [79] but the study conducted by Ali *et al.* disagreed, as confirm the complex relationship between scanning strategy and material behaviour.

As stated above, the microstructure development is affected by the scanning strategy. Due to the partial remelting of previous layers and to the directional thermal gradients within the melt pool, grains generally grow following preferred orientations in LPBF and a wide range of alloys adopt a <001> fiber solidification texture [139]. Thijs *et al.* [60] found a textured microstructure in AlSi10Mg

processed by LPBF, which however changed from a strong fiber texture aligned to the build direction to a weak cubic texture when scanning strategies passed from unidirectional to 90° rotate scan strategy, respectively. Island (or checkboard) scanning strategy was even more effective in further reducing the texture.

The authors also reported that the rotate scan strategy was effective in reducing the porosity of the parts as compared to the unidirectional line scanning strategy because it reduced the possibility of stacking the defects produced in a layer, which led to interconnected porosity [60]. Yadroitsev *et al*. [124] suggested then the double laser exposure per layer and the 90° rotate scanning strategy to contrast the formation of interconnected defects while processing 316 stainless steel, Inconel 625 and cobalt-chromium. Aboulkhair *et al.* [43] found that the double exposure strategy per layer was actually effective in reducing keyhole porosity in AlSi10Mg compared to the single exposure per layer, regardless the type of scanning strategy, whilst the metallurgical pores increased and the overall porosity remained slightly the same. In other words, double exposure per layer affected rather the type of pore than the porosity level itself. An effective reduction of porosity was assessed by adopting the pre-sinter scanning strategy, consisting in the double exposure of the layer where the first scan was at half laser power [43].

As regard mechanical properties, Guan *et al.* [138] found that among different scanning angles between consecutive layers (90°, 105°, 120°, 135°, 150°), 304 stainless steel samples fabricated at hatch angle of 105° had the highest yielding and ultimate tensile strengths. Since the strong oriented-growth nature of the LPBF process inducing strong anisotropy in microstructure and thus in mechanical properties, scanning strategies able to have a random-like filling patter would allow not only to accumulate less defects during the building but also of reducing anisotropy. Hatch angle of 105° provided the highest number of layers before the scanning directions become the same and thus the highest degree of random-like filling.

1.4.7 Platform temperature

The platform temperature is a process parameter that can help in reducing the residual stresses because it acts on the decrease of the thermal gradients (or cooling rate) during processing [79,80]. However, the material fabricated at high building temperature undergoes a kind of heat treatment from the bottom to the top of the part, which can induce significant variations also in microstructure, consolidation mechanisms and mechanical properties of as-built specimens.

Buchbinder *et al.* [140] observed a significant coarsening of the Si dendrites in AlSi10Mg samples when fabricated with pre-heating at 200 °C, due to the lower cooling rate. Because of the microstructure coarsening, the hardness also decreased. Still related to the lower thermal gradients experienced by the material, Shi *et al.* [141] recently observed that the amount of large columnar grains decreased in favour of small equiaxed ones when platform temperature increased from 35 °C to 200 °C while processing Scalmalloy, an Al-Mg-Sc-Zr alloy. Moreover, the higher platform temperature yielded higher mechanical anisotropy between the bottom and

the top of the specimens, due to the more prolonged heat treatment at the base of the sample [141]. The authors also reported that higher platform temperatures resulted in consistently better densification of the material as compared to the material processed at room temperature, especially at low energy density. Moreover, the platform temperature was found to affect the pore number and size on samples fabricated at 200 °C. On the one hand, the higher building temperature enhanced the fluidity of the melt and the filling of the small lack-of-fusion defects, decreasing the overall number of pores, but it also accelerated the gas expansion and the coalescence of gas bubble, increasing the number of large metallurgical pores.

1.4.8 Process atmosphere

The process atmosphere during LPBF is another parameter closely related to the densification behaviour, the type and amount of defects generated during the process and thus to the final properties of LPBFed parts.

First of all, while processing alloys highly susceptible to oxidation, such as aluminium alloys, inert gas atmospheres are necessary in order to prevent oxidation reactions both in the solid and liquid metals, which can affect the wettability to the previous layer and the final density [97]. Wang *et al.* [142] investigated the effect of three different purging gases, namely argon, nitrogen and helium, on the densification behaviour of AlSi12 alloy. They did not asses any significant difference in hardness and density among samples processed with different gases, even if isolated pore clusters suppressing the ductility of the material were observed in samples processed under helium atmosphere. Differently, Zhang *et al.* [143] found a more significant influence of the protective gas on densification behaviour while processing 316L stainless steel. In particular, Ar and N_2 yielded densities > 99% while He promoted the formation of continuous and linear porosities, which resulted in material densification < 90%. The reason for such different behaviours between Ar and N_2 on one side and He from the other side was related to the different plasma conditions, which occurred above the melt pool. Helium gas forms a plasma shielding the laser beam at higher height than Ar and N_2 do, due to its higher ionization energy and lower specific gravity. The laser energy transport to the powder bed can be thus dramatically hindered due to the increased distance between the plasma and the melt pool, rationalizing thus the formation of pores and lack of fusion defects characteristic of low energy input.

Another parameter related to the process atmosphere is the gas flow rate. During LPBF processing, the inert gas is continuously purged within the chamber creating a gas recirculation, which helps in removing the spatter produced during the process [49]. Studying the effect of gas flow rate in spatter removal is thus important to improve the properties, quality and homogeneity of LPBFed parts. Ferrar *et al.* [144] reported that slow gas flow rate reduced the density and compression strength of CpTi samples due to the lower efficiency in condensate and spatter removal from the powder bed. Condensate are small particles formed as consequence of metal vaporization which absorb and scatter a fraction of the

incident radiation, reducing the effective energy delivered to the powder bed and increasing the size of the sintered area weakly consolidated near the laser beam [144]. Recently, Nguyen *et al.* [50] investigated the effect of gas flow on the homogeneity of properties of samples manufactured by LPBF. Due to the directional flow of the gas stream, the quality of samples was found to be affected by both the position over the building platform and the gas flow rate. The authors found that the porosity of samples close to the inlet gas was lower than the one of samples positioned at greater distance (Figure 26), likely due to the redistribution of spatter over the building surface, resulting then in low product homogeneity. Moreover, higher flow rates reduced the overall porosity and the porosity-gap between samples positioned close to the gas inlet and to the gas outlet probably because of the higher removal efficiency.

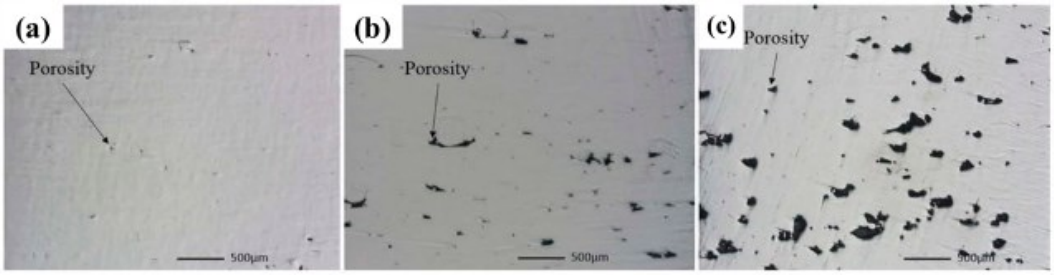

Figure 26. Variation of the porosity of manufactured Ti-6Al-4V parts processed with the same machine parameters following the purging gas flow direction (a) closet the inlet, (b) middle position and (c) close to the outlet [50].

1.5 Materials for LPBF

The alloys suitable to be processed by LPBF must fulfil different criteria. They must have good weldability and narrow solidification range, low segregation and low elemental losses in order to prevent from liquation cracking phenomena, defects formation upon solidification as well as instability phenomena within the melt pool [145]. In addition, they must be available in the form of gas-atomized alloy powders, with tight compositional tolerances and homogenous composition as well as flowing and packing properties optimized for the layer-wise manufacturing process [146], as anticipated in 1.3 Powder properties paragraph.

To date, there is a limited number of alloys that fulfil the above-mentioned requirements and that are able to be processed by LPBF for commercial applications. Table 3 lists the most important alloy compositions available, consisting in Titanium and Titanium alloys, Cobalt-Chrome alloys, Nickel-based superalloys, Steels, few Aluminium alloys and since recently precious metals, few Copper-based alloys, refractory alloys and BMGs. The research on the development of new materials is thus of current interest so to catch the broad opportunities opened up by LPBF in many industrial fields.

Table 3. Main materials commercially available for LPBF.

Material class	Alloy composition	References
Ti-based alloys	Cp Ti grade 2 Ti-6Al-4V Ti-6Al-4V ELI	[147]
Co-Cr alloys	MP1 (Co28Cr6Mo) SP2 (Co25Cr5Mo)	[147]
Ni-based superalloys	Inconel 625 Inconel 718 Hastelloy X	[147]
Tool steels	MS1 (Maraging Steel or 300) H13	[147]
Stainless steels	316L 17-4 (GP1) 15-5 PH (PH1) CX	[147]
Al-based alloys	AlSi10Mg AlSi7Mg (A357) AlSi12 ScalmalloyRP® A20X™	[147] [148] [148] [149] [150]
Precious metals	Red/Yellow/White Au Pt	[151] [152]
Refractory alloys	W Ta	[147,153] [154]
Copper-based alloys	Pure Copper Copper alloys	[155] [156]
Bulk metallic glasses (BMGs)	Zr-Cu-Al-Nb BMG	[157,158]

On the one hand, the industries and universities have driven intensive research on the development of conventional alloys able to be processed by LPBF and great interested has been addressed on LPBF of low densities Aluminium alloys.

As shows the pie chart in Figure 27, over the last 9 years, the percentages of scientific publications related to LPBF of Al-based alloys (around 30 %) was second only to that related to Ti-based alloys (around 35 %). The dominant role played by Titanium and Titanium alloys with respect to other alloy systems is motivated by significant manufacturing costs and time reduction that LPBF of these alloys yield as compared to the traditional machining route. Titanium and Titanium alloys are broadly applied in the medical and biomedical fields for the production of customized prostheses and implants as well as for the manufacturing of lightweight structural components for the aerospace field [159] and studies aimed to their optimization and/or development by LPBF allow the manufacturing of more critical and complex parts.

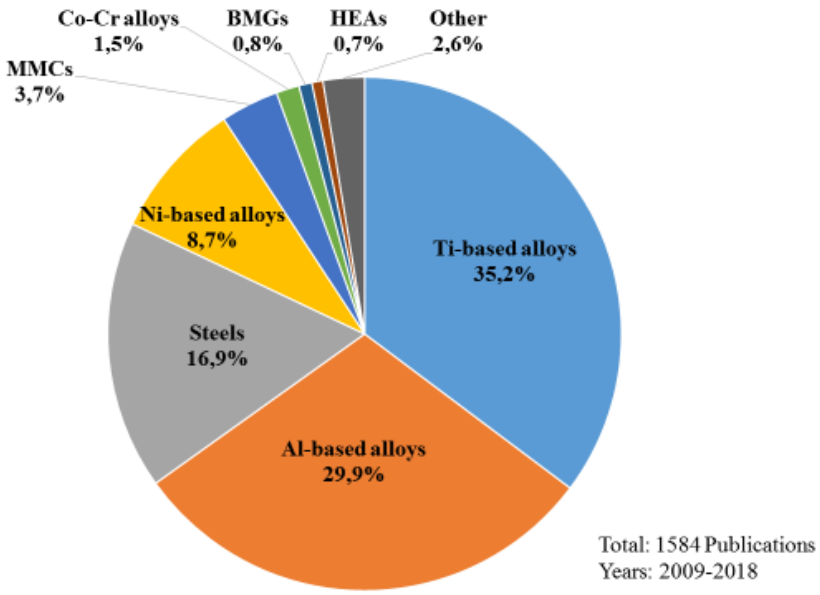

Figure 27. Pie chart of recent 9 years (2009-2018) publications of different alloy systems produced by LPBF. 'Other' includes precious metals, Cu-based alloys, refractory metals, shape memory alloys and Mg alloys (source: www.scopus.com).

On the contrary, the low density and outstanding properties of Aluminium alloys motivate the broad interest in their development for LPBF, being ideal candidate for the manufacturing of high strength-to-weight components for the automotive and aerospace fields. However, with respect to the vastness of Aluminium systems available for traditional manufacturing routes, the portfolio of Aluminium alloys able to be processed by LPBF is limited to few alloys mostly belonging to the Al-Si system. The following reasons can be given in order to rationalize the existing gap and limited number of Aluminium alloys for LPBF [22,72]:

- Aluminium alloys can be easily processed by machining and casting, differently to i.e. Ti alloys. For this reason, they have been employed for LPBF applications quite late.

- Aluminium is significantly cheaper to purchase than other materials, i.e. Ti, and thus the actual material/cost savings adopting AM is less significant and it yields lower commercial advantages as compared to other materials.

- Aluminium alloys are highly reflective to the wavelength usually adopted in commercial LPBF systems, posing challenges in the manufacturing of full dense parts. Moreover, they have high thermal conductivity that is effective in limiting thermal stresses by reducing temperature gradients within the melt pool but it makes necessary to provide more energy for melting the material. In addition, the high

thermal conductivity affects the minimum melt pool width, thus the minimum feature that can be realized by LPBF.

- Many traditional high-strength Aluminium alloys, i.e. those belonging to the series 2xxx, 6xxx and 7xxx, are 'unweldable' and susceptible of the liquation-cracking phenomenon, which yields cracked samples. Moreover, the vaporization of hardenable volatile elements, such as Zn in Al7075 alloy, creates turbulences in the melt pool and spattering phenomena that increase the porosity and lower the quality of the LPBFed part.

- Aluminium alloys have poor spreading behaviour due to the non-perfectly spherical shape of powder particles and to their low density, which induce high cohesive forces among particles.

To date, the most processed and almost unique Aluminium alloy for LPBF is AlSi10Mg [19], which is a cast Al-Si-Mg alloy (A360) belonging to the series 3xx.x. Its commercial success over other systems, such as the high-strength Aluminium alloys belonging to the 2xxx, 6xxx and 7xxx series, lies on its good processability by LPBF, due to the good castability, narrow solidification interval, low viscosity at the molten stage and low coefficient of thermal expansion [145]. Aside with AlSi10Mg, other Aluminium alloys - all belonging to the Al-Si system - are commercially available for LPBF, including AlSi12 [111,160,161], AlSi7Mg0.6 (A357) [162–164], AlSi12CuNiMg [162] and AlSi9Cu3 [162]. However, over the years, AlSi10Mg only has gained maturity thanks to the vast number of studies, which focused on optimizing its processability [109,165,166] and on investigating and characterizing its microstructure [60,120,167,168], mechanical properties - both static and dynamic [169] - and corrosion resistance [170–174], further consolidating its leading position in the field of LPBF of Aluminium alloys. Although AlSi10Mg and the other Al-Si alloys have been reported to have a broad range of mechanical properties, all meet around a yielding strength of about 200-250 MPa, a ductility as low as 5% in the as-built conditions and thermal resistance up to 250 °C [175–177], which render them not suitable for aeronautical structural applications. At the moment, one exception exists readily available on the market and it is represented by SCALMALLOY®RP, a new Aluminium-Magnesium-Scandium (Al-Mg-Sc) alloy developed by Airbus Group with high corrosion resistance, high specific strength and outstanding fatigue and toughness properties [178]. It has a yielding strength of 470 MPa, ductility of 13% and thermal resistance up to 350 °C [149]. However, it is extremely expensive due to the presence of Sc. Great attention is thus given on expanding the portfolio of Aluminium alloys able to be processed by LPBF and with superior properties than conventional AlSi10Mg.

On the other hand, recently, the extremely tailorable and promising properties of HEAs - as it will be deeply discussed in Chapter 4 - has motivated both a

considerable – if it is considers the novelty of the topic – and growing interest in their development for LPBF, as shows the histogram reported in Figure 28.

By tailoring the concentration and the type of the constitutive elements, in fact, HEAs can exhibit high specific strength, good thermal stability, oxidation and wear resistance for potential applications in the automotive field [179] or excellent thermal stability and resistance to the thermal softening, for potential applications in the aerospace field [180]. In 2015 Brief *et al.* [181] demonstrated that LPBF was suitable for producing chemically homogenous CoCrFeNi HEA with single phase structure.

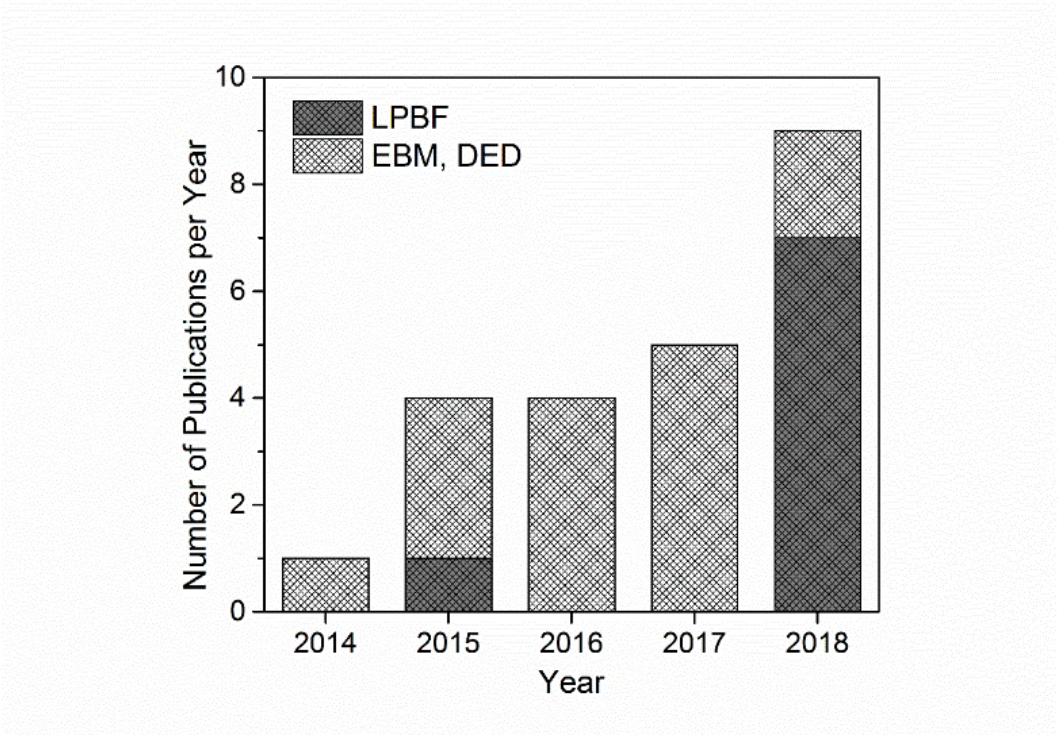

Figure 28. The publication rate for HEAs processed by MAM techniques (LPBF, EBM and DED). Data gathered from Scopus by searching for "High Entropy Alloys" in the article title, abstract field and limiting the research to results containing "additive manufacturing" keyword (source: www.scopus.com).

1.5.1 Material development opportunities for LPBF

Jan Van Humbeeck and Bey Vrancken [17] said that MAM technologies, in particular LPBF, can provide great material development opportunities. By tailoring the alloy compositions so to take advantage of the effects of the rapid solidification then materials with new microstructures, phases and precipitates - and thus properties – but also enhanced processability can be obtained [65].

There are at least two successful stories of material development for LPBF that worth to mention here. Firstly, the development of SCALMALLOY®RP. This case has revealed that the addition of Sc to an Al-4.6Mg-0.42Zr alloy beyond its solubility limit produced a supersatured solid solution of Sc under rapid cooling, which promoted the formation of an ultrafine microstructure with high-density of

nanostructured Sc-precipitates and unique combination of yielding strength and ductility [182,183]. Details on the microstructure development of this alloy during LPBF will be given in Chapter 2, specifically focused on Aluminium alloys. What it is worth to add here is that the composition of SCALMALLOY®RP was specifically tailored for LPBF in order to take advantages of the rapid solidification during the process and to produce high quality objects, with low residual porosity and optimal microstructure and properties. Secondly, the development by Exmet AB company of a full amorphous and dense Zr-Cu-Al-Nb bulk metallic glass (BMG) component by LPBF using an alloy powder with a chemical composition hardly processable through traditional casting route [157,158]. Bordeenithikasem *et al.* [157] demonstrated that the cooling rate during LPBF was sufficiently high to vitrify feedstock powder with high content of oxygen. A material thicknesses never achieved with the same material processed by casting route was obtained by LPBF, leading the way to the overcoming of the upper limitation in size for amorphous metal components produced by traditional casting route thanks to the use of LPBF.

Beyond these successful cases, when attempting to develop materials whose compositions are specifically tailored for LPBF, the capability of the market of effectively providing gas-atomized alloy powders suitable to be processed by LPBF and with customized compositions should be considered. Gas-atomized alloy powders with customized composition, in fact, can be rather difficult to readily source commercially and/or extremely expensive, because of the limited number of powder producers available on the market and/or the large size of the minimum batches that the producers push to gas-atomize. In addition, some alloy compositions can be intrinsically difficult to gas-atomize, creating biases into the quality or chemical composition of the purchased powder. For instance, certain alloying elements, i.e. Zr, added to Aluminium alloys can modify the properties of the melt, making gas atomization of the feedstock material difficult [88]. For some HEAs compositions, the broad differences among the constitutive elements in their physical properties (melting points and vapour pressures) at high temperatures make hard the production of homogenous melts and thus the subsequent gas-atomization. For all these reasons, recently, many studies highlighted the flexibility offered by LPBF of processing powder mixtures of different materials for producing *in-situ* new materials, without resorting to gas-atomized powders [184–190]. The possibility of *in-situ* alloying different powders during LPBF would allow to overcome the issues related to the poor availability/high costs of gas-atomized alloy powders with customized compositions, by processing a multiple-powders batch with the required final alloy composition. Then, it would allow to overcome technological limitations and/or difficulties in the atomization of some alloy compositions, by resorting to the use of commercially available powders only. In addition, it would allow innovating alloys with high composition flexibility, avoiding to purchase large batches of gas-atomized alloy powders of fixed composition. Sing *et al*. [184] demonstrated the capability of LPBF of producing a novel TiTa alloy with potential application in the biomedical field processing powder mixture of Ti-50wt%Ta. The authors pointed out on the importance of the

energy density for fully melting the powder mixture and homogenising the composition. Other researchers foresee material development opportunities for LPBF in the processing of several powder mixtures with different compositions in order to evaluate the effects of the concentration of a particular alloying element on the phases, microstructures and resulting properties and to accelerate the design of a composition suitable for LPBF to eventually gas-atomize in a subsequent research step [89,186,191–193]. For instance, with the aim of developing novel antibacterial biomedical materials based on CoCrW alloy, Lu *et al.* [191] preliminarily investigated the effect of Cu on microstructures, mechanical properties, corrosion behaviour and cytotoxicity by mixing different amounts of Cu to the base CoCrW alloy.

Another aspect that should be considered when attempting to develop new materials for LPBF concerns the great financial resources invested in the purchase, use and consumption of material in the powder form. Methodologies aimed to preliminarily investigate the processability of new materials by LPBF without consuming large amount of materials can avoid the wastage of precious resources and the Single Scan Track (SST) technique is commonly adopted with this purpose. In SST, a thin layer of powders, generally around 50 μm and spread over a substrate, is laser scanned according to one directional line at fixed laser power and scanning speed. The characterization of the SSTs has been extensively used for capturing the effect of certain physical phenomena, such as keyholing or balling, on the SSTs morphology, which hinder from obtaining dense bulk samples [194,195]. In this regard, Aversa *et al.* [194] adopted the SST technique for defining an optimal process window for obtaining stable and continuous SSTs of AlSi10Mg, which enabled the manufacturing of dense AlSi10Mg bulk samples. Nevertheless, the characterization of the SST can be extremely useful not only for optimizing the processability of commercially available materials but also for having a first insight into the behaviour of new compositions under the laser beam during LPBF as well as their solidification microstructure and mechanical properties. For instance, Nie *et al.* [193] adopted the SST technique for finding the optimal processing parameters for obtaining dense and crack-free Al-Cu-Mg alloy bulk samples. In addition, the analysis of the SST cross section allowed to gain information on the microstructure development of the material below the laser beam, the distribution of the elements within the melt pool as well as on the local mechanical properties through nanohardness measurements. The authors observed different microstructures moving from the edge to the centre of the SST, due to the variations of the temperature gradients within the melt pool. Li *et al.* [196] performed a preliminary study into the feasibility of manufacturing $Al_{86}Ni_6Y_{4.5}Co_2La_{1.5}$ metallic glass by LPBF by producing SSTs at different laser power over a porous substrate obtained by spark plasma sintering of the same material. Due to the non-homogenous Gaussian-energy distribution of the laser and to the heat transfer phenomena within the melt pool, the material experienced different cooling rates and the authors observed the formation of gradient-like microstructures with local crystallization of the amorphous phase. Thermal fluctuations within the melt pool caused inhomogeneous chemical distribution and severe devitrification and the high

thermal gradients produced several cracks, due to the thermal stresses [196]. In a recent study, Piglione *et al.* [197] produced SSTs of CoCrFeMnNi HEA alloy powders spread over a stainless steel substrate, in order to assess the printability of the material by LPBF as well as the resulting solidification microstructure. Due to the heat conduction through the substrate, the cells were found to grow normal to the fusion line and oriented along the <001> orientation, aligned to the direction of the maximum heat flux. Moreover, due to the high cooling rate during LPBF, the authors observed that the solidification cells were extremely fine.

These studies point out on the significance of SSTs characterization for gaining information into the processability of novel materials by LPBF, the phase transformations that may occur as consequence of the different cooling rates within the melt pool, the resulting solidification microstructure as well as mechanical properties.

In the light of the concepts introduced in the present chapter, the next two sections will focus on the development of Aluminium alloys or HEAs with targeted properties. In both cases, strategies aimed to prevent from the use of gas-atomized alloy powders and/or limit the consumption of material in the powder form will be adopted.

Chapter 2

First section: Literature review on Aluminium Alloys

The scope of the present chapter is to provide a summary of the main findings in the literature regarding the development of new Aluminium alloys for LPBF. The chapter will begin with the strengthening mechanisms commonly adopted for improving the mechanical properties of Aluminium alloys and it will go through the efforts did in the past for developing high-strength Aluminium alloys by traditional rapid solidification techniques, i.e. melt spinning. Then, the microstructure and properties of AlSi10Mg, the most processed Aluminium alloy by LPBF, will be summarized, along with the most significant trials up to this moment done for developing novel Aluminium alloys by LPBF.

2.1 Aluminium alloys

Aluminium alloys possess properties considered outstanding for many demanding industrial fields, i.e. automotive, transportation, defence and aerospace. Their low density (2.7 g cm^{-3}), high strength and good corrosion resistance have made them suitable candidates for high strength-to-weight structural components [18].

Wrought aluminium alloys based on the series 2xxx (Al-Cu, Al-Cu-Mg), 6xxx (Al-Mg-Si) and 7xxx (Al-Zn-Mg, Al-Zn-Mg-Cu) are heat treatable and find applications in aircraft and automobile industry. For instance, Al7075 has high strength but very limited weldability. The alloy 6061 has medium strength but better weldability [18].

On the contrary, cast aluminium alloys based on the Al-Si-Mg (3xx.x series) system are attractive mainly for the automotive industry. Alloys such as A356 and A357 are used for wheels, transmissions and cylinder heads parts. They have excellent castability and weldability coupled to high strength induced by precipitation of Mg_2Si phase, which make the alloys also heat-treatable. The AlSi9.5Cu3Mg is a common piston alloy used for internal combustion engines. The addition of Cu to cast Al-Si-Mg alloys also induces age-hardening, further strengthening the alloy but reducing castability, ductility and corrosion resistance [18]. AlSi12CuMgNi2 is another common piston alloy used for internal combustion engines. Alloying with Ni boosts the thermal strength of the Al-Si-Mg system by promoting the formation of thermally stable intermetallic compounds that also induce dispersion hardening [18].

2.1.1 Strengthening mechanisms

The main strengthening mechanisms adopted to improve mechanical properties of Aluminium alloys are solid solution strengthening, Hall-Petch strengthening and particle strengthening.

2.1.1.1 Solid solution strengthening

Solid solution strengthening occurs when the alloying element forms a solid solution with the base alloy. It arises from atomic size differences between the solute and the solvent atoms. The presence of alloying elements in the base alloy, indeed, generates stress and induces a lattice strain that impedes the dislocation motion, thereby increasing the hardness and the yielding strength [198].

The increase in the yielding strength $\Delta\sigma_{ss}$ due to solid solution is related to the atomic concentration of the alloying species (c) and to the atomic misfits (ε) between the species, as follows [18]:

$$\Delta\boldsymbol{\sigma_{ss}} = \mathbf{3.1}\frac{\boldsymbol{\varepsilon G\sqrt{c}}}{\mathbf{700}} \tag{2.1}$$

Where G is the matrix shear modulus.

The alloying elements with the highest equilibrium solid solubility in Al are the most effective straighteners. Nevertheless, relatively few elements have an equilibrium solid solubility exceeding 1 at%, so to induce a significant solid solution strengthening effect, namely Si, Mg and Cu. In addition, these elements have relatively high diffusivity in Aluminium, resulting in alloys with poor thermal stability. Rapid solidification processes (RSPs), due to the increased solid solubility of the solutes far beyond the equilibrium limit, are effective in increasing the alloy strength by solid solution strengthening. Moreover, RSPs make possible to obtain supersatured solid solution of elements with intrinsically low solid solubility limits in Al, such as Ni, Cr, Fe etc., opening up to novel compositions with enhanced mechanical as well as thermal properties [18].

2.1.1.2 Hall-Petch strengthening

The Hall-Petch strengthening arises from the interaction between the grain and subgrain boundaries and the dislocations. Grains and subgrains, indeed, impede the dislocation motion producing an increase in the hardness and the yielding strength of the alloy. The higher the grain boundaries area per unit of volume (smaller grain size) the more effective are the grains in blocking dislocation movement and thereby the strengthening effect.

Basing on the Hall-Petch equation, the yielding strength increase of the material ($\Delta\sigma_{Hall-Petch}$) is related to the grain size (d) as follows [18]:

$$\Delta\boldsymbol{\sigma_{Hall-Petch}} = \boldsymbol{\sigma_0} + \frac{\boldsymbol{k_y}}{\sqrt{\boldsymbol{d}}} \tag{2.2}$$

Where σ_0 is the stress of the grain-free material and k_y is a material-related constant. Rapid solidification processes, due to the refinement of microstructural features, are effective in increasing the alloy strength due to the Hall-Petch effect.

2.1.1.3 Particle/precipitation strengthening

Particle strengthening is the result of the interaction between the dislocations and the particles precipitating or the local strain around them, which impede dislocations mobility and thus the deformation.

There exist two main particle strengthening mechanisms, namely cutting and Orowan mechanism, depending on the properties of the precipitate, its size, distribution and coherency with the matrix [198].

Cutting mechanism inducing order-strengthening occurs when coherent precipitates, nanometric in size and spaced few nanometres each others, are forced to create anti-phase boundaries (APB) due to the passage of a glide dislocation, which cuts through the precipitates (Figure 29a). The resulting stress increase ($\Delta\sigma_{APB}$) can be calculated as follows:

$$\Delta\boldsymbol{\sigma_{APB}} = \frac{\mathbf{3.1}\boldsymbol{\gamma_{APB}^{3/2}}}{\boldsymbol{b^2}}\left(\frac{\boldsymbol{rV_p}}{\boldsymbol{G}}\right)^{\mathbf{1/2}} \quad (2.3)$$

Where $\gamma_{APB}$is the ABP surface energy, b is the Burger vector, r is the mean radius of the precipitates and V_p is the particle volume fraction. The individual precipitating particle has a small effect in impeding the shearing of glide dislocations and the large part of the yielding increase results from the high volume fraction of precipitates [18]. Moreover, the formation of new solute-solvent bonds as consequence of the shearing induces an additional strengthening, known as chemical hardening, controlled by the precipitate-matrix interfacial area and the difference of stacking fault energy between the particle and the matrix [18].

Orowan mechanism inducing dispersion-strengthening occurs when the precipitate particles are intrinsically strong, impenetrable, large and widely spaced so that the dislocations can readily bypass the particles, bow out between them and then rejoin, leaving loops of dislocations around the particles (Figure 29b) [18]. Dispersion-strengthening mechanism was first described by Orowan and the resulting stress increase ($\Delta\sigma_{Orowan}$) for spherical particles can be calculated as follows [18]:

$$\Delta\sigma_y = \frac{Gb}{2\pi\sqrt{1-\nu}} \times \frac{1}{\lambda} \times \ln\frac{\pi d}{4b} \quad (2.4)$$

Where ν is the Poisson's ratio, λ is the inter-particle spacing and d is the diameter of the particle.

As previously anticipated, the relevance of each mechanism is related to properties of the precipitate. Cutting is the dominant mechanism at small particle size while Orowan will be favourable with large particle size finely distributed. The

transition from cutting to Orowan mechanism, resulting in a peak of strengthening effect, occurs at a critical particle size (Figure 29c).

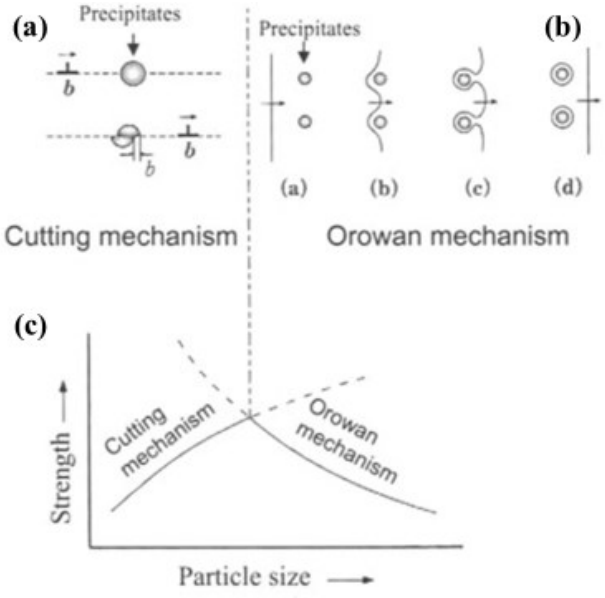

Figure 29. Schematic representation of the main particle-strengthening mechanisms, (a) cutting and (b) Orowan, and (c) the relationship between strength and particle size [199].

The above-shown strengthening curve as function of the particle size is typical of age-hardnenable aluminium alloys, such as those belonging to the series 3xx.x (Al-Si-Mg) and of wrought aluminium alloys belonging to the series 2xxx, 6xxx and 7xxx [18].

In order to achieve a microstructure with best properties and strengthening effect, precipitation must be controlled thought a specific heat treatment. The treatment involves:

- a solution treatment at relatively high temperature in order to dissolve the alloying elements.
- the rapid cooling (or quenching) of the alloy to room temperature in order to obtain a metastable supersatured solid solution (SSSS) of the alloying element.
- an ageing (or precipitate hardening) treatment at intermediate temperature in order to decompose the SSSS and to form finely dispersed precipitates.

The precipitation hardening in age-hardnenable aluminium alloys was deeply studied for the Al-Mg-Si system [18,200,201]. The metastable SSSS α_0 obtained after rapid cooling decomposes yielding the precipitation of the stable strengthening β phase (Mg_2Si) according to the following precipitation reaction [201]:

$$\alpha_0 \rightarrow \ GP\ zones \rightarrow \beta'' \rightarrow \beta' \rightarrow \beta$$

The first phase that forms after quenching or upon the early stage of ageing is Guinier-Preston (GP) zones. GP zones are ordered, solute-rich clusters of atoms, one or two atomic layers thick, which retain the structure of the matrix and for this reason they are said to be coherent. Nevertheless, they can produce appreciable local elastic strain around themselves in the surrounding matrix.

The β'' and β' phases are metastable transition phases, partially coherent with the matrix and that may nucleate at or from the GP zones but also heterogeneously at lattice defects. At the same time, the decomposition of the matrix proceeds and yields the formation of the equilibrium precipitate β with a complete loss of coherency with the parent lattice. A similar precipitation sequence occurs in Al-Cu alloy systems and yields the formation of stable θ (Al_2Cu) phase throughout the formation of metastable θ'' and θ' phases [18,200].

This precipitation sequence is crucial for the age hardening response of the material. At the beginning the strength of the alloy is limited to the only solid solution contribute, whilst a SSSS had formed upon rapid cooling. The resistance to the dislocation movement increases as consequence of the formation of GP zones and intermediate β''phase. At this stage, strengthening mechanism is a combination of cutting and dislocation blocking (peak of strength in graph in Figure 29c). The strength of the alloy gradually decreases due to the formation of even less coherent, large and coarsely dispersed β' and β phases [18].

2.1.2 Rapid solidification processing of Aluminium alloys

As anticipated in 1.2.7 Thermal regimes and metallurgical effects paragraph, Aluminium alloys processed by LPBF undergoes solidification rates up to 10^6 K s^{-1} [64], close to those achieved in other traditional rapid solidification processes (RSPs), such as melt spinning, atomization, splat quenching and laser surface melting [65]. Under these pronounced non-equilibrium solidification conditions, some unique features are achieved, namely a refined microstructure, formation of metastable phases, increased chemical homogeneity and extension of solid solubility limits [65].

The common products resulting from the adoption of traditional rapid solidification techniques include mainly ribbons and powders. They are normally consolidated into full dense billets by time-consuming hot or cold pressing operations or by expensive HIPing route, limiting in any cases the shape, size and complexity of the final object [65,202]. Nevertheless, RSPs have been extensively studied in the past decades since they have offered new opportunities for developing novel compositions and microstructures, which exploited different strengthening mechanisms in a more effective way and for producing materials with superior mechanical properties as compared to those achieved with traditional manufacturing routes [203–205].

In regards to aluminium alloys, RSPs - particularly melt spinning - have been extensively studied with the attempt of developing a new generation of Aluminium alloys with superior properties [202]. Since the early ‘80s, rapidly solidified Aluminium alloys were studied for elevated temperature applications on aerospace

components [203,206–208]. Indeed, among the three main ways to improve properties of Aluminium alloys, namely by (i) increasing the alloying elements content, (ii) improving the alloy chemical homogeneity and (iii) producing refined crystalline phases, rapid solidification processes have been revealed capable to address to all of them [202].

It was reported that the RS of Aluminium alloys based on the general Al-TM system (being TM transition metal like Ni, Cr, Fe, V, Ti, Sc etc.) can achieve strength levels exceeding those of traditional ones [209]. In addition, due to the industrial interest of Al-Si alloys, the RS of Al-Si-TM systems have been extensively investigated for improving wear resistance, mechanical and thermal stability of foundry alloys [208,210–212].

Firstly, RSPs are effective in increasing the alloy strength through solid solution strengthening. In addition to elements such as Si, Mg, Cu - with intrinsically high solubility in Aluminium – RS allows to increase up to two order of magnitude the solid solubility limits of elements with intrinsically low solid solubility in Aluminium, such as Ni, Cr, Fe, Sc, etc. Moreover, they are able to confer to the alloy enhanced mechanical strengths due to the precipitation of fine strengthening intermetallic phases and to increase the thermal resistance of the alloy due to low diffusivity of the constitutive elements in Aluminium [18]. Table 4 reports some examples of the increases in the solid solubility limits achieved for some TMs due to RS together with their diffusivity in Aluminium.

Table 4. Increased solid solubility in some binary aluminium alloys due to RSP [18]**.**

Solute	**Maximum equilibrium solubility (at. %)**	**Reported extended solubility (at. %)**	**Diffusion coefficient D_0 at 425 °C ($mm^2\ s^{-1}$)**
Cr	0.44	5-6	$7.7 * 10^{-21}$
Fe	0.025	4-6	$2.2 * 10^{-18}$
Ni	0.023	1.2-7.7	$5.2 * 10^{-15}$
Sc	0.22	3.2 [213]	10^{-17}
Cu	2.4	17-18	$4.3 * 10^{-15}$
Mg	18.5	36-40	$1.5 * 10^{-14}$
Si	1.59	5 [214]	

For instance, in 2010 Palm *et al.* [182] reported that the high cooling rate achieved during melt spinning of a Sc modified Al-Mg-Zr alloy were able to retain into solid solution up to 1.4 wt.% of Sc (against an equilibrium value of 0.38 wt.%), which induced an exceptional response to the subsequent ageing treatment. Fine

$Al_3(Sc_{1-x}:Zr_x)$ precipitates 10-20 nm in size formed along grain boundaries and yielded a hardness up to 2 times higher than the as-melt spun material [182].

Some authors investigated the alloying behaviour of Cr. Aluminium alloys with high content of Cr have been reported to exhibit high resistance to solute clustering and precipitate coarsening at high temperature [215]. Escorial *et al.* [215] reported that Al-3at.%Cr-1at.%Ni ribbons produced by melt spinning formed a supersatured solid solution of Cr which decomposed at 420 °C. Other studies pointed out on the enhanced corrosion resistance of binary Aluminium alloys when alloyed with Cr [216,217]. Esquivel *et al.* [218] reported that Cr – more noble than Al – improved/ennoble the pitting potential in Al-5at.%Cr supersatured solid solution alloy. As reported by Moshier *et al.* [216], Cr forms a protective barrier layer that hampers the oxidation of the aluminium substrate and inhibits the anions to reach the metal/film interface.

Many RSP aluminium alloys reported in literature belong to the Al-Fe system. Alloying with Fe has been studied because of its interesting features, particularly high liquid-state diffusivity and low solid-state diffusivity, which ensured high chemical homogeneity in the Aluminium matrix and high thermal stability [210]. Precipitates such as Al_3Fe obtained under RSP exhibit a fine equiaxed morphology in place of harmful acicular morphology and they are resistant to coarsening at high temperatures [18]. Allied-Signals and Pratt & Whitney companies developed the high strength Al-8.5Fe-1.3V-1.7Si alloy with structural stability up to 350 °C for aircraft applications [205]. Alloying with V and Si under RS conditions seemed to alter the kinetics of precipitation normally occurring in binary Al-Fe system and allowed the precipitation of high volume fractions of tiny spherical particles of cubic α-$Al_{12}(Fe, V)_3Si$ phase, with a very low coarsening rate induced by the low diffusivity of constituting TMs [219]. Whilst the high lattice mismatch of the silicide with α-Al (around 3.5%), the dispersoids had a low interfacial energy with the Al matrix, which conferred them thermal stability [220]. The stability of the generic α-$Al_{12}(Fe, TM)_3Si$ phase was reported to increase in the sequence Cr→Mo→V due to the decrease in the diffusion coefficient of the TM [205].

In traditional Al-Si casting alloys, the amount of Fe must be controlled in order to limit the formation of large and brittle needle-like β-AlFeSi intermetallic compound, which degrades mechanical properties of the Al-Si alloys [18]. In physical metallurgy of casting Aluminium alloys, Mn addition have been reported to neutralize the detrimental effect of Fe by promoting the formation of less harmful, finer and more rounded α-Al(Fe, Mn)Si phase, also indicated as α-$Al_{15}(Fe, Mn)_3Si_2$ or α-$Al_{12}(Fe, Mn)_3Si_2$, with a characteristic so-called Chinese script or star-like morphology [221]. The addition of Cr has been reported to have a similar effect, even stronger, by promoting the formation of more rounded α-Al(Fe, Cr)Si thermally stable phase [222]. Under RSP, Unlu *et al.* [210] reported that melt spinning was effective in hindering intermetallic formations in hypoeutectic Al-10Si-3.3Fe alloy and in producing a supersatured solid solution of Si and Fe in α-Al. Due to the solution strengthening effect of Fe, microhardness was about 3 times higher than the as-cast alloy. Ahmed *et al.* [223] investigated the microstructure and mechanical properties of a near-eutectic Al-Si alloy with high Fe-content produced

by melt spinning. They reported that RS of Al-11Si-11Fe was not able to suppress intermetallic formation. However, rapidly solidified ribbons exhibited a very fine microstructure consisting of major contents of thermally stable ultrafine needle-shaped β-AlFeSi particles and minor contents of ultrafine metastable cubic-shaped α-AlFeSi particles, whose were responsible of the high hardness of the material in the as-melt spun state (277 HV). Cai *et al.* [224] found that addition of 2 wt.% Cr to the hypereutectic Al-25Si-5Fe-3Cu alloys obtained by spray forming remarkably decreased the amount of harmful β-AlFeSi phase and promoted the formation of less harmful rod-like and blocky β-Al(Fe,Cr)Si intermetallics and fine granular α-Al(Fe, Cr)Si intermetallics with a size lower than 3 μm. The addition of Cr was found not only to introduce a new reaction at around 900 °K due to crystallization of α-Al(Fe, Cr)Si phase but also to change the onset temperatures of other thermal reactions [224].

Other authors examined the alloying behaviour of Ni. Gonzalez *et al.* [225] investigated the influence of cooling rate on the precipitation phenomena in a hypereutectic Al-4at.%Ni alloy produced by melt spinning. They observed the precipitation of nanometric globular-like Al_9Ni_2 intermetallic plus minor quantities of Al_3Ni. Globules were mainly distributed at the α-Al grain boundaries. Under metastable RS conditions, the first phase that formed was the Al-rich Al_9Ni_2 intermetallic. The subsequent formation of α-Al grains enriched the liquid of solute, especially at grain boundaries, where further intermetallic phase precipitation, namely Al_9Ni_2 and Al_3Ni phases, occurred. The strengthening effect resulting from the alloying was dramatic. Microhardness of the as-melt spun material was more than 6 times higher the as-cast material with the same composition, which they ascribed to the increased dislocation density and to the fine distribution and morphology of Al_9Ni_2 particles achieved under RS [225]. Similar results were found by Karakose *et al.* [206] while processing Al-6Ni-2Cu-1Si by melt spinning. The precipitations of Si and Al_2Cu phases were suppressed and the microstructure was composed only of fine α-Al grains and finely dispersed Al_3Ni precipitates. The microhardness of ribbons was about 3.2 times higher than the as-cast alloy, which they ascribed to the supersaturation of the α-Al grains and to the precipitation of fine Al_3Ni [206]. Todeschini *et al.* [212] also reported that the addition of 1.1 wt.% Ni to rapidly solidified Al-12Si alloy significantly improved mechanical properties at expenses of ductility [212]. Some outcomes came from Tawfik *et al.* [208] on Al-12.5Si-1Ni ribbons. The hardness was up to 1.9 times higher than the as-cast alloy with the same composition and the ultimate tensile strength significantly increased as well. Upon thermal annealing treatment, hardness decreased due to a combined effect of silicon precipitation/coarsening and relief of internal stresses [208]. Many authors, however, reported also that Ni addition decreased the ductility of the alloys [206,208,212,225].

Lee *et al.* [226] investigated the simultaneous addition of Ni and Ce to rapidly solidified hypereutectic Al-Si alloys, reporting a significant enhancement in the hardness and strength. Rapid solidification of Al-19Si alloy at increasing content of Ni and Ce was found to extend the solubility of Si in Aluminium up to the formation of a supersatured solid solution of Si, Ni and Ce [226]. The subsequent

consolidation of powders at high temperature produced a fine dispersion of eutectic Si, Al_3Ni and Al_3Ce precipitates with sizes of roughly 100 nm and alloy hardness up to 2.1 times higher than the TM-free alloy [226]. Recently, Wang *et al.* [227] reported similar microstructures, phases and mechanical properties for rapidly solidified and hot consolidated Al-Si-Ni-Ce alloys, pointing out that the combination of high hardness, moderate tensile strength and elongation of Al-Si alloys coupled to optimized composition and rapid solidification processing under non-equilibrium conditions can provide novel types of promising engineering alloys.

According to what has been presented here, modification of the alloy composition through the addition of TM can be promising for improving mechanical properties Aluminium alloys processed by RSPs, particularly by LPBF.

2.2 LPBF of AlSi10Mg: microstructure and properties

To date, AlSi10Mg is the most processed Aluminium alloy by LPBF [19]. AlSi10Mg is a cast Al-Si-Mg alloy (A360) belonging to the series 3xx.x. that has been widely used in the automotive industry for thin-walled complex-shape parts [228] such as transmission casing [18]. AlSi10Mg is currently used to manufacture complex-shaped LPBF components with high strength-to-weight ratio for aerospace and automotive applications, i.e. wheel suspensions [229] and cooling jackets [230]. The typical composition of AlSi10Mg is reported below in Table 5.

Table 5. Nominal composition of AlSi10Mg (A360) alloy.

Element	Si	Mg	Fe	Cu	Mn	Zn	Ni
Wt.%	9±11	0.4±0.6	< 2.0	< 0.60	< 0.35	< 0.50	< 0.50

The presence of Si as major alloying element allows to have an alloy optimized for casting and welding, with enhanced fluidity at the molten stage, narrow solidification range and low coefficient of thermal expansion [18]. The phase diagram of the Al-Si alloy system presented below in Figure 30, indeed, shows that the Aluminium solid solution containing 1.65 wt% Si and the pure Si form an eutectic at 12.6 wt% Si and at a temperature of 577 °C. The presence of Mg, one of the most effective strengthening alloying element for Aluminium alloys due to its high solubility, induces the precipitation of Mg_2Si phase, which strengthens the alloy and makes it age-hardenable [18]. Moreover, Mg confers excellent corrosion resistance.

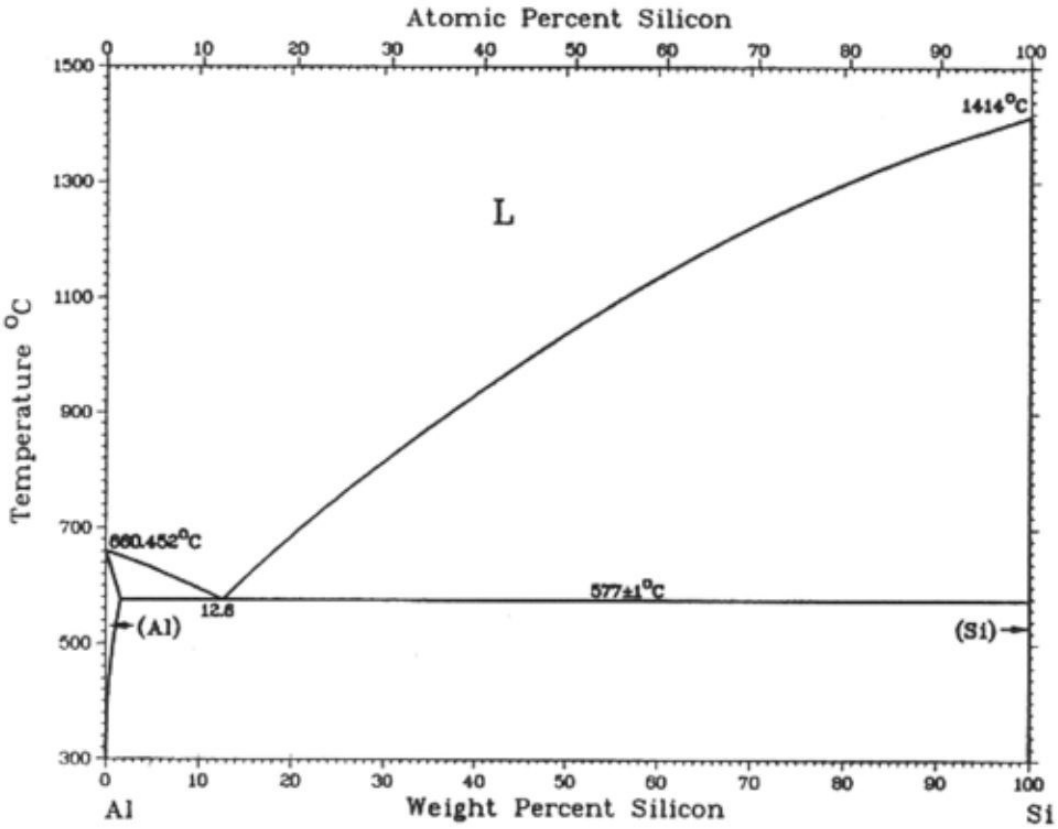

Figure 30. The Al-Si phase diagram showing the maximum equilibrium solid solubility of Si in Al of 1.65 wt.% and the eutectic reaction at 12.6 wt.% Si and at 577 °C [231].

AlSi10Mg alloy processed by LPBF exhibits microstructure and resulting properties radically different from the ones observed in the same alloy processed by traditional casting route.

The overall microstructure of LPBF AlSi10Mg is composed by overlapping melt pools, whose morphology and orientation are strictly influenced by the scanning strategy (Figure 31). Manfredi *et al.* [70,232] reported that unidirectional scanning strategy produced parallel scan tracks oriented in the same way along the building direction due to the overlapping of subsequent layers and half-cylindrical melt pools. On the contrary, the 67° rotated scanning strategy produced complex microstructures, due to the asymmetrical overlapping between consecutive layers. Nevertheless, in both cases, overlapping regions between adjacent tracks and subsequent layers, which identify the melt pools borders, were clearly visible at light microscope due to the different reflection.

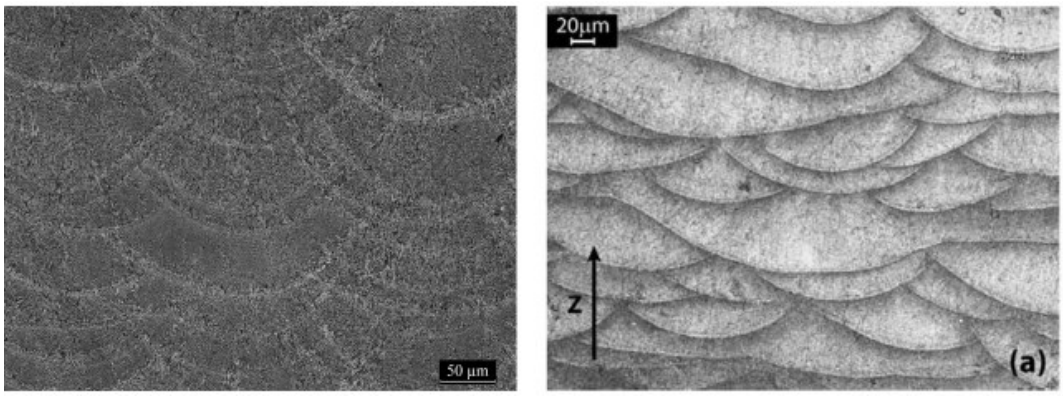

Figure 31. Optical micrographs of the vertical cross section of AlSi10Mg produced by LPBF adopting (a) unidirectional scanning strategy (along the x axis) and (b) a 67° rotated scanning strategy [70]**.** The overlapping between adjacent tracks and consecutive layers produced a unique microstructure.

At the slow cooling rate of traditional casting route (10^{-3}-10^{0} K s^{-1}), AlSi10Mg shows a typical hypoeutectic solidification structure consisting of primary coarse dendritic α-Al grains, with a size of several dozens of microns, and interdendritic eutectic structure of Al and Si (Figure 32) [18].

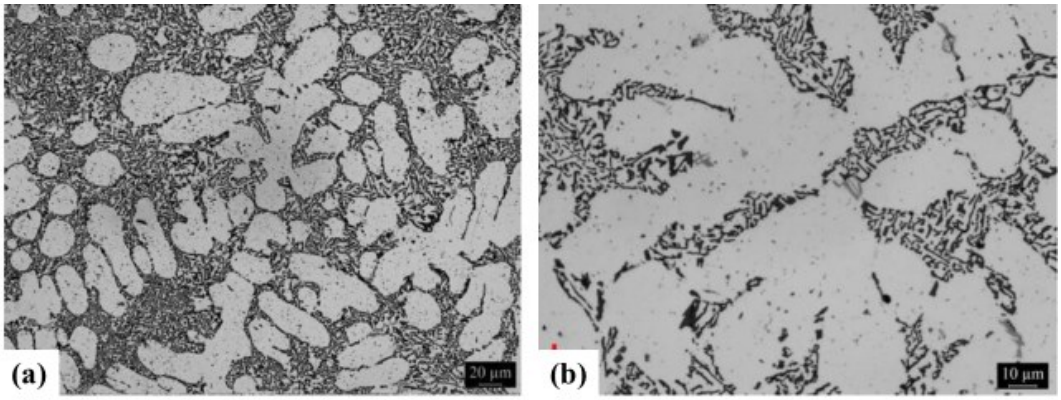

Figure 32. Optical micrographs showing the microstructure of AlSi10Mg alloy produced by casting at (a) low and (b) high magnifications [233]. The phase contrast indicates the α-Al grains in white and the Al-Si eutectic in grey.

The same material processed by LPBF undergoes a change in the microstructure development and it forms a metastable microstructure influenced by the thermal history during LPBF. Due to the high temperature gradients during LPBF, Wu *et al.* [234] reported a solidification microstructure for AlSi10Mg consisting of cellular dendritic α-Al cells elongated in the direction of heat flow separated by a network of segregated eutectic Si [61]. The α-Al cells were supersatured of silicon. Marola *et al.* [235] calculated that the solubility of Si in α-Al was extended up to 4 at% as consequence of the rapid cooling during LPBF, much beyond the equilibrium solubility limit of 1.59 at% at the eutectic temperature [235]. Similarly, Prashanth *et al.* [161] reported that during LPBF of AlSi12 the non-equilibrium solidification of primary α-Al grains due to the high cooling rate

caused the entrapment of excessive amount of Si in Al, leading to the formation of supersatured α-Al grains. Part of the entrapped Si then drove out from Al and accumulated along the α-Al grains, rationalizing in this way the formation of the eutectic network [161]. Still Marola *et al.* [235] investigated the metastable microstructure of the as-built AlSi10Mg by means of DSC analysis and they found two main exothermic peaks for the as-built AlSi10Mg, as reported in Figure 33 [235]. The first major peak at around 200 °C was right attributed to the precipitation of Si from the supersatured α-Al cells and the second major peak at approximately 317 °C was attributed to the precipitation of Mg_2Si still from the primary α-Al phase supersatured in Mg. Moreover, a third weak peak was found at around 340 °C and it was attributed to the precipitation of Fe-containing compounds.

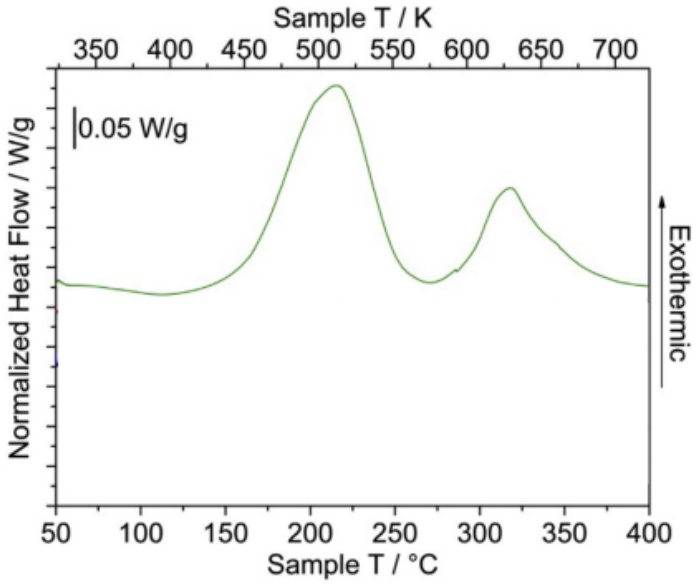

Figure 33. DSC curves showing precipitation peaks for as-built AlSi10Mg [235].

The scale of segregated phases in LPBF AlSi10Mg was strongly refined as compared to the cast material. The cellular-dendritic α-Al cells of the LPBFed material were approximately 0.5 μm in size and the segregated network of eutectic Si along the α-Al cells had thickness of about 0.2 μm [234]. The dimension of α-Al cells was found to be strongly related to the cooling rate. Tang *et al.* [236] investigated the effect of local heat input – and thus process parameters - in controlling the cell size in AlSi10Mg. They found that the cell spacing closely followed the well-established correlation between the α-Al cell size λ (μm) and the cooling rate $\dot{T}$ (K s^{-1}) found in literature and developed by Matyja *et al.* [236] for rapidly cooled aluminium alloys, as follows:

$$\boldsymbol{\lambda = 43.2\dot{T}^{-0.324}} \tag{2.5}$$

Thijs *et al* [60] demonstrated that the specific fine microstructure of as-built AlSi10Mg leads to a material with higher hardness (127 $HV_{0.5}$) than the as-cast material (95-105 HV).

Nevertheless, the size of microstructural features in AlSi10Mg was not homogenous at the melt pool scale. Thijs *et al.* [60] reported that microstructure consisted of fine cellular structure, coarse cellular structure and heat affected zone (HAZ) when moving across the melt pool from the centre to the border, as shown in Figure 34 and Figure 35. The difference in fineness between fine and coarse areas of melt pool was ascribed to the differences into cooling rates between the melt pool centre and border, respectively [60]. The HAZ, just outside the melt pool in previously deposited layer, represented the region thermally affected but not melted during the deposition of the new layer. Due to the thermally activated diffusion of Si, in the HAZ the intercellular network was broken and the Si particles coarsened [60,70]. On the plane perpendicular to the building direction (xy plane), the α-Al cells were slightly equiaxed (Figure 34) while along the vertical direction (z axis), the α-Al cells were oriented in the direction of thermal extraction, with finer columnar-dendritic cells at the core (Figure 35).

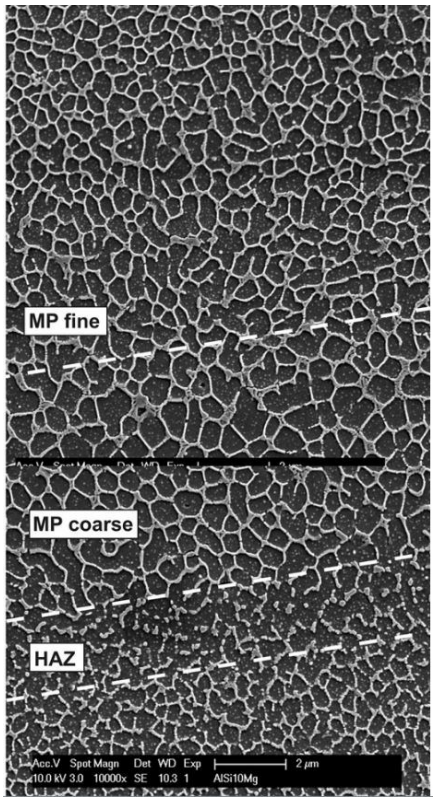

Figure 34. FESEM micrographs showing the microstructure of the horizontal cross section of LPBF AlSi10Mg (xy plane) [60].

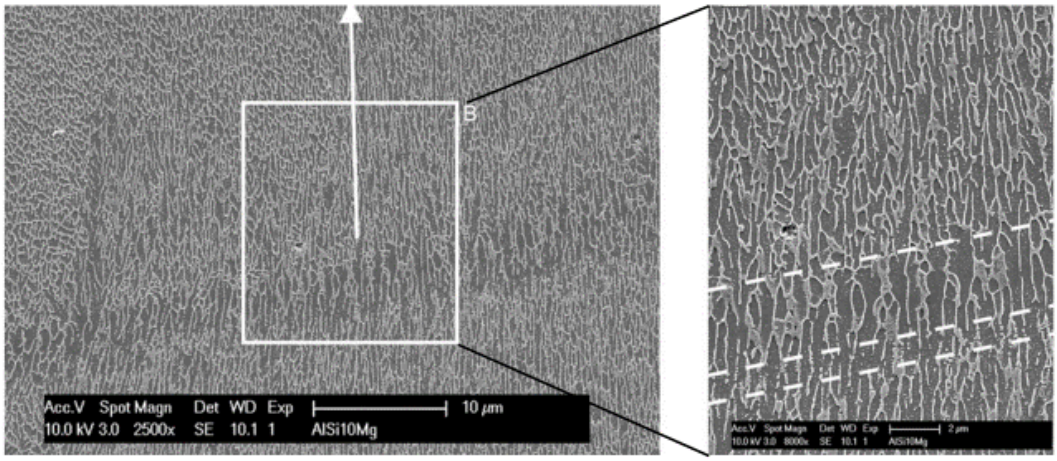

Figure 35. FESEM micrographs showing the microstructure of the vertical cross section of LPBF AlSi10Mg (xz plane) [88].

Since AlSi10Mg is an age-hardenable alloy, some studies investigated the response of the material to conventional T6 heat treatment (ST at 520 °C/1 h + WQ + 160 °C/6 h) [168,169]. Aboulkhair *et al.* [168] reported little benefits to the mechanical properties of AlSi10Mg as compared to the material in the as-built condition, as summarized in Table 6. Both nano- and micro-hardness decreased as consequence of the rupture of the extremely fine eutectic network. The thermally-activated diffusion of the homogenous distributed Si into solid solution induced the formation of coarser spherical Si particles, whose strengthening effect however was not able to overcome the refined grain size and solid solution strengthening effects of the as-built material. Moreover, as consequence of coarsening, spatial variation of properties within the tested regions increased, improving dishomogeneities. Similar results were found by Manfredi *et al.* [232] while investigating the effect of annealing (ST at 530 °C for 5h + furnace cooling), T4 (ST at 530 °C for 5h + WQ + NA at RT for two weeks) and T6 (ST at 530 °C for 5h + WQ + AA at 160 °C for12 h) heat treatments on hardness, yielding strength and ductility of AlSi10Mg. Material softening upon T6 treatment opposes to the strengthening of conventionally manufactured age-hardnenable AlSi10Mg after heat treatment. The difference was ascribed to the differences existing in starting microstructures between the as-built (Figure 34 and Figure 35) and as-cast material (Figure 32), fine and supersatured the former and coarse and segregated the latter [168,169]. Annealing treatment is fundamental to ensure dimensional and physical stability to the LPBFed part and to decrease the detrimental residual stresses induced by the process. Martens *et al.* [237] found that after stress relieving treatment of AlSi10Mg at 250 °C for 2 h, yielding and ultimate tensile strengths decreased of 12% and 2%, respectively, and elongation at break increased of 80%.

Table 6. Summary of the effect of conventional T6 heat treatment at 520 °C/1 h (WQ) + 160 °C/6 h on mechanical response of AlSi10Mg. The change in mechanical behavior in respect to the as-built material is expressed as percentage [168].

Property	**Effect of heat treatment (%)**
Nano-hardness	− (16±1) ↓
Micro-hardness	− (20±1) ↓
Ultimate tensile strength (UTS)	− (12±5) ↓
Yield strength (YS)	− (11±5) ↓
Tensile elongation at failure	+ (179±57) ↑

There have been also some studies investigating the corrosion resistance of LPBF AlSi10Mg [173,174,238,239].

Leon *et al.* [239] reported the preferential corrosion of α-Al at the melt pool boundaries and, in general, a slightly reduced corrosion resistance of the LPBF material in 3.5% NaCl solution as compared to the cast-material. Cabrini *et al.* [174] found similar results in aerated diluted Harrison's solution. In their study, the corrosion resistance of LPBFed aluminium alloys was found to be affected by different factors, namely microstructure, surface roughness and passive oxide layers. As regard the microstructure, Cabrini *et al.* ascribed the preferential dissolution of α-Al in the melt pool borders and HAZ to the presence in these regions of coarser Si – more noble than Al – as separate phase instead of being into supersatured solid solution. The high content of Si in solid solution into the melt pool, indeed, increased corrosion resistance of the alloy in this region. The remarked influence of the melt tracks texture in controlling corrosion behaviour of the material was further confirmed by observing a lower corrosion resistance of the vertical surfaces (parallel to the building direction) than the horizontal ones, due to the higher density of melt pool borders. Moreover, the generally high surface roughness of LPBF materials also exerted a detrimental effect on the corrosion resistance of the material because of the increase in the area susceptible to corrosion. In the study, the authors suggested that surface corrosion was aggravated by the presence of surface defects, such as pores, acting as initiator of localized attacks. In addition, the formation during LPBF and subsequent heat treatment of a passive oxide layer less protective than that formed naturally in air was reported to contribute in further decreasing the corrosion resistance of LPBF AlSi10Mg. For these reasons, mechanical actions of the surface such as shot peening and surface polishing up to 0.1 μm, aimed to decrease surface roughness and/or remove the weak passive film formed during LPBF, helped in reducing corrosion rate of LPBF AlSi10Mg.

2.3 LPBF of new Aluminium alloys

In theory, the alloy compositions should be tailored for the particular manufacturing technology, so to obtain the best properties while limiting the defects during manufacturing.

As concern the development of new Aluminium alloys for LPBF, the compositions must fulfil different criteria. They must have narrow solidification range, good fluidity at the molten stage, low segregation and low elemental losses in order to prevent from liquation cracking phenomena and defects formation upon solidification [145]. Moreover, in order to enhance the mechanical properties as well as the thermal resistance, the alloy composition should be tailored in order to take advantages of the rapid solidification, so as already discussed in previous paragraphs. At the end, they should be tailored so to promote the precipitation of coherent strengthening phases with the potential of exerting a control of the microstructure during its development.

2.3.1 Effect of transition metals (TMs)

To date, only few studies investigated the effect of TMs additions to properties of Aluminium alloys processed by LPBF.

2.3.1.1 Microstructure and properties of Al-Mg-Sc-Zr alloy (Scalmalloy®RP)

By far, the most cited as well as the most successful case of material development for LPBF is related to the concept "ScalmalloyRP". In 2011, Schmidtke *et al.* [240] presented their results on the properties and processability of a scandium-modified AlMg-alloy (5xxx series) manufactured by LPBF, proving its suitability to be used as structural material for aerospace applications.

Preliminary studies on the metallurgical effects of scandium additions on cast aluminium alloys were conducted by Russians and Americans scientists across the 1970s [213]. Scandium possesses properties considered outstanding for the aerospace field, namely a low density combined to a high strengthening effect. Seidman *et al.* [241] reported an increment in strength of about 50 MPa per 0.1 wt.% Sc. However, due to the high buy-to-fly ratio and high cost of scandium, alloying with this TM did not caught the interest of industry at that time.

The main effects of scandium on properties of aluminium alloys are related to the formation of Al_3Sc particles, which induce (i) grain refinement during casting or welding, (ii) precipitation hardening by Al_3Sc particles and (iii) control of the grain structure at high temperatures.

Al-Sc phase diagram shows an eutectic transformation L → α-Al + Al_3Sc at approximately 655 °C and 0.6 wt.% Sc. Upon slow cooling, a hypereutectic Al-Sc solid solution decomposes producing Al_3Sc as first phase. Al_3Sc has cubic LI_2 crystal structure and lattice parameters of 0.411 nm close to that of aluminium (0.405 nm), inducing then a lattice mismatch as low as 0.5% [213]. Due to the high coherency of phases and similarities between the atomic structures, the Al_3Sc

precipitates act as seed crystals for heterogeneous nucleation of α-Al grains upon further cooling, inducing a very effective grain refinement effect [178].

The Al_3Sc precipitates, then, are age-hardener and yield high strength. As showed in previous paragraph in Table 4, the solid solubility of the Sc can be significantly extended under rapid solidification. The precipitation of Al_3Sc from a supersatured solid solution obtained under RS occurs at temperatures between 275-325 °C, significantly higher than those used in traditional age-hardenable alloys (150-200 °C). Al_3Sc precipitates are thus stable against coarsening up to temperatures significantly higher as compared to traditional age-hardenable 2xxx, 6xxx and 7xxx series Aluminium alloys, based on Mg, Si and Cu precipitates stable only up to 250 °C [241]. Moreover, the presence of thermally stable Al_3Sc precipitates preferably at the grain boundaries is also effective in hindering the grain boundaries movement and thus recrystallization up to 500 °C. The beneficial effects of scandium precipitates in controlling the grain structure of aluminium alloys were found to be enhanced when Sc was added together with Zr. Al_3Sc particles, indeed, tend to solubilize a certain fraction of Zr forming $Al_3(Sc_{1-x}:Zr_x)$ particles with a very low coarsening rate and a characteristic core/shell structure [242]. The nucleation of initial Al_3Sc particles, indeed, is controlled by Sc diffusion upon the early stages of ageing while the late growth and coarsening of $Al_3(Sc_{1-x}:Zr_x)$ particles is controlled by Zr diffusion, which is lower than Sc one [178].

Spierings *et al.* [183,243] investigated into detail the microstructure of the Sc- and Zr- modified Al-Mg alloy (Al-4.6Mg-0.66Sc-0.42Zr), Scalmalloy®RP, processed by LPBF, reporting a microstructure significantly different from the one obtained processing traditional Al-Si alloys by LPBF. The Sc-/Zr-modified AlMg alloy exhibited a bi-modal grain size distribution, namely fine randomly orientated equiaxed grains at the melt pool border interspaced with large columnar grains growing in the <001> direction along the temperature gradient within the melt pool, resulting in a material with a weakened texture in the building direction and lower anisotropy (Figure 36) [183].

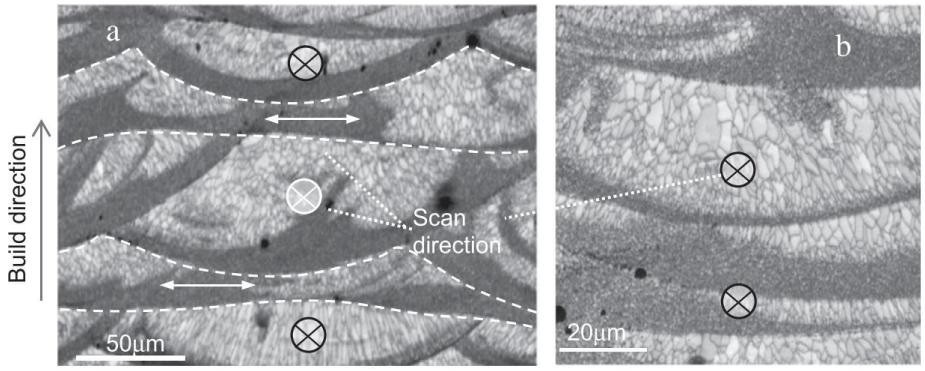

Figure 36. OM micrographs showing the microstructure of a Sc-/Zr-modified AlMg (Scalmalloy®RP) alloy manufactured by adopting a 90° alternating scanning strategy. The etched microstructure reveals fine equiaxed grains structure in the melt pool border (dark grey regions) and a coarse elongated grain structure within the melt pool (light grey region) [243].

The authors ascribed the formation of the duplex microstructure to the different solidification mechanisms while processing. Fine-grained equiaxed microstructures formed as consequence of the precipitation in the remelting zone of coherent $Al_3(Sc_{1-x}:Zr_x)$ and AlMg-oxides particles with very low lattice misfits with Al matrix, acting thus as strong inoculants towards forming α-Al grains. Basing on Scheil-simulation conducted by Pandat-software coupled to the modelling of the temperature-field within the melt pool, Spierings *et al.* [243] demonstrated that the temperatures within the melt pool were higher than the dissolution temperature of $Al_3(Sc_{1-x}:Zr_x)$ particles (around 800 °C). The formation of large columnar coarse grains was thus ascribed to the low number density of precipitates seed crystals acting as inoculants within the melt pool and to the higher temperature gradients [243]. Figure 37 shows SEM and STEM micrographs of the transitions zone between the fine- and the coarse-grained structures as well as the different concentrations of particles at the grain boundaries.

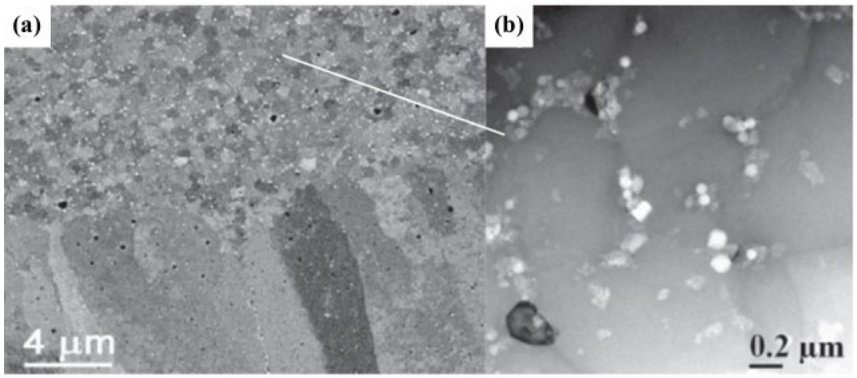

Figure 37. (a) SEM micrograph showing the microstructure of the fine grain and coarse grain regions in Scalmalloy®RP and (b) HAADF-STEM image of oxide particles in the fine-grain region [243].

In a recent study, Yang *et al.* [244] demonstrated that a fully equiaxed grain structure can be obtained in a Sc-modified Al-Mg-Zr alloy by tailoring the process parameters, in particular by increasing the applied volumetric energy density and the building platform temperature. They induced a combined effect of increasing the density of nuclei, extending the remelting zones areas and reducing the thermal gradients.

In another recent study, Spierings *et al.* [245] reported that varying the scanning speed was effective in tailoring precipitation behaviour of Al_3Sc particles during LPBF, while grain size distributions remained pretty the same. Low scan speed (high energy density) favoured the continuous precipitation of a high number density of intragranular coherent nanometric Al_3Sc particles, differently to high scan speed where no intragranular precipitates were observed. The authors reported that the higher cooling rate at higher scanning speed was responsible for the lack of Al_3Sc particles due the retention of higher fractions of Sc and Zr into supersatured solid solution. However, unexpectedly, a slight increase in hardness was observed at high scanning speed in samples with no intragranular precipitates. The authors pointed out on the complex interactions existing between different strengthening

mechanisms, namely solid solution hardenings, precipitation and dislocation density and on the difficulties in extricating their individual effects [245].

2.3.1.2 Al-20Si-5Fe-3Cu-1Mg

Ma *et al.* [246] studied the microstructure and phases of as-built and heat treated hypereutectic Al-20Si-5Fe-3Cu-1Mg alloy, showing that the as-built microstructure consisted of fine primary Si, homogenous Al-Si eutectic and high volume fraction of a fine acicular Al-Fe-Si compound identified as the metastable δ-Al_4FeSi_2 phase. Under metastable condition induced by rapid solidification during LPBF, indeed, peritectic reaction L + δ → Si + β was mostly suppressed. Only upon thermal treatment at high temperature the metastable δ-Al_4FeSi_2 phase coexisted with fine β-AlFeSi intermetallic [246].

The authors pointed out that that the precipitation of metastable δ-Al_4FeSi_2 intermetallic prior to eutectic reaction helped in refining the Al-Si eutectic in respect to the hypereutectic LPBF Al-20Si alloy. The presence of randomly distributed δ-Al_4FeSi_2 phase in the matrix, indeed, restricted the formation of the eutectic to smaller areas interspaced by the metastable intermetallic. Moreover, the addition of Fe, Cu and Mg to the alloy composition was found to hinder the growth of primary Si both while processing that during subsequent heat treatment at high temperature. The authors ascribed this behaviour to certain amounts of Fe dissolved into Si, which decreased the activation of Si. In addition, the homogenous distribution of thermally stable δ-Al_4FeSi_2 hindered the inter-particle diffusion of Si, which causes the coarsening and growth of primary Si.

2.3.1.3 Al-8.5Fe-1.3V-1.7Si

Sun *et al.* [247,248] and Zheng *et al.* [76] investigated the microstructure, hardness and thermal stability of Al-8.5Fe-1.3V-1.7Si produced by LPBF. The as-built material consisted of supersatured α-Al cellular grains and an extremely fine distribution of $Al_{12}(Fe, V)_3Si$ and θ-$Al_{13}Fe_4$ thermally stable phases [76]. TEM analysis revealed that the distribution of phases was not homogenous across the melt pool and that it was affected by the local cooling rates during LPBF. Supersatured fine α-Al cells with nanoscale $Al_{12}(Fe, V)_3Si$ particles formed within the melt pool due to the high cooling rate. Submicron rectangular-like θ-$Al_{13}Fe_4$ particles were preferably found in the melt pool border - solidifying at lower cooling rate - and globular $Al_{12}(Fe, V)_3Si$ particles nucleated in the HAZ under the influence of the heat conducted upon thermal cycles [249]. Due to the refined size of precipitating particles and the solid solution strengthening under rapid solidification, the hardness of LPBFed material was around 150 HV, up to 3.5 times higher than the as-cast alloy. Moreover, samples processed at low scanning speed gave a corresponding hardness values slightly higher than those obtained at high scanning speed, probably because of the differences in cooling rates [76].

2.3.1.4 Al-based metallic glasses

In literature it is reported that particular combinations of transition metals and rare earth elements together with Aluminium may induce the formation of amorphous structures under rapid cooling, exerting good combination of strength, ductility, density and corrosion resistance [204,250]. For this reason, some studies investigated the processability of some Al-based metallic glasses (BMGs) by LPBF, taking advantage of the rapid cooling during processing.

Prashanth *et al.* [251] manufactured dense, high strength and thermally stable $Al_{85}Nd_8Ni_5Co_2$ by LPBF. The BMG exhibited a composite-like microstructure constituted by submicron-sized platelets-like $AlNdNi_4$, Al_4CoNi_2 and $AlNd_3$ intermetallics dispersed in the Al-matrix, which yielded high compressive strength at high temperatures. Intermetallic phases, indeed, hindered the grain coarsening as well as the increased mobility of dislocations at high temperatures. Moreover, intermetallics played an important role in arresting and/or deflecting cracks, resulting in superior compressive yielding and ultimate strengths [251].

2.3.2 2xxx, 6xxx and 7xxx series Aluminium alloys

Other authors focused on the processability, microstructure and mechanical properties of commercial heat treatable wrought alloys belonging to the 2xxx, 6xxx and 7xxx series. As already discussed in 1.2.9 Liquation cracking paragraph, the high concentration of low melting point elements (Cu, Mg, Zn) characteristic of these alloy systems typically results in broad solidification ranges, which coupled to the high thermal gradients and cooling rates during LPBF, cause hot cracking and defects formation. This phenomenon adds to the high thermal conductivity, high laser reflectivity and oxidation susceptibility of Aluminium alloys in general, which makes further challenging the processing of these alloy systems. Nevertheless, these alloy systems are intersecting for the aerospace and automotive fields due to the high strength, high temperatures and corrosion resistance and for these reasons their development has received much attention.

Zhang *et al.* [252] produced full dense Al-Cu-Mg samples (2xxx series), with a chemical composition similar to commercial AA 2024 alloy, under optimized building conditions. The as-built Al-Cu-Mg microstructure consisted of extremely fine α-Al cells with a cellular-dendritic morphology supersatured with Cu and Mg. The rapid cooling during processing, indeed, suppressed the precipitation of second phases. A strong XRD peak intensity of the (200) reflection of α-Al, causing <100> texture in the material and anisotropy, was found in the pattern of the LPBFed material and it was ascribed to the directional solidification of α-Al grains during cooling. The material exhibited microhardness 1.4 times higher than the AA 2024 alloy in the annealed state and high mechanical properties (YS and UTS of 276 MPa and 402 MPa, respectively). The authors ascribed the higher mechanical properties to the simultaneous grain refinement effect and solid solution strengthening induced by rapid cooling during LPBF [252]. Upon thermal solution heat treatment, the mechanical properties improved due to the precipitation of Al_2CuMg phase inducing precipitation strengthening as well as the elongation,

probably due the suppression of the dislocation microstructure of the as-built material and the homogenization of the minor chemical segregations [253]. In addition, Zhang *et al.* [252] pointed out that, in order to produce cracks-free Al-Cu-Mg samples, high values of volumetric energy density were necessary, which allowed to produce sufficient amounts of liquid phase. The high scanning speeds, indeed, increased crack susceptibility of the alloy.

Recently, Zhou *et al.* [254] reported the fabrication of dense and crack-free Al-6Zn-2Mg alloy (7xxx series) by modifying the alloy composition with TMs Sc and Zr, using gas-atomized alloy powders. The material showed a microstructure similar to that of Scalmalloy®RP, with small columnar grains within the melt pool and small equiaxed grains in the melt pool border. The authors demonstrated that the precipitation of coherent Al_3(Sc, Zr) particles served as heterogeneous nucleation seed crystals for the formation of α-Al grains upon solidification, reducing the crack susceptibility of the 7xxx series alloy. Microstructure control induced by the Sc-/Zr-presence allowed to reach high tensile properties in the as-built condition (YS and UTS of 283 MPa and 386 MPa, respectively) with tensile elongation as high as 18% [254].

Some authors rather explored the possibility of modifying *in-situ* the composition of these hardly processable Aluminium alloys in order to improve their processability. In a recent study, Zhang *et al.* [89,255] reported that the addition of Zr to the crack-susceptible Al-Cu-Mg alloy had positive effects on processability and properties. Indeed, the Zr addition eliminated the cracks by forming low melting point phases, which could backfill the voids during final stage of solidification. Moreover, it induced the formation of ultra-fine equiaxed microstructure and the precipitation of sub-micrometric coherent Al_3Zr ($L1_2$) precipitates, which toughened the matrix and strengthened the material [89,255]. Figure 38 shows the effect of Zr addition on microstructures of Al-Cu-Mg processed by LPBF.

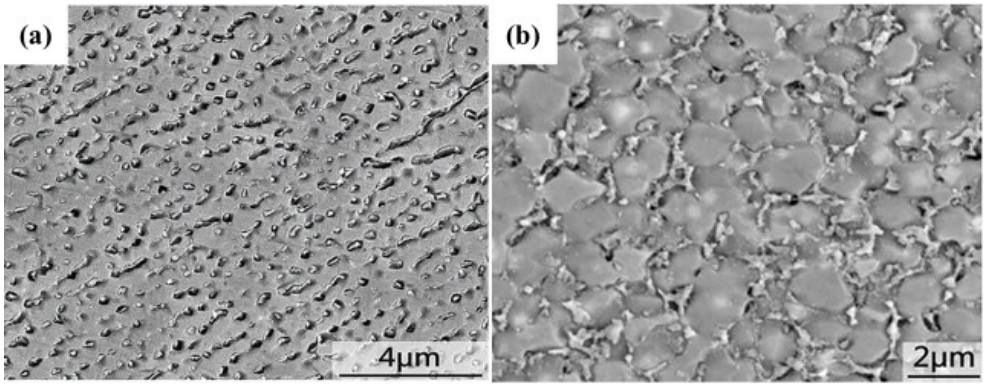

Figure 38. Micrographs showing (a) Cellular dendritic microstructure Al-Cu-Mg alloy [252] and (b) equiaxed refined microstructure of Zr/Al-Cu-Mg alloy [89] processed by LPBF.

Montero *et al.* [94] investigated the effect of silicon addition to the hardly processable Al7075 wrought aluminium alloy, by reporting the increase in the density and the reduction of microcracks. Alloy doping with silicon, indeed,

promoted the formation of a new eutectic at lower temperature with significant grain refinement and the enhancement of the fluidity of the alloy at the molten stage.

In 2017, Martin *et al.* [88] were among the first to demonstrate the possibility of producing crack-free Al7075 and Al6061 alloys by modifying *in-situ* compositions, particularly decorating the surfaces of powder particles with ZrH_2 nanoparticles. The introduction of nanoparticles changed the solidification mechanism during LPBF by promoting a columnar to equiaxed-dendritic transition (CET), which resulted in fine-grained crack-free microstructures. Zr-based nanoparticles, indeed, reacted during processing into the melt pool and induced the formation of many Al_3Zr precipitates strongly coherent with the fcc Al phase. Al_3Zr offered a low energy site for heterogeneous nucleation of many tiny equiaxed α-Al grains, which better accommodated the thermal strains upon solidification, resulting in a material with enhanced resistance to liquation cracking [88]. The Zr-modified Al7075 alloy exhibited YS and elongation comparable but slightly lower than the conventional wrought counterpart and the strength was 80% higher than AlSi10Mg manufactured by LPBF. Similarly to Scalmalloy®RP, in which the alloy composition was specifically tailored for taking advantage of the kinetics of LPBF and for producing microstructures and phases optimal for the process, the study conducted by Marten *et al.* [88] demonstrated the applicability of a novel metallurgical approach, which might enable the design of new alloys specifically tailored for LPBF.

2.3.3 Metal-matrix composites (MMCs)

New opportunities for improving properties of Aluminium alloys processed by LPBF come also from the *in-situ* production of reinforced Aluminium matrix composites (AMCs).

The introduction of ceramic particles such as Al_2O_3, SiC, TiB_2 and TiC to Al-based alloys, indeed, has been extensively investigated because considered promising for obtaining materials with enhanced mechanical properties and wear resistance [184–190]. For instance, Gu *et al.* [189] synthesized a novel Al-based composite by blending AlSi10Mg with SiC. They reported that high energy density induced in-situ reaction between the matrix and the reinforcement resulting in the formation of Al_4SiC_4 reinforcement, which induced enhanced mechanical properties. The extent of the in-situ reaction as well as the homogeneity of the microstructure were found to increase as the SiC particle size decreased [189].

Gu *et al.* [256] manufactured Al-Si-Mg-based nanocomposites by blending AlSi10Mg and TiC reinforcement through mechanical alloying. The authors reported that the composite exhibited higher microhardness and tensile strength as compared to the unreinforced AlSi10Mg, without any elongation reduction [256]. Moreover, the dispersion of the reinforcement within the matrix was found to be strongly related to the laser energy density applied. Gu *et al.* [188] reported also that wear resistance of AlSi10Mg/TiC composites produced by LPBF was strongly related to the building parameters. The best wear behaviour was observed at

intermediate linear energy density, where the sufficient densification of the material was combined with uniform distribution of the reinforcement.

2.3.4 *In-situ* alloying of powder mixtures

Although the largest part of materials commercially available or preliminarily investigated for LPBF are in the form of alloy powders produced by gas-atomization, which ensure good chemical homogeneity and stability during the process, some authors pointed out on the poor availability/high-cost of gas-atomized powders as well as on the resulting strong limitations in composition flexibility [190,192,257]. The *in-situ* alloying of powder mixtures has been explored as a possible way both to synthesize commercially available compositions and/or to innovate novel Aluminium alloys with higher composition flexibility.

For instance, Kang *et al.* [258] studied the microstructure and wear behaviour of a hypereutectic Al-Si alloy fabricated from a mixture of Al-12Si prealloyed powder and pure Si, assessing admissible differences in respect to the prealloyed method. The material exhibited good consolidation at intermediate laser powers, above which the porosity increased due to excessive boiling of Aluminium. The morphology of Si changed from irregular to spherical by increasing the amount of energy transferred to the material, which the authors ascribed to the full melting of Si and to its subsequent segregation upon solidification. The high density of the samples coupled to fine spherical Si particles resulted in higher hardness and better wear behaviour as compared to cast hypereutectic Al-Si-Cu alloy [258]. Roberts *et al.* [259] followed a similar approach for processing the hardly-processable Al6061 starting from elemental powder mixtures, showing promising results and opening up to the possibility of expending the method to other materials.

Alternatively, Bartkowiak *et al.* [260] investigated the feasibility of manufacturing custom-developed high-strength Al-*x*Cu alloys from blended powders by producing single scan tracks at different scanning speeds. They were crack free and they showed a fine microstructure with supersatured crystals and fine precipitates. Moreover, using high scanning speeds resulted in more homogenous and finer microstructures together with a fine dispersion of intermetallic phases. Beyond the results, the authors pointed that the single scan track method on powders mixtures could be very promising for developing custom compositions, preliminarily assessing microstructural features and processability.

Recently, Wang *et al.* [192] exanimated phases and microstructure of Al-*x*Cu wt% alloys produced by LPBF from the powders mixture of prealloyed Al-4.5Cu powders and pure Cu. Phase analysis by XRD revealed that all the Cu reacted during processing by producing Al_2Cu intermetallics and supersatured α-Al grains. However, microstructure analysis showed different features, including defects and solute-rich zones characterizing an inhomogeneous microstructure (Figure 39a). The authors pointed out that, when processing powders mixtures, the thermal regime within the melt pool, causing the rapid solidification and thus the limited diffusivity of the solute in the matrix, generated pronounced compositional gradients around solute particles yielding different microstructures (Figure 39b).

Nevertheless, the thermal regime induced by the overlaps of adjacent tracks and subsequent layers promoted a kind of solute re-diffusion into adjacent regions, slightly homogenising the composition [192].

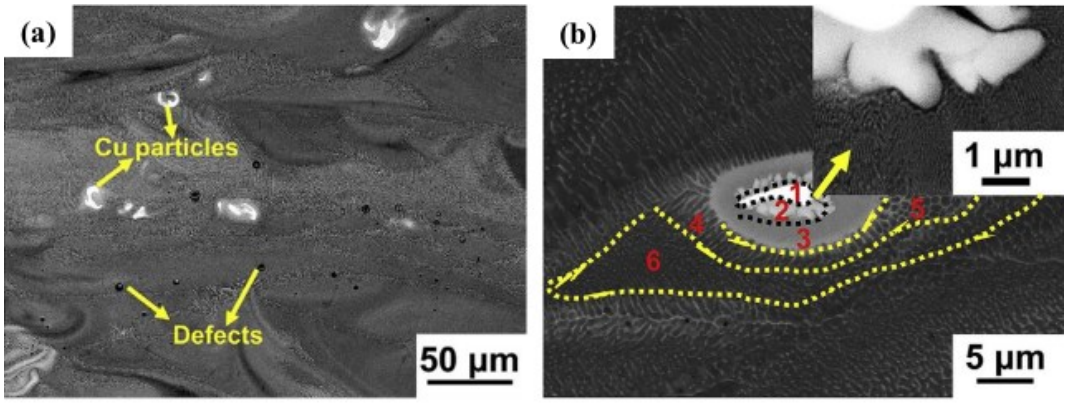

Figure 39. BSE-SEM micrographs of Al-xCu alloy showing (a) different microstructural features, including defects and Cu-rich zones and (b) different eutectic structures around a Cu-rich particle induced by the local concentration gradients [192].

Recently, Kang *et al.* [190,261] investigated into detail the *in-situ* synthesis of an Al-based MMC with high hardness, strength and wear resistance starting from a mixture of $Al_{65}Cu_{20}Fe_{10}Cr_5$ quasicrystal (QC) and pure Al powders. Phase analysis by XRD revealed that all the starting QC powder reacted with Al during processing, producing a supersatured α-Al solid solution matrix reinforced with a novel Al-Fe-Cr ($Al_{91}Fe_4Cr_5$) QC phase. No Cu intermetallic was found, which the authors ascribed to the extension of the solid solubility of Cu in Al under the rapid solidification regime during LPBF [261]. It was found that the process parameters actively affected the in-situ reactions, particularly the volume fraction of $Al_{91}Fe_4Cr_5$ QC phase and the degree of supersaturation of the α-Al phase, because of the different cooling rates. The samples were dense whilst the composite produced at low energy density was prone to crack due to the residual stresses during processing as well as to the intrinsic low ductility of the QC phase [261]. However, the in-situ reaction produced a new material with better wear resistance than other LPBF processed hypereutectic Al-Si alloys used in wear applications [261].

At low magnifications, the microstructure appeared homogenous. The partially melted QC phase was finely distributed within the matrix (Figure 40a). The authors pointed out that the semispherical shape of the melt pool caused by thermocapillary phenomena forced the partially melted particles at the bottom, along the boundary, resulting in the characteristic linear arc-like morphology of the partially melted QC phase, as observed in Figure 40a. However, at higher magnifications, the microstructure showed different features (Figure 40b-c). At the melt pool scale, the microstructure consisted of α-Al regions, partially melted QC and fine regions of reacted products. The authors ascribed this behaviour to the chemical inhomogeneity of the feedstock powder and to the differences in physical properties among the powders (i.e. thermal conductivity, melting temperature, etc.), which hindered the homogenization of the microstructure. In addition, the high

temperature gradients within the melt pool and the rapid solidification were considered to not favour homogenization [190]. Nevertheless, heat treatment at high temperature was found to slightly homogenize microstructure, by reducing the extent of Al-rich regions.

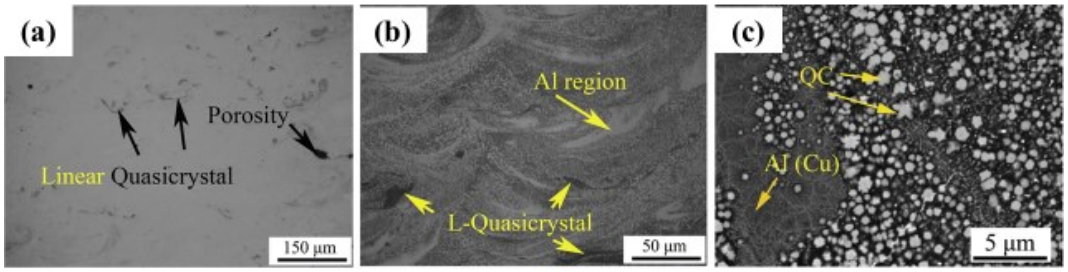

Figure 40. Microstructures at different magnifications of *in-situ* manufactured Al/QC composite. (a) low magnification OM showing homogenous distribution of partially melted QC phase, (b) high magnification OM showing heterogeneous microstructure at the scale of the melt pool consisting of α-Al rich regions, partially melted QC phase and a reacted fine region and (c) SEM micrograph showing inhomogeneous microstructure consisting of star-like fine QC phase and α-Al [190].

The present chapter provides evidences that the addition of transition metals such as Ni, Cr, Fe etc. can significantly increase the mechanical properties of Aluminium alloys produced by RSPs technique, such as melt spinning, by promoting both the formation of supersatured solid solutions and the precipitation of fine strong precipitate particles finely dispersed [212,215,224,226]. In addition, transition metals can boost the thermal resistance and/or stability of Aluminium alloys, having low diffusion coefficient [18] and lower coefficient of thermal expansion than that of Aluminium [262]. The unique features of LPBF consisting in the deposition of the localized laser energy and in the complex melting and solidification dynamics of the molten alloy within the melt pool, then, allow to produce Aluminium alloys with unique microstructures, metastable phases and often enhanced properties. Moreover, recently, the flexibility offered by LPBF in processing powder mixtures has been explored by some researchers for *in-situ* alloying different elemental and/or prealloyed powders both for producing already established materials or innovating novel alloys [185,258]. This approach could be very promising for the research and development of new high strength Aluminium alloys for LPBF.

Chapter 3

Development of two Aluminium alloys through LPBF of different powders mixtures

The present chapter reports the studies conducted for the *in-situ* synthesis of two novel Aluminium alloys, namely Al-Si-Ni and Al-Si-Ni-Cr-Fe.

The aim of the study is to investigate the possibility of improving the mechanical properties of AlSi10Mg, the most widely used Aluminium alloy by LPBF, by adopting an alloying strategy based on the *in-situ* introduction of small amounts of transition metals, by gradually increasing the compositional complexity of the powder system. In particular, the Al-Si-Ni and Al-Si-Ni-Cr-Fe will be obtained by mixing AlSi10Mg powder with pure Ni or nickel-base superalloy Hastelloy X powder containing Ni, Cr and Fe as main alloying elements, respectively.

3.1 Al-Si-Ni

Part of the results that will be presented in the present chapter had been published in the paper "A study of the microstructure and the mechanical properties of an Al-Si-Ni alloy produced via Selective Laser melting", Journal of alloys and compounds, 695, 2017, 1470-1478 [263].

3.1.1 LPBF system and powder properties

Within this work, an EOSINT M270 Dual Mode commercial machine (EOS GmbH, Germany) LPBF system was used. The main characteristics of the machine system will be presented below.

For conducting the *in-situ* synthesis of Al-Si-Ni alloy, AlSi10Mg and pure Ni powders were used. The characteristics of each powder, including the chemical composition, the particles shape and morphology as well as the size distribution, will be also provided within the following section. The description of the equipment used for powder characterization is reported in Appendix A.1.1 Powder Characterization.

3.1.1.1 EOSint M270 machine system

The EOSint M270 Dual Mode machine (Figure 41a) was equipped with a Yb fiber laser with a nominal laser power of 200 W, continuous scanning speed up to 7000 mm s^{-1}, a nominal laser spot size of 100 μm and layer thickness ranging between 20 and 100 μm. The internal building chamber has a dimension of 250 mm × 250 mm × 215 mm.

The electro-optical galvanometers installed above the building chamber, within the laser station, allow to precisely control the laser movement and to focus the laser beam over the building platform. The skywriting function available in this machine system allows to limit the inertia of galvanometer mirrors in accelerating and decelerating by switching on/off the laser when scanning speed changes. The skywriting function, when active, allows thus to have a linear and constant scan speed (and thus transferred amount of energy) during all the effective laser exposure.

The building platform is placed within the building chamber and over the heater system. The heater system allows to heat up the building platform at a temperature ranging between 35 and 200 °C. On the right side of the building chamber there is the dispenser chamber where the metal powder to be processed is placed while on the left side of the building chamber there is the collector chamber (Figure 41b).

The whole process takes place under flowing Ar inert atmosphere and the machine can work only when the residual O_2 content within the process chamber is below 0.1 % (100 ppm of residual oxygen). However, during the process, this value can vary between 0.01 and 0.12 % without compromising the building process. In order to limit the consumption of Ar during the process, the machine is equipped with a recirculating filter system, which continuously extracts, filters and reinserts the gas into the process chamber.

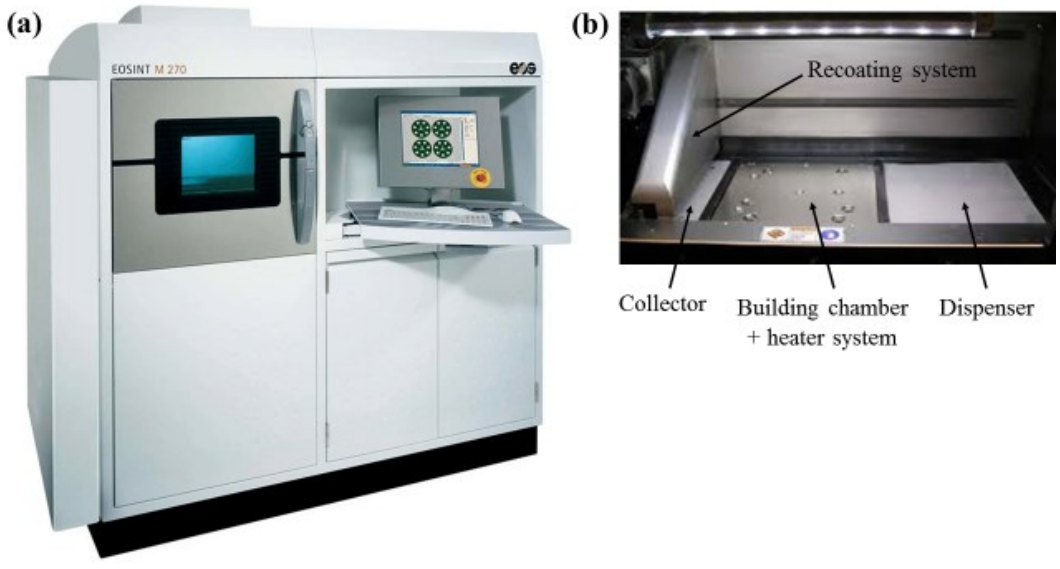

Figure 41. EOSINT M270 machine used for the present study and (b) details of the internal process chamber.

3.1.1.2 AlSi10Mg powders

The AlSi10Mg gas-atomized powders used for the synthesis of Al-Si-Ni alloy were provided by EOS GmbH.

The nominal composition, so as declared by the supplier in the material datasheet, is reported in Table 7. FESEM investigation of the powder revealed that particles had mostly spherical morphology with occasionally some satellites, which originated during the atomization process due to particle collisions (Figure 42). The mean diameters (calculated by laser granulometry under a volumetric assumption) corresponding to the 10% ($d_{10,}$), 50% (d_{50}) and 90% (d_{90}) of the total particles population were 12.9 μm, 27.1 μm and 42.6 μm, respectively [24].

Table 7. Nominal chemical composition of the EOS GmbH AlSi10Mg powder [147].

Elements	Al	Si	Mg	Fe	Ti	Cu	Mn
Wt.%	Bal.	9-11	<0.2-0.45	<0.55	<0.15	<0.05	<0.45

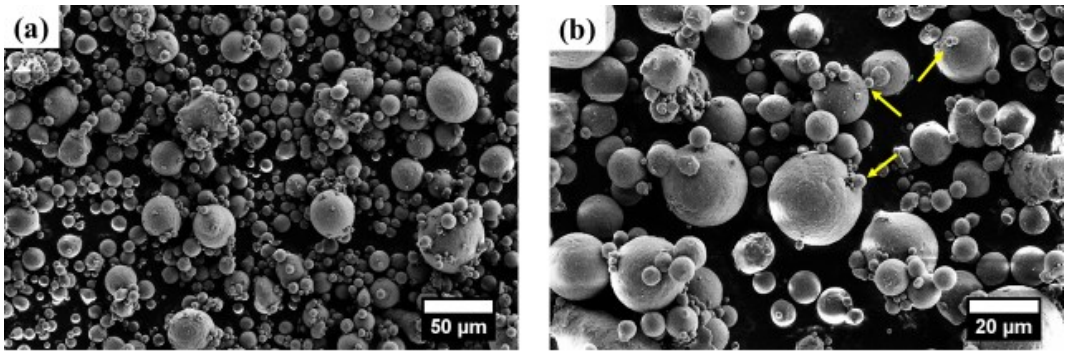

Figure 42. Field Emission Scanning Electron Microscopy (FESEM) images of AlSi10Mg powders supplied by EOS GmbH for the Al-Si-Ni study taken at (a) 1.00 kX and (b) 2.50 kX. Yellow arrows points at satellites.

3.1.1.3 Ni powders

Pure Ni gas-atomized powders were provided by Alfa Aesar and they were mainly constituted by roughly spherical-shaped particles with many fine particles and occasionally few satellites (Figure 43). Overall particles are fine. The mean diameters corresponding to the 10% ($d_{10,}$), 50% (d_{50}) and 90% (d_{90}) of the total particles population – so as declared by the supplier - were as low as 4.1 μm, 12.2 μm and 29.8 μm, respectively. Small average dimension of powder particles is expected to enhance the uniformity of mixing and the chemical homogeneity of the powder mixture. If it considers the significantly higher melting temperature of Ni with respect to that of AlSi10Mg (1455 °C and ~590 °C, respectively), in fact, better melting and diffusion of Ni in AlSi10Mg can occur if Ni particle size is smaller than AlSi10Mg one.

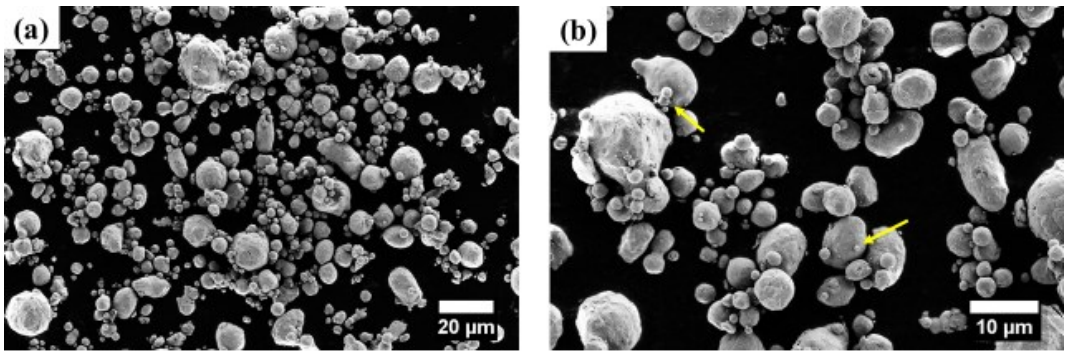

Figure 43. FESEM images of pure Ni powders used for the Al-Si-Ni study taken (a) at 2.00 kX and (b) 5.00 kX magnification. Yellow arrows point at satellites.

3.1.2 Design of the alloy composition

The mixing ratio between the AlSi10Mg and pure Ni powders was selected as to have a mean composition for the Al-Si-Ni ternary alloy close to the eutectic one. At the eutectic, indeed, the alloy exhibits a narrow solidification range, which avoids liquation cracking phenomena during LPBF [145]. In the ternary Al-Si-Ni alloy system, the eutectic occurs at 567 °C with 10.98 wt.% Si and 4.9 wt.% Ni [264].

The AlSi10Mg and pure Ni powders were dry mixed in ceramic jars rotating at 60 rpm for 48 h, without any grinding medium in a weight proportion AlSi10Mg:Ni of 95:5. The mean chemical composition of the powder mixture is reported in Table 8

Table 8. Mean calculated chemical composition of the Al-Si-Ni alloy obtained by mixing AlSi10Mg + 5 wt.% Ni powders.

Elements	**Al**	**Si**	**Ni**	**Mg**	**Fe**	**Mn**	**Ti**
Wt.%	Bal.	8.5-10.5	5.1	0.18-0.42	<0.55	<0.45	<0.15

In Figure 44 the BSE-SEM images of the AlSi10Mg-Ni powders mixture are reported. Although the occasional presence of spare large Ni particles with size as high as approximately 30 µm, the mixing method allowed to obtain a fine dispersion of the different powders particles. However, because of the small size of the melt pool and the fast solidification of the molten alloy during LPBF, the presence of large particles could affect the homogeneity of the alloy composition after LPBF.

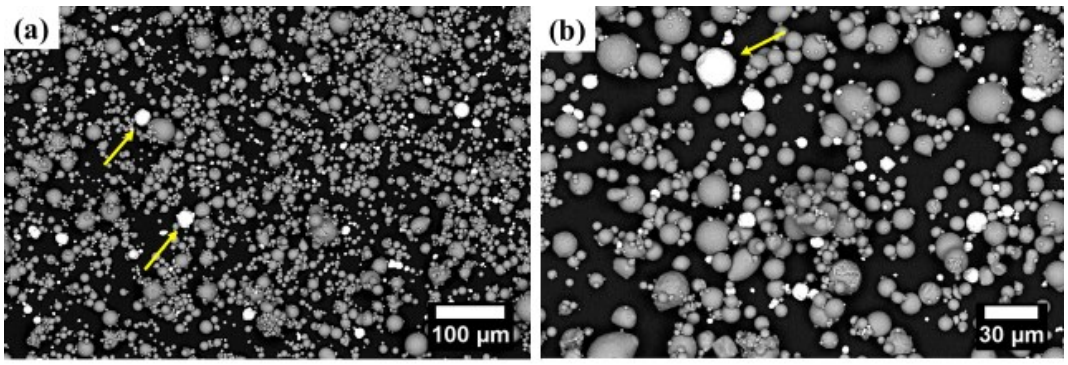

Figure 44. Back-scattered electron (BSE)-SEM images of the Al-Si-Ni powder mixture. Grey spheres represent AlSi10Mg powder particles and white spheres are Ni powder particles. Yellow arrows point at large Ni particles [263].

3.1.3 Consolidation

The specimens were fabricated using the EOSINT M270 LPBF machine. Cubic samples ($10 \times 10 \times 10$ mm^3) were built on an Aluminium platform with a constant powder layer thickness of 30 µm, which is the standard one for LPBF of AlSi10Mg with the present machine, and a 67° rotated scanning strategy, in which each layer in scanned once and the direction of scanning is rotated by 67° between consecutive layers.

Twenty cubic samples were built at different laser power, scanning speed, hatching distance and stripe width values, within the values ranges listed in Table 9. Some parameters combinations, such as low laser power and extremely high scanning speed, were not taken into account because were likely to yield insufficient melting and poor consolidation. Moreover, a minimum scanning speed of 600 mm s^{-1} was set in order to ensure the cooling rates during samples fabrication were sufficiently high [64]. Before starting the process, the building platform was pre-heated at 100 °C and the whole building process took place at the same temperature.

Table 9. Parameters and theirs variation ranges used for the fabrication of Al-Si-Ni samples by LPBF.

Elements	P (W)	v (mm s^{-1})	H_d (mm)	Stripe width (mm)
Min.	120	600	0.1	1
Max.	195	1200	0.17	Whole part

Initially, LPBFed specimens were characterized for the residual porosity by Archimedes method (Appendix A.1.2.1 Archimedes method) in order to assess the influence of the processing parameters on the densification behavior of the material.

The results were discussed referring to the laser energy density Ψ (J mm^{-3}) parameter already introduced in 1.4.5 Energy density paragraph and defined as:

$$\Psi \left[\frac{J}{mm^3}\right] = \frac{P}{v \times h \times t}$$

where P is the laser power (J s^{-1}), v is scanning speed (mm s^{-1}), h_d is hatching distance (mm) and t is layer thickness (mm).

Figure 45 reports the porosity data of the Al-Si-Ni samples manufactured by LPBF at different energy density values. The results revealed that the *in-situ* synthesized Al-Si-Ni alloy exhibited a very good consolidation behaviour, with few percentages of residual porosity within a broad range of energies inputs. This could be ascribed to the narrow solidification range of the eutectic composition selected for the present study and to the presence of high content of silicon, which provided good fluidity of the alloy at the molten state [94].

According to the presented results, the sample fabricated at 47.8 J mm^{-3} (P = 195 W, v = 800 mm s^{-1}, h_d = 0.17 mm) exhibited the lowest percentage of residual porosity of 0.1% with the lowest energy input and for this reason it was selected for further characterizations.

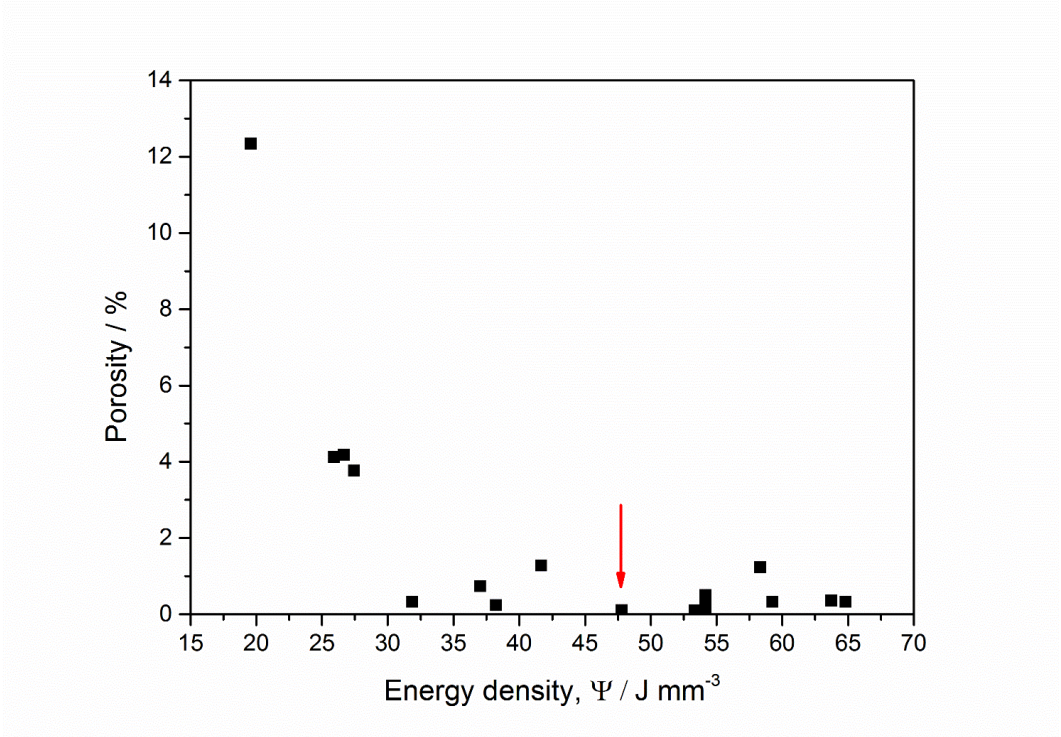

Figure 45. Influence of the energy density on the residual porosity calculated by Archimedes method on Al-Si-Ni processed by LPBF.

The metallographic investigation of the Al-Si-Ni alloy sample though Optical Microscopy, OM (Appendix A.1.4.1 Optical microscopy) confirmed the high density of the material. The vertical cross section of Al-Si-Ni reported in Figure 46, indeed, revealed only few residual pores and no cracks were found. In addition, the material exhibited the characteristic non-homogenous microstructure of LPBFed

materials [161]. As already discussed in 2.2 LPBF of AlSi10Mg: microstructure and properties paragraph, the layer-wise manufacturing of parts by LPBF process yields a unique microstructure composed by the overlapping of individual melt pools, whose morphology and orientation are strictly influenced by the scanning strategy [232]. The overlapping regions between adjacent tracks and subsequent layers, which identify the melt pools borders, could be clearly seen in Figure 46.

The microstructure of the Al-Si-Ni produced by LPBF strongly differed from the conventional cast one, in which, according to the ternary Al-Si-Ni phase diagram, coarse primary α-Al grains surrounded by the eutectic containing Si and Al_3Ni irregular platelets would be observed [265]. Figure 46 also revealed that some micrometric agglomerates/precipitates existed in the Al-Si-Ni microstructure. Their distribution and size did not follow any specific pattern correlated to the laser scanning strategy adopted for sample fabrication. This observation suggested that their presence could be related to some issues in the powder preparation method, in particular to some large Ni particles present in the starting powder mixture (as observed in Figure 44), rather than to specific thermo-physical conditions occurring within the melt pool during the LPBF process [263].

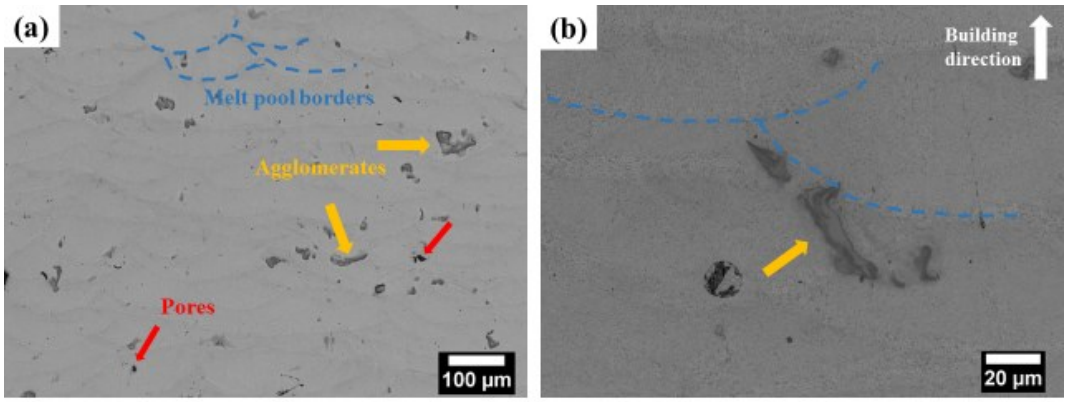

Figure 46. OM images at different magnitudes of the vertical cross section of Al-Si-Ni processed by LPBF. The blue dotted lines trace the melt pool borders, the red arrows point at residual pores and yellow arrows indicate large agglomerates/precipitates.

As previously said, no cracks were observed in the cross sections of sample processed with the optimal process parameters. The absence of cracks was supported by DTA curve reported in Figure 47. The melting range for the Al-Si-Ni (Figure 47a), indeed, was narrow and even lower than that of AlSi10Mg (Figure 47b). A narrow melting range is known to contribute in avoiding the occurrence of liquation cracking phenomena, which are usually observed in high strength Aluminium alloys [89–91].

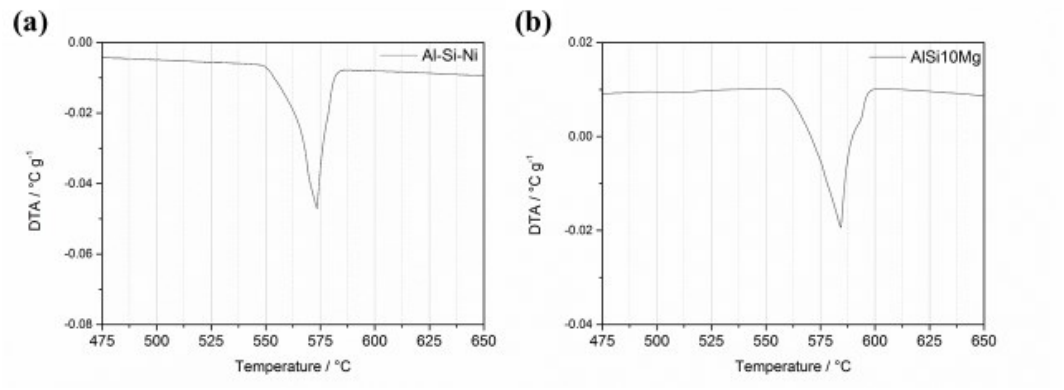

Figure 47. Differential Thermal Analysis (DTA) curves of (a) Al-Si-Ni and (b) AlSi10Mg manufactured by LPBF showing the narrow melting range of the *in-situ* synthesized Al-Si-Ni alloy.

3.1.4 Microstructural and compositional features

The experimental XRD pattern of Figure 48 (Appendix A.1.3 X-ray diffraction analysis) revealed that the LPBF Al-Si-Ni alloy consisted of α-Al, Si and Al_3Ni. This suggests that precipitates observed above in Figure 46 were probably mainly constituted by Al_3Ni, whilst it could not be excluded that they represented partially melted Ni particles whose diffraction peaks were no longer visible after LPBF. Gonzalez *et al.* [225] assessed the precipitation of Al_9Ni_2 in Al-Si-Ni materials rapidly solidified by melt spinning. The continuous heating and cooling cycles occurring during LPBF resulting from the repeated laser tracks could be the reason why, whilst the high cooling rates during the LPBF process, the Al_9Ni_2 phase was not assessed in LPBF Al-Si-Ni.

The low intensity of the Si reflections indicated that the largest amount of Si was retained into supersatured solid solution within the α-Al phase. Many authors assessed the extension of the solid solubility of Si into the Al lattice at the high cooling rates during LPBF, which caused a reduction in the amount of segregated Si and thus the resulting decrease in the XRD peak intensities [161]. Moreover, the absence of Ni reflections suggested that all the elemental powder reacted with Aluminium during LPBF, producing Al_3Ni. Considering Ni as the limiting reactant, the amount of Al_3Ni in Al-Si-Ni alloy was thus estimated being 12 wt.%.

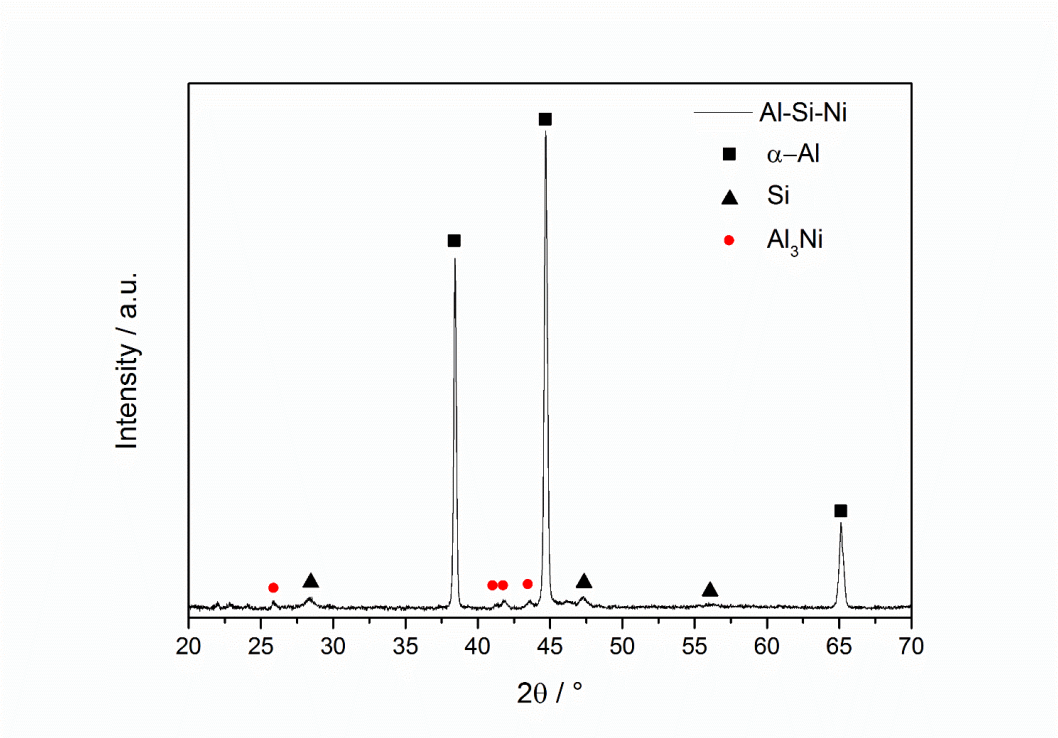

Figure 48. XRD pattern of the Al-Si-Ni produced by LPBF showing the phases existing in the as-built material.

A detailed microstructural analysis through FESEM was conducted on Al-Si-Ni and the main results are presented below in Figure 49(a-d) (Appendix A.1.4.2 Electronic microscopy).

As expected, the material exhibited a very fine microstructure as consequence of the high cooling rate during the LPBF process. Along the vertical cross section, the melt pool centre presented a fine cellular structure of α-Al, while elongated cells were found at the melt pool borders due to the thermal gradient. As already discussed in 1.2.7 Thermal regimes and metallurgical effects paragraph, this cellular-like solidification microstructure forms because of the non-equilibrium solidification of primary α-Al grains due to the high cooling rate and to the subsequent rejection of the eutectic phase that accumulates along the cells boundaries [161].

Figure 49b shows a typical Al_3Ni coarse precipitate. The irregular shape and morphology could be related to the highly dynamics within the melt pool. On the other hand, the high magnification images presented in Figure 49(c,d) highlighted that additional regularly shaped submicrometric Al_3Ni precipitates - related to the eutectic transformation - existed alienated to the melt pool border. During LPBF, in fact, the material undergoes repeated melting and cooling cycles as the laser beam processes adjacent scan tracks and consecutive layers and solid phase transformation leading to the formation of stable phases can occur [76].

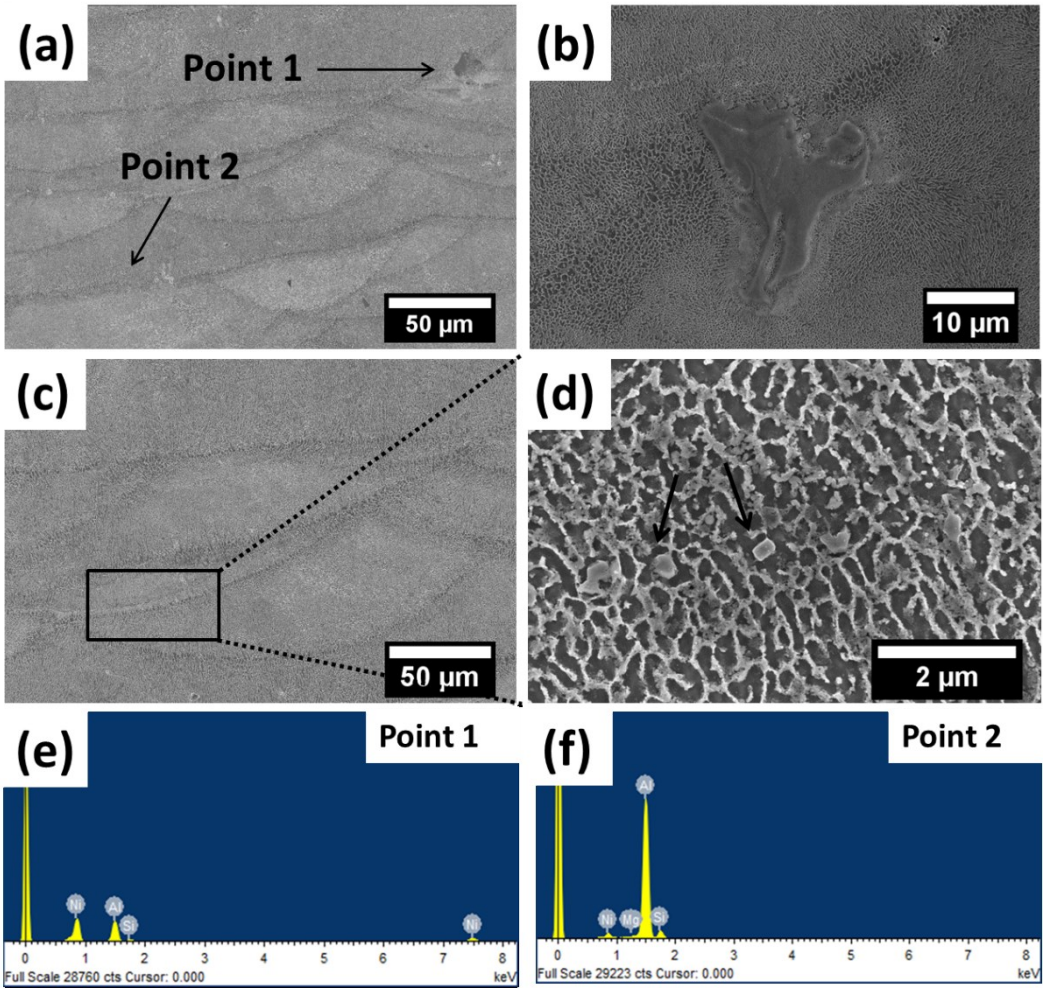

Figure 49. (a-d) FESEM images of the vertical cross section of Al-Si-Ni synthesized by LPBF with optimized process parameters, (d) detail of the micrometric precipitates observed along the melt pool border, (e) and (f) EDX spectra for point 1 and point 2 reported in (a), respectively [263].

The EDX data reported in Table 10 and in Figure 49(e-f) confirmed the coarse micrometric agglomerates/precipitates like that observed in Figure 49b were Al_3Ni and that far from such agglomerates the composition was close to the nominal one of the Al-Si-Ni alloy. This observation suggested that the phenomena occurring within the melt pool, such as the temperature-induced surface tension gradient know as Marangoni flow and the recoil pressure effect, were effective in distributing the Nickel of the starting powder mixture within the alloy, yielding the chemical composition within the melt pool close to that nominal of the AlSi10Mg-Ni powder mixture. EDX maps reported in Figure 50, in fact, revealed that within the melt pool, when micrometric precipitates were not present, the Nickel was finely dispersed throughout the microstructure. In addition, the network of segregated eutectic Si along the α-Al cells boundaries could be clearly seen [161].

Table 10. Chemical composition (wt. %) given by SEM-EDX point analysis of point 1 and point 2 of Figure 49a. The nominal mean composition of Al-Si-Ni is reported below as reference for comparisons.

Wt.%	Al	Si	Ni	Mg
Point 1	37.7	4.3	57.9	0.1
Point 2	84.3	10.7	4.7	0.3
Al-Si-Ni nominal composition	Bal.	10.5	5.1	0.3

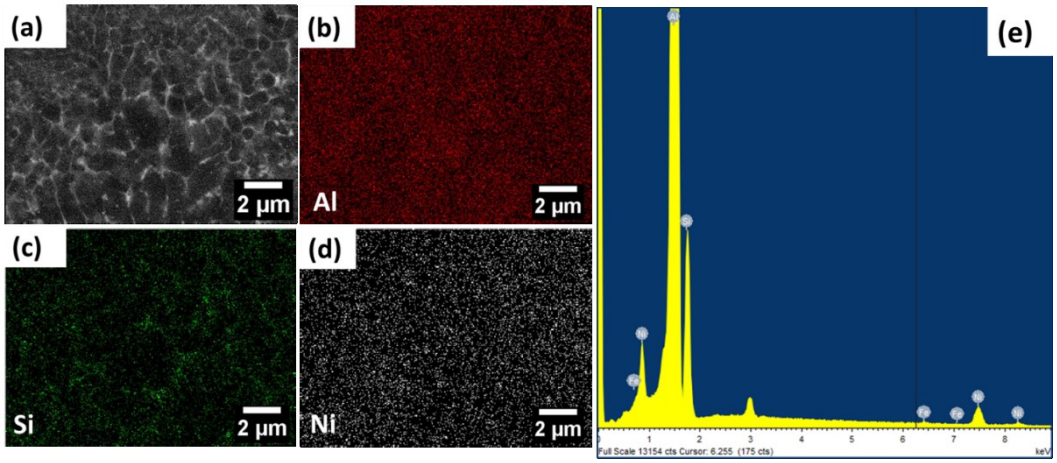

Figure 50. (a-d) SEM-EDX maps including the elemental distribution of Al, Si and Ni and (e) EDX spectrum of the vertical cross section of LPBF Al-Si-Ni alloy. The EDX maps shows the homogenous distribution of Ni throughout the microstructure and the segregation of Si along the α-Al cells [263].

The thermal behaviour of the Al-Si-Ni alloy was compared to that of AlSi10Mg by conducting differential thermal analysis (DTA) in the low temperature range between 150 and 400 °C and the results are presented in Figure 51.

For both the materials, two main exothermic peaks were found between 200 and 350 °C. Whereas the first peak at around 250 °C did not change significantly by modifying the AlSi10Mg composition with Ni addition, the second peak at around 320 °C slightly shifted to higher temperature in the Al-Si-Ni alloy. As already discussed in 2.2 LPBF of AlSi10Mg: microstructure and properties paragraph, Marola *et al.* [235] correlated the first and the second peaks to the precipitation of Si and Mg_2Si from the supersatured α-Al phase, respectively [235]. Nevertheless, in literature different authors do not perfectly agree on that and Biffi *et al.* [266] ascribed the second peak to the diffusion of Si. According to this peak indexing, the slight upward shift observed in the second peak of the Al-Si-Ni alloy could be ascribed to some kind of hindering effect on the diffusion of Si related to the presence of small amounts of Ni. On the other hand, this shift to higher

temperature had been already observed in others Al-Si alloys as consequence of Fe, Mg and Cu addition [267].

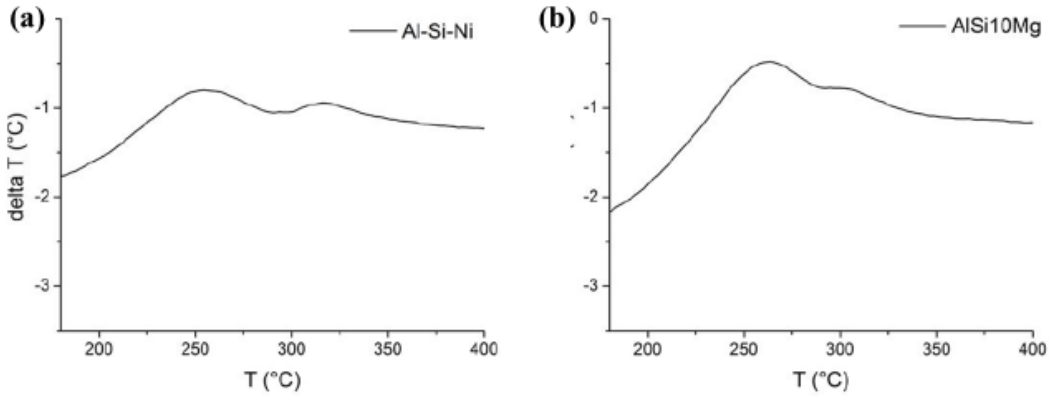

Figure 51. Differential Thermal Analysis (DTA) curves of (a) Al-Si-Ni and (b) AlSi10Mg as built samples produced by LPBF [263].

Thermo-mechanical analysis (TMA) was conducted on as-built LPBF Al-Si-Ni specimen in the temperature range between 50 and 400 °C (Appendix A.1.5.2 TMA) in order to have a first insight into the thermal resistance of the *in-situ* synthesized Al-Si-Ni alloy, through the calculation of its coefficient of thermal expansion (CTE). Alloying with Ni is expected to reduce the CTE of the base alloy, having Ni a lower CTE than that of Al [262], contributing in increasing the thermal stability of the material.

The results reported in Figure 52 showed that during the first heating ramp residual stresses were released. For Al-Si-Ni, residual stresses relaxed in the temperature range 200-260 °C [268]. In LPBF process, residual stresses rise as consequence of the thermal strains induced by the cyclic thermal expansion and shrinkage of the material, the high temperature gradients and the high cooling rate of the molten material. When residual stresses are too high, they can bring to deformation, warping, delamination and cracking [269]. The second heating ramp allowed to evaluate the CTE for the Al-Si-Ni alloy. An average value of 20.8×10^{-6} $°C^{-1}$ was calculated within the temperature range 100-400 °C. This value was significantly lower than that calculated by Marchese *et al.* [270] for AlSi10Mg within the same temperature range and corresponding to 25.3×10^{-6} $°C^{-1}$. This result gives further evidences of the effectiveness of the *in-situ* alloying between AlSi10Mg and pure Ni during LPBF, which allowed to produce a new material with different and enhanced thermal properties.

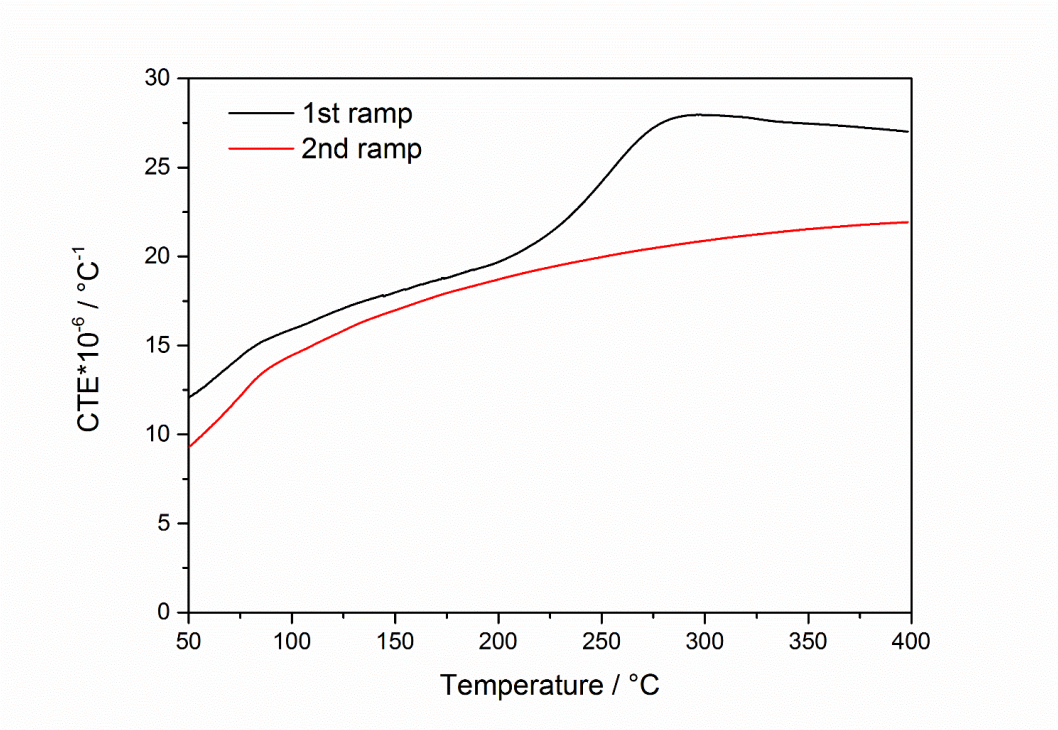

Figure 52. TMA curves for the Al-Si-Ni alloy after LPBF showing the variation of the CTE during the first heating ramp. The heating rate was 5 °C min^{-1}.

3.1.5 Hardness

The hardness data of the novel Al-Si-Ni alloy manufactured by LPBF are presented in Table 11 (Appendix A.1.6 Micro-hardness evaluation). Hardness values were compared to that of traditional LPBF AlSi10Mg and to that of an Al-Si-Ni alloy with similar composition and produced by rapid solidification melt spinning technique.

With respect to the LPBF AlSi10Mg alloy, the introduction of Nickel caused a strong increase in the hardness. This could be ascribed to the formation of fine Al_3Ni particles, which interacted with the dislocations by different mechanisms such as Orowan strengthening, whilst additional solid solution strengthening due to the Ni atoms into solid solution within the α-Al phase could not be excluded. The presence of Ni atoms in the host lattice, in fact, generates stress and induces a lattice strain that impedes the dislocation motion, further increasing the hardness of the material. In addition, the comparison with an Al-Si-Ni alloy with similar composition in both the as-melt spun and aged conditions, demonstrated that LPBF technology is effective in enhancing the mechanical behaviour of the material already in the as-built condition.

Table 11. Mechanical properties of the Al-Si-Ni produced by LPBF as compared to other materials and/or processing routes.

Composition	Technology	HB	$HV_{0.1}$
Al-Si-Ni	LPBF	158 ± 3.0	179.5 ± 3.0
AlSi10Mg	LPBF	128.6 ± 1.9	135.0 ± 0.9
Al-Si12.5-Ni1 [208]	Melt spinning	-	139.0
Al-Si12.5-Ni1 [208]	Melt spinning + ageing (180 °C/20 h)	-	71.4

3.1.6 Nanoindentation

In order to assess the mechanical behaviour of the material at the melt pool scale and the influence of Ni addition to the base AlSi10Mg alloy, nanoindentation measurements were carried out on both AlSi10Mg and Al-Si-Ni (Appendix A.1.7 Nano-hardness evaluation). During nanoindentation test a controlled load is applied to the specimens through an indenter and then removed, producing traditional force versus displacement curves. The analysis of the curves, then, provides local information regarding the mechanical properties of the specimen. For Al-Si-Ni, a grid of 11×11 with 121 indentations, distant 2 μm from each other, was realized.

It was found that the nanohardness of Al-Si-Ni, calculated by averaging the nanoindentation values within the indentation grid, was around 2.2 ± 0.35 GPa, against a mean calculated value of 2.0 ± 0.15 GPa for AlSi10Mg.

A coloured representation of the indentation grid is reported in Figure 53(a,b) for AlSi10Mg and Al-Si-Ni, respectively. It is possible to observe that the distribution of nanohardness changed between the two alloys, being the representation of the nanohardness map of AlSi10Mg more homogenous than that of Al-Si-Ni. In this regard, additional information were gained from the investigation of the microstructure beneath the nanoindentation grids throughout FESEM and the results are presented in Figure 54 (a,b).

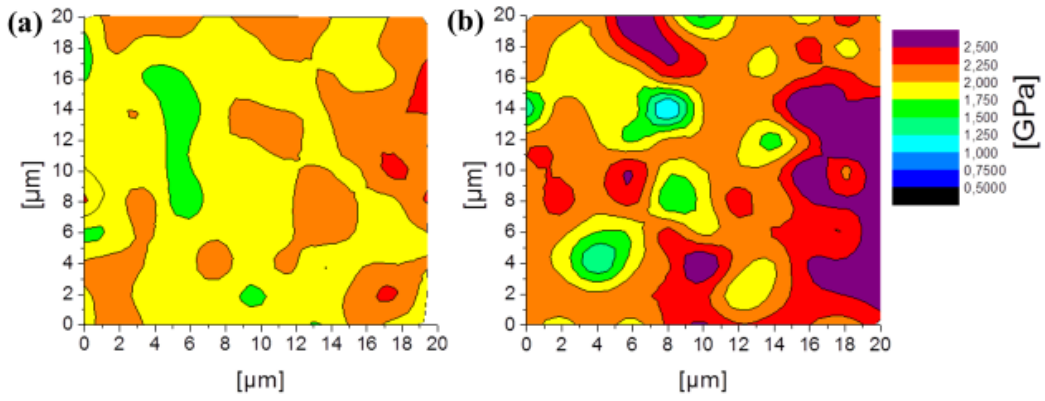

Figure 53. Nanohardness coloured maps of the vertical cross section of LPBF (a) AlSi10Mg and (b) Al-Si-Ni in the as-built state. The nanohardness coloured maps are continuum representations in which a colour is attributed to each indentation, and thus hardness value, according to the hardness scale reported to the top right of the figure [263].

The microstructure of AlSi10Mg corresponding to the nanoindentation map (Figure 53a) revealed that the highest nanohardness value of around 2.4 GPa was measured where a finer microstructure existed (Figure 54a). The finer size of the columnar α-Al cells caused a local increase in the material hardness in AlSi10Mg.

The same effect was observed in Al-Si-Ni sample, whilst the local nanohardness value was for the largest part controlled by the submicrometric Al_3Ni precipitates formed during LPBF process. As visualizes Figure 54b, in fact, the highest value of nanohardness of around 3.0 GPa (Figure 53b) was reached where Al_3Ni submicrometric precipitates formed. According to these results, it can be said that the high microhardness assessed in Al-Si-Ni is most probably due to the presence of submicrometric Al_3Ni precipitates distributed throughout the material.

According to this observation, it is reasonable to conclude that a more homogenous distribution of Ni in the powder mixture could contribute in further enhancing the mechanical properties of Al-Si-Ni by reducing the formation of large micrometric Ni-rich agglomerates, as that reported in Figure 49b, in place of fine Al_3Ni precipitates homogenously distributed. The distribution of Ni particles in the powder mixture could improve by reducing the fraction of coarse Ni particles - with dimension comparable to the average size of AlSi10Mg particles - and by increasing the fraction of "fines" Ni particles at the same time. In this way, the melting and mixing of Ni particles during laser exposure would be enhanced. In addition, the compositional homogeneity of the powder mixture could improve by optimizing the mixing method or by reducing the moisture content over particles surfaces. AlSi10Mg powder, in fact, is known to quickly absorb the moisture from the environment, which produce hydrogen bonds among the particles favouring the agglomeration of these latter [110]. Such agglomerates can lower the compositional homogeneity of the mixture and for this reason their presence should be limited, i.e. with a drying treatment in oven of the AlSi10Mg powder.

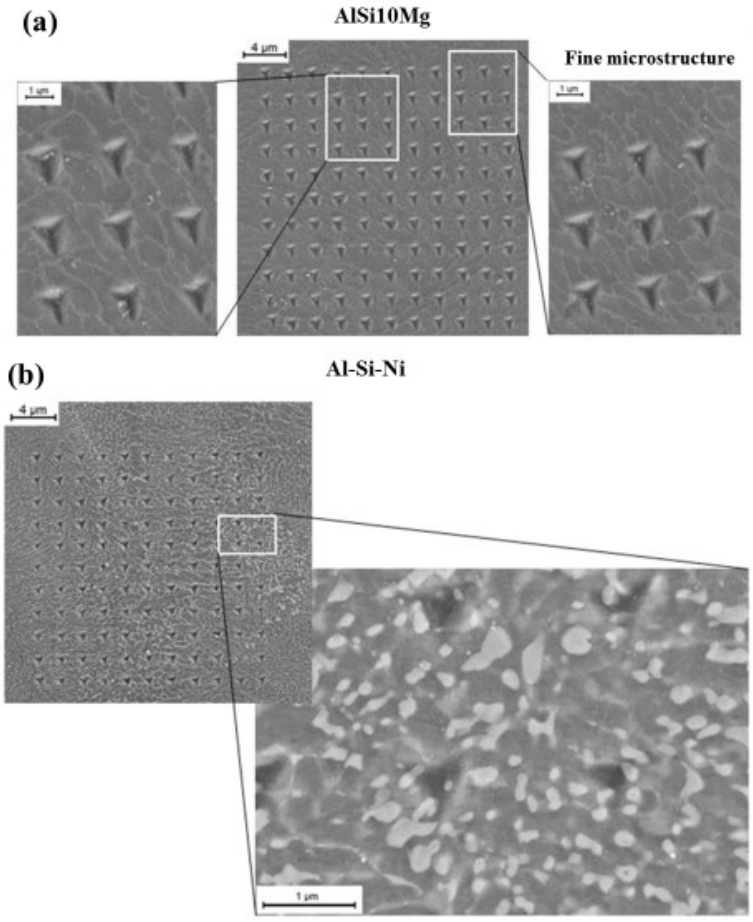

Figure 54. FESEM micrographs showing the nanoindentation grids of (a) AlSi10Mg and (b) Al-Si-Ni. White spots in (b) most probably represents Al_3Ni precipitates formed during the eutectic transformation L = Al + Al_3Ni + Si, whilst it cannot be excluded they represent submicrometric metastable product phases formed during rapid solidification.

3.1.7 Conclusion

Within this work, it was demonstrated that dense and crack-free Al-Si-Ni samples could be manufactured by *in-situ* alloying of AlSi10Mg and pure Ni powders throughout the selection of an alloy composition close to that eutectic. The narrow solidification range avoided the occurrence of liquation cracking phenomena and the high content of silicon enhanced the fluidity of the alloy at the molten stage, resulting in an alloy composition with a good consolidation behaviour under the experimental condition adopted in the present study.

The microstructure was heterogeneous and showed the presence of some large precipitates randomly distributed, micrometric in size and rich in Nickel, probably formed due to the incomplete melting of the spare large Ni particles observed in the powder mixture. Nevertheless, the largest part of precipitates found in Al-Si-Ni microstructure were sub-micrometric and were preferably located along the melt pool borders while within the melt pool the chemical composition was close to the nominal one.

As expected, the rapid cooling during LPBF induced the formation of fine cellular dendritic α-Al cells supersatured in Si and separated by the eutectic network. Nevertheless, the addition of Ni only slightly altered the precipitation behaviour of Si with respect to that of the base AlSi10Mg alloy.

The modification of the alloy composition is effective in improving the strength of materials produced by LPBF. In particular, it was evaluated that the microhardness increased more than 33% with respect to the base AlSi10Mg alloy, as consequence of the addition of 5 wt.% of Ni, which induced the precipitation of submicrometric Al_3Ni particles.

Finally, it is worth to mention here that the residual stresses for the *in-situ* synthesized LPBF Al-Si-Ni samples caused the distortion of the samples during manufacturing, with the resulting detachment of the part from the building platform (Figure 55). This behaviour is probably related to the low ductility and high stiffness of Al-Si-Ni alloys caused by the precipitation of high amounts of Al_3Ni intermetallics. Due to the high Young's Modulus of Al_3Ni, around 140 GPa [271], the maximum elastic strain that the alloy can cope with before the plastic deformation occurs decreases.

Further studies on the Al-Si-Ni alloy produced by LPBF should be aimed in improving the homogeneity of the microstructure, in reducing the thermal stresses causing warping as well as optimizing supporting structures.

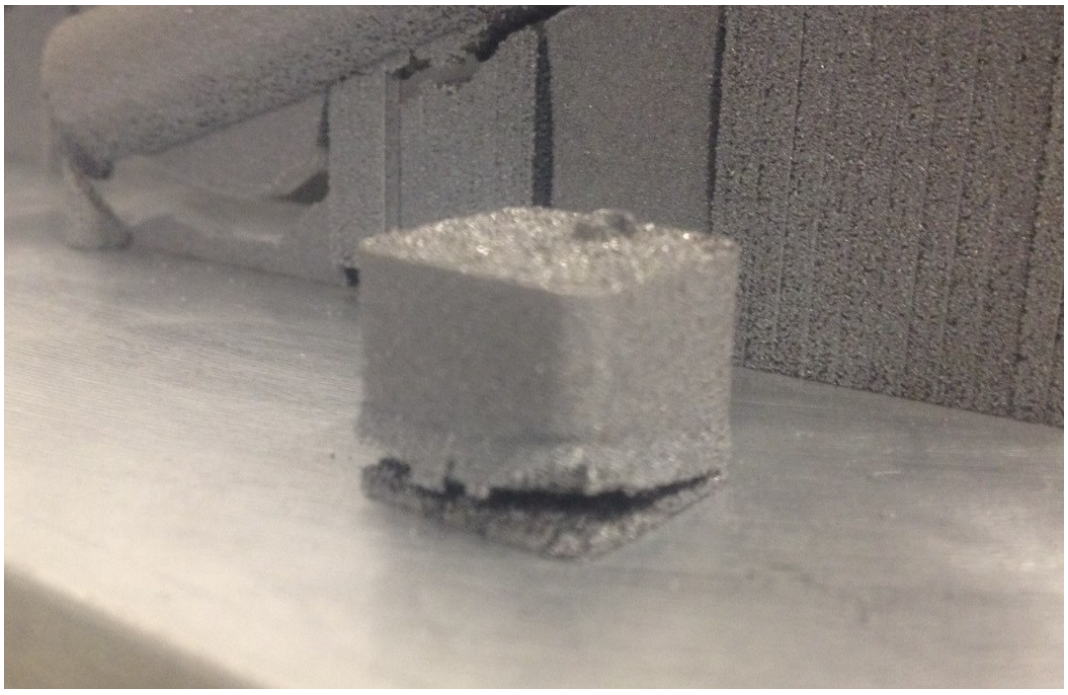

Figure 55. Deformed LPBF Al-Si-Ni sample and detachment of the supporting structures due to the residual stresses.

3.2 Al-Si-Ni-Cr-Fe

The experimental work presented and discussed in the following section was carried out at the Department of Material Science and Engineering of the Monash University (Melbourne, AU) as part of a scientific collaboration between Politecnico di Torino and Monash University along the period October 2017 – April 2018. The local laboratory facilities, materials, equipment and instrumentations were used and the work was supervised by Prof. Nick Birbilis.

3.2.1 LPBF system and materials

Within this work, a MLab Cusing commercial LPBF machine system (Concept Laser GmbH, Germany), whose main characteristics will be soon presented, was adopted.

For conducting the *in-situ* synthesis of Al-Si-Ni-Cr-Fe alloy, AlSi10Mg and nickel-base superalloy Hastelloy X (HX) alloy powders were used. The characteristic of each powder, including the chemical composition, the particles shape and morphology and the size distribution, will be also provided in the section below. The description of the equipment used for powder characterization is reported in Appendix A.1.1 Powder Characterization.

3.2.1.1 MLab Cusing machine system

The MLab Cusing R machine used for the Al-Si-Ni-Cr-Fe study was equipped with a Yb fiber laser with a nominal laser power of 100 W, continuous scanning speed up to 7000 mm s^{-1}, nominal laser spot size of 50 μm (-5, + 25 μm) and layer thickness ranging between 15 and 30 μm. The internal building chamber had a dimension of 90 mm × 90 mm × 80 mm. The machine was equipped with a handiling station for secure and safe handling of reactive materials (Figure 56).

The building platform is placed within the building chamber and it is mechanically fixed to the base plate. No heater system is available in this machine system so that the process occurs between 15 and 35 °C. The entire process takes place under flowing Ar inert atmosphere when the residual O_2 content within the process chamber is below 0.2 % (200 ppm of residual oxygen).

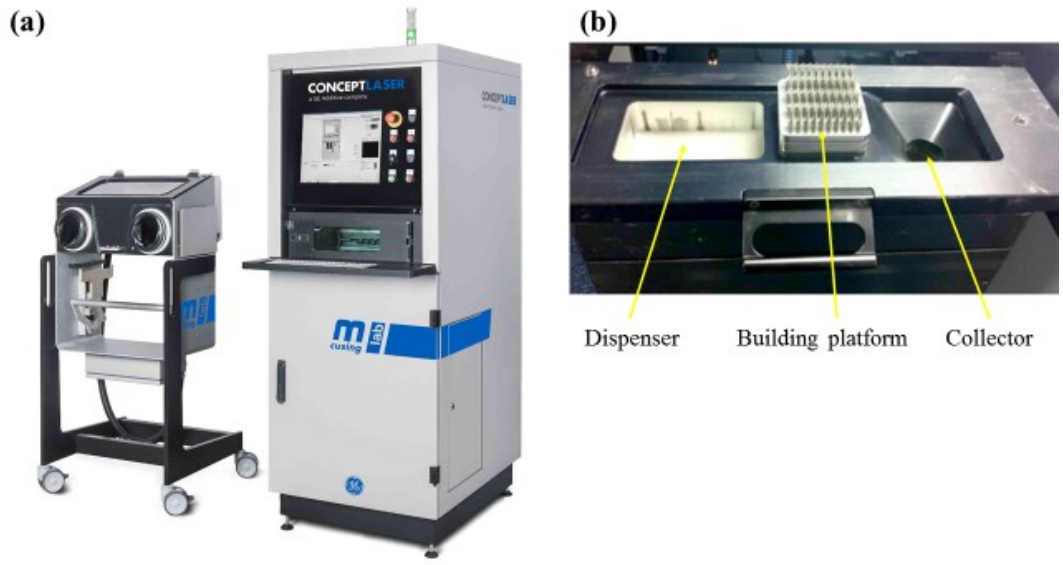

Figure 56. (a) MLab Cusing machine used for the Al-Si-Ni-Cr-Fe study and (b) a detail of the internal process chamber.

3.2.1.2 AlSi10Mg powders

The AlSi10Mg gas-atomized powders used for the synthesis of Al-Si-Ni-Cr-Fe alloy were provided by TLS Technik (Germany).

The chemical composition of the gas-atomized powder is reported in Table 12. FESEM investigation revealed that powder particles had mostly a spherical morphology but many satellites forming agglomerates were found (Figure 57).

Figure 58 illustrates the particle size distribution (volume and cumulative) obtained by laser diffraction (Appendix A.1.1.2 Laser granulometry). The particle size distribution was wide, slightly unsymmetrical and with a long tail shifted towards large diameters, probably due the presence of the above-mentioned agglomerates. The mean diameters corresponding to the 10% (d_{10},), 50% (d_{50}) and 90% (d_{90}) of the cumulative size distribution were measured at 14.1, 29.5 and 48.4 μm, respectively. These values are close – whilst slightly larger - to those calculated for the AlSi10Mg EOS GmbH powder used along the Al-Si-Ni study.

Table 12. Chemical composition of AlSi10Mg feedstock powder supplied by TLS assessed by Inductively Coupled Plasma Atomic Emission Spectroscopy (ICP-AES) analysis.

Elements	**Al**	**Si**	**Mg**	**Fe**	**Ti**	**Cu**	**Mn**
Wt.%	Bal.	10.7	0.48	0.19	0.01	<0.01	<0.01

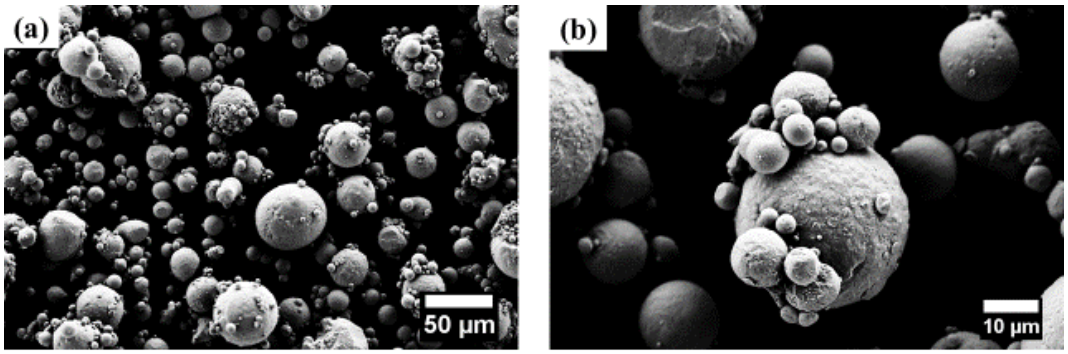

Figure 57. FESEM images of AlSi10Mg powders supplied by TLS for the Al-Si-Ni-Cr-Fe study taken at (a) 1.00 kX and (b) 4.00 kX showing an agglomerate.

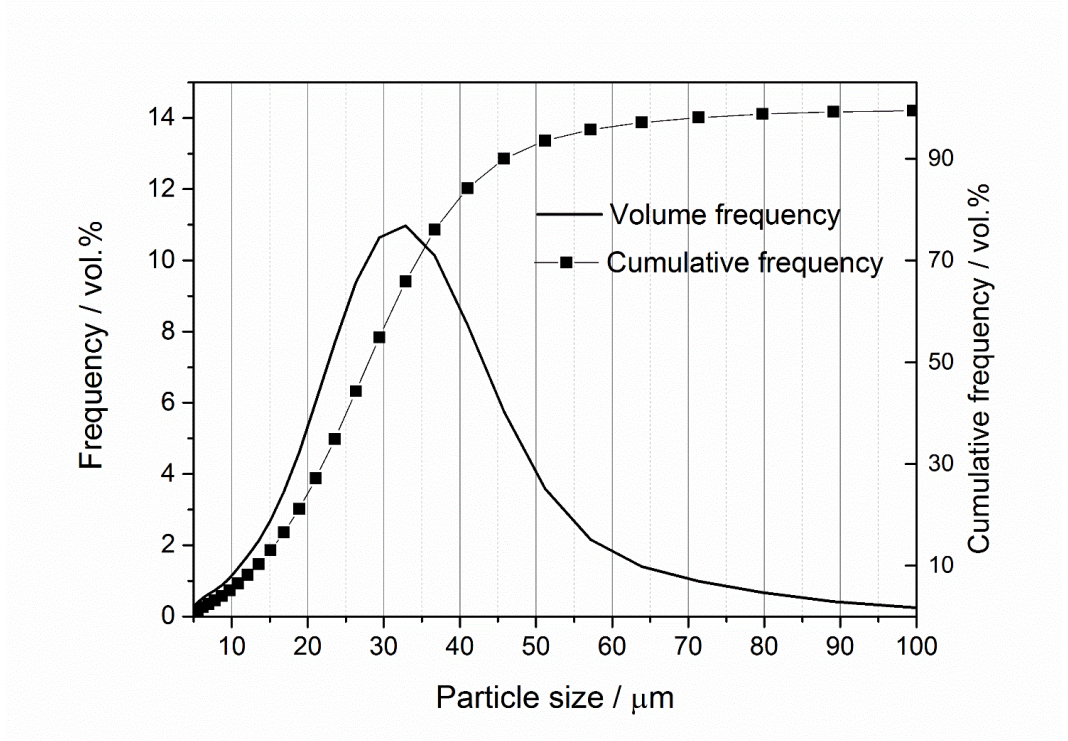

Figure 58. Frequency curves measured by laser diffraction under volumetric assumption showing the size distribution (volume and cumulative) of AlSi10Mg powders supplied by TLS. The d_{10}, d_{50} and d_{90} are 14.1, 29.5 and 48.4 µm, respectively

3.2.1.3 Hastelloy X (HX) powders

The gas-atomized HX powders used for the modification of AlSi10Mg were provided by H.C. Starck (Germany). The chemical composition of powders is reported in Table 13. Hastelloy X is a nickel-base superalloy, whose main constitutive elements are Ni, Cr and Fe, accounting for 92 at.% of the whole composition. Mo, W and Co are present as minor alloying elements. FESEM investigation revealed that particles were highly spherical, with a limited number of satellites and occasionally some irregularly shaped particles (Figure 59).

Figure 60 illustrates the particle size distribution (volume and cumulative) calculated by laser diffraction. The particle size distribution was narrow and almost centred along the mean d_{50} particle size. This is probably related to the low amount of agglomerates. The mean diameters corresponding to d_{10}, d_{50} and d_{90} were measured as 18.2, 28.9 and 42.9 μm, respectively. These values were similar to the values calculated for AlSi10Mg TLS powder.

It is worth to note that the mean diameter of Hastelloy X powder particles was significantly larger than that of pure Ni powder used in the Al-Si-Ni study, which would most probably affect the homogeneity of the powders mixture and of the alloy composition after LPBF.

Table 13. Chemical composition of Hastelloy X feedstock powder as assessed by Inductively Coupled Plasma Optical Emission Spectroscopy (ICP-OES) analysis.

Elements	**Ni**	**Cr**	**Fe**	**Mo**	**W**	**Co**	**Si**	**Ti**
Wt.%	47.6	21.8	18.2	8.9	1.9	1.35	0.15	0.1

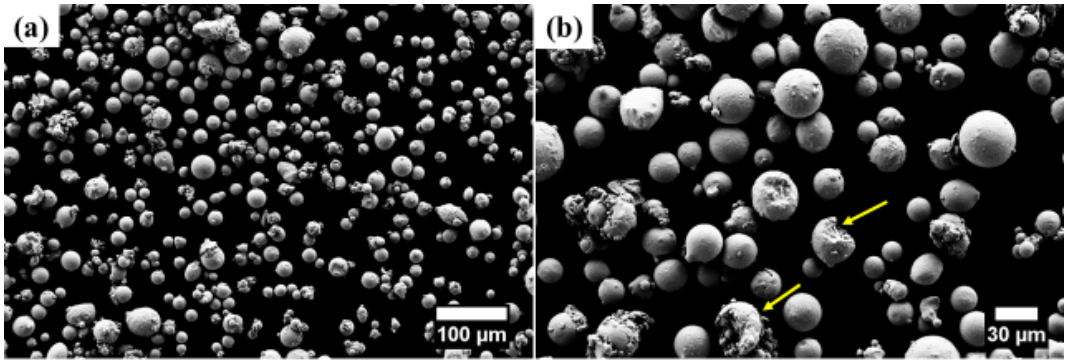

Figure 59. FESEM images of Hastelloy X powders (a) at 0.50 kX and (b) 1.00 kX magnifications. Yellow arrows point at spare irregular particles.

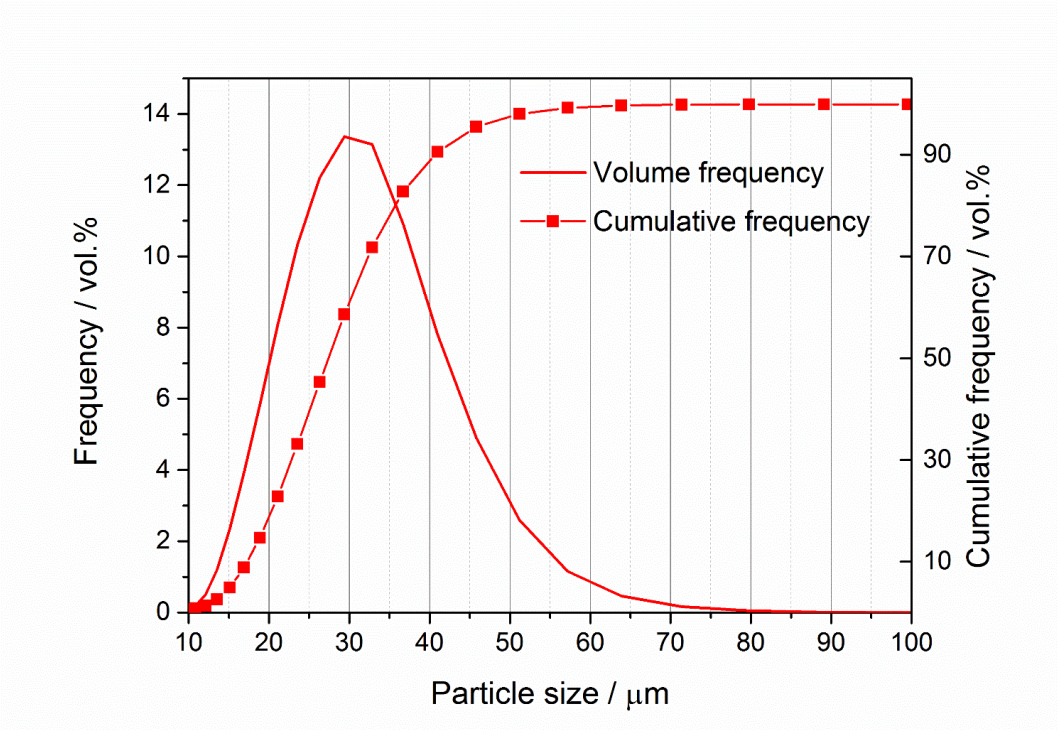

Figure 60. Frequency curves measured by laser diffraction under volumetric assumption showing the particle size distribution (volume and cumulative) of Hastelloy X powders. The d_{10}, d_{50} and d_{90} were measured as 18.2, 28.9 and 42.9 μm, respectively.

3.2.2 Design of the alloy composition

In order to avoid liquation cracking phenomena, which hinder the processability of many aluminium alloys by LPBF, the alloy composition should have a narrow solidification range. Moreover, if occurs, the segregation and/or precipitation of strengthening alloying elements and/or phases should preferably occur during the early stage of solidification, at low fraction of solid, when the associated thermal shrinkage of the material, which causes the opening of cracks, is low [88].

These prescriptions were easily applied for the Al-Si-Ni system of the previous study and the design of the Al-Si-Ni composition was quite straightforward. The mixing ratio between the AlSi10Mg and pure Ni powders, in fact, was chosen as to have a mean composition for the ternary Al-Si-Ni alloy close to that eutectic, whose value was easily found in the literature from previous experimental studies. Then, the mean composition of the powder mixture of the Al-Si-Ni alloy was easily achieved since based on the only addition of pure Ni to the base AlSi10Mg. The use of a pure elemental powder allows great flexibility in tailoring the final composition of the powder mixture.

On the contrary, for the Al-Si-Ni-Cr-Fe system, the design of the composition to be processed by LPBF represented itself an issue and it was not easy to solve. Firstly, because no experimental data were found for the eutectic reaction in the quinary Al-Si-Ni-Cr-Fe system. Secondly, because the quantity of Ni, Cr and Fe to

add to AlSi10Mg, and thus the final composition of Al-Si-Ni-Cr-Fe, were not individually tailorable. The weight proportions among the alloying elements, in fact, were fixed by the chemical composition of the starting Hastelloy X prealloyed powder. So, the *in-situ* alloying with a prealloyed powder poses additional challenges with respect to the alloying with a pure elemental powder still in the selection of a proper composition to process by LPBF and in its achievement and approximations and compromises need to be accepted.

A mixing ratio of 94:6 between AlSi10Mg and Hastelloy X was selected as first trial for the present study. The choice of an amount of 6 wt.% of Hastelloy X to add to AlSi10Mg was motivated by the starting assumption of contributing to the AlSi10Mg composition with an overall amount of main transition elements of HX (Ni, Cr and Fe) close to that in the Al-Si-Ni with 5 wt.% of only Ni. The mean composition of the resulting Al-Si-Ni-Cr-Fe alloy is reported in Table 14.

Table 14. Mean calculated chemical composition (wt.% and at.%) of the Al-Si-Ni-Cr-Fe alloy obtained by mixing AlSi10Mg + 6 wt.% HX powders.

Elements	**Al**	**Si**	**Ni**	**Cr**	**Fe**	**Mg**	**Mo**
Wt.%	Bal.	10.1	2.7	1.2	1.2	0.45	0.5
At.%	Bal.	10.1	1.3	0.7	0.6	0.5	0.2

Initially, Scheil calculations based on the selected composition of Al-Si-Ni-Cr-Fe were conducted using Pandat software package with thermodynamic data taken from the PanAl_2012 database [272]. The Scheil calculations were carried out in order to gain preliminary information on the phase constitution and solidification behaviour of the choosen composition as first trial and to see whetever the alloy was suitable for LPBF or not, i.e. by calculating its solidification range. Differently to the phase diagram calculation, which provides information on the phases that would form upon solidification at full equilibrium, the Scheil calculation gives information on the distribution of solutes upon slightly non-equilibrium solidification of the alloy, without considering the diffusion in the forming solid phase [273].

Figure 61 shows the mass fraction of phases formed upon solidification so as calculated by Pandat for AlSi10Mg and Al-Si-Ni-Cr-Fe. As expected, during the solidification of AlSi10Mg, α-Al grains crystallized as primary phase from the liquid, followed by the precipitation of Si. As the eutectic transformation proceeded, the liquid gradually concentrated of solutes until no liquid phase existed at approximately 550 °C (Figure 61a). According to the Pandat simulation, the addition of Ni, Cr and Fe solutes had the effect of inducing the precipitation of two high temperature phases prior the crystallization of α-Al phase (namely, $Al_{13}Cr_2$ and β-AlFeSi), of extending the main eutectic transformation down to 530°C and of inducing the precipitation of Al_3Ni phase during the final solidification stage (Figure 61b). As already discussed in 2.3.1.1 Microstructure and properties of Al-

Mg-Sc-Zr alloy (Scalmalloy®RP) and in 2.3.1.2 Al-20Si-5Fe-3Cu-1Mg paragraphs, the crystallization of high-temperature phases prior the formation of α-Al grains could be beneficial for refining the microstructure of LPBF aluminium alloys, as it occurs when alloying with Sc [243]. As reported by Spierings *et al.* [183,243], in fact, $Al_3(Sc_{1-x}:Zr_x)$ and AlMg-oxides particles precipitating prior α-Al phase acted as strong inoculants towards forming α-Al grains, promoted also by the low lattice mismatch between phases. A strong refinement of the eutectic phase was also reported when adding Fe, Mg and Cu to hypereutectic Al-Si alloys, which promoted the precipitation of primary intermetallics [246]. According to the calculated Scheil calculations, upon solidification of Al-Si-Ni-Fe-Cr, around 8 wt.% of both $Al_{13}Cr_2$ and β-AlFeSi intermetallics should form, together with α-Al, Si and 6 wt.% of Al_3Ni.

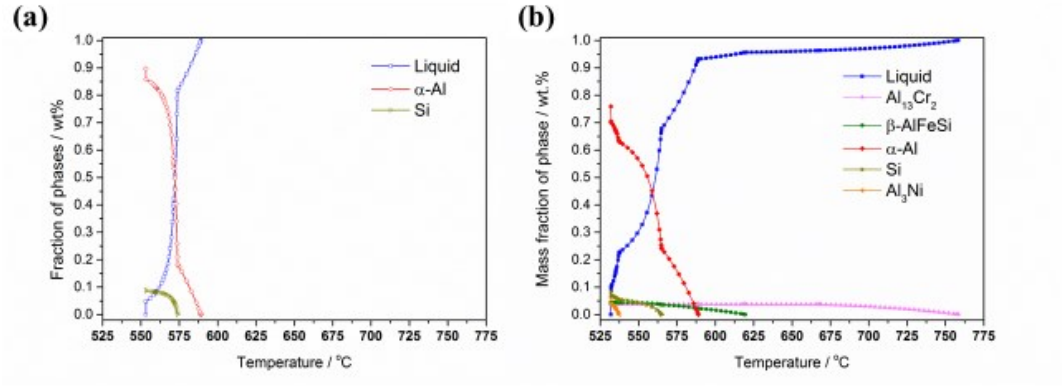

Figure 61. Mass fraction of phases with temperature during solidification of (a) AlSi10Mg and (b) Al-Si-Ni-Fe-Cr, calculated by Pandat based on Scheil Model.

The Scheil-solidification curves showing the fraction of solid formed upon solidification were reported in Figure 62 for AlSi10Mg and Al-Si-Ni-Fe-Cr and helped in better visualizing the different solidification behaviour between the alloys. The sharp turnover of the solidification path of Al-Si-Ni-Cr-Fe at low solid fraction visualizes the precipitation of the strengthening phases during the early stages of solidification. Alloying with Ni, Cr and Fe, then, had the major effect of broadening the solidification range for the main eutectic reaction with respect to the base AlSi10Mg. However, the extent of the reaction for Al-Si-Ni-Cr-Fe was still narrow and comparable to that of AlSi10Mg. For AlSi10Mg and Al-Si-Ni-Cr-Fe the predicted solidification ranges are, in fact, 36 °C and 56 °C, respectively, suggesting that the composition selected might have low susceptibility to liquation cracking [145]. The experimental DTA curve (Appendix A.1.5.1 DTA) reported in Figure 63 supported the output of the thermodynamic Pandat simulation, showing for the LPBF Al-Si-Ni-Cr-Fe alloy a solidification range slightly larger than that of AlSi10Mg.

Basing on the data gathered from Pandat simulation and the experimental DTA analysis, the Al-Si-Ni-Cr-Fe alloy composition obtained by adding 6 wt.% of Hastelloy X to AlSi10Mg seemed a promising composition to further investigate by LPBF.

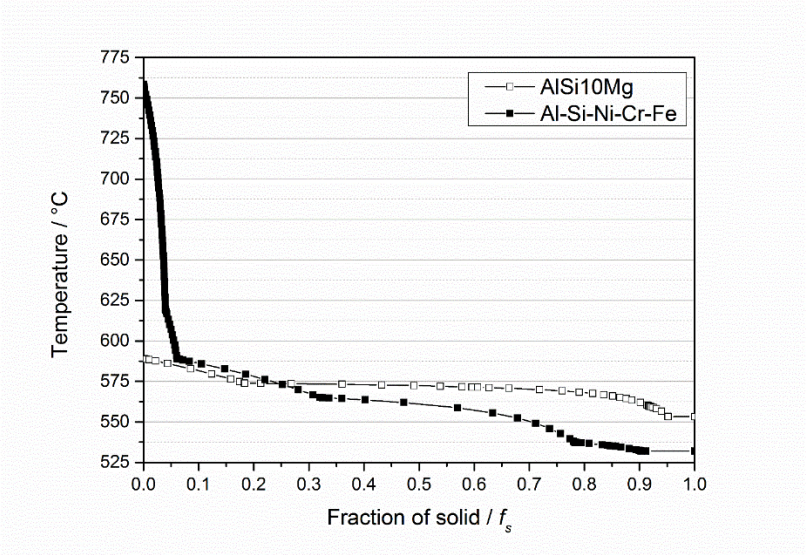

Figure 62. Fraction of solid phase with temperature during solidification of AlSi10Mg and Al-Si-Ni-Cr-Fe, showing the slightly different solidification ranges between alloys. Simulation was conducted using Pandat software based on Scheil Model.

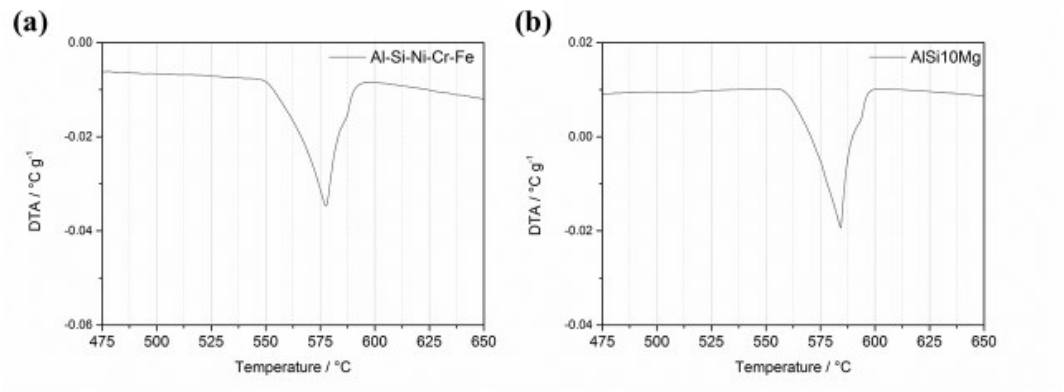

Figure 63. Differential Thermal Analysis (DTA) curves in the range 475-650 °C of (a) Al-Si-Ni-Cr-Fe and (b) AlSi10Mg manufactured by LPBF, showing the slightly larger solidification range of Al-Si-Ni-Cr-Fe.

The AlSi10Mg and the HX powders were mixed in the weight proportion AlSi10Mg:HX of 94:6 and homogenized within a jar placed upon two bars rotating at 70 rpm for 60 minutes. Figure 64 shows the BSE-SEM picture of the powder mixture. It goes without saying that HX particles were weakly distributed and that some HX particle have a dimension close to that of the largest AlSi10Mg particles. These features could affect the homogeneity of the alloy composition after LPBF.

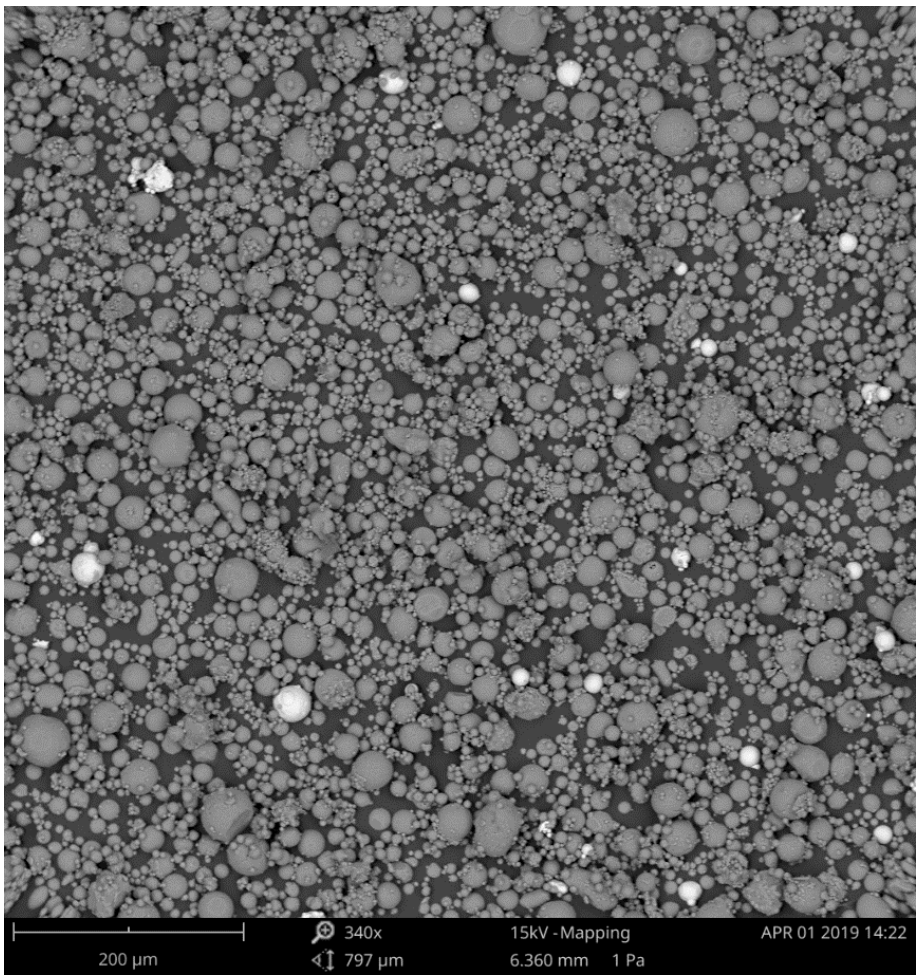

Figure 64. BSE-SEM image of the Al-Si-Ni-Cr-Fe powder mixture. Grey and white spheres represent AlSi10Mg and HX particles, respectively.

3.2.3 Design of the experiment (DoE)

As already said, the specimens were fabricated using the MLab Cusing machine. Cubic samples ($12 \times 12 \times 12$ mm^3) were built on an Aluminium platform adopting a constant layer thickness of 30 µm and the alternated X and Y scanning strategy (Figure 65). In X-Y alternating scanning strategy, each layer in scanned once and the scan direction is rotated by 90° between consecutive layers. The layer thickness of 30 µm was chosen in analogy with the previous Al-Si-Ni study. Only few studies, in fact, provided details on the layer thickness adopted for processing Aluminium alloys using LPBF systems with maximum laser power of 100 W [43,97].

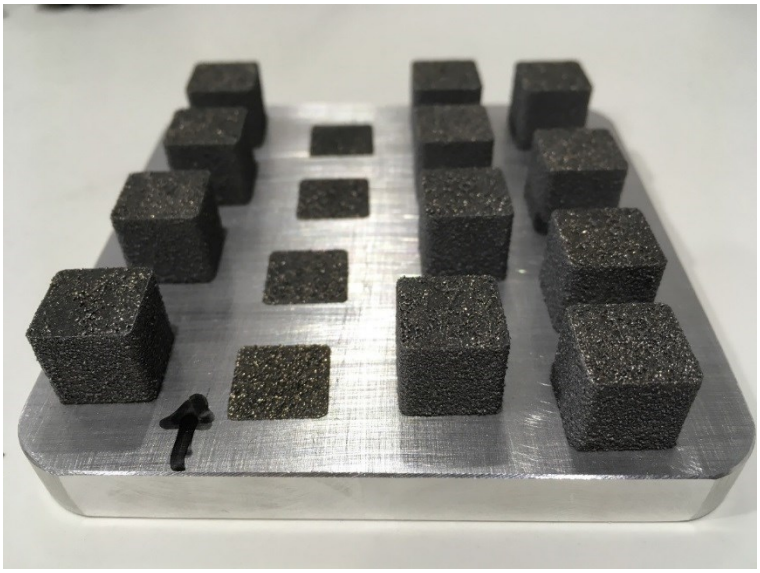

Figure 65. LPBF Al-Si-Ni-Cr-Fe cubic specimens built on Aluminium platform. The specimens did not show any evidences of external cracks, warping or delamination.

In order to assess the effect of process parameters on densification and alloying behaviour of the powder mixture, a full factorial design of experiments (DoE) made by 2 factors, scanning velocity (v) and hatching distance (h_d), with 4 levels each and with a total of 2^4 combinations, was used. Laser power was kept constant at the maximum value of 95 W. Aluminium alloys, indeed, reflect more than 90% of the incident radiation [43] and high energy for melting can be provided to the material by increasing the laser power [115]. Table 15 summarizes the factors and the levels used for the fabrication of Al-Si-Ni-Cr-Fe samples by LPBF.

Table 15. Factors and levels varied during the LPBF process for the fabrication of Al-Si-Ni-Cr-Fe samples.

Factors	Levels
Scanning speed, v [mm s^{-1}]	350 500 650 800
Hatching distance, h_d [mm]	0.05 0.07 0.09 0.11

3.2.4 Densification behaviour

Initially, LPBF Al-Si-Ni-Cr-Fe specimens were characterized for residual porosity in order to assess the influence of processing parameters on the densification behaviour. Table 16 summarizes the set of process parameters used for the fabrication of each sample, together with the resulting average percentage

of residual porosity calculated by image analysis of five different micrographs taken along the vertical cross sections (XZ) and the related standard deviation S. D. (Appendix A.1.2.2 Image analysis). Four samples processed at low hatching distance and scanning speed values (samples no. 1, 2, 3, and 5), whose resulting energy density value exceeded 100 J mm^{-3}, were not tested. During the processing of the first layers, indeed, these samples provided evidences of powder burning and their manufacturing was interrupted (as shown Figure 65) in order to avoid that the entire job could fail.

Under the experimental conditions adopted in the present study, the remaining Al-Si-Ni-Cr-Fe samples were highly porous. The percentage of residual porosity calculated along the vertical cross section ranged between 22.1 ± 2.9 % and 10.9 ± 2.4 %. Similar values were calculated along the horizontal cross section, whose residual porosity varied between 18.0 ± 3.0 % and 9.1 ± 3.1 %. The lowest percentage of porosity (10.9 ± 2.4 %) along the vertical cross section was assessed for sample no. 12, built at 95 W laser power, 650 mm/s scanning speed and 0.11 mm hatching distance.

Table 16. Experimental DoE, reporting the combination of process parameters, the resulting volumetric energy density, the porosity response and the resulting standard deviation (S.D.) as calculated along the vertical cross sections (XZ) of Al-Si-Ni-Cr-Fe samples produced by LPBF. S.D. refers to the measuring error of the same samples.

Sample no.	*v* [mm/s]	h_d [mm]	Power [W]	Energy density [J mm^{-3}]	Porosity XZ [%]	S.D.
1	350	0.05	95	181.0	-	-
2	350	0.07	95	129.3	-	-
3	350	0.09	95	100.5	-	-
4	350	0.11	95	82.3	16.6	3.3
5	500	0.05	95	126.3	-	-
6	500	0.07	95	90.5	15.4	2.0
7	500	0.09	95	70.4	11.6	1.3
8	500	0.11	95	57.6	12.8	1.4
9	650	0.05	95	97.4	20.1	3.1
10	650	0.07	95	69.6	18.8	2.9
11	650	0.09	95	54.1	16.0	2.5
12	**650**	**0.11**	**95**	**44.3**	**10.9**	**2.4**
13	800	0.05	95	79.2	22.1	2.9
14	800	0.07	95	56.5	13.0	1.4
15	800	0.09	95	44.0	14.8	0.4
16	800	0.11	95	36.0	11.9	0.9

Figure 66 reports the percentage of residual porosity of Al-Si-Ni-Cr-Fe samples as function of the hatching distance and scanning speed.

Whilst the DoE was not full (as anticipated, four samples were interrupted and not tested), Figure 66 clearly showed that the residual porosity of Al-Si-Ni-Cr-Fe was higher for specimens processed at lower hatching distance. The samples processed at hatching distance value as low as 50 µm, in fact, reported the highest values of residual porosity. Moreover, there was a different porosity response according to the scanning speed. The samples processed at scanning speed as high as 800 mm s^{-1} exhibited a sharp decrease of residual porosity when slightly increasing the hatching distance to 70 µm and then porosity slightly changed (orange curve in Figure 66). Differently, the specimens processed at 650 mm s^{-1} scanning speed gradually and continuously improved their densification behaviour at increasing hatching distance values (blue line in Figure 66). For the other scanning speed values, the investigated conditions are not adequate for processing the powder mixture.

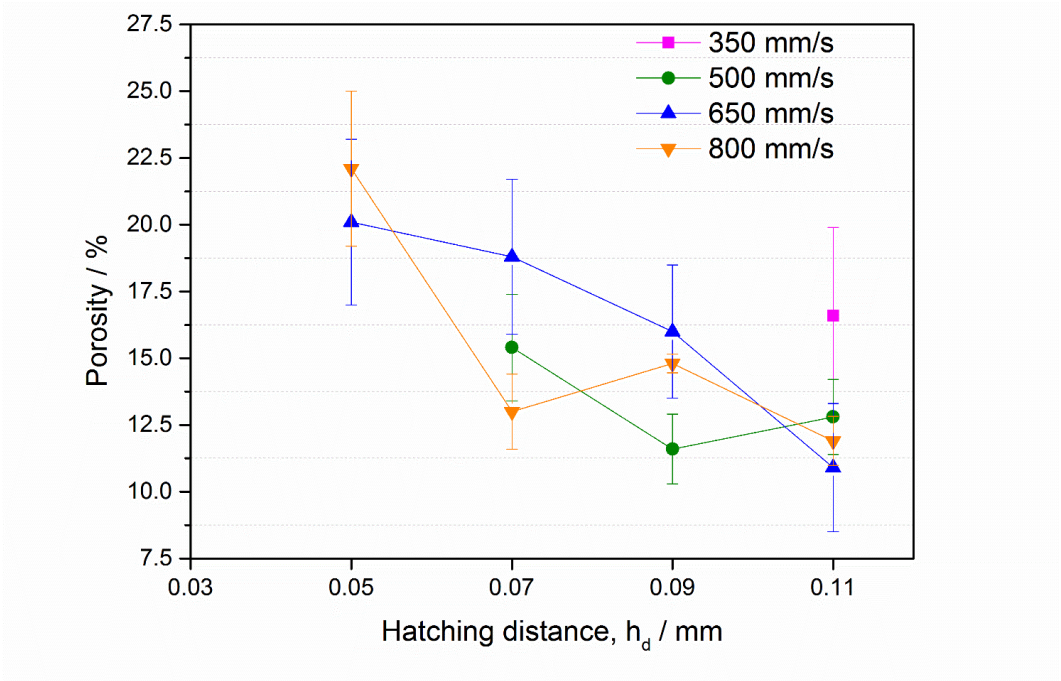

Figure 66. Influence of the hatching distance and scanning speed on the residual porosity calculated by image analysis along the vertical cross section of LPBFed Al-Si-Ni-Cr-Fe samples (P = 95 W).

However, the quantification of the residual porosity gives a partiall overview of the phenomena that occurred during laser scanning. Further information on the causes which led to the poor consolidation of Al-Si-Ni-Cr-Fe processed by LPBF were gained from the investigation of the sample cross sections through the optical microscope OM and hypotheses were drown.

Figure 67 illustrates that the vertical cross section of Al-Si-Ni-Cr-Fe samples fabricated with different process parameters and resulting energy input values (indicated in white boxes), not only gave different percentages of residual porosity

(reported in orange boxes) but also resulted in defects with different size, shape and distribution. For instance, for specimens fabricated at hatching distance as low as 50 µm, large and elongated defects dominated over small and randomly distributed defects, which on the contrary were preferably present in samples fabricated at hatching distance value of 110 µm. Same variation was assessed when increasing the scanning speed from 350 to 800 mm s^{-1}.

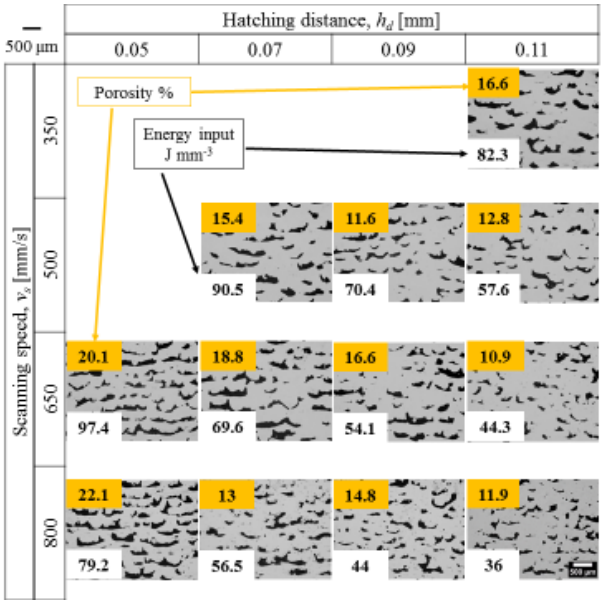

Figure 67. OM images of the polished vertical cross section of Al-Si-Ni-Cr-Fe samples manufactured under various hatching distance and scanning speed values. The orange boxes report the percentage of residual porosity (pooled st. dev. 2.2%) and the white boxes report the energy input for samples fabrication (volumetric energy density).

In order to rationalize the effect of the hatching distance and scanning speed on the type of defects formed, three Al-Si-Ni-Cr-Fe sample cross sections representative of three different process parameter combinations and consolidation behaviours were analysed into detail and Figure 68 illustrates their microstructure. To be more precise, Figure 68 compares two samples fabricated at different hatching distances and same scanning speed (Figure 68(a,b)) and two samples fabricated at different scanning speeds and same hatching distance (Figure 68 (b,c)).

The sample no. 13 fabricated at high scanning speed (800 mm s^{-1}) and hatching distance as low as 50 µm (Figure 68a) formed macroscopic pores horizontally aligned and the highest percentage of residual porosity equal to 22%. Voids had lengths up to several millimetres and they were periodically alternated to full dense regions spanning a width of several layers. The average vertical distance among voids was calculated as 200 ± 30 µm. Although the high energy input of sample fabrication (79.2 J mm^{-3}), insufficient remelting of the underlying layers seemed to occur. Thijs *et al.* [77] also reported the formation of similar horizontal voids periodically alternated to dense regions when processing Ti-6Al-4V at hatching distance as low as 50 µm and the authors ascribed their formation to some interaction between adjacent laser tracks. As reported by Louvis *et al.* [97], when increasing excessively the overlapping area between adjacent tracks the laser

mainly interacts with the previously consolidated material, which has higher reflectivity than the powders, resulting in lower energy input for melting and/or remelting of the previous layers. Moreover, due to the high thermal conductivity of Aluminium alloys, the melt could not have the time to properly wet the beneath material, causing the high density of binding faults and the balled and rough re-solidified tracks reported in Figure 68a. These phenomena might thus account for the high residual porosity and morphology of pores of samples no. 13 processed at very low hatching distance and high scanning speed.

On the contrary, Al-Si-Ni-Cr-Fe sample no. 16 (Figure 68b) processed at same scanning speed, higher hatching distance (110 μm) and thus lower energy input (36.0 J mm^{-3}) exhibited the typical lack of fusion defects [43]. The irregular, small and randomly distributed defects designated an unappropriated energy input, whilst overall the sample had lower residual porosity (11.9%) with respect to that fabricated with higher energy input (Figure 68a). In fact, no large horizontally aligned void was found, suggesting that the detrimental interactions between adjacent tracks did not occurred when increasing the hatching distance and the energy was transferred to the powder bed in a more effective way. Nevertheless, the rapid solidification of the molten material due to the high scanning speed of 800 mm s^{-1} caused high density of defects likely due to incomplete filling of the cavities [43,274].

In the end, for sample no. 4 (Figure 68c) processed at the same hatching distance (110 μm), lower scanning speed (350 mm s^{-1}) and thus higher energy input (82.3 J mm^{-3}) than those of sample no. 16 (Figure 68b), the density of the irregular and randomly distributed small lack of fusion defects decreased. This observation suggested that the energy input was sufficient to melt the material and the scanning speed low enough to produce smooth tracks and to let the melt to fill most of the small cavities. Nevertheless, the formation of few large defects, similar to those observed in sample no. 13 (Figure 68a), contributed in increasing the specimen porosity to 16.6%. At low scanning speed, the time of exposition of the material to the laser beam increases as well as the melt pool width and depth [64] so that, even at hatching distance as high as 110 μm, the laser might again interact with previously consolidated material locally decreasing the energy input for substrate remelting.

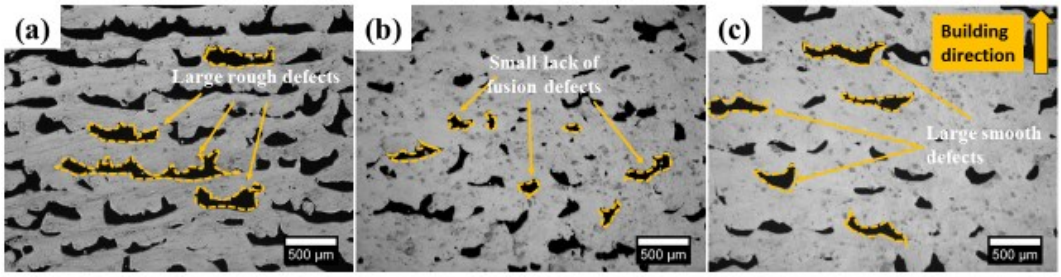

Figure 68. OM images of polished vertical cross sections of the LPBF-processed Al-Si-Ni-Cr-Fe samples showing the effect of the hatching distance and scanning speed on pores morphology and distribution. (a) Sample no. 13, v = 800 mm/s, h_d = 50 μm; (b) sample no. 16, v = 800 mm/s, h_d

= 110 μm and (c) Sample no. 4, v = 350 mm/s, h_d = 110 μm. The OM images were taken at 50x magnification.

All together, these observations demonstrated that energy density and the percentage of residual porosity alone do not give complete information on the densification behaviour of the material and that the interaction among the process parameters mostly matter. Under the experimental conditions adopted in the present study, energy input as high as 80 J mm^{-3} arising both from hatching distance as low as 50 μm and scanning speeds as low as 350 mm s^{-1} produced large defects and residual porosity higher than 16%. The formation of such defects could be ascribed to the excessively high track-to-track overlaps, which induced poor energy transferred to the material and poor substrate remelting and interlayer bonding. On the contrary, lower energy input resulting from hatching distance as high as 110 μm and scanning speed higher than 350 mm s^{-1} mainly produced lack of fusion defects randomly distributed along the samples cross section but lower overall residual porosity, probably due to a more effective energy transfer to the material (see Figure 67). Nevertheless, whilst the enhanced densification behaviour, samples were still porous. The residual defects observed at the hatching distance value of 110 μm should be then ascribed to the use of a powder layer thickness not appropriate to the process parameters window adopted [126]. At powder layer thickness of 30 μm, the energy input probably was not sufficient to provide an effective remelting of the material beneath. Moreover, the high thermal conductivity of Aluminium alloys rapidly dissipates the heat, solidifying the melt before wetting the substrate or filling the cavities. This mostly contributed in producing poorly-consolidated samples. Trials for improving samples density should be then addressed to the use of a lower layer thickness. Recently, Gharbi *et al.* [275] obtained high density samples of AA2024 processed with the same LPBF system by using a powder layer thickness of 25 μm and a slightly lower laser power (80 W).

Regardless the low samples density, which needs to be improved through a second DoE for porosity optimization, the OM images of the internal cross sections of Al-Si-Ni-Cr-Fe samples processed with different process parameters did not show any cracks. These observations further supported the results from the DTA curve of Al-Si-Ni-Cr-Fe reported in Figure 63 concerning the low cracking susceptibility of the selected composition.

3.2.5 Microstructure and compositional features

Figure 69(a,b) shows the experimental XRD patterns of the AlSi10Mg-HX powders mixture and of the Al-Si-Ni-Cr-Fe alloy fabricated by LPBF (Appendix A.1.3 X-ray diffraction analysis).

The XRD pattern of the powders mixture displayed the superimposition of the diffraction peaks of the constitutional powders phases, that is α-Al and Si as concerned AlSi10Mg powder and a single fcc phase as concerned HX powder (Figure 69a).

After LPBF, HX reacted and its peaks were no longer visible (Figure 69b). Overall speaking, the LPBF Al-Si-Ni-Cr-Fe alloy mainly consisted of α-Al and Si phases and an intermetallic phase, whose diffraction pattern did not match with any of the phases, namely $Al_{13}Cr_2$, β-AlFeSi and Al_3Ni, provided by Pandat Scheil calculation (Figure 61). Irrespective of the chemical composition and just in terms of crystallography the phase was indexed as the cubic $Al_{4.01}MnSi_{0.74}$ compound by more than eight observed reflections (PDF 01-087-0528). By comparing then the diffraction patter of the intermetallic found in the LPBF Al-Si-Ni-Fe-Cr with those found in Al-Si alloys of similar composition in the literature, the intermetallic phase was finally indexed as the thermally stable α-Al(Fe,Cr)Si phase, also referred as α-$Al_{15}(Fe, Cr)_3Si_2$ [222,276].

The experimental phase constitution went against that predicted by Pandat simulation for that concerning the intermetallic phases. This might be reasonable because at the high cooling rates during LPBF the formation of $Al_{13}Cr_2$, β-AlFeSi and Al_3Ni phases could be kinetically hindered. Escorial *et al.* [215] reported that under rapid solidification by melt spinning, the Al-3at.%Cr-1at.%Ni alloy formed a metastable supersatured solid solution of Cr, which produced stable $Al_{13}Cr_2$ phase only after heating at 420 °C. Cai *et al.* [224] found that, under rapid cooling, the addition of Cr to hypereutectic Al-25Si-5Fe-3Cu hindered the formation of β-AlFeSi in place of fine granular α-Al(Fe,Cr)Si intermetallics. The rapid solidification during LPBF, then, could be the reason why also Al_3Ni did not form. Lee *et al.* [226], in fact, reported that the gas-atomization of hypereutectic Al-Si alloy with the addition of 2 at.% of Ni produced a supersatured solid solution of Si and Ni, with no precipitation of Ni intermetallics.

The discrepancy between the Scheil calculation and the experimental phase constitution could be also associated to the complexity of the alloy system, based on a mixture of two different alloy powders and not on a homogenous melt composition, as that assumed for the Pandat calculation. In addition, it is worth to remember that care should be always taken when conducting thermodynamic simulations, especially when new compositions are investigated. The Pandat thermodynamic database used in the present study was optimized for conducting thermodynamic simulations on multi-component Aluminium alloys, whose compositional boundaries of major and minor alloying elements fell within the ranges of commercial casting and wrought alloys. The amounts of Ni, Cr and Fe transition metals in the nominal Al-Si-Ni-Cr-Fe composition here studied exceeded the suggested compositional ranges for these solutes, which correspond to wt.% 0 ~ 0.5 both for Ni and Cr and wt.% 0 ~ 1.0 for Fe [272]. Therefore, any simulation conducted beyond the compositional ranges of the database need to be properly evaluated.

As revealed by XRD patterns in Figure 69b, the reflections of α-Al(Fe,Cr)Si phase were broad, which implied the fine size of its crystallites. The same outcomes could be deducted for Si phase, whose diffraction peaks were broad. Moreover, the intensity of Si reflections was very low, indicating that most of the Si was trapped into supersatured solid solution within the α-Al phase. As reported in many studies

[161,235], indeed, the rapid cooling during LPBF caused the entrapment of excessive amount of Si in Al, leading to the formation of supersatured α-Al grains.

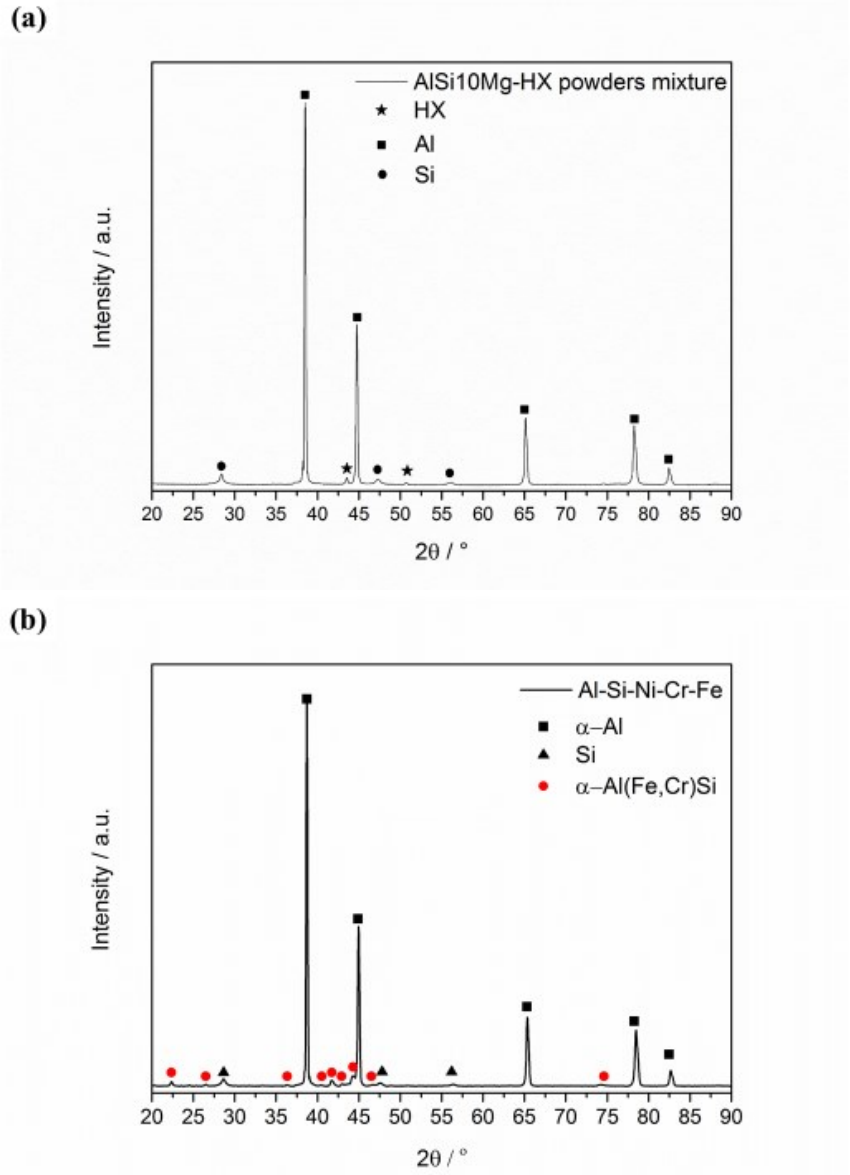

Figure 69. XRD patterns of (a) AlSi10Mg-HX powder mixture and (b) Al-Si-Ni-Cr-Fe after LPBF.

A detailed phase analysis was also conducted on Al-Si-Ni-Cr-Fe samples processed at different scanning speeds, since this parameter generally influences the cooling rate of the melt during LPBF [64] and thus likely it is able to affect the resulting phase constitution of the alloy.

Figure 70 shows the detailed XRD analyses in the range 25°-60° of Al-Si-Ni-Cr-Fe samples synthesized at 350, 500, 650 and 800 mm s^{-1}. In general, scanning speed revealed no evident effects on the phase constitution of *in-situ* synthesized Al-Si-Ni-Cr-Fe. Nevertheless, scanning speed affected the volume fraction of formed phases. The intensities of major reflections of cubic α-Al(Fe,Cr)Si and Si clearly increased when the laser beam velocity decreased from 800 mm s^{-1} to 350 mm s^{-1} (Figure 70). Kang *et al.* [277] reported that during LPBF of Al-Cu-Fe-Cr

alloy, the lower scanning speeds increased the amount of crystalline θ-Al_2Cu because the higher energy input decreased the melt cooling rate. Moreover, Li *et al.* [64] found that the cooling rate of the molten pool decreased from 6.2×10^6 to 1.2×10^6 °C s^{-1} when the scanning speed reduced from 400 mm s^{-1} to 100 mm s^{-1} during LPBF of AlSi10Mg. The scanning speed influences the time of exposition of the material to the laser beam and thus the energy input, the melt pool lifetime and the solidification rate of the molten material [278]. In the present study, when the laser scanning speed decreased, the AlSi10Mg and HX powders could be further mixed, the alloying process could be enhanced because of the higher energy input and and a higher volume fraction of α-Al(Fe,Cr)Si phase formed.

In addition, a higher fraction of Si could be rejected from the supersatured α-Al phase at scanning speed as low as 350 mm s^{-1}, due to the lower cooling rate of the melt (Figure 70).

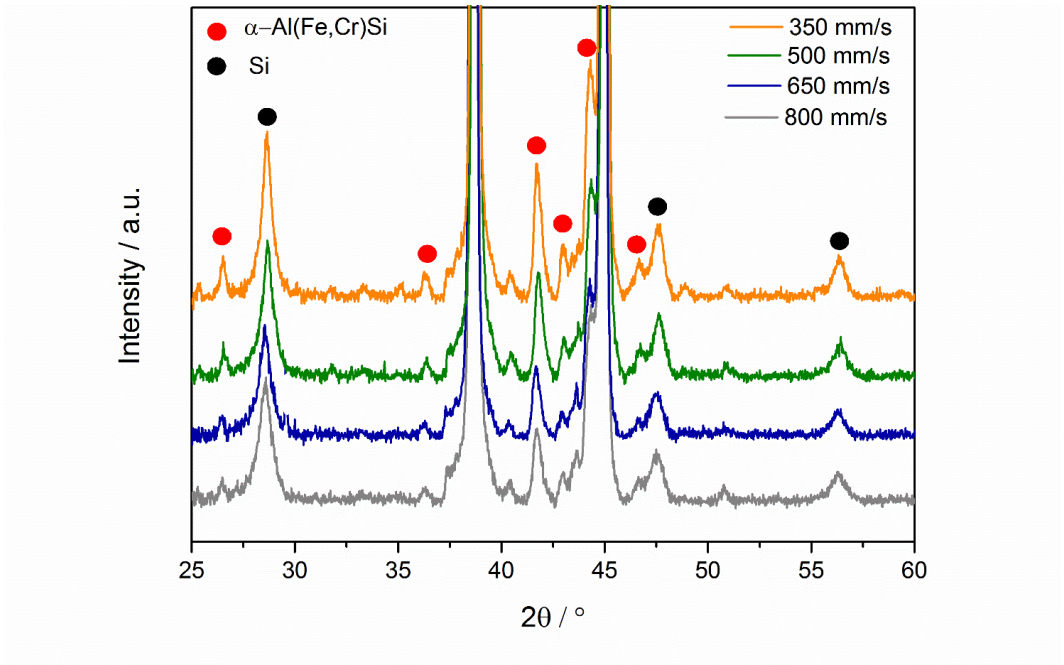

Figure 70. XRD patterns of Al-Si-Ni-Fe-Cr alloy synthesized at different scanning speeds, showing the major peaks intensities of α-Al(Fe,Cr)Si and Si phases varying with the scanning speed (P = 95 W and h_d = 0.11 mm).

The variation in the degree of supersaturation of the α-Al phase in Al-Si-Ni-Cr-Fe processed at different scanning speeds was supported by the calculation of the lattice parameters of α-Al phase (Appendix A.1.3 X-ray diffraction analysis) is highlighted in Figure 71. Considering that the solute Si induces a negative variation of the lattice parameter of the α-Al phase [279], the slight decrease of the lattice parameter at increasing scanning speeds could be right account of the higher fraction of Si into supersatured solid solution, as consequence of the higher cooling rate of the melt. Nevertheless, the decrease of the lattice parameter should to be related not only to Si but also to additional amount of Cr, Fe and/or Ni solutes, which induce a negative variation of the host α-Al lattice parameter [279].

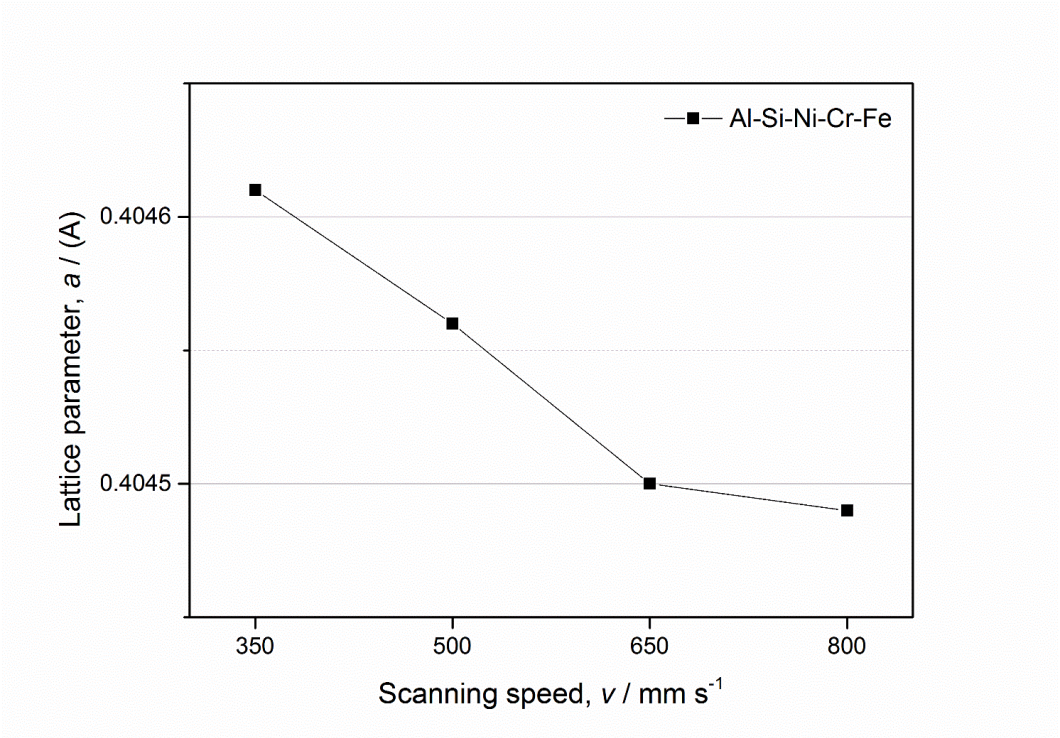

Figure 71. Lattice parameter of α-Al phase in Al-Si-Ni-Cr-Fe processed at different scanning speeds by LPBF (P = 95 W and h_d = 0.11 mm).

High-angle annular dark-field (HAADF)-TEM image and the corresponding EDX maps including the elemental distribution of Al, Si, Ni, Cr and Fe provided significant information on the solidification behaviour of LPBF Al-Si-Ni-Cr-Fe under rapid cooling and results are reported in Figure 72 (Appendix A.1.4.3 Transmission electronic microscopy).

Firstly, TEM-HAADF image confirmed that as consequence of the rapid cooling a very fine microstructure formed, with elongated α-Al cells several micrometres in length and less than 500 nm in width. As reported by Wu *et al.* [234], upon solidification the cellular dendritic α-Al cells formed because of the high temperature gradients during LPBF. Subsequently, the α-Al cells rejected the eutectic liquid along cell boundaries. According to Prashanth *et al.* [161], in fact, the rapid solidification of primary α-Al grains in hypoeutectic Al-Si alloys caused firstly the entrapment of excessive amount of Si in α-Al, which then partially drove out during the late stages of solidification, accumulating along the α-Al cells. The TEM-EDX maps in Figure 72 including the elemental distribution of Si clearly showed the eutectic network segregated along the α-Al cells boundaries. The segregated eutectic network along the α-Al cells, together with the significant amount of Si and Mg – as already reported by Maeshima *et al.* [280] in as-built LPBF AlSi10Mg – contained also Ni, Fe and Cr, as confirmed the EDX point analysis of region 1 in Figure 72 detailed in Table 17. During solidification, the liquid phase gradually concentrated of solutes (Si, Mg, Ni, Cr, Fe), which were then partially rejected during the late stage of solidification along the cell boundaries.

Considerable amounts of Si existed also into supersatured solid solution within α-Al cells, as confirmed the EDX point analysis of region 2 in Figure 72 reported in Table 17. The retained amount of Si within α-Al cells was as high as 2.6 at.%, which was considerably higher than the maximum equilibrium solubility of Si in Al, corresponding to 1.59 at.%. For LPBF AlSi10Mg, a slightly lower value ranging between 2.0 and 2.2 at.% was reported in literature [234,280]. These differences could be reasonably ascribed to the different chemical composition and/or LPBF machine system adopted. In addition, as consequence of the *in-situ* alloying with different solutes and under the rapid solidification during LPBF, easily exceeding 10^6 °C s^{-1} [64], α-Al cells of Al-Si-Ni-Cr-Fe were found the be supersatured not only with Si but also with Fe and contained Cr and Mg into solid solution (region 2 in Table 17). The amount of Mg into solid solution within α-Al cells was 0.5 at.%, higher than that reported by Maeshima *et al.* [280] for LPBF AlSi10Mg, corresponding to 0.1 at.%. This variation could be ascribed to slightly differences into the chemical composition among the starting AlSi10Mg powders. More importantly and unexpectedly, no fraction of Ni solute was found within the α-Al cells. Even though Ni had a very low equilibrium solubility into Al (0.023 at.%), in fact, rapid solidification processing was reported to easily extend to 1.2-7.7 at.% the solid solubility of Ni in Al [18]. On the contrary, in LPBF Al-Si-Ni-Cr-Fe, the TEM-EDX maps revealed that most of Ni was preferably segregated along the α-Al cell boundaries (point 3 in Figure 72), often together with a considerable amount of Mg and minor quantities of Fe and Cr. The lack of Ni into supersatured solid solution within α-Al cells rich in Si, Fe and Cr could be a consequence of the repeated heating and cooling during LPBF. The intrinsic thermal effect resulting from the processing of adjacent tracks and subsequent layers, in fact, probably enhanced the diffusion of Ni solute, its rejection from the α-Al phase and accumulation along the cell boundaries. At 425 °C, the diffusion coefficient D_0 of Ni, Fe and Cr in Al had a magnitude of approximately 10^{-15}, 10^{-18} and 10^{-21} m^2 s^{-1}, respectively [18], which might account for the higher mobility of Ni atoms with respect to Fe and Cr, which on the other hand remained into solid solution within α-Al. The thermal effect could also explain the segregation of Mg together with Ni along the cell boundaries (see point 3 in Figure 72), since the diffusion coefficient D_0 of Mg in Al is as low as 10^{-14} m^2 s^{-1} at 425 °C.

What is evident from the TEM-EDX investigation is that the *in-situ* alloying with HX under the high cooling rate of LPBF was effective in producing α-Al cells of Al-Si-Ni-Cr-Fe supersatured with Si and Fe and with considerable amounts of Cr and Mg into solid solution. In addition, the repeated heating and cooling during processing probably promoted the segregation of major amounts of Ni along α-Al cells boundaries. In the end, fine globules (red arrows in Figure 72) containing a major amount of Cr and Fe and a minor content of Ni were also observed, which most probably represented nanometric α-Al(Fe,Cr)Si intermetallics.

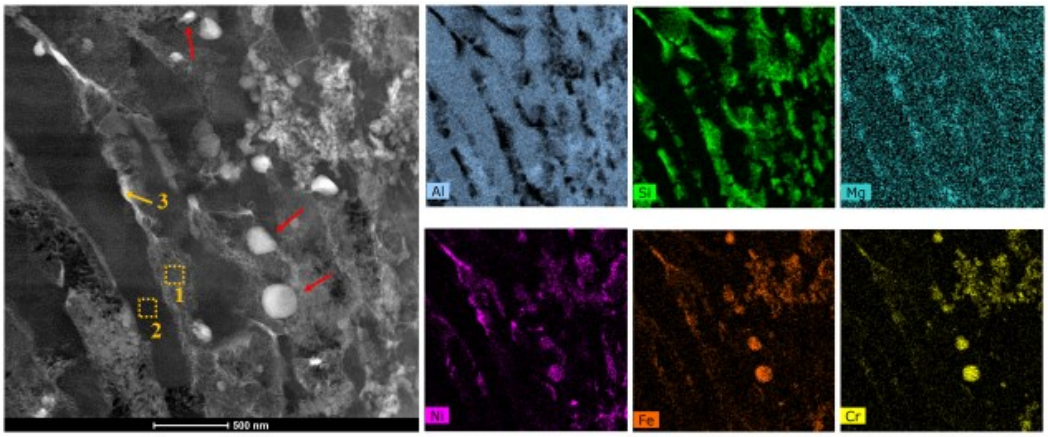

Figure 72. HAADF-TEM image and energy-dispersive X-ray spectroscopy (EDX) of the vertical cross section of LPBF Al-Si-Ni-Cr-Fe including the elemental distribution of Al, Si, Mg, Ni, Fe and Cr. Numbers in HAADF-TEM image indicate sites of point EDS analyses whose values are reported in the table below. Region 1 and region 2 refers to the eutectic network and α-Al grains, respectively and point 3 referes to a Ni-Mg-Si rich phase segregated along the cells. Red arrows point at globules intermetallics rich in Cr, Fe and Ni, probably representing nanometric α-Al(Fe,Cr)Si. P = 95 W, v = 350 mm s^{-1} and h_d = 0.11 mm.

Table 17. Chemical composition (at %) given by TEM + EDS point analyses of LPBF Al-Si-Ni-Cr-Fe. First row represents the nominal chemical composition of Al-Si-Ni-Cr-Fe and the second one represents the maximum equilibrium solid solubility of Si, Ni, Cr and Fe in pure Al [18].

	Element (at.%)						
	Al	**Si**	**Mg**	**Ni**	**Cr**	**Fe**	**Mo**
Al-Si-Ni-Cr-Fe	86.7	10.1	0.52	1.3	0.65	0.6	0.15
Max. solubility in Al	-	1.59	-	0.023	0.44	0.025	-
Region 1 (eutectic)	49.7	46.5	2.1	0.5	0.4	0.8	-
Region 2 (α-Al cell)	96.7	**2.6**	0.5	-	0.1	**0.1**	-
Point 3	77.8	**9.3**	**4.7**	**4.7**	1.2	2.1	0.2

Figure 73 shows the effect of HX addition on the microstructure of Al-Si-Ni-Cr-Fe, as observed through the OM at high magnification, before and after electrochemical etching (Appendix A.1.4.1 Optical microscopy).

The typical non-homogenous LPBF microstructure was found [70,232]. During the LPBF process, the consolidation of the powder bed proceeded track after track

and layer after layer, generating a microstructure consisting of an array of semielliptical melt pools separated by melt pool borders. The orientation of melt pools was not uniform throughout the cross section because of the X-Y 90° rotated scanning strategy. The regions in which the material underwent remelting constituted the melt pool borders, easily visible after the electrochemical etching and traced by the blue dotted lines in Figure 73. In addition, the microstructure of Al-Si-Ni-Cr-Fe alloy showed the presence of small defects, mainly residual pores (red arrows in Figure 73) and of large agglomerates (yellow arrows) irregularly shaped, distributed along the cross section with no apparent pattern.

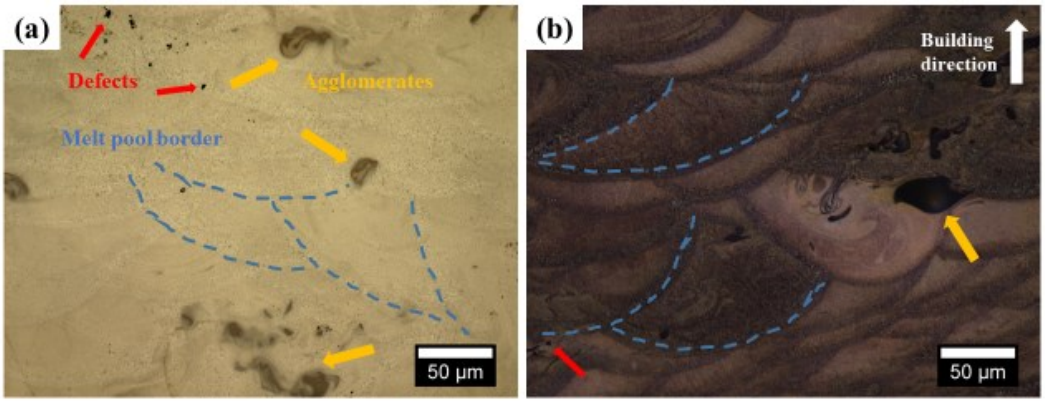

Figure 73. OM images of the vertical cross section of LPBF Al-Si-Ni-Cr-Fe (a) before and (b) after electrochemical etching. Blue dotted lines trace melt pool borders, red arrows point at small consolidation defects and yellow arrows point at large agglomerates. The OM images were taken at 500x magnification.

BSE-SEM image of Figure 74 helped in gaining information on the agglomerates above observed together with the visualization of the distribution of the solutes in Al-Si-Ni-Cr-Fe as results of the *in-situ* alloying with HX powder.

The compositional contrast given by the higher atomic number of Ni, Cr and Fe transition metals (TMs) with respect to that of Al revealed that the agglomerates represented local enrichment of TMs, probably due to large HX particles not fully melted. The HX powders used for this study, in fact, had a mean particle size as high as 30 µm. Whilst the diffraction peaks of HX were no longer visible after LPBF (as assessed through the XRD analysis reported in Figure 69), sharp compositional differences still existed in the microstructure of Al-Si-Ni-Cr-Fe. The reason for this behaviour should be ascribed to the different physical properties between the starting powders, such as melting temperature, thermal conductivity etc. but also to the ultra-high solidification rate during LPBF, which caused incomplete diffusion of the solutes especially around large HX particles.

In addition, Figure 74 shows blurred light-grey bands tracking the diffusion paths of TMs in the melt. The local variations in the contrast of the bands indicated solute-rich and solute-poor regions. Occasionally, the light-grey bands followed the convective patterns occurring within the melt, which were generated by the severe temperature gradients [26]. Nevertheless, the blurred bands did not always trace the semielliptical shape of the melt pool. This is a consequence of the scanning strategy

during LPBF and of the continuous overlapping between adjacent tracks and subsequent layers, which exposed the already consolidated materials to multiple irradiation and to remelting.

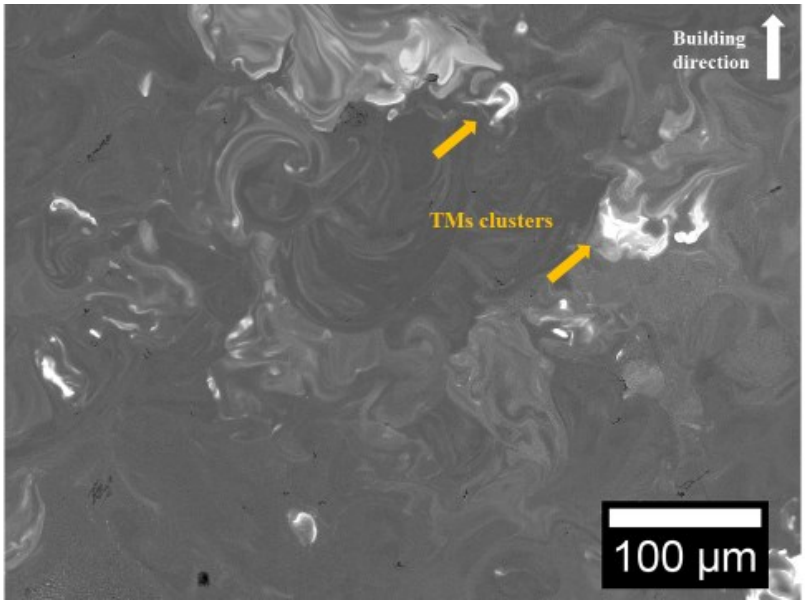

Figure 74. BSE-SEM micrograph of vertical cross section of LPBF Al-Si-Ni-Cr-Fe showing compositional differences. Yellow arrows point at agglomerates rich in TMs. The SEM image was taken at 230x magnification.

Figure 75 shows the BSE-SEM micrographs and EDS maps of LPBF Al-Si-Ni-Cr-Fe and it is clearly visible that the blurred bands tracked the distribution of Ni, Cr and Fe solutes of the starting HX powder. Even at high magnifications, the microstructure was inhomogeneous, consisting of Al-rich regions belonging to the starting AlSi10Mg powder alternated to Ni-, Cr- and Fe-rich bands, whose constitutive elements belonged to the HX powder. The existence of these bands with such elemental distribution further confirmed that the solidification within the melt pool occurred so fast that neither when the HX particles had been fully melted, the distribution within the melt pool could be truly homogenous. The elemental constitution of the blurred bands tracked that of the starting HX powder, showing that the *in-situ* alloying with an alloy multicomponent powder further complicated the homogenization of the composition with respect to the addition of a pure elemental powder. The slightly more homogenous elemental distribution of Fe with respect to those of Ni and Cr in Figure 75 could be reasonably ascribed to the fact that starting AlSi10Mg powder contained itself a low quantity of Fe (see the chemical composition in Table 12).

During LPBF, the melting of the powders occurs in a time of the magnitude of few µs [30] and the melt cools down so rapidly that the melt pool lifetime can be as low as 3 ms [31,281]. These solidification conditions can be even more severe when processing Aluminium alloys, due to the high thermal conductivity and rapid extraction of the heat from the previously consolidated material. During LPBF, thus, not only the cooling but also the melting occurs rapidly. Under these conditions, solutes belonging to HX could not have the time to diffuse at the liquid

state and to homogenise the composition within the melt pool, despite the scanning strategy, rationalizing in this way the formation of the blurred solutes bands.

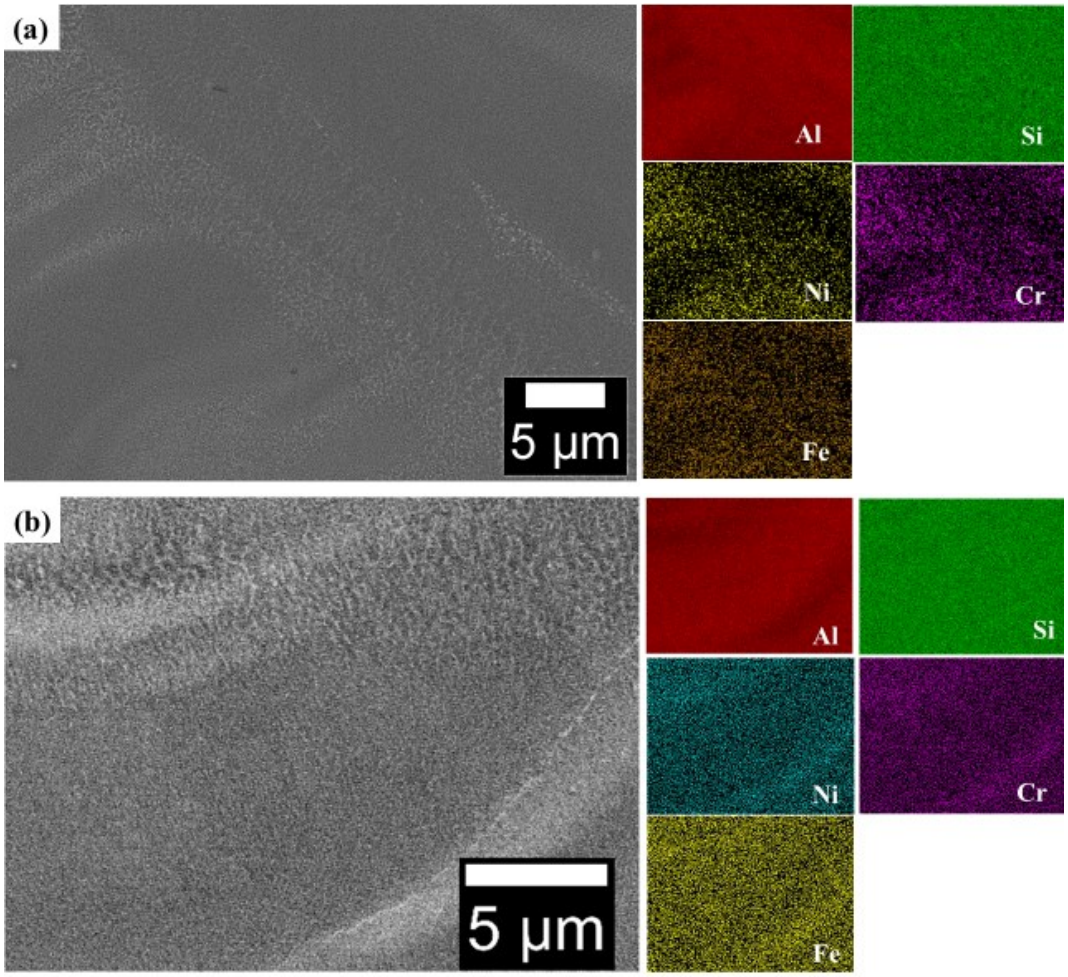

Figure 75. (a, b) BSE-SEM micrographs and EDS maps including elemental distribution of Al, Si, Ni, Cr and Fe of the vertical cross section of LPBF Al-Si-Ni-Cr-Fe alloy.

3.2.6 Nanoindentation

The nanoindentation map (Appendix A.1.7 Nano-hardness evaluation) of the vertical cross section of LPBF Al-Si-Ni-Cr-Fe and the corresponding BSE-SEM image with the indentation grid reported in Figure 76(a,b) suggested that locally the mechanical behaviour of the Al-Si-Ni-Cr-Fe was strongly influenced by the incomplete diffusion of solutes and existence of the blurred solutes bands.

The existence of solute-rich and solute-poor regions due to the rapid solidification of the melt, in fact, arose in fairly non-homogenous distribution of the nanohardness values. The regions where the concentration of solutes was high, corresponding to the brightest regions in the BSE-SEM image in Figure 76b, had a local value of hardness as high as 4.2 GPa (red-violet bands in the nanoindentation map). Whereas, the Al-rich areas, corresponding to the dark-grey regions in the BSE-SEM image, had local values of hardness ranging between 2.1 and 2.4 GPa (green-yellow bands in the nanoindentation map).

Overall, alloying with HX resulted in a significant improvement of the mechanical properties with respect to both AlSi10Mg and previously investigated Al-Si-Ni alloy. The nanohardness of the Al-Si-Ni-Cr-Fe alloy, in fact, was around 2.75 ± 0.5 GPa, considerably higher than that of AlSi10Mg (2.0 ± 0.15 GPa) and of Al-Si-Ni (2.2 ± 0.35 GPa) [263]. In the case of LPBF AlSi10Mg, the high nanohardness in the as-built state was reported to be mainly related to the small size of the α-Al cells while for Al-Si-Ni the additional strength was mostly due to the precipitation of submicrometric Al_3Ni [263]. It was shown here that *in-situ* synthesized Al-Si-Ni-Cr-Fe the solute-rich bands forming because of the rapid solidification of the melt contributed in increasing the nanohardness of the material. The local increase in the hardness of the solute-rich area can be reasonably ascribed to solid solution effect of different solutes. The TEM-EDX analysis previously presented (Figure 72), in fact, had provided evidences that due to the high cooling rate during LPBF of Al-Si-Ni-Cr-Fe the α-Al cells contained not only Si into solid solution but also considerable amounts of Fe, Cr, Mg and it cannot be excluded also the local presence of Ni. The presence of solutes into solid solution, due to the high cooling rate during LPBF of Al-Si-Ni-Cr-Fe, causes the deformation of the host lattice because of the atomic misfits between the species, which are effective in impeding the progress of the dislocations, thereby increasing locally the hardness of the material [198].

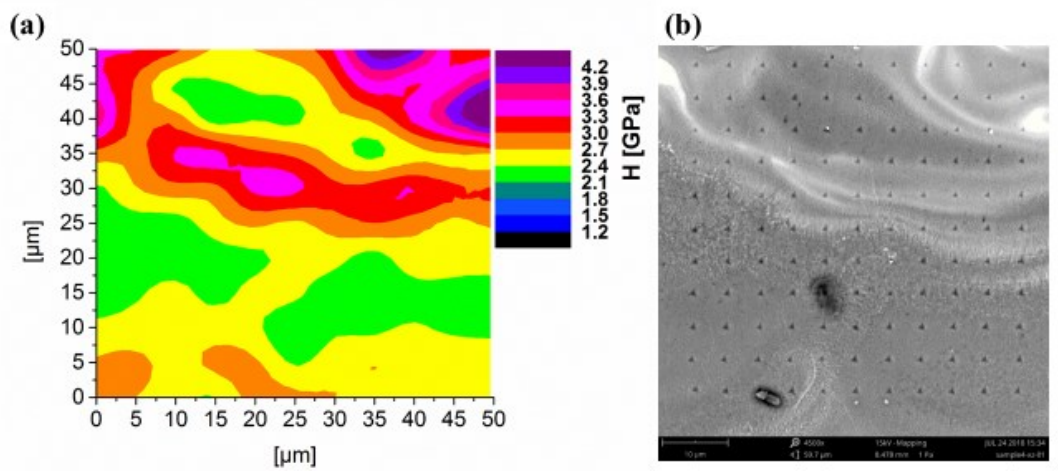

Figure 76. (a) Nanohardness coloured map and (b) BSE-SEM micrograph showing the corresponding nanoindentation grid of the vertical cross section of LPBF Al-Si-Ni-Cr-Fe (P = 95W, v = 350 mm s^{-1}, h_d = 0.11 mm). The nanohardness coloured map is a continuum representation in which a colour is attributed to each indentation value according to the hardness scale reported to the right of the figure.

3.2.7 Conclusion

The present study investigated the *in-situ* synthesis by LPBF of a novel Al-Si-Ni-Cr-Fe alloy by LPBF from a mixture of AlSi10Mg and Hastelloy X powders. The consolidation behaviour and the resulting microstructure and mechanical properties were investigated.

As consequence of the highly localized energy input during LPBF process, the HX powders react and the as-built Al-Si-Ni-Cr-Fe samples mainly consist of α-Al, Si and α-Al(Fe,Cr)Si intermetallic phases.

The scanning speed was found to influence the extent of the reaction between the starting powders. As the laser scanning speed decreases, the energy input increases and the cooling rate decreases, so that the AlSi10Mg and HX powders could be further mixed and a higher fraction of α-Al(Fe,Cr)Si intermetallics formed.

The typical heterogeneous laser track microstructure was found in LPBF Al-Si-Ni-Cr-Fe. TEM-EDX analysis confirmed that a very fine microstructure formed due the rapid cooling during LPBF, with elongated α-Al cells surrounded by the Al-Si eutectic containing minor amount of the other solutes. The α-Al cells were supersatured with Si and Fe and contained also Cr and Mg into solid solution. Ni was preferably segregated along the cells boundaries, probably because of the thermal effect during LPBF.

The microstructural investigation showed that large solute-rich clusters – probably representative of partially-molten HX particles - were randomly distributed over the sample microstructure while solutes-rich bands tracking the diffusion paths of solutes formed due to the rapid melting and solidification of the melt pool. These features characterized a non-homogenous microstructure and suggested that challenges exist in the *in-situ* homogenization of the composition from a mixture of different alloy powders.

Nevertheless, the LPBF Al-Si-Ni-Cr-Fe samples manufactured are crack-free thanks to the selection of a chemical composition with a narrow solidification range and do not exhibit evidences of warping and/or delamination. More importantly, the introduction of Ni, Cr and Fe generated up to 50% enhancement of the microhardness with respect to AlSi10Mg, as shows in Figure 77, which could be reasonably ascribed to the solid solution as well as to the Orowan strengthening effects of solutes and intermetallics, respectively. The increase of the hardness at low scanning speed can be right account of the higher fraction of α-Al(Cr,Fe)Si intermetallics. The pooled standard deviation as high as 12 HV, then, accounts of the many heterogeneities found in the microstructure, such as solute-rich and solute-poor bands with different hardness response but if it is consider the high residual porosity of Al-Si-Ni-Cr-Fe samples, the hardness results are interesting and suggest that the composition could be promising for further development by LPBF.

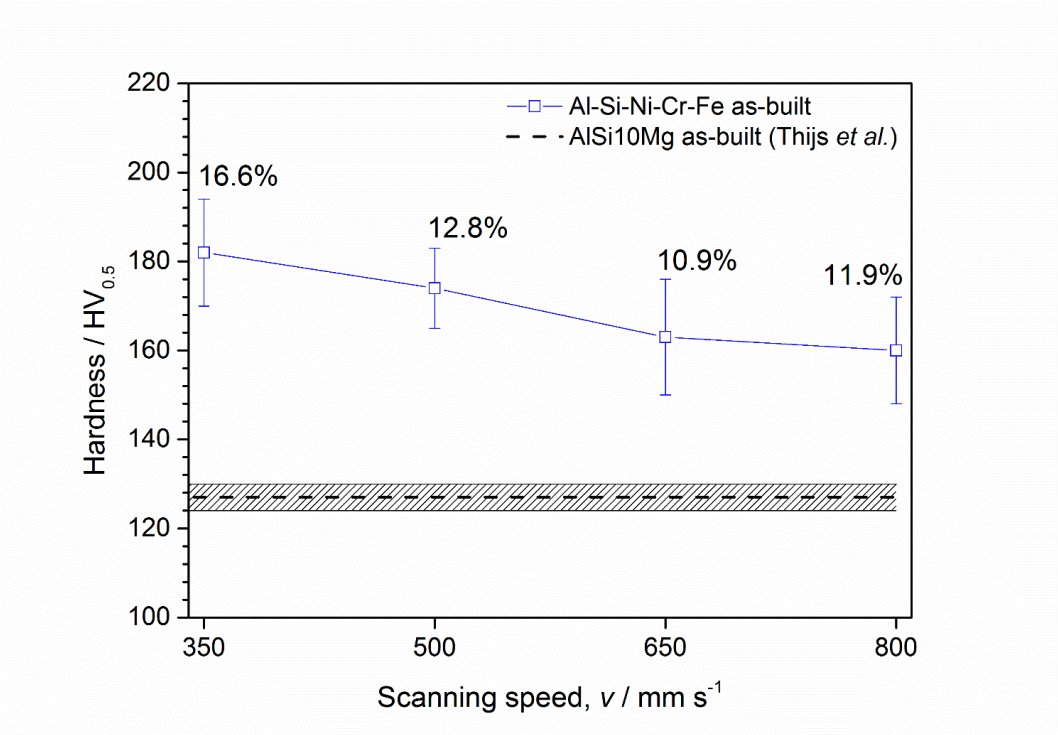

Figure 77. Vickers microhardness and percentage of residual porosity of LPBF Al-Si-Ni-Cr-Fe samples processed at different scanning speeds (P = 95 W h_d = 0.11 mm). Microhardness of AlSi10Mg was added as reference [60]. The pooled standard deviation for Al-Si-Ni-Cr-Fe is 12 HV.

Chapter 4

Second section: Literature review on High Entropy Alloys

In the last fifteen years, a new class of metallic alloys has represented a topic of intense research in the field of metallurgy. They are the so-called High Entropy Alloys (HEAs), which in their broader definition are multi-component alloys composed by more than four elements in equi- or near equi-atomic concentration, preferably forming simple microstructures constituted by disordered fcc and/or bcc solid solutions.

This new alloy concept have opened up research community to the exploration of a vast composition space. Broad possibilities have been perceived for designing new materials with combinations of properties promising in many industrial fields. Virtually, the HEA composition, and thus the type and concentration of the constitutive species, can be designed as for exhibiting desired microstructures and targeted sets of properties, often unusual for traditional materials, such as high temperature resistance and low density at the same time. Nevertheless, the still weak knowledge of the interactions existing among the species in concentrated solutions often produce unexpected microstructures, which are far to be simples and with many brittle intermetallic phases negatively affecting properties. This occurs because the relationship between composition, microstructure and properties, which is fundamental for designing materials with desired properties, is still weak established for this young class of alloys. The scope of the present chapter is to provide a panorama of the material design opportunities opened up by the introduction of the HEAs concept, providing at the same time a critical summary of the relationship between composition, microstructure and properties up to know established for the most studied HEA families.

The chapter will start with an overall description of the HEAs, from their discovery to the evolution of their theoretical understanding and great attention will be given to the description of the thermodynamic parameters affecting phase constitution in HEAs. Most important HEA families will be then presented and the relationship between composition, microstructure and properties through conventional melt and casting technique will be summarized. In conclusion, a section will be dedicated to the summary of the main manufacturing techniques for producing bulk HEAs - including AM technologies.

4.1 Discovery of High Entropy Alloys

Since the Bronze Age, alloys have been traditionally developed following the 'base element' approach. This strategy begins with one principal element, such as nickel in superalloys and iron in steels, which is chosen for its characteristic "base" properties (i.e. density and elastic moduli) and subsequently a minor alloying approach is adopted in order to obtain alloys with enhanced properties. In particular, small amounts of alloying elements are added or removed until optimized properties for a certain application are found, while characteristic properties of the base element - that make the alloy family attractive - are retained. In the end, the final material is likely to be composed of one or two principal elements plus minor quantities of several other elements. The construction of singular, binary, ternary up to few quaternary phase diagrams are then used for the predictions of phases in metallic alloys.

Figure 78 shows schematically a ternary and a quaternary phase diagram. The corners indicate the most investigated regions where the conventional *minor alloying* strategy focuses. The information and understanding of these portions of the phase diagrams are highly developed. Differently, the blank extended region at the centre of the phase diagrams, where the proportion of elements is near-equiatomic, is much less investigated. The weak interest in these regions has been generally motivated by the underlying assumption that when increasing the concentration of elements within a system considerably, beyond that of "minor alloying", complex brittle intermetallic compounds or amorphous structures would form.

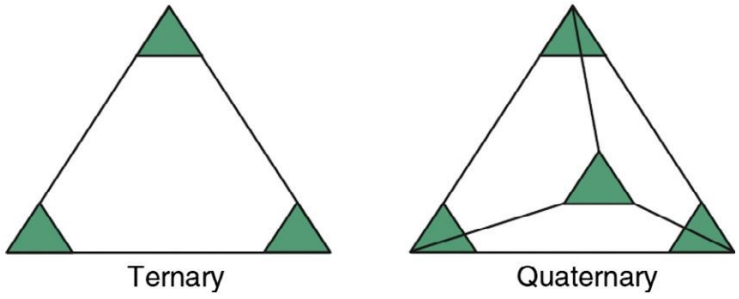

Figure 78. Schematic representation of a ternary and quaternary phase diagram, showing the regions where traditional alloy systems exists and the conventional strategy has focused (green) and the unexplored regions near the centre (white) [282].

Vincent [283] in 1981 and Knight [284] in 1995 were the firsts to publish two theses aimed on understanding features of materials located in the blank unexplored central area of the phase diagram and named these systems *multicomponent* alloys. More than one decade later, in 2004, Cantor *et al.* [285] and Yeh *et al.* [286] published independently their works on multicomponent alloys with near-equiatomic compositions and both pointed out on the ability of these systems to form simple face-centered cubic (fcc) or body-centered cubic (bcc) crystalline structures in place of expected complex and brittle intermetallic compounds.

Cantor motivated its study on the five-component equiatomic CoCrFeMnNi alloy (termed as *Cantor alloy*) as an attempt "to investigate the unexplored central regions of multicomponent alloy phase space". For these alloy systems, he kept the name of *multicomponent alloys*.

Differently, Yeh firstly coined the term *High Entropy Alloys* (HEA). He was motivated on his own theory that the high configurational entropy (S_{Conf}) of a multi-principal element system was the main factor in determining the formation of simple crystal structures and the enhanced properties which might have challenged conventional steels in strength, hardness, thermal and corrosion resistances [287].

Since the first studies conducted by Cantor *et al.* and Yeh *et al* on the so-called high entropy alloys, the number of publications on the topic has been steadily increasing, accounting in less than 15 years of research in more than 2000 publications (see Figure 79). The great interest in understanding the fundamental principles for controlling the microstructure as well as for optimizing the multi-principal element alloy properties are some of the reasons that have driven the research into HEAs.

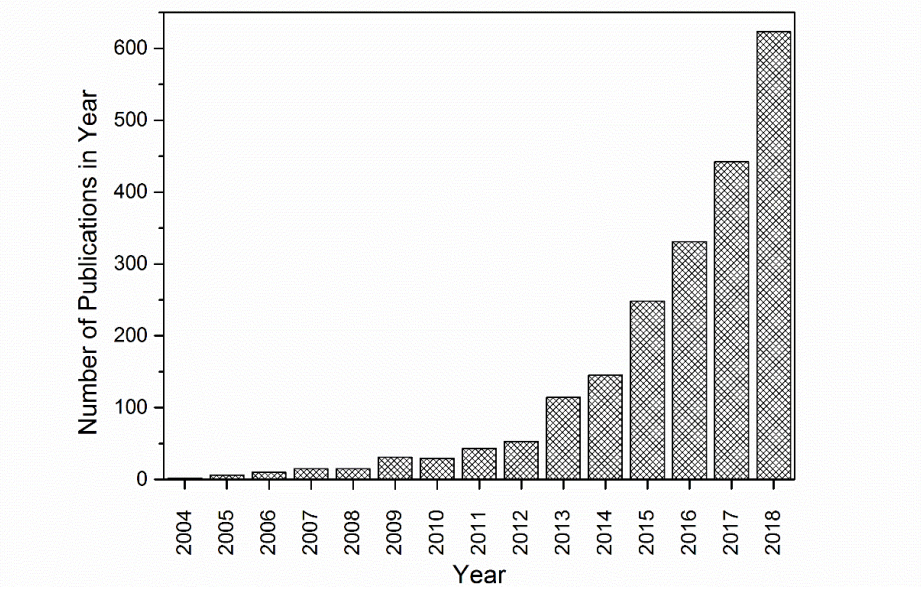

Figure 79. The publication rate for HEA literature since 2004. Data gathered from Scopus by searching for "High Entropy Alloys" in the article title, abstract keywords field and limiting the subject area to "Materials Science" and "Engineering".

As consequence of the rapid evolution of this field, researcher community does not always agree on the interpretation of results and on what exactly constitutes a HEA because several ambiguous definitions and descriptions have been given over the years [288–290]. For instance, one of the earliest definition reported by Yeh *et al*. [286] describes HEAs as "… those composed of five or more elements in equimolar ratio … [containing] principal elements with the concentration of each element being between 35 and 5 at.%". This definition, which stresses on the composition boundaries of the systems (number and concentration of the alloying elements), does not contain explicitly any requirement on the number and/or kind of phases and it opens then to two different opinions: (i) A HEA refers to a mixture

of five or more elements in near equiatomic concentrations, regardless the resulting phase. Many multiple-phased microstructures made of simple and complex phases such as fcc and/or bcc solid solutions plus intermetallic compounds have been assessed under this condition [291,292]; (ii) a HEA refers to alloys that both contain five or more elements in equiatomic or near equiatomic concentrations and that can produce a simple crystalline phase (fcc and/or bcc solid solution). This latter definition is narrower and makes a lot more sense if we consider the technological consequences. Regardless the opinion that we accept, apparently the quaternary systems have been ignored. Nowadays, it has been broadly assessed that simple crystal structures can form also in systems with four elements (i.e. AlTiVNb [293]).

Nevertheless, whether deliberated or not, the term HEA has progressively become tightly correlated with obtaining single-phase solid solutions by controlling the number and concentration of the elements. This fact produces debates and diverts the attention from the original major purpose that is "to investigate the unexplored central regions of multicomponent alloy phase space" [285]. For this reason, terms like multi-principal element alloys (MPEAs) or compositionally complex alloys (CCAs), that evoke the amplitude of the composition space rather than the magnitude of entropy as factor influencing the number and type of phases, have emerged over the years [294–296]. In this thesis, we will use the term MPEA and HEA interchangeably but we will prefer the term latter when the intent of producing or referring to a single-phase solid solutions is of major interest.

At this stage of the thesis, a fair definition of high entropy alloys could be *those alloys composed of four or more alloying elements in near equiatomic concentration, which may form simple crystal structures, such as fcc and/or bcc solid solutions.*

In the next section, critical literature review will be addressed to the evolution of the theoretical understanding of HEAs.

4.1.1 Basic thermodynamic concept

The Gibbs phase rule gives the relationship between the number of components and phases under equilibrium condition in a system.

At constant pressure, the relationship is [282]:

$$\boldsymbol{P + F = C + 1} \tag{4.1}$$

where F is the number of thermodynamic degrees of freedom in the system, which are the intensive variables such as composition, temperature, pressure, etc; C is the number of components and P is the number of phases under equilibrium. The minimum number of degrees of freedom F is zero so that, at an invariant reaction, the maximum number of phases under equilibrium is higher than the number of components as:

$$\boldsymbol{P_{max} = C + 1} \tag{4.2}$$

For instance, in a binary system (C = 2) the maximum number of phases corresponding to an invariant reaction (i.e. an eutectic point) is 3 and similarly in a ternary or quaternary system the maximum number of phases under equilibrium are 4 or 5, respectively. It is worth to note that equilibrium conditions at an invariant point rarely exist at room temperature and, for instance, binary systems usually consist of 1 or 2 phases at room temperature under equilibrium conditions [282].

Many material processing and manufacturing methods operate far from the equilibrium conditions. During non-equilibrium, segregation of alloying element, high-temperature, transitionary and/or off-stoichiometric phases can develop at room temperature so that the maximum number of phases can be greater than that predicted by Gibbs phase rule under equilibrium:

$$\boldsymbol{P_{max} > C + 1} \tag{4.3}$$

Therefore, binary systems often can consist of more than 3 phases at room temperature and ternary and quaternary systems may exhibits even more than 4 or 5 phases at room temperature.

Even though HEAs are composed by multiple elements (more than four) they unexpectedly exhibit a number of phases that is often far below the maximum equilibrium number allowed by Gibbs phase rule, normally 1 single phase solid solution or no more than 3 or 4 phases. Moreover, if we consider that most processing techniques work under non-equilibrium conditions (i.e. melt and casting), the fact is still more surprising and the reason for this is still a topic of debate.

However, this is not to say that every multi-principal element system existing near the centre of the phase diagram will form a solid solution. As we will see soon, there exist semiempirical methods and strategies that help in predicting which phases and/or structures would form from an alloy composition and consequently which alloy compositions are more likely to form simple crystal structures.

A theoretical description of HEAs can be conducted starting from the Gibb's free energy equation:

$$\boldsymbol{\Delta G = \Delta H - T\Delta S} \tag{4.4}$$

Here, ΔG is the change in free energy of the system, ΔH is the change in enthalpy, ΔS is the change in entropy and T is the temperature at which mixing of elements occurs. Minimization of the Gibb's free energy is the standard method to assess which phases are thermodynamically stable in alloys. Thus, the phase or combination of phases that yield the lowest ΔG at the given temperature T is the equilibrium state.

The original main idea behind HEAs is to drive minimization of ΔG by maximizing the entropic contribute ΔS of a potential crystalline solid solution phase. This can be done because, in the light of the Boltzmann's hypothesis on the relationship between entropy and system complexity [297], the energy gain from

the inherent disorder of a solid solution can minimize the Gibb's free energy when compared to competing ordered intermetallic phases, at high temperature.

When considering the contributions to the entropy of mixing ΔS, the HEA literature almost entirely focuses on the configurational entropy (S_{Conf}) of an ideal solution. Rigorously, there are many other non-configurational terms, influenced by atomic vibrations, electronic effects and magnetic moments. However, the relative contribution by each of these terms to the total entropy is unequal and in many cases it is almost exclusively controlled by the configurational term [298].

From a point of view of statistical thermodynamics, the configurational entropy of an ideal solution ΔS_{conf} (from now on will be referred as the entropy of mixing), can be derived from the Boltzmann's equation for entropy (S_B):

$$\boldsymbol{S_B = k_B \ln \omega} \tag{4.5}$$

where k_B is the Boltzmann's constant and ω is the number of microstates (total number of unique arrangements) corresponding to a given macrostate (the system as a whole). This equation can be applied to a disordered alloy composed of *n* components in which the total number of atoms is $N = \sum_{i=0}^{n} N_i$ and $\omega = \frac{N!}{\prod_i N_i}$, deriving the general equation for Gibb's entropy of an ideal solid solution as:

$$\boldsymbol{\Delta S_{conf} = -R \sum_{i=0}^{n} x_i \ln x_i} \tag{4.6}$$

where R is the universal gas constant (8.314 J K^{-1} mol^{-1}) and x_i is the atomic fraction of the i^{th} component. When the system is in equiatomic concentration $x_i = x_{i+1} = \cdots = x_n$ expression (4.6) simplifies as:

$$\boldsymbol{\Delta S_{conf} = R \ln n} \tag{4.7}$$

This last equation tell us that for a given number of constitutive elements the entropy of mixing of an ideal solid solution is maximized at equiatomic composition and that it scales with the number of elements. Hence, higher ΔS_{conf} values can be obtained by increasing the number of components (Table 18).

Table 18. Configurational entropy as function of the number of elements for equiatomic alloys.

n	1	2	3	4	5	6	7	8	9
$\boldsymbol{\Delta S_{conf}}$	0	5.7	9.1	11.5	13.4	14.9	16.2	17.3	18.3

It is hard to transfer the physical basis for the configurational entropy contribute of the Gibb's free energy from an ideal gas to that of a solid solution. Nevertheless,

it is valid the assumption that each site of the lattice is indistinguishable from the other (same size of the atoms), each atom has the same probability to be found on each lattice site (random distribution), that there are no chemical interactions ($\Delta H_{mix} = 0$) and atoms are loosely packed.

For real alloys, whose constituent elements can differ significantly in the atomic size and have dense packing at low temperature, the concept of maximizing configurational entropy only through the composition according to equation 4.7 is then no longer valid and the real entropy of mixing can deviate from the ideal one. Recently, Ye *et al.* [299] suggested a correction term that accounts for the excess configurational entropy due to the mismatch in atomic radii and packing fraction in MPEAs, assuming a hard-sphere model for the solid solution (Figure 80). Moreover, mixing of unlike atoms will inherently change the probability of finding each atom in a random position, by introducing a chemical selectivity effect. Regular [300] and sub-regular solution [301] models somewhat account of this effect, whilst it is only introduced into the enthalpy term of Gibb's equation.

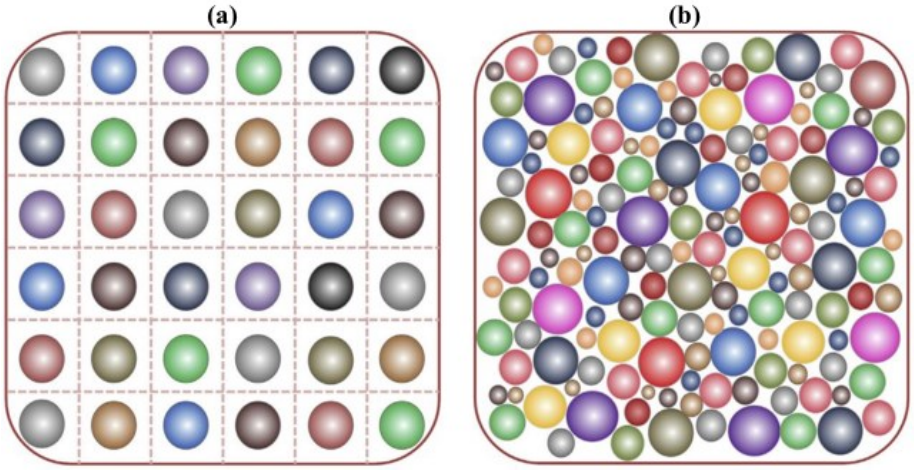

Figure 80. Schematic representation of the atomic configuration in a multi-component alloy according to (a) the ideal-solution model and (b) the hard-sphere mixture model. In the ideal solution model the elements have the same atomic size and a loose atomic packing and the entropy of mixing only depends on the number and concentration of elements differently to the hard-sphere mixture model where the entropy of mixing depends also on the atomic size and packing density [21].

The implication of the equation for configurational entropy of an ideal solid solution (eq. 4.7) led Yeh *et al.* to hypothesize that alloys with a higher number of elements would have possessed configurational entropy of mixing values high enough to stabilize a disordered solid solution against the tendency to ordering and/or segregation [286]. As already said, the failure of this hypothesis is confirmed by many publications which reported the formation of multi-phase microstructures based on ordered compounds rather than disordered solid solutions [291,292].

I will go through this aspect in the next sections. Before that, I will introduce some key features that have been traditionally adopted to describe microstructures and rationalize properties of HEAs.

4.1.2 Core effects of HEAs

The HEA field opens up to the idea of intentionally exploring the vast composition space made by the near-equi-atomic concentration of multiple element systems. The current knowledge of physical metallurgy is mostly based on outcomes gained from conventional alloys, but HEA compositions are different from the conventional ones, hence attention must be paid in investigating this field.

Since their discovery, microstructures and properties of HEAs have been described referring to four core effects, that is [302]: (1) Thermodynamics: high-entropy effect; (2) Structures: severe lattice distortion; (3) Kinetics: sluggish diffusion; and (4) Properties: "cocktail" effects.

It is worth to note that three of these effects are hypotheses and were first introduced basing on the information available at the time of the very earliest publications. Some of the above-mentioned concepts have nowadays been reinterpreted and their validity has been drastically narrowed.

The *high entropy effect* is the key concept of HEA, meaning that the increased configurational entropy of multicomponent alloys stabilizes the formation of simple crystal structures in place of competing complex intermetallic compounds. This effect has been hence traditionally used to explain the existence of simple solid solution in multi-principal element systems.

The high-entropy effect's idea has found confirmation in the quaternary 3-d transition metal FeCoCrNi fcc alloy, in which no evidence of long-range chemical ordering was observed in the as-cast and heat treated conditions [303]. Similarly, the entropy-driven phase stability was demonstrated in the fcc $Al_{0.5}CoCrCuFeNi$ alloy [304]. Another reported system is the equiatomic AlNbTiV refractory HEA, which forms a simple bcc structure [293]. To better visualize the high-entropy effect, Figure 81 shows the X-ray diffraction (XRD) patterns of an equimolar series of CuNiAlCoCrFeSi HEA from the binary to the septenary alloy produced by casting [305]. Whilst the increasing number of incorporated elements, the high-entropy inhibited the formation of complex intermetallic phases and the microstructures consisted of simple solid solutions of fcc and bcc phases.

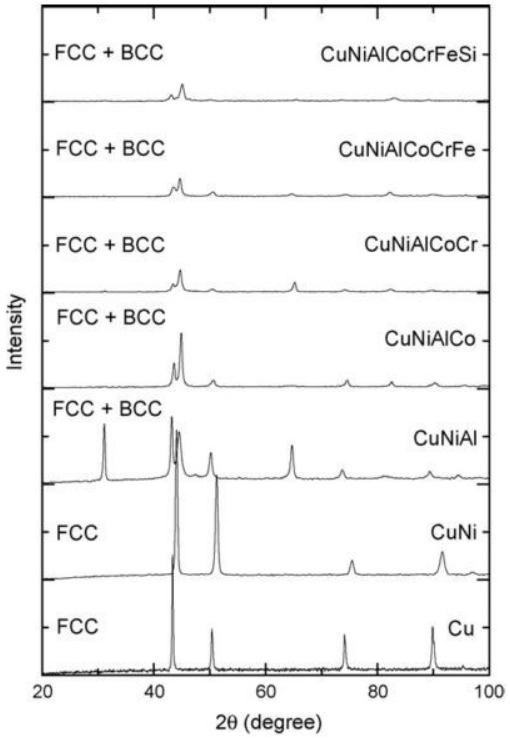

Figure 81. XRD patterns of an equimolar CuNiAlCoCrFeSi as-cast HEA obtained by increasing the number of incorporated elements from the binary alloy to the septenary one [305].

The severe *lattice distortion effect* originates from the large difference in atomic sizes among constituent alloying elements and it is claimed to correlate with thermodynamic, kinetic and mechanical properties of HEAs.

In conventional alloys, lattice sites are mostly occupied by the dominant constituent atoms, resulting in low lattice distortion. In HEAs, there are many principal components and each element atom has the same possibility to occupy the lattice sites to form a solid solution. Atoms with varying sizes cause then higher lattice distortions and additionally create local uncertainty in atom positions. This uncertainty in atomic positions becomes more significant increasing the atomic size mismatch and the concentrations, resulting in extra configurational entropy. Some experimental studies have reported that lattice distortion effect contributes to decrease the XRD peak intensities [305,306], to reduce the thermal and electrical conductivity [302] and to increase the solid solution hardening [302], especially in bcc-structured HEAs [307,308]. Whilst these studies are quite interesting and the claims seem physically reasonable, more investigations addressed to quantify these effects and to isolate them from other contributions are required, in order to gain confidence with such hypotheses.

Figure 82 depicts a schematic representation of the lattice structures of a pure metal, a conventional alloy and a multi-principal element alloy, showing the progressive distortion of the lattice as consequence of the multi-principal element alloys.

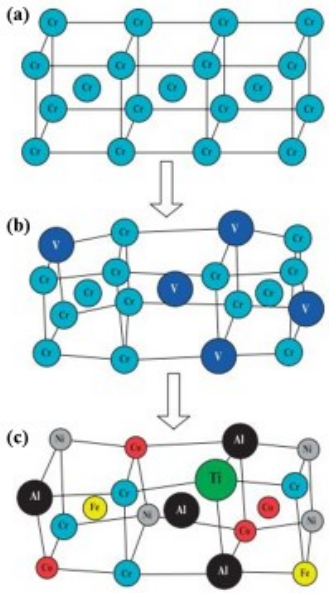

Figure 82. Schematic representation of a bcc crystal structure of (a) a perfect Cr lattice, (b) a distorted lattice containing one additional component (V) with different atomic size and (c) severe distorted lattice caused by the presence of different-sized atoms randomly distributed in the crystal lattice [31].

The *sluggish diffusion effect* has been traditionally used to comment some secondary observations in HEAs, including the formation of nano-sized precipitates and some amorphous structures upon solidification.

It was proposed that the long-range diffusion and phase transformation kinetics were slower in HEAs than in the conventional alloys, due to the difficulties encountered in HEAs in cooperating the diffusion of many different kinds of atoms but also to the lattice distortion effect that hinders atomic movements [302]. Although indirect observations of the appearance of nanocrystals in the as-cast equimolar AlCoCrCuFeNi alloy [286] and the retention of nanocrystals in AlCrMoSiTi alloy after annealing [309] are compatible with a slow kinetics, rigorously they do not prove that diffusion in HEAs is slower than in conventional alloys. Diffusion is hard to measure and to date only one study has reported experimental values for self-diffusion coefficients that support the sluggish diffusion hypothesis in HEAs [310].

Figure 83 shows that diffusion coefficients of the constitutive elements of the 3d-transition metal CoCrFeMnNi Cantor alloy are the smallest in different matrices, supporting the sluggish diffusion hypothesis.

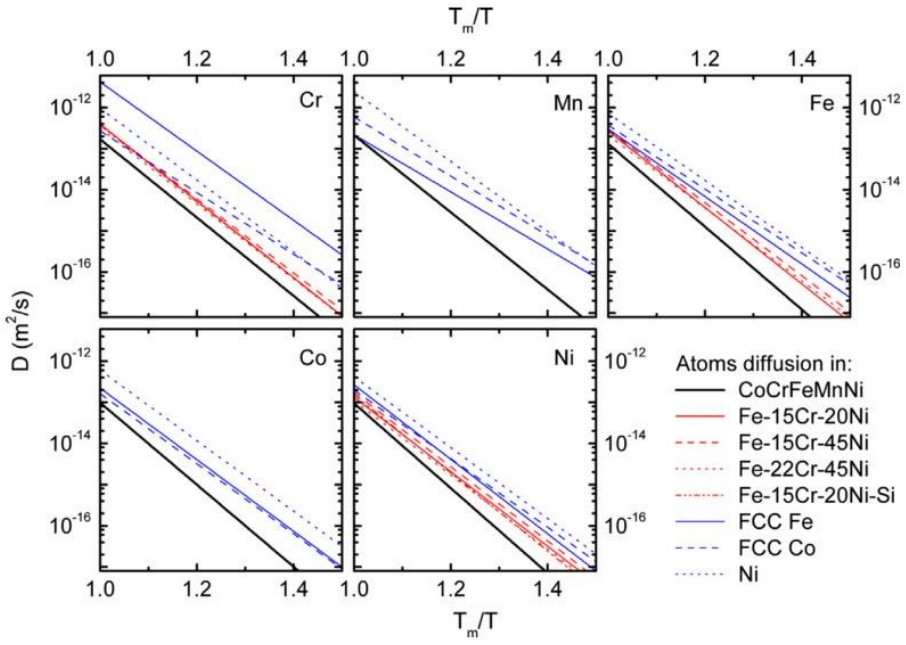

Figure 83. Temperature dependence of the diffusion coefficients for the constituting elements of the CoCrFeMnNi HEA in different matrices [33].

The *'cocktail' effect* is a suggestive expression first used by Ranganathan S. [311]. It indicates that in multi-component alloy systems the behavior of the alloy and its properties can deviate from the simple rule of mixture. Unexpected results and non-linear properties, which could not be obtained from any of the single elements, can be obtained by combining different elements together.

Differently to the other core effects, the 'cocktail effect' is not a hypothesis and thus requires no evidence. One major implication of this effect is that the alloy properties can be tailored by changing the composition, as reported for the $Al_xCoCrFeNi$ system [312]. For this system, in fact, the increase in Al content produces a dramatic increase in the hardness, unexpected if we consider that Al is a relatively soft element. Actually, Al atoms promote a structural change of the microstructure, which undergoes a transition from fcc → fcc + bcc → bcc structure at increasing quantity of Al (see Figure 84). Duplex fcc + bcc structure starts to form at around $x = 0.5$. The same trend as function of the Al content was observed in the Cu-containing $Al_xCoCrCuFeNi$ system [286]. The high lattice strain effect subsequent to the introduction of Al causes an increase in the lattice constants and it results in the strengthening of the alloy.

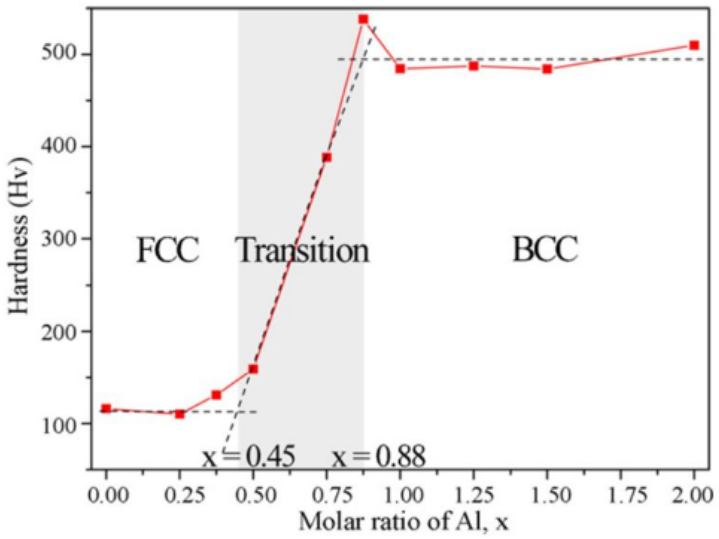

Figure 84. Hardness of the $Al_xCoCrFeNi$ HEA when x (content of Al in atomic fraction) increases from 0 → 2 [35].

4.1.3 Alloy design criteria: predicting the formation of HEAs

Originally Yeh *et al.* [286] hypothesized the configurational entropy being the dominant factor affecting the formation of solid solutions in HEAs. Single phase, multiphase microstructures based on intermetallics and even bulk metallic glasses were experimentally assessed at the same values of entropy of mixing (see Figure 85), refuting occasionally the *high-entropy effect* hypothesis and making evident the inability of this parameter to solely describe phases observed in multi-component systems.

A crucial point concerning HEAs was then to develop methods and strategies to control phase formation, able to predict which type of phases (solid solutions, intermetallic, amorphous phase) would form once known the type, number and concentration of the constitutive elements of the system. This point is of great interest if it considers it may provide useful guidelines for searching and/or designing MPEAs with selected microstructures, and thus properties.

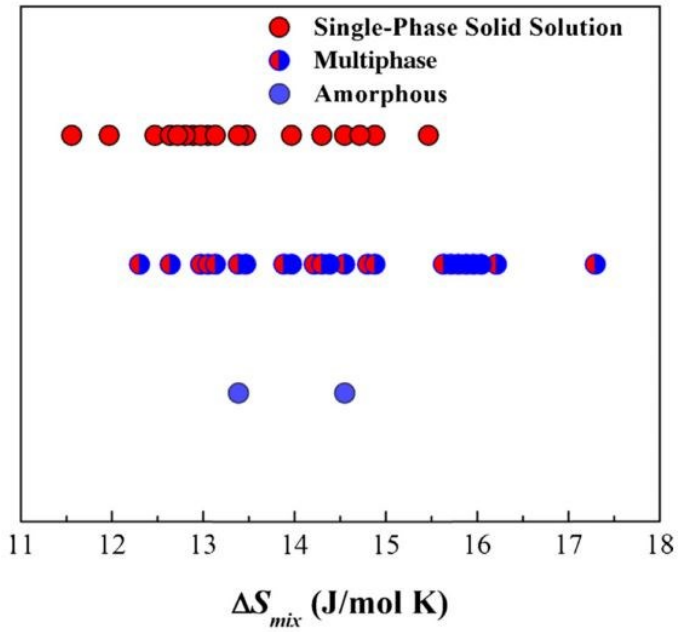

Figure 85. Phase selection in HEAs by plotting type of phase (single-phase solid solutions, multiphase and amorphous structure) with the configurational entropy of an ideal solid solution [313]. The plot shows that same values of entropy of mixing characterize systems exhibiting different phases.

In 1935, William Hume-Rothery [314] derived four empirical rules to predict the formation of a solid solution in a binary metallic system:

1. The *atomic size difference* between the solvent and the solute in the binary solid solution should not exceed 15%.

2. The *crystal structure* of solute and solvent must be similar.

3. Complete solubility occurs when the solvent and the solute have the same *valency*.

4. The solute and the solvent should have similar *electronegativity*. If the electronegativity difference is too great, intermetallic compounds tend to form in place of a solid solution.

Hume-Rothery's rules state thus that solid solutions are favoured when element selection allows having components with similar atom sizes, crystal structures, valencies and electronegativities. The concept of these rules is generally accepted for binary systems and their extrapolation to multi-component systems has been adopted as an approach to design HEAs.

The majority of current strategies developed to control phase formation in MPEAs are addressed to empirical approaches derived also from bulk metallic glasses (BMGs) and take into accounts other parameters than entropy of mixing that is the enthalpy of mixing (ΔH_{mix}), the atomic size difference (δ) and the valence electron concentration (VEC).

- The *enthalpy of mixing* ΔH_{mix} has a large effect on the Gibb's free energy. This term corresponds to the heat consumed (endothermic) or released (exotermic) during the mixing of elements and it accounts for the chemical similarity/difference between species. In the largest part of literature on HEAs, enthalpy of mixing is calculated adopting a regular solution model as [315]:

$$\Delta \boldsymbol{H_{mix}} = \sum_{\boldsymbol{i,j=1;\ i\neq j}}^{\boldsymbol{n}} \boldsymbol{4\Delta H_{ij} c_i c_j} \tag{4.8}$$

Where n is the number of alloying elements, c_i and c_j is the atomic concentration of the ith and jth component, and ΔH_{ij} is the formation enthalpy of the equiatomic liquid binary alloy calculated using Miedema's model [316].

- The *atomic size difference* δ describes the polydispersity resulting from different atomic-sizes in multi-component systems. It allows to determinate the atomic mismatch as [317]:

$$\boldsymbol{\delta} = \sqrt{\sum_{\boldsymbol{i=1}}^{\boldsymbol{n}} \boldsymbol{c_i}\left(\mathbf{1} - \frac{\boldsymbol{r_i}}{\sum_{\boldsymbol{i}}^{\boldsymbol{n}} \boldsymbol{c_i r_i}}\right)^{\mathbf{2}}} \tag{4.9}$$

Where n is the number of alloying elements, c_i and r_i are the atomic concentration and the atomic radius of the ith component, respectively.

- The *Valence Electron Concentration* (VEC) indicates the number of all the valence electrons in the alloy per atom and it is useful in defining the structure and properties of the alloys. For a multi-component system it is defined as [318]:

$$\boldsymbol{VEC} = \sum_{\boldsymbol{i=1}}^{\boldsymbol{n}} \boldsymbol{c_i VEC_i} \tag{4.10}$$

where n is the number of alloying elements, c_i and VEC_i are the atomic concentration and the number of d-electrons in the valence band of the ith component, assuming that in HEAs each alloying element contributes to the overall *VEC* with a number of valence electrons equal to that of the parent metal.

In 2008, Zhang *et al.* [317] proposed the use of the three parameters ΔH_{mix}, δ and ΔS_{mix} to predict the formation of HEAs. Interestingly, they found that the solid solutions formed at slightly positive or not highly negative values of enthalpy of mixing, at small atomic size difference and at high values of the entropy of mixing. In contrast, BMGs were more likely to form when $\Delta H_{mix}$was more negative and δ was larger. One significant merit of their work was to firstly attempt to find out the rules governing phase selection in HEAs by statistically analysing many alloy systems, assessing for each of them the type of phases and considering other thermodynamic parameters than the solely entropy of mixing. However, they did not capture the marginal influence of the entropy of mixing in determining the final structure of the alloy and they provided only qualitative information on the influence of the other parameters.

Under the same line of work, S. Guo and T. Liu [318] analysed the relationship between the Hume-Rothery's rules and phases observed in a large number of multi-component alloys. They found electronegativity and *VEC* did not have any influence on the phase formation and solid solution formation was rather influenced by mixing enthalpy, atoms-size mismatch and entropy of mixing when the three parameters felled in the ranges $-22 < \Delta H_{mix} < 7$ K J mol^{-1}, $0 < \delta < 8.5\%$ and $11 < \Delta S_{mix} < 19.5$ J K^{-1} mol^{-1} simultaneously.

Later on, in another study, Guo *et al.* [319] modified the boundaries and suggested a two-parameters scheme to capture phase selection in HEAs, corresponding to the region $-11.6 < \Delta H_{mix} < 3.2$ K J mol^{-1} and $\delta < 6.6\%$. The two parameters together were able to separate different areas forming solid solutions and amorphous phase quite accurately but a broad overlapping region existed in the δ-ΔH_{mix} map where intermetallic compounds simultaneously existed with solid solutions and amorphous phase, respectively (Figure 86). Recently, Tsai *et al*. [320] argued that the existence of intermetallic phases (i.e. σ and μ phase) having simultaneously near-zero enthalpy of mixing and small atomic size differences can be the reason for these mispredictions and suggested to incorporate models specifically targeted for these intermetallics to improve the prediction accuracy.

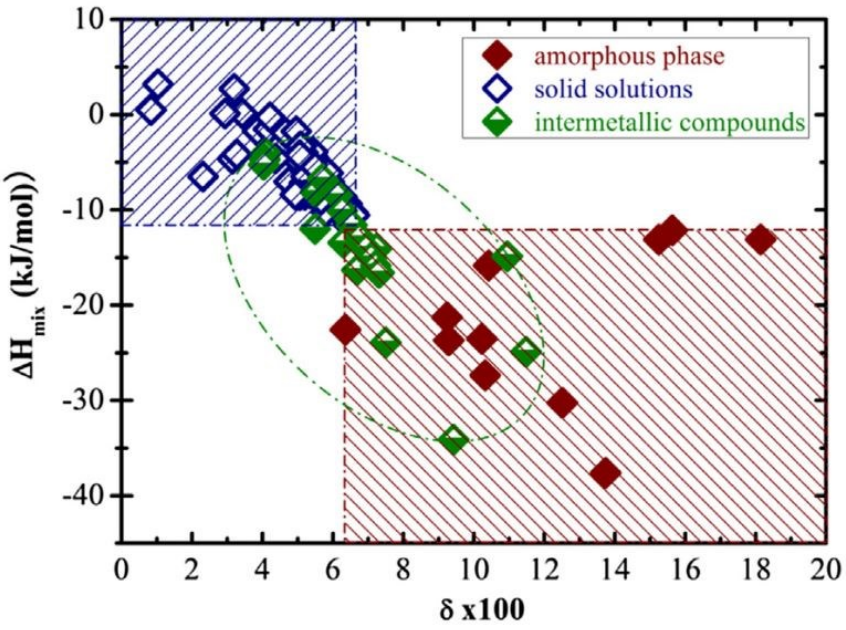

Figure 86. Phase selection in HEAs using δ - $\Delta \boldsymbol{H_{mix}}$ plot on experimental data of around 90 alloys, showing the individual regions where solid solutions, intermetallic and amorphous phase form as well as overlapping regions [41].

In 2012, Yang *et al.* [321] proposed to use the dimensionless parameter ω as solid solution formability index in multi-component systems, defined as the ratio between the two contributes to the Gibb's free energy as:

$$\boldsymbol{\omega} = \frac{\boldsymbol{T_m \Delta S_{mix}}}{|\boldsymbol{\Delta H_{mix}}|} \tag{4.11}$$

Where $T_m = \sum_i^n c_i T_{m_i}$ is the melting temperature of the alloy calculated under a rule of mixtures assumption, T_{m_i} is the melting temperature of the i^{th} element of the system and c_i is the atomic concentration of the i^{th} component.

The solid solution formability index ω was more effective in separating solid solution from intermetallic phases and bulk metallic glasses (BMGs) by using a δ-ω plot (see Figure 87) in place of the δ-ΔH_{mix} plot but it failed again in separating exactly HEAs forming solid solution from those forming dual phase solid solution + intermetallics. Nevertheless, it worth to say that the methodology employed by Yang *et al.* in designing the ω parameter is not obvious. As already done by Guo *et al.* [319] , Yang *et al.* captured the importance of using more than one parameter for the prediction of solid solutions in multi-component systems as well as the critical role played by the atomic-size parameter δ and the enthalpy of mixing in discriminating solid solutions and the amorphous phase. Additionally, they were able to interpret the different roles played by the two Gibb's free energy contributes $T_m \Delta S_{mix}$ and ΔH_{mix} during phase formation. Experimental information available for binary alloy systems show that ΔH_{mix} in the liquid phase affects phase formation [322]. Yang *et al.* assumed that ΔH_{mix} had a similar effect in multi-component systems: highly negative ΔH_{mix} tends to combine elements together to

form intermetallic compounds while positive ΔH_{mix} tends to separate elements leading to poor miscibility and phase segregation. The argument in favor of this approach is thus that $|\Delta H_{mix}|$ has the same effect in contrasting the formation of the solid solution. If the alloy yields $T_m \Delta S_{mix}$ large enough to surpass $|\Delta H_{mix}|$ then a solid solution will be favored, i.e. the numerator in equation 4.11 is larger than the denominator and solid solutions are then expected when ω > 1.1 and δ < 6.6.

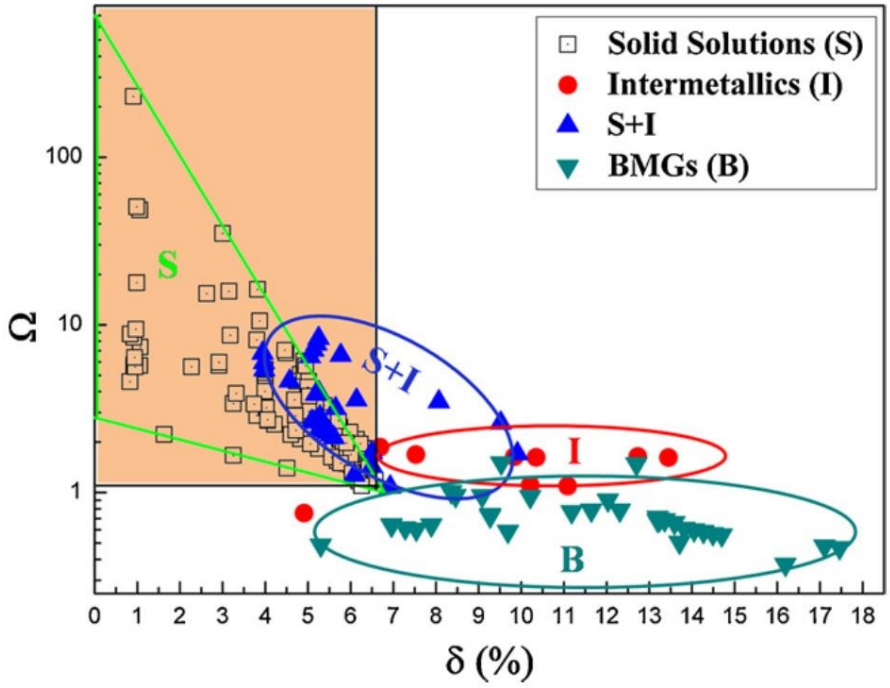

Figure 87. Phase selection in HEAs using δ-ω plot showing the results from experimentally characterized systems that form solid solutions, intermetallics, multiphase solid solutions + intermetallics and BMGs [321]. The method successfully predicted the formation of solid solutions on 95 alloys over 123 experimentally investigated in the study.

Since then, many other alloy design criteria and physical parameters have been suggested [323–326]. For instance, Sing *et al.* [323] developed a purely geometrical parameter $\Lambda = \Delta S_{mix}/\delta^2$, in which δ^2 was conceptualized as a measure of the strain energy arising from the different atomic sizes. According to this definition, the higher the Λ parameter the higher the probability of forming solid solutions and a critical value of Λ = 0.96 was prescribed. However, main limitation of the criteria like that of Sing *et al.* [323] is the lack of applicability and reproducibility. It prescribes a general rule that represents a necessary condition for obtaining solid solutions in multicomponent systems but not a sufficient one. More importantly, these models did not take into account other important thermodynamic parameters such as the mixing enthalpy and no work in this direction has been conducted by far. On the other hand, the method based on the *ω* and δ parameters also gives some shortcomings derived from the use of a regular solution model and gives an overlapping region unable to sharply discriminate - in some cases - solid solutions from multiphase solid solutions + intermetallics. However, the method introduced by Yang *et al.* is to date the most widely used alloy design criterion for predicting

phases in HEAs and the one with the highest reproducibility. It has been successfully applied to a large number of alloy systems [321], also considering different systems than those experimentally investigated in the original publication, including quaternary ones [293,296,327].

The well-established concept of *VEC* was also applied to HEA to predict phase structure. Preliminary studies did not show any correlation between phases formed and *VEC*, when a large number of alloys was statistically analysed [318]. As already seen, whether phase will form (solid solution, intermetallic, BMG) is mostly affected by atom-size difference and mixing enthalpy. However, *VEC* can be helpful in predicting crystal structure of HEAs. Guo *et al.* [328] were the first to experimentally found specific relations between *VEC* and structure in alloys containing Al-Co-Cr-Cu-Fe-Ni and thus predictions work quite accurately for alloys belonging to this system. Nevertheless, it was found that bcc solid solutions and fcc solid solutions are stable at $VEC < 6.87$ and $VEC \geq 8$, respectively, and that duplex fcc + bcc structures form when $6.87 < VEC \leq 8$. Recently, the formation of some intermetallic phase, i.e. the σ phase, has been related to the *VEC* value in some HEAs containing Cr and/or V [329]. A more detailed and in-depth analysis on the effect of the electronic parameters on phase selection in HEAs can be found in the study published by Poletti and Battezzati in 2014 [330].

It is worth to mention here that, alternatively to the empirical approaches, the semiempirical computational approach known as CALPHAD (CALculations of PHase Diagrams) has been applied to HEAs in order to gain general information on the alloy system behavior and to screen a large number of alloy compositions. CALPHAD approach uses experimental data available for binary and ternary alloy systems in order to predict equilibrium phases and thus this method is database dependent. Nevertheless, the applicability of CALPHAD approach to the design of HEAs was found to be more challenging than that for conventional alloys, mainly due to limited composition space covered by commercially available databases [331]. A remarked discrepancy has been found between experimental results and the CALPHAD simulations of HEAs [313], especially predictions of low temperature phases, while phase selection at high temperature was found to be trusty in a qualitative way for selected alloy systems [332]. A challenging step towards the broader application of CALPHAD approach to the design of HEAs compositions may came from the development of more accurate databases, with a larger number of subsystems able to describe the compositional space of multi-component systems [327].

4.2 HEAs families: phases constitution and properties

Although compositionally complex, the very first systems investigated - the equiatomic CoCrFeMnNi alloy [285] and the $Al_xCoCrCuFeNi$ systems [286] - exhibited the formation of simple fcc and/or bcc solid solutions. Most notably these systems showed microstructures and resulting properties could also be tailored by varying the chemical composition, i.e. the Al concentration. The novel alloy-design strategy has allowed thus great opportunity for exploring, discovering and

developing new classes of alloys with different microstructures and enhanced properties.

Nowadays, HEAs or MPEAs broadly speaking refer to alloys belonging to six major families. Miracle *et al.* [333] classified them according to the different constituting elements (3d transition metals, refractory metals, light metals, lanthanide (4f) transition metals, brasses and bronzes and precious metals), producing a wide range of microstructures, spanning from single phase solid solution to multi-phase structures (solid solutions and/or intermetallic phases). Sometimes precipitates can be in the form of nano- to micro-scale phases [286] thus beneficial for the mechanical properties due to the effect of precipitate strengthening. It is also possible that complex ordered compounds, which make microstructure brittle, form, even if they are generally undesired.

Because of their promising properties suitable especially for structural applications, MPEAs based on 3d transition metals and refractory metals have been among the most investigated MPEA families. Their characteristic microstructures, phases, mechanical and functional properties will be reported in the following section. Light metal MPEAs have been getting more interest because of their interesting specific properties but results are still few and thus they will be only briefly presented. The remaining alloy families based on lanthanide (4f) transition metals [334], brasses and bronzes [335] and precious metals [336] are still young and their study has been mainly motivated by scientific curiosity rather than real applications. For this reason, they will not be treated here.

4.2.1 3d transition metal HEAs

The so-called *3d transition metal* MPEAs represent by far the most studied alloy family. They are based on the use of Co, Cr, Cu, Fe, Mn, Ni transition metals as main elements but Al, Si, Ti, V and Nb are usually added in order to tailor structures and properties. This MPEA family contributes in giving alloys with varying single-phase and multi-phase microstructures, although single phase fcc disordered solid solutions are the most common ones [333].

Table 19 lists some physical properties of the most common elements used in 3-d transition metal MPEAs. With the exclusion of the 4d transition metal Nb and the non-transition elements Al and Si, physical properties such as melting point and density spread over a tight range and the atomic radii for typically used Cr, Mn, Fe, Co, Ni, Cu elements are also quite similar. Then, Table 20 shows the enthalpy of mixing of the binary systems as measure of the attractive (largely negative) or repulsive (large positive) chemical interaction among the elements used in 3-d transition metal MPEAs. With the exclusion of Si, Al and Cu contribute in giving the highest attractive and repulsive interactions with the other constitutive elements, respectively.

Table 19. List of the melting point, density and atom radius for common elements used in 3d-transition metal MPEAs, with the addition of Nb as 4d-transition element and Al and Si as non-transition elements [333,337].The highest and lowest values for each property are in bold.

Element	Melting Point (°C)	Density (g cm^{-3})	Atom radius (pm)
Ti	1668	**4.50**	**146.15**
V	**1910**	6.12	131.6
Cr	1907	7.14	124.91
Mn	1246	7.47	135
Fe	1538	7.88	**124.12**
Co	1495	8.84	125.10
Ni	1455	8.91	124.59
Cu	**1085**	**8.94**	127.8
Nb	2477	8.57	142.9
Al	660	2.70	143.17
Si	1414	2.33	115.3

Table 20. Mixing enthalpies (KJ mol-1) of the different atomic-pair for common elements used in 3d-transition metal MPEAs [316].

Element	Ti	V	Cr	Mn	Fe	Co	Ni	Cu	Nb	Al	Si
Ti	0										
V	-2	0									
Cr	-7	-2	0								
Mn	-8	-1	2	0							
Fe	-17	-7	-1	0	0						
Co	-28	-14	-4	-5	-1	0					
Ni	-35	-18	-7	-8	-2	0	0				

Cu	-9	5	12	4	13	6	4	0			
Nb	2	-1	-7	-4	-16	-25	-30	3	0		
Al	-30	-16	-10	-19	-11	-19	-22	-1	-18	0	
Si	-66	-48	-37	-45	-35	-38	-40	-19	-56	-19	0

In 3d-transition metal MPEAs there is a strong relationship among composition, microstructure and mechanical properties. Although it is hard to generalize a whole family of alloys with complex composition, some frequent trends can be found.

Alloys belonging to the Co-Cr-Fe-Ni-Mn system usually form simple fcc solid solutions with low room temperature mechanical strength, which make them not attractive for applications (CoCrFeMnNi, CoCrFeNi).

The presence of Cu in the system is usually associated to the formation of a mixture of fcc phases, namely a disordered solid solution and a segregated Cu-rich fcc phase at the interdendritic regions, as observed in the CoCrCuFeNi alloy [338]. The behaviour of Cu is attributed to its strong repulsive interaction with the other 3d transition elements, not surprisingly described by the highly positive enthalpy of mixing of Cu with Fe, Cr, Co and Ni constitutive elements (see Table 20) [339]. This is an example in which the increased entropy of the system (in the form of an additional element) is not sufficient to surpass the enthalpy driven reaction.

Chen *et al.* [340] added Al into the CoCrFeNiCu system to study its alloying effect. As already discussed in 4.1.2 Core effects of HEAs, crystal structure transforms from single phase fcc to a mixture of fcc and bcc phases to single phase bcc, with the increase in Al concentration. Consistent to literature, bcc-type structure refers both to the disordered (A2) and ordered (B2) bcc structures. In the $Al_xCoCrCuFeNi$ ($0 < x < 3$) system, when the amount of Al exceeds 0.8 atomic ratio, together with the fcc Cu-rich phase, a mixture of A2 and B2 solid solutions forms through spinodal decomposition, until a single-phase B2 ordered solid solution is obtained at very high Al contents [341]. The drive for packing shift from fcc to bcc is attributed to a geometric reason [342]. Al has a larger metallic radius as compared to the other 3d transition metals and its presence imposes a strain on the fcc lattice with further alloying. At a certain point, the high lattice strain is easily accommodated by shifting to a more openly packed bcc structure. This is a general trend assessed in many 3d transition metal MPEAs and supported by the increase in the lattice parameter of the fcc phase when Al is added [286]. A similar transition was also observed in the $Al_{0.5}CoCrCuFeNi$ system alloying with Si [343]. However, lattice strain only does not explain the reason why it observes the formation of a B2 ordered phase in place of a disordered A1 phase with further Al addition. To do so, we need to refer to the electronic properties of Al. The B2 ordering in Al-containing 3d transition metal MPEAs is well reported. Aluminium, indeed, has high electron density (the outermost shell holds three electrons) and high ionization tendency.

Thus, Al prefers to transfer electrons to Ni, Co, Cr, Fe and Mn transition metals, creating hard atomic clusters where the bond in nature is covalent [344]. Then, since Al content in the alloy is relatively low, Al atoms are still randomly distributed in the lattice and solid solutions (either disordered or ordered) are observed [345]. Together with the structural transformation, alloying with Al is also followed by an increase in the hardness. For the as-cast $Al_xCoCrCuFeNi$ ($0 < x < 3$) system, the hardness increased from 133 HV to 655 HV [286] and such strengthening effect is generally related to the increase in lattice distortion upon alloying with Al and to the formation of the harder bcc structure [340].

Other researchers studied the alloying effect of Ti and Nb on the general Al-Co-Cr-(Cu)-Fe-(Ni) system and reported the formation of different intermetallic phases. In the $Al_{0.5}CoCrCuFeNiTi_x$ ($0.2 < x < 2$) system the hardness increased from 225 HV to 700 HV with the increase in the Ti concentration. The change of hardness in this system was ascribed primarily to the transformation from fcc to a mixture of fcc and bcc structures at low amount of Ti, and then also to the precipitation of ordered intermetallic compounds, such as the σ and Ti_2Ni-like (TL) phases, at higher Ti concentration [346]. In the $AlCoCrFeNiNb_x$ ($0.1 < x < 0.5$) system, the increase in the Vickers hardness resulting from the alloying with Nb was ascribed to the formation of a bcc solid solution with gradually higher amounts of the ordered Laves phase of the hcp (CoCr)Nb-type [347].

Phase constitution and hardness of the above-discussed systems are listed in Table 21.

Table 21. Phase constitution and hardness for some characteristic as-cast 3d transition metal MPEAs with different compositions and microstructures.

Alloy system	Phase constitution	Hardness (HV)	Ref.
CoCrFeMnNi	Fcc	-	[282,285]
CoCrFeNi	Fcc	135	[348]
CoCrFeNiCu	Fcc + Cu-rich phase	133	[338]
$Al_xCoCrCuFeNi$ ($0.3 < x < 0.5$)	Fcc + Cu-rich phase	180-208	[340]
$Al_xCoCrCuFeNi$ ($0.8 < x < 2.5$)	Fcc + Cu-rich phase + bcc	271-600	[340]
$Al_xCoCrCuFeNi$ ($2.8 < x < 3$)	B2 + Cu-rich phase	655-623	[340]
$Al_{0.5}CoCrCuFeNi$	Fcc + Cu-rich phase	263	[343]
$Al_{0.5}CoCrCuFeNiSi_{0.8}$	Fcc + Cu-rich phase + bcc	653	[343]
$Al_{0.5}CoCrCuFeNiTi_{0.2}$	Fcc	275	[346]

$Al_{0.5}CoCrCuFeNiTi_x$ ($0.4 < x < 0.6$)	Fcc + bcc	325-460	[346]
$Al_{0.5}CoCrCuFeNiTi_x$ ($0.8 < x < 1$)	Fcc + bcc + σ	590-630	[346]
$Al_{0.5}CoCrCuFeNiTi_x$ ($1.4 < x < 2$)	Fcc + bcc + TL	660-700	[346]
$AlCoCrFeNiNb_{0.1}$	Bcc	569	[347]
$AlCoCrFeNiNb_{0.25}$	Bcc + Laves	669	[347]
$AlCoCrFeNiNb_{0.5}$	Bcc + Laves	747	[347]

A significant amount of experimental data is available for tensile behaviour of 3d transition metal MPEAs obtained by casting route. Although it is difficult to compare directly data due to the differences in the type and concentration of constituting elements, phase constitution, thermo-mechanical processing and/or temperature and duration of post-process heat treatment, some general observation can be made.

Characteristic tensile properties of 3d transition metal MPEAs are compared to those of some conventional alloys in Table 22. Characteristic fcc single phase CoCrFeMnNi HEA is not particularly strong, having σ_y and σ_{UTS} below 400 and 700 MPa, respectively. However, this alloy is extremely ductile (plastic deformation >50%), especially at low temperature (opposite to conventional behavior) and it does not exhibit the characteristic ductile-to-brittle transition temperature. Moreover, it has a fracture toughness exceptionally superior to many traditional metallic alloys, surpassing 200 MPa $m^{-1/2}$ and tensile strength over 1000 MPa maintained down to cryogenic temperatures [349]. The superior fracture toughness of CoCrFeMnNi was ascribed to 100% ductile fracture due to microvoid coalescence and to a shift in the deformation mechanism from planar-slip dislocation at room temperature to mechanical nanotwinning at low temperature, arising in a steady strain hardening.

As already seen, many reported 3d transition metal MPEAs are based on 3d transition metals alloyed with Al. The $Al_{0.5}CoCrCuFeNi$ (9.1 at% Al) consists of two fcc phases, being the first the primary solid solution and the second the segregated Cu-rich fcc phase. The σ_y and σ_{UTS} slightly change with respect to the Al-free CoCrFeMnNi alloy but the elongation to failure drops to 19 %. The as-cast AlCoCrCuFeNi alloy with the highest Al content (16.7 at%) has a complex microstructure with two fcc phases and a bcc phase, resulting in a material with the highest σ_y and σ_{UTS} reported and the least elongation to failure (0.2 %) with a quasi-cleavage fracture. The trade-off between strength and room temperature ductility following to Al addition is found in many 3d transition metal MPEAs. Both strength and ductility require to be optimized to make these alloys attractive for real structural applications and results to date suggest further investigation is warranted.

Table 22. Mechanical properties under tensile stress for different as-cast 3d transition metal MPEAs and for conventional alloys.

Alloy	Phase constitution	σ_y (MPa)	σ_{UTS} (MPa)	ε (%)	Ref.
CoCrFeMnNi	fcc	362	651	51	[349,350]
$Al_{0.5}$CoCrCuFeNi	Fcc + fcc	360	707	19	[351]
AlCoCrCuFeNi	Fcc+fcc + bcc	790	790	0.2	[352]
Al alloys		250-550	300 - 600	>10	[290]
Ti alloys		800-1400	900 - 1600	3-15	[290]
Ni alloys		400-1300	1000 - 1600	15-30	[290]

Most of the research in 3d transition metal MPEAs has focused on the analysis of the relationship between microstructures and mechanical properties. In order to develop new alloys for structural applications, the oxidation resistance is usually taken into account during the second screening step. This is the reason why a comparatively limited number of studies have focused on this topic.

In metallic alloys, the process of oxidation can be complex [353]. Within this context, the term oxidation relates to the interaction of a surface or bulk metal with gaseous oxygen. Alloys that exhibit a good oxidation resistance form a compact and dense oxide layer on the surface of the material, preventing it from further oxidation. Al, Cr and Si are among the elements that do this best by creating a healing Al_2O_3, Cr_2O_3 and SiO_2 layer, which reduces the solubility of oxygen in the alloy and its diffusivity in the matrix [354]. On the contrary, alloys with poor oxidation resistance will form a porous metal oxide layer that does not offer any barrier to the diffusion of gaseous oxygen. "Runaway oxidation" occurs and the bulk material continuously reacts with fresh oxygen forming metal oxide. In addition, when there is a solubility of the oxide in the matrix, then the material embrittles too. Refractory alloys based on Ti and V are well-known to do this.

One of the method to measure thus the oxidation susceptibility of a material is to assess the change in mass over a period. Table 23 lists the weight gain per area for some commercial alloys and 3d transition metal MPEAs.

CoCrFeMnNi Cantor HEA alloy is by far the system where most of the efforts have focused. It exhibits good oxidation resistance as compared to some steels or titanium alloys. Laplanche *et al.* [355] found parabolic weight gain up to 900 °C for 100h in air, revealing the formation of protective oxide layers (weight gain of 2.1 mg cm^{-2}). A triple oxide layer was observed between 700 and 900 °C, namely consisting of an outer Mn-oxides layer, an intermediate-layer of Mn, Cr oxides and of an inner Cr_2O_3 oxide layer [356]. In all the temperature ranges, Cr and Mn are main factors affecting the oxidation behaviour of this alloy, the first through the

formation of stable and dense oxide layer and the latter because of its high diffusivity [357]. The diffusion of Mn through the oxides was indeed considered the rate-limiting process [357]. As expected, alloying with Al results in the enhancement of oxidation resistance ability of the HEA, through the formation of dense Al_2O_3 oxide [356,358]. Whilst some results seem promising, none study is available on the diffusion kinetics and long-term stability of HEAs and further work into this field is required.

Table 23. Weight gain per area for some commercial alloys and 3d transition metal MPEAs when exposed to air atmosphere at 800 °C for 24 h.

Material Sample	Weight gain per area (mg/cm^2)	Ref.
SKH51 (AISI M2) High speed steel	22	[359]
Ti-6Al-4V	11	[360]
Fe-16%Al	2	[361]
Type 304 stainless steel	0.3	[362]
CoCrFeMnNi	1.4	[363]
$Al_{0.3}CrFe_{1.5}MnNi_{0.5}$	0.9	[358]
AlCoCrFeNi	0.05	[356]

A limited number of publications focused also on some functional properties of HEAs, such as their thermal and electrical behaviour. Table 24 compares the thermal and electrical conductivity of the $Al_xCoCrFeNi$ ($0 < x < 2$) alloys to some representative pure metals and conventional alloys. Chou *et al.* [364] found that the thermal conductivity of the $Al_xCoCrFeNi$ alloys is much lower than in pure metallic elements (as expected) but it is similar to some highly alloyed steels or nickel superalloys. The electrical resistivity was found to be sensibly higher than both pure metallic elements and conventional alloys. Moreover, the addition of Al was found to affect both the electrical and thermal conductivity of the $Al_xCoCrFeNi$ alloys, presumably due to the higher lattice distortion.

Table 24. Thermal conductivity and electrical resistivity of the $Al_xCoCrFeNi$ ($0 < x < 2$) MPEA system produced by casting methods, pure elements and conventional alloys [365].

Category	Composition	Thermal conductivity ($W\ m^{-1}\ K^{-1}$)	Electrical resistivity ($\mu\Omega$ cm)
HEAs	CoCrFeNi (fcc)	12	142
	$Al_2CoCrFeNi$ (bcc)	16	211
Pure elements	Cu	398	2
	Al	237	3
	Ni	91	7
	Fe	80	10
	Ti	22	42
Conventional alloys	7075 Al alloy	121	6
	304 Stainless steel	15	69
	Inconel 718	11	125
	Ti-6Al-4V	6	168

4.2.2 Refractory metal HEAs

The *refractory metal* MPEA family, also reported as refractory high-entropy alloys (RHEAs), comprises systems containing a combination of the following refractory elements: W, Mo, Ta, Nb, Ti, Zr, Hf, V and Cr plus Al. In its wider definition, the category of refractory elements also includes Ir, Os, Re, Rh and Ru whilst to date these metals have not been used in refractory MPEAs.

Until now, there are not many studies on RHEAs and results are not as mature as for 3d transition metal MPEAs. Most of the available studies on mechanical properties of refractory element MPEAs reports only hardness and compression test results, and tensile test data are still rather limited. However, some RHEAs possess sufficient room temperatures compressive ductility, indicating that these alloys might also possess useful tensile ductility. Only few RHEAs, including HfNbTiZr [180] and HfNbTaTiZr [366], were tested for tensile properties, reporting significant ductility. Microstructures usually consists of single-phase bcc structure or bcc with the addition of Laves phases, especially for those systems containing Cr, V, Zr often together with Al.

Refractory metal MPEAs can be considered as a new class of high temperature materials for structural applications and probably represent the first attempt directly aimed to design a class of MPEAs that fulfils selected requirements. Aluminium, titanium and nickel superalloys are the most used structural materials, especially in aerospace industry. Broadly speaking, titanium and its alloys stay between the low density (2.6-2.9 g cm^{-3}) and low operating temperatures (<150 °C) Al-based alloys and the high-density (8-9 g cm^{-3}) and high-operating temperatures (600-1100 °C) nickel superalloys, having density (4.4-4.6 g cm^{-3}), elastic moduli and working temperature (< 450°C) that are in between [290]. Titanium alloys exhibit excellent corrosion behavior and strength comparable to nickel superalloys in addition to creep resistance up to 325 °C [18,367]. However, in high temperature applications, Ti alloys cannot satisfy creep, oxidation and wear resistance requirements and the

more performant superalloys are used. Refractory metal MPEAs were then initially designed for exploring the behavior of systems made by multi-principal elements with high melting temperatures (differently to 3d transition metals) in order to develop alloys with higher strength, operating temperature, oxidation resistance and lower density than competing nickel superalloys employed in aerospace industry [289]. Diversely to 3d transition metal MPEAs, in which elemental physical properties among the constitutive elements are quite similar or spread over a tight range, the palette of refractory metals offers a broad range in the elemental physical properties, i.e. melting point, density and atom radius (see Table 25). On the one hand, this provides significant flexibility in tailoring the alloy composition to meet specific properties. For example, alloy compositions containing W, Ta, Mo and Nb high-melting point elements may promote high melting temperature RHEAs, while alloy compositions containing low-density Ti, V, Zr and Cr refractory elements may promote low-density RHEAs. On the other hand, such a broad range of elemental properties reflects in a broader range of microstructures and mechanical properties and gives also additional challenges in processing RHEAs. Later in this dissertation, I will return on this topic and provide a more comprehensive analysis.

Table 26 reports the enthalpy of mixing for the binary systems of the constitutive elements of refractory MPEAs. Even here, Al contributes in giving the highest attractive interactions with the other constitutive elements.

Table 25. List of melting point, density and atom radius for common refractory elements used in RHEAs, with the addition of Al [333,337]. The highest and lowest values for each properties are in bold.

Element	Melting Point (°C)	Density (g cm^{-3})	Atom Radius (pm)
W	**3422**	**19.41**	143
Ta	3017	16.68	136.7
Mo	2623	10.23	136.26
Nb	2477	8.57	142.9
Hf	2233	13.28	157.75
V	1910	6.12	131.6
Cr	1907	7.14	**124.91**
Zr	1855	6.51	**160.25**
Ti	**1668**	**4.50**	146.15
Al	660	2.70	143.17

Table 26. Mixing enthalpies (KJ mol-1) of the different atomic-pair for common elements used in refractory metal MPEAs [316]. Al (in bold) is the element giving the highest attractive interactions.

Element	W	Ta	Mo	Nb	Hf	V	Cr	Zr	Ti	Al
W	0									
Ta	-7	0								
Mo	0	-5	0							
Nb	-8	0	-6	0						
Hf	-6	3	-4	4	0					
V	-1	-1	0	-1	-2	0				
Cr	1	-7	0	-7	-9	-2	0			
Zr	-9	3	-6	4	0	-4	-12	0		
Ti	-6	1	-4	2	0	-2	-7	0	0	
Al	-2	-19	-5	-18	-39	-16	-10	-44	-30	0

The first two RHEAs were developed by Senkov *et al.* in 2010 by vacuum arc melting [289]. In the as-cast condition, MoNbTaW and MoNbTaVW alloys formed a single-phase bcc structure with coarse grains and dendritic/interdendritic microstructures. These RHEAs had high microhardness of 460 and 530 HV, respectively. Furthermore, their structure was exceptionally stable up to 1400°C with useful compressive strength above 800 °C, outperforming behavior of traditional nickel superalloys, Haynes 230 [368] and Inconel 718 [369], as shown in Figure 88. The strong resistance to the high-temperature softening was ascribed to the slow diffusion kinetics of the atoms and to the high T_m of the alloys. However, despite the very high temperature resistance, density was very high (13.75 g cm^{-3} and 12.36 g cm^{-3}, respectively) and the alloys lacked of room temperature ductility (lower than 2.5 %) [289,370]. At this point, it is worth to note that most of the RHEAs reported in the literature lack of room-temperature ductility. One main challenge for employing RHEAs as structural materials is therefore their room temperature ductility, which is strongly related to the selection of constituent elements and to the phase constitution. Recently, Han *et al.* [371] reported a significant enhancement of the room temperature compressive strength and ductility of MoNbTaW and MoNbTaVW RHEAs by alloying with Ti. Alloys still

exhibited single-phase bcc structure with dendritic/interdendritic microstructures but the interdendritic regions were found to be rich in Ti and Nb. It is accepted that during the compressive test, the stress is easily concentrated at the interdendritic regions and therefore the enhanced ductility - up to 14 % of elongation for TiMoNbTaW alloy - was related to the segregation of ductile elements in those regions. The superior mechanical properties of TiNbMoTaW and TiMoNbTaVW over the Ti-free alloys were then ascribed to the solid solution hardening effect resulting by Ti addition [372].

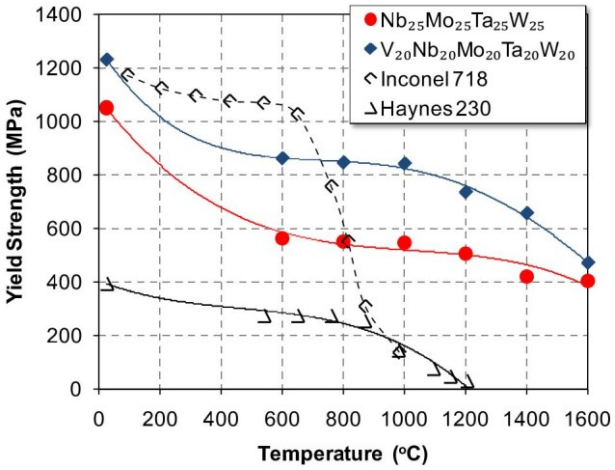

Figure 88. Yield strength variation with temperature for two different refractory metal MPEAs, MoNbTaW and MoNbTaVW, as compared to the two nickel-base superalloys Haynes 230 and Inconel 718 [370].

Whilst the first RHEAs showed the potential to increase the operating temperature and/or the operating stress of structural components, the density of these systems was too high, as compared to the competing nickel-base superalloys. In respect to the development of new refractory-metal MPEAs, the efforts gradually have focused in exploring the alloying effect of low-density refractory elements such as Cr, V, Zr, Ti plus Al. Complex microstructures based on intermetallic compounds have been often found. Stepanov *et al.* [373] studied the Al alloying effect on the NbTiVZr system with density around 6.5 g cm^{-3} and reported the formation of a bcc disordered solid solution as main phase and fractions of hexagonal Laves (C14) ordered phase rich in Zr and V. The addition of Al contributed in stabilizing the intermetallic phase, increasing also significantly the hardness and compressive strength of the alloys but gradually reducing the ductility, until no plastic deformation was observed in the $Al_{1.5}$NbTiVZr alloy with high Al content. A dramatic decrease of ductility as consequence of the increasing amount of intermetallic phases driven by the addition of Al was observed in the Cr-containing Al_xCrNbTiVZr alloys (x = 0.25; 0.5; 1) [374]. The formation of complex brittle structures in Zr-containing refractory metal MPEAs have been recently investigated [375] and it was reasonably ascribed to the high negative mixing enthalpy of intermetallic phase formation in the Al-Zr binary system. For instance, the enthalpy of formation of the binary Zr_5Al_3-type phase is as low as -51.5 KJ mol^{-1} [376]. Moreover Zr has the highest atom radius (r_{Zr} = 160.25 pm) as compared to

the other constitutive elements (r_{Al} = 143.17 pm, r_{Nb} = 142.9 pm, r_{Zr} = 146.15 pm, r_V = 131.6 pm) and this was argued to play a role in favouring the formation of ordered phases over the formation of competing solid solutions with larger lattice strain and higher lattice distortion energy. A similar role was hypothesized for Cr, which has the smallest atomic radius (r_{Cr} = 124.91 pm) over the other constitutive refractory elements and thus promoting the precipitation of ordered compounds [377].

Senkov *et al.* [377,378] characterized two Al-free CrNbTiZr and CrNbTiVZr alloys with densities around 6.6 g cm^{-3}. These alloys exhibited multi-phase microstructures made by one major bcc disordered solid solution and additional amount of fcc Laves (C15) ordered phase, based on V and/or Cr. Whilst the multi-phase microstructure, the CrNbTiZr and CrNbTiVZr systems showed attractive specific high temperature strength as compared to traditional nickel-base superalloys. They also had some room temperature ductility, high enough to let suggest a potential improvement of the mechanical properties through the modification of the composition and the control of the microstructure.

To date, the $AlMo_{0.5}NbTa_{0.5}TiZr$ alloy with density as low as 7.40 g cm^{-3} has given the highest room temperature compressive strength among the RHEAs, together with 10% compressive elongation. The microstructure of this alloy was initially reported to consist of two disordered bcc phases in the form of interpenetrating nanolamellae [379]. Nevertheless, later on a more detailed analysis has revealed that microstructure consists of a discontinuous disordered bcc (A2) phase in the form of nanometric cuboids rich in Nb, Ti and Ta surrounded by a continuous ordered bcc (B2) phase of nano-lamellae enriched in Al and Zr [295].

This observation allows us to introduce a general comment on the effect of Al in refractory MPEAs. The role of Al in 3d transition metal MPEAs is well established. Al, indeed, acts as a strong bcc-type structure stabilizer. The B2 ordering commonly reported in Al-containing 3d transition metal MPEAs is generally ascribed to the electronic properties of Al, as already discussed in 4.2.1 3d transition metal . However, in refractory metal MPEAs the role of Al is still not well-established. To date, only few studies have reported the formation of the B2 phase in Al-containing RHEAs. Qiu *et al.* [296] experimentally assessed the presence of the ordered phase in the AlTiVCr quaternary alloy demonstrating that for this alloy the ordered B2 phase was thermodynamically more stable than the bcc disordered solid solution. Yurchenko *et al.* [375] also assessed the presence of the B2 phase in the AlTiVNb alloy, apparently refusing outcomes from Stepanov *et al.* which did not find any ordering in the bcc structure of the same alloy [293,380]. Together, these ambiguities suggest that limitations of experimental techniques used for structure analysis might lead to misleading outcomes. High quality of XRD data and more detailed investigations (i.e. TEM) are required in order to assess the presence of B2 ordering in Al-containing RHEAs and to correctly assess phase constitution in Al-containing RHEA [375].

Among the refractory MPEAs, the AlTiVNb alloy is characterized by the lowest density (5.59 g cm^{-3}**)**. In the as-cast condition, this system consists of a single-phase B2 ordered crystal structure with dendrite/interdendrite morphology

and dendrite cores enriched in Nb and depleted in Al and Ti. It has high σ_y at room temperature but limited ductility (around 5%) and brittle fracture. However, compressive strength is surprisingly maintained up to 800 °C, outperforming behavior of some multiphase-structure refractory MPEAs (CrNbTiVZr, CrNbTiZr, $Al_{0.3}NbTaTi_{1.4}Zr_{1.3}$, $Al_{0.5}NbTa_{0.8}Ti_{1.5}V_{0.2}Zr$) [293]. The unusual superior mechanical properties at high temperature of AlTiVNb with respect to the Zr and Cr-containing refractory MPEAs were ascribed to the larger amount of Al, which increases the compressive strength of the alloy by forming stable and strong interatomic Al-TM bonds (TM = Nb, Ti, V) [379] but at expenses of room temperature ductility. Controlling the Al concentration has then been proposed for tailoring mechanical properties in refractory MPEAs and limiting their room temperature compressive brittleness.

As already anticipated, only few publications report tensile properties for RHEAs, including the quaternary HfNbTiZr [180] and quinary HfNbTaTiZr [366]. Table 27 summarizes phase constitution and mechanical properties for some of the most investigated refractory MPEAs produced by casting route.

Table 27. List of various as-cast refractory metal MPEAs with different phase constitution, density, microhardness and compression testing results.

Alloy	Phase constitution	ρ (g cm^3)	HV	σ_y (MPa)	ε %	Ref.
MoNbTaW	Bcc	13.75	460	1058	2.6	[370]
MoNbTaVW	Bcc	12.36	530	1246	1.7	[370]
TiMoNbTaW	Bcc	12.20	499	1343	14.1	[371]
TiMoNbTaVW	Bcc	10.96	510	1515	10.6	[371]
NbTiVZr	Bcc + Laves	6.49	380	1320*	4.2*	[373]
$Al_{0.5}$NbTiVZr	Bcc + Laves	6.04	470	960*	4*	[373]
AlNbTiVZr	Bcc + Laves	5.79	540	1080*	2.2*	[373]
$Al_{1.5}$NbTiVZr	Bcc + Laves	5.55	620	-	0	[373]
CrNbTiZr	Bcc + Laves	6.67	418	1260	6	[378]
CrNbTiVZr	Bcc + Laves	6.57	481	1298	3	[378]
$AlMo_{0.5}NbTa_{0.5}TiZr$	Bcc + B2	7.40	591	2000	10	[379]
$Al_{0.3}NbTaTi_{1.4}Zr_{1.3}$	Bcc + bcc	8.18	489	1965	5	[381]

$Al_{0.5}NbTa_{0.8}Ti_{1.5}V_{0.2}Zr$	Bcc + bcc	7.42	499	2035	4.5	[381]
AlTiVNb	B2*	5.59	448	1000*	6*	[293, 380]
AlTiVCr	B2	5.06	500	-	-	[296]
HfTaNbTiZr**	bcc	9.94	-	1145	9.7	[366]
HfNbTiZr**	bcc	8.40	-	879	14.9	[180]

* After annealing treatment

** Tensile data

Scientific and technological interest to the high temperature oxidation resistance of refractory metal MPEAs is still rather limited compared to the attention given on the alloy development for improving mechanical properties [382]. The oxidation resistance ability of refractory MPEAs represents a potential obstacle to the application of these materials as high-temperature structural alloys.

Conventional refractory alloys have in fact extremely poor oxidation resistance at high temperature. Refractory Ti, Zr and Hf elements have the highest thermodynamic activity towards oxygen and refractory V, Nb and Ta elements also strongly oxidize at temperatures above 400 °C [383]. Oxidation of V produces V_2O_5 oxide with low melting point (690 °C) and boiling point (1750 °C), which fuses or volatilizes at high temperature producing an unstable and/or porous oxide scale. Continuous oxygen reaction at the metal-oxide interface is then induced, resulting in the acceleration of the oxidation process [382]. Diversely, Nb alloys form an oxide that is stable at high temperature but with high solubility and diffusivity of oxygen and thus detrimental [384]. Oxidation of conventional Nb alloys occurs in fact rapidly and protective coatings are generally required.

Alloying with stable oxide forming elements such as Al, Cr, and Si has been used in the past to enhance the oxidation resistance of conventional refractory alloys. However, the addition of such elements requires a compromise, since Al, Cr and Si are very chemically active towards other elements and tend to promote the formation of brittle intermetallic compounds such as Nb_3Al, $NbCr_2$ and Nb_5Si_3 detrimental for room temperature ductility/toughness [385]. The introduction of the refractory MPEA concept is thought to be promising in this regard.

Table 28 lists the weight gain per area for some commercial refractory alloys and refractory metal MPEAs. With respect to conventional refractory alloys, oxidation resistance of refractory metal MPEAs can be improved.

For instance, the AlCrMoTaTi refractory HEA showed good oxidation behavior, with the lowest specific weight gain per area reported to date for a refractory HEA and a parabolic oxidation kinetics law. Despite the high amount of refractory elements, indeed, AlCrMoTaTi refractory HEA forms a protective dense and compact alumina scale after air exposure at 1000 °C for 48 h, which obstacles the evaporation of detrimental Mo oxides detected in the metallic substrate [386]. The $CrMo_{0.5}NbTa_{0.5}TiZr$ refractory HEAs, with a near parabolic weight gain

dependence, gave a mass change in air after 100 h exposure at 1000 °C significantly lower than some commercial Nb alloys as well as NbSiMo and NbSiAlTi refractory materials, whilst the scale consisted of many complex oxides [387,388]. Due to the highly allowing, oxygen diffusion in the $CrMo_{0.5}NbTa_{0.5}TiZr$ refractory HEAs was found to be two orders of magnitude lower than in pure Nb, contributing in improving the oxidation resistance [387,389]. The oxidation resistance of Ti-6Al-4V substrate at 800 °C in air was significantly improved through the deposition of a AlTiVCrSi HEA coating which formed a dense and adherent scale of SiO_2, Cr_2O_3, TiO_2 and Al_2O_3 oxides [360].

Nevertheless, a crucial point of the research into refractory HEAs is represented by the compromise between high oxidation resistance and low ductility/toughness resulting from the macro alloying with stable-oxides forming Al, Cr and Si elements. It was previously reported that alloying with Al and/or Cr often induces precipitation of brittle compounds that make the alloy less ductile. The recently developed $HfNbTaTi_3Zr_2$ refractory HEA showed ductile bcc single phase structure but catastrophic oxidation between 600 °C and 800 °C, because it lacked of elements which formed an adherent protective oxide scale [390,391]. On the contrary, the above introduced $CrMo_{0.5}NbTa_{0.5}TiZr$ refractory HEAs with good oxidation resistance lacked of room temperature ductility due to the presence of brittle Laves phase rich in Cr [392]. Also the AlCrMoNbTi refractory HEAs, despite a slight increase in the oxidation resistance upon the alloying with Si, gave poor mechanical properties and it exhibited no plastic deformation at room temperature [393,394].

Whilst interesting, these results show that there is still lot of work to do before refractory metal MPEAs can be really employed for high temperature applications.

Table 28. Weight gain per area for some commercial refractory alloys and for some refractory metal MPEAs when exposed to air atmosphere at 1000 °C for 24 h.

Material Sample	Weight gain per area (mg/cm^2)	Ref.
Nb-10Si-9Al-10Ti	95	[388]
Nb-8Si-11Al-15Ti	51	[388]
Nb-18Si-26Mo	45	[388]
$CrMo_{0.5}NbTa_{0.5}TiZr$ HEA	50	[387]
AlCrMoTaTi HEA	0.5	[386]
AlCrMoNbTi HEA	4	[393]
AlCrMoNbTiSi HEA	2.1	[393]

The *light metal* MPEAs are a new alloy concept that has been recently introduced. The composition is designed with the aim of developing new low-density structural alloys for the aviation industry. Systems belonging to this alloy family are based on the following elements: Al, Be, Li, Mg, Sc, Si, Sn, Ti and Zn. Very few systems has been investigated to date and none yet exhibits simple microstructure with a promising combination of strength and ductility.

Table 29 compares phase constitutions and mechanical properties for the available systems.

Table 29. List of various light metal MPEAs obtained by casting route with different phase constitution, density, microhardness and compression testing results.

Alloy	Phase constitution	ρ (g cm^{-3})	HV	σ_y (MPa)	ε (%)	Ref.
$Mg_{20}(AlCuMnZn)_{80}$	Hcp + Al-Mn phase	4.29	431	428	3.3	[395]
$Mg_{33}(AlCuMnZn)_{77}$	Hcp + Al-Mn + Mg_7Zn_3	3.26	315	437	3.4	[395]
$Mg_{43}(AlCuMnZn)_{57}$	Hcp + Al-Mn + Mg + Mg_7Zn_3	2.51	255	500	3.7	[395]
$Mg_{45.6}(AlCuMnZn)_{54.4}$	Hcp + Al-Mn + Mg + Mg_7Zn_3	2.30	225	482	4.1	[395]
$Mg_{50}(AlCuMnZn)_{50}$	Hcp + Al-Mn + Mg + Mg_7Zn_3	2.20	178	400	4.8	[395]
AlLiMnZnSn	Al + Zn + Sn + Mg_2Sn/Li_2MgSn	4.23		600	1.2	[396]
$Al_{80}(LiMgZnSn)_5$	Al + Sn + Mg_2Sn/Li_2MgSn	3.05		415	16	[396]
$AlBeFe_{0.5}Si_{0.75}Ti_{1.75}$	Hcp + Si_3Ti + $Al_2(Ti, Fe)$	3.91	911			[397]
$AlLiMg_{0.5}ScTi_{1.5}$*	Fcc → hcp @ 500°C	2.67	591 → 500	-	-	[398]

* Mechanical alloying

Two *light metal* MPEAs systems worth to be mentioned here. Recently, Tseng *et al.* [397] reported the development of a lightweight $AlBeFe_{0.5}Si_{0.75}Ti_{1.75}$ alloy produced by casting method which exhibited a density of 3.91 g cm^{-3} and an exceptionally high hardness of 911 HV, with excellent oxidation resistance at 700 and 900 °C, making it a promising system to further develop for high temperature applications. The as-cast microstructure consists of one major hcp solid solution phase and two minor intermetallic hcp phases. Secondly, to date the lightest single-phase MPEA discovered, corresponding to the $AlLiMg_{0.5}ScTi_{1.5}$ alloy composition, with a density of 2.67 g cm^{-3} and high hardness [398]. The alloy was synthesized by Youssef *et al.* [398] in 2015 through mechanical alloying and it consisted of a nanocrystalline single-phase fcc structure in the as-milled condition and it evolved into a hcp structure after annealing at 500 °C for 1 h. The as-milled powder with

high levels of N and O impurities from the milling process showed a single-phase fcc structure stable up to 800 °C for 1 h.

Whilst promising, the low density $AlBeFe_{0.5}Si_{0.75}Ti_{1.75}$ and $AlLiMg_{0.5}ScTi_{1.5}$ MPEAs lack of any mechanical characterization to date, which would give a measure of their strength and ductility. Further investigation to assess the mechanical response of these novel systems are thus necessary.

4.3 Processing techniques for HEAs

Multi-principal element alloys can be synthesized starting from different states, mainly liquid and solid but also gas and from electrochemical processes [179]. At the present, a wide range of techniques within ingot metallurgy, coating technology or powder metallurgy is thus adopted for processing MPEAs. Obviously, phase selection of MPEA systems cannot be predicted by thermodynamic alone and kinetics effects or solidification conditions characteristic of each processing route are crucial in shaping the final microstructure and in assessing the outcome of the competition between solid solution(s) and intermetallic phases in MPEAs.

Figure 89 visualizes in a pie chart the major processing routes that have been used for processing MPEAs from 2004 to 2018.

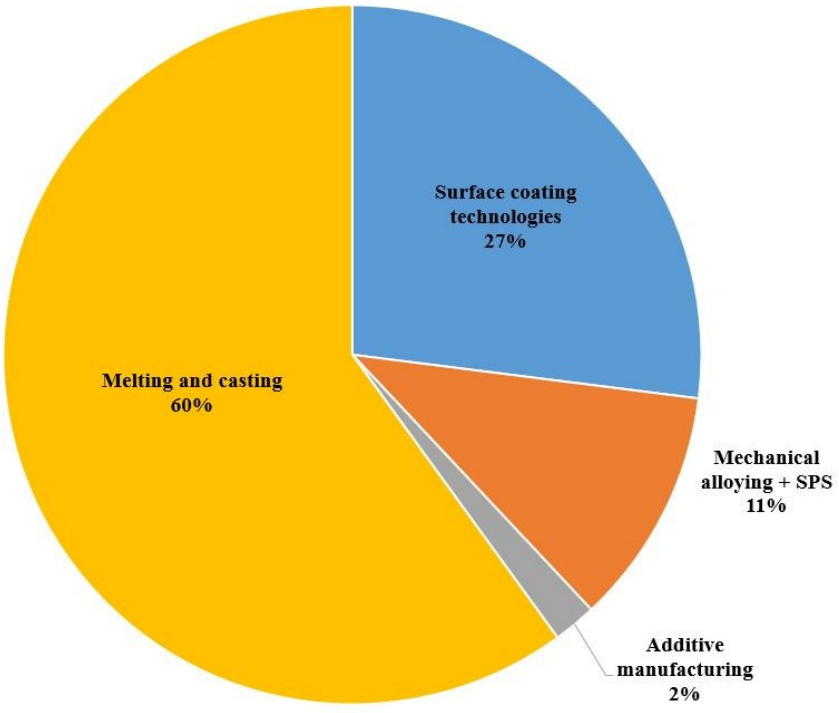

Figure 89. Processing routes used for the synthesis of HEAs between 2004 and 2018. Data gathered from Scopus by searching for "High Entropy Alloys" in the article title, abstract keywords field and limiting the subject area to "Materials Science" and "Engineering" (source: www.scopus.com).

MPEAs have been traditionally processed through vacuum arc or induction melting followed by casting. Most of the phase constitution, properties and influence of alloying element reported in literature and resumed in previous sections were assessed on MPEA systems prepared through casting route. Liquid-state technique based on casting route accounts for more than half of the all production methods, it is time- and cost- efficient and it offers the flexibility of processing most of the elements in the periodic table. Whilst versatile, to produce homogenous bulk MPEAs, the process itself requires lots of control, from the compositional homogeneity of the melt to the solidification conditions and post thermal treatments. Kinetics conditions that realizes during conventional casting at the typical cooling rates of 10-20 K s^{-1} [339] often induce elemental segregation and the development of coarse dendritic and interdendritic microstructures. In MPEAs based on elements with poor chemical affinity, the formation of dendritic/interdendritic structures is exclusively attributed to the differences in their physical properties (i.e. melting point), with the dendrite cores generally consisting of a solid solution phase rich in the elements with the highest melting point [399]. This was observed in characteristic fcc single-phase 3d transition metal MPEAs based on the CoCrFeMnNi system [285] and in many single-phase refractory MPEAs [289,293]. For instance, a dendrite/interdendrite morphology ascribed to compositional microsegregation of high-melting elements formed in the single-phase AlTiVNb refractory MPEA produced by casting route, then homogenized through a post annealing/homogenization treatment (Figure 90) [293].

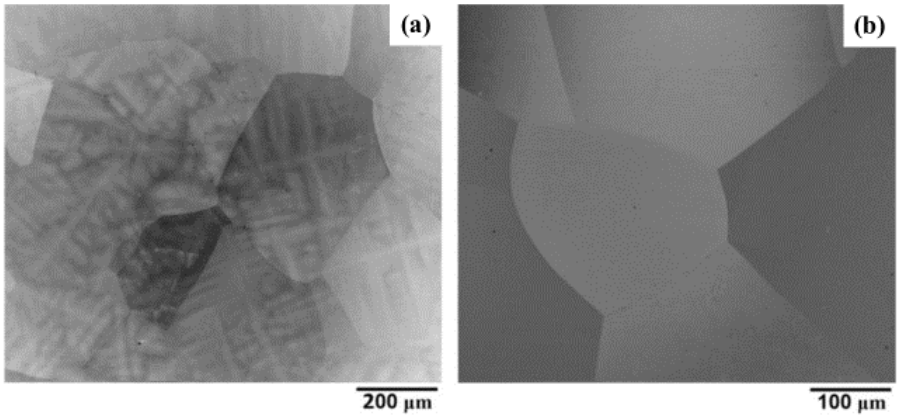

Figure 90. SEM-BSE images of the AlTiVNb alloy (a) in the as-cast condition and (b) after homogenization treatment at 1200 °C/24 h. Dendrite cores (light area) are enriched in high melting Nb and depleted of low-melting Al and Ti, oppositely to the interdendritic regions (dark). Homogenization treatment eliminated dendritic segregations [293].

As already assessed in previous sections, then, multiple phase microstructures may also form in cast MPEAs, for instance in some Al- and/or Cu-containing systems. The AlCoCrCuFeNi MPEA cooled in "normal" conditions formed five phases: the interdendritic regions consisted of a Cu-rich phase and the dendrites cores contained several Cu-rich nanometric precipitates, Al-Ni-rich plates and Cr-Fe rich interplates precipitates [339]. It is evident, in this case, that that the high positive mixing enthalpy of Cu with the other constitutive elements motivated its

prior segregation. The formation of Ni-Al-, Cr-Fe- and Al-Ni-Fe-rich phases at the dendrite regions is not surprising ascribed to the strong attractive interactions among these elements and to the large negative enthalpy of mixing of their binary systems. Alloys exhibiting this type of as-cast multiphase dendritic/interdendritic microstructure are hard to homogenize though annealing treatment and new solid solutions and/or intermetallic phases usually appear [400].

The inherent composition complexity of MPEA systems make the production of homogenous microstructures by casting route complex, aside with the intrinsic shape and size limitations of casting route.

Surface coating technologies (i.e. laser cladding [401], magnetron sputtering [402], RF sputtering [403], plasma spray [404], etc.) have been also traditionally used to synthesize MPEAs. They represent the second most common route and their exploitation has been motivated by the potential of many MPEA systems to find applications as protective coating materials against wear [405], corrosion [406] and/or oxidation [360].

In recent years, solid-state processing based on mechanical alloying (MA) followed by consolidation through spark plasma sintering (SPS) has been extensively used in place of casting methods for obtaining bulk MPEAs. During mechanical alloying, the elemental powder blend is placed in a rotating jar where powder particles are repeatedly deformed, cold-welded, fractured and rewelded by the impact of the grinding balls with the jar walls and the alloying process occurs in severe non equilibrium conditions [103]. These pronounced non equilibrium conditions allow to extend the solid solubility of single elements though a mechanism of enhanced solid-state diffusivity that was well described by Huang *et al.* [407] and to obtain supersatured solid solutions alloy powders with nanocrystalline structures and high chemical homogeneity. Due to the solid-state synthesis, indeed, MA bypasses the potential problems of casting route that is the formation of non-homogenous microstructures with coarse dendrite/interdendrite structures, improving the distribution of the constitutive elements. MA has gained ground over liquid-state synthesis methods also because has made less challenging the processing of MPEA systems based on elements with broad range in their physical properties (i.e. melting temperature or vapour pressure), whose processing by traditional casting route might be difficult, as for some HEAs compositions containing refractory elements [408,409]. Recently, Guo *et al.* [410] synthesized chemically homogenous TiVNbTa refractory HEA powders by MA and Tong *et al.* [411] produced ultrafine MoNbTaW refractory HEA. The authors concluded that the production of chemically homogenous HEA powders by MA combined with any powders consolidation technique, including AM, could be extremely attractive for developing HEAs bulk samples or coatings with customized compositions [411]. MA, in fact, is extremely versatile because it offers high composition flexibility, it allows to synthesize small amount of powders and it provides thus extremely high flexibility when experimenting novel compositions.

However, care must be taken to the subsequent consolidation process if the as-milled structure of powders needs to be retained, especially in those MPEA systems in which strong attractive and/or repulsive interaction among the elements exist or

the high atomic size difference among the element may induce the formation of intermetallics. MA produces a metastable supersatured solid solution, which may evolve during the consolidation step. Praveen *et al.* [412] characterized the structure of AlCoCrCuFe MPEA prepared by MA + SPS. A major fcc phase was found in the as-milled powder, which evolved in a Cu-rich fcc phase, a ordered bcc phase (B2) and intermetallic σ phase rich in Cr after SPS. Densification at high temperature resulted in more stable phases by the segregation of Cu and Cr from the supersatured solid solution.

Among the liquid-state fabrication methods, in the last few years, advanced AM technologies such as Laser Powder-Bed Fusion (LPBF), Electron Beam Melting (EBM) and Direct Energy Deposition (DED) technologies based on blown-powders systems have been also used for developing bulk HEAs.

From an industrial point of view, these technologies allow to control the microstructure in a site-specific manner thanks the localized energy source and to manipulate the microstructure across a broader length scale as compared to traditional casting route [60]. It was said that the high level of local process control and the high solidification rates of AM would be beneficial for the development of MPEAs because might enhance the chemical homogeneity, refine the microstructure and impede the formation of multiple phases [181]. Additionally, these technologies allow to fabricate components with more sophisticated shapes. In 2015, Brif *et al.* [181] conducted a pioneering work on LPBF of FeCoCrNi HEA, which successfully demonstrated that LPBF can be used for fabricating HEA with single phase fcc structure and tensile strength and ductility comparable to other engineering materials, like stainless steels, using pre-alloyed gas atomized powders.

However, the following aspects should be considered when processing HEAs by AM technologies [415]:

- Although generally high, the heating and cooling rate can locally vary sensibly during the AM process, due both to the Gaussian energy profile of the laser beam and to the cyclic thermal regime during the process. Under these circumstances, the formation and/or transformation of different phases can be induced in the processed HEA, affecting the expected phase constitution.

- In some HEA alloy powders, due to broad ranges into physical properties among the constitutive elements, the preferential vaporization of the most volatile elements, along with creating turbulences in the melt pool, can modify the chemical composition, depressing the chemical homogeneity and deteriorating the properties of the fabricated material.

- Although most of the AM processes are carried out in inert gas atmosphere, the tiny residual amount of oxygen within the process chamber can be sufficient to induce the formation of oxides or undesired intermetallic phases.

The studies available on the microstructure development of MPEAs at high solidification rates mostly derive from coating technologies, i.e. splat quenching or laser cladding. In 2001, Singh *et al.* [339] and Zhang *et al.* [413] investigated the role played by the cooling rate in the competition between solid solution(s) and intermetallic phases in MPEA systems. Figure 91 gives a schematic representation of the of microstructure formation that they assessed under different kinetics conditions. From a thermodynamic point of view, the high configurational entropy of the MPEAs at the molten stage would potentially facilitate the formation of high entropy disordered solid solutions, in place of ordered compounds [302]. When the cooling rate is low, as occurs during normal casting, irrespective to the thermodynamics, a dendritic microstructure with micro-segregation of the elements develops. In addition, in the interdendritic regions, an unstable disordered solid solution may form because of the constituent deviation from the nominal melt composition, with the resulting decrease in the entropy of mixing. If the cooling rate is too slow, then, intermetallics may develop in place of solid solution. Rapid solidification produces deviation from the equilibrium and metastable phases may form [414]. If the cooling rate is high enough, a disordered solid solution with complete solute trapping and equiaxed microstructure develops. Singh *et al.* [339,413] gave a detailed kinetics of microstructure formation for the AlCoCrCuFeNi MPEA solidified under two different cooling regimes. On the one hand, rapid solidification of the AlCoCrCuFeNi by splat quenching (10^6-10^7 K s^{-1}) produced a single-phase alloy with bcc structure and hindered the development of any multiple phase microstructure. On the other hand, the as-cast "normal" cooled alloy exhibited two fcc + several bcc phases.

This work demonstrated that for some MPEAs, a homogenous single-phase solid solution could only form at relatively high cooling rates, in which the high entropy of the molten stage may be retained at ambient temperature in a metastable condition.

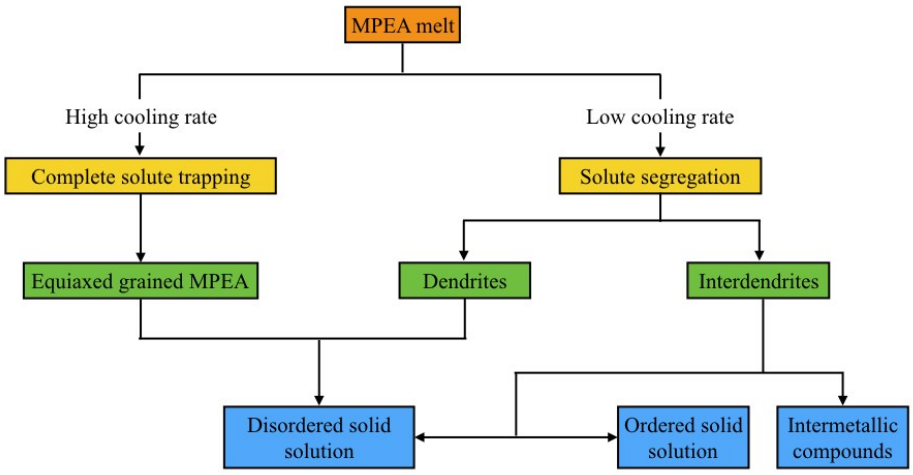

Figure 91. Schematic representation of the microstructure and phase selection of MPEA melts cooled under different kinetics conditions [339,413].

4.3.1 *In-situ* alloying of HEAs from powder mixtures by AM technologies

To date, the processing of HEAs by AM technologies has been mostly addressed to the use of alloy powders obtained by gas-atomization [181,197,416–422]. However, for some material compositions, the obtainment of a homogenous melt is intrinsically challenging, making the production of prealloyed powders either not possible or extremely expensive. This is particularly true for refractory HEAs, for which the broad differences in the physical properties of the constitutive elements at high temperatures make hard the production of homogenous melts. Moreover, the high oxidation susceptibility of refractory elements makes challenging the production of non-oxidized products, even under high-vacuum environments during high temperature arc-melting [423].

For these reasons, to date, the processing of HEAs by AM technologies has been mostly addressed to the use of 3d transition metals MPEAs [424], for which the production of a homogenous melt and the subsequent gas-atomization process are less challenging than for refractory HEAs, because of the similarities into physical properties among the constitutive elements. The poor availability and the high costs of gas-atomized MPEAs alloy powders can be said to hinder the development of customized HEAs compositions for AM, particularly of refractory ones.

In order to overcome issues related to the gas-atomization of HEAs with customized composition, to date some authors have reported trials for *in-situ* alloying by AM. For instance, Ocelik *et al.* [425] reported that laser-processing was a versatile tool for synthesizing HEAs from elemental powder mixture by AM laser cladding technology. Nevertheless, critical issues in their approach were related to the differences existing into sizes, shapes, densities and melting points among the constitutive elemental powders, which hindered from the obtainment of a homogenous microstructure with equiatomic composition. In fact, whilst the use of high-power laser up to 650 W, residual unmelted Tantalum particles existed in the laser-clad AlCrFeNiTa coating obtained from elemental powders mixture. Moreover, dramatic evaporation of Al took place due to the high energy-input and multiple phases formed. Dobbelstein *et al.* [426] was the first to report direct metal deposition (DMD) of MoNbTaW refractory HEA from blown mixture of elemental powders. The authors pointed out on the challenging aspects of laser parameter selection when manufacturing weld tracks from an equiatomic mixture of many different powders with broad ranges into physical properties and/or powder morphologies. Even in their study, deviations from the equiatomic composition of the precursor powder mixture were assessed in the consolidated material. The single laser track with a pulsed laser power as high as 800 W produced an inhomogeneous and rough weld track with incomplete powders mixing and many residual unmelted powder particles. However, a more homogenous mixing of the powder particles was achieved when the weld track was remelted up to three times at higher laser power. Zhang *et al.* [427] processed MoNbTaW HEAs from elemental powders mixture by LPBF. The authors concluded that LPBF was a feasible way of

manufacturing refractory HEAs by elemental powder mixture. Although samples were porous (no process optimization for density was conducted), in fact, a bcc solid solution was assessed after LPBF. Nevertheless, slight deviations from the equiatomic composition of the powders mixture were still found in the consolidated material, which the authors mostly related to the different melting point and density among constitutive elements but also to the different powder energy absorptions, metal liquid viscosities, burning losses, etc.

The present chapter gives an overview of the alloy design opportunities introduced by the HEA design concept, whilst significant studies are still required for gaining confidence with the physical metallurgy of these compositionally complex alloy systems. The kinetics can play a significant role in determining the outcome of the competition between solid solution and intermetallics in HEAs, justifying the recent interest in adopting AM technologies for processing HEAs. Nevertheless, gas-atomization of HEAs compositions, especially those based on refractory elements, can be extremely challenging and - more importantly – does not allow compositional flexibility in tailoring the HEA composition. The limitations posed by the gas-atomization of HEA powders for AM technologies have motivated, recently, the interest in processing powders mixtures containing refractory species for *in-situ* alloying them. Although the high potential, the processing is itself technologically challenging due to the presence of many elements with different physical and powder-related properties. In this regard, mechanical alloying (MA) could represent a promising processing route for the production of compositionally and morphologically homogenous HEAs prealloyed powders containing refractory elements to process by AM technologies.

Chapter 5

Development of two HEAs through Single Scan Track (SST) experiments on different powders systems

The present chapter reports the studies conducted for the assessment of the alloying behaviour of two HEAs powders, namely AlTiCuNb and AlTiVNb, produced without resorting to expensive gas-atomized alloy powders and without consuming large amount of material. The aim of the study is that of investigating the feasibility of producing Single Scan Tracks (SSTs) of selected HEAs based on refractory species using different powder systems, namely mixtures of the elemental constitutive species or alloy powders synthesized by mechanical alloying. The optimization of these techniques could contribute in accelerating the development of HEAs for LPBF.

The first part of the study concerns the description of the criteria adopted for selecting the alloy systems. Then, the optimization of the milling parameters during mechanical alloying for producing the chemically and morphologically homogenous HEAs powders is carried out. The second part of the study concerns the comparative analysis on the alloying behaviour of the mixed and milled powders when irradiated with the laser beam during the formation of the SSTs.

5.1 Design of the composition

5.1.1 *Palette of elements* for targeted HEAs

The methodology applied to select the MPEA systems here investigated was derived from the paper by Miracle *et al.* [290]. The authors developed a master list of elements for the exploration and development of MPEA systems for structural applications.

For the present work, a palette of seven elements with low density and/or refractory properties was selected in order to design lightweight and heat-resistant MPEAs. The selection was addressed to elements available into powder form and with the criterion of being lighter than Cu ($\rho < 8.96$ g cm^3).

The following palette of elements was selected: Al, Ti, V, Mn, Fe, Cu, Nb. The main physical properties of the elements are reported in Table 30.

Table 30. Density (ρ), melting point (T_m), atomic radius (r), atomic weight (A) and crystal structure for constitutive elements in the selected palette.

Element	ρ ($g\ cm^{-3}$)	T_m (°C)	r (pm)	A ($g\ mol^{-1}$)	Crystal structure
Al	2.70	660	143.17	27.0	A1 (Fcc)
Ti	4.50	1668	146.15	47.9	A3 (hcp)
V	6.12	1910	131.6	50.9	A2 (Bcc)
Mn	7.47	1246	135	54.9	A12 (cl58)
Fe	7.88	1538	124.12	55.9	A2 (Bcc)
Nb	8.57	2477	142.9	92.9	A2 (Bcc)
Cu	8.94	1085	127.8	63.6	A1 (Fcc)

5.1.2 Screening criteria for the selection of the HEAs

The second stage of the design step was aimed to identify systems with the potential of forming HEAs. This step was conducted by calculating the thermodynamic parameters, namely entropy of mixing ΔS_{mix}, enthalpy of mixing ΔH_{mix} and atomic size difference δ, used for determining the formability of solid solutions in HEAs.

A desktop study was conducted by combining the elements of the above-presented *palette of elements* into equiatomic alloy compositions constituted by 4 or 5 elements, in order to assess whether the multi-component alloy systems designed would have exhibited probability to form a single-phase solid solution or not. For doing so, the empirical phase-prediction rule developed by Yang *et al.* [321] was used. The rule is based on the values of the dimensionless parameters ω and δ defined as:

$$\omega = \frac{T_m \Delta S_{mix}}{|\Delta H_{mix}|} \tag{5.1}$$

$$\delta = \sqrt{\sum_{i=1}^{n} c_i \left(1 - \frac{r_i}{\sum_i^n c_i r_i}\right)^2} \tag{5.2}$$

For any information on the empirical rule and the meaning of the above-reported equations, the reader is invited to look at eq.4.6, eq.4.8, eq.4.9 and eq.4.11.

According to the above-reported empirical phase prediction rule, single-phase solid solutions are expected when ω > 1.1 and δ < 6.6. Table 31 lists the MPEA

systems fulfilling the empirical criterion and thus exhibiting a strong possibility to form a single-phase solid solution.

It is worth to note that the screening of the alloy systems was conducted also by excluding MPEAs having a theoretical density (ρ_{th}) higher than 6 g cm^{-3}. The theoretical density of the alloy system was estimated using a rule of mixture assumption of a disordered solid solution and calculated as follows [289]:

$$\omega = \frac{\sum_{i=1}^{n} c_i A_i}{\sum_{i=1}^{n} c_i \frac{A_i}{\rho_i}} \tag{5.3}$$

Where n is the number of alloying elements, c_i the atomic concentration of the ith component, A_i is the atomic weight and ρ_i is the density of the element i, respectively.

According to the calculated values of δ and ω for the MPEA systems reported in Table 31, the AlTiCuNb and AlTiVNb MPEA systems were selected for this work as they revealed a strong possibility to form a BCC solid solution.

Additional thermodynamic and electronic parameters for the selected MPEAs system are listed in Table 32.

Table 31. List of some physical and thermodynamics parameters, namely theoretical density ρ_{th}, atomic size difference δ and parameter ω, for selected MPEA systems having theoretical density lower than 6 g cm^{-3}, δ < 6.6 and ω > 1.1. The systems in bold were selected for the present work.

System	ρ_{th} (g cm^3)	δ %	ω
AlTiVCu	5.25	5.59	1.40
AlTiVMnFe	5.45	5.65	1.26
AlTiVNb	5.50	3.94	1.38
AlTiVMnCu	5.62	4.74	1.72
AlTiVFeCu	5.68	5.92	1.83
AlVMnFe	5.75	5.13	1.38
AlTiVMnNb	5.80	2.53	1.61
AlTiVFeNb	5.86	5.50	1.39
AlTiMnFeCu	5.90	5.09	1.62
AlVMnCu	5.99	4.22	2.47
AlTiCuNb	6.00	5.11	1.52

Table 32. Additional Thermodynamic and electronic parameters of the equaitomic AlTiCuNb and AlTiVNb systems investigated in this work.

Alloy	ρ_{th} [g cm^{-3}]	VEC	δ	ΔH_{mix} [kJ mol^{-1}]	ΔS_{mix} [J K^{-1} mol^{-1}]	ω
AlTiCuNb	6.0	5.75	5.11	-13.25	11.53	1.52
AlTiVNb	5.5	4.25	3.94	-16.25	11.53	1.38

5.2 Synthesis of AlTiCuNb and AlTiVNb HEAs powders by high energy mechanical alloying (HEMA)

As already anticipated, this part of the study will go through the optimization of the milling parameters for producing chemically homogenous AlTiCuNb and AlTiVNb HEAs powders by HEMA.

Because of the different chemical composition of AlTiCuNb and AlTiVNb MPEA systems, it is expected that their alloying behaviour during mechanical alloying would be different. As broadly discussed in Chapter 4, in fact, the phase constitution of HEA systems is strongly affected by the mutual interactions existing among its constitutive species. These interactions are strongly related to the physical as well as thermodynamic properties of each element. For this reason, in order to be as clearer as possible during the presentation and discussion of the results, the MPEA systems will be described one at a time. For each system, the results of the mechanical alloying synthesis will be firstly presented and then discussed basing on the literature available on systems with similar composition and then the conclusions will be drown.

Before doing that, the following section will go through the preliminarily characterization of the elemental powders used within this work, the description of the HEMA technique, the equipment used, the main process variables during mechanical alloying as well as the experimental processing condition adopted for the synthesis of AlTiCuNb and AlTiVNb HEAs powders by HEMA.

5.2.1 Materials and HEMA system

5.2.1.1 Pure elemental powders

Commercial raw elemental powders were used as starting materials for synthesizing the equiatomic AlTiCuNb and AlTiVNb MPEAs powders. Table 33 lists the main features of each elemental powder, such as purity and particle sizes, so as declared by the supplier.

Table 33. Characteristics of the elemental powders used in this work.

Element	Purity (%)	Particle size (µm)	Supplier
Al	99.5	<45	Alpha Aesar
Ti	99.2	15-45	TLS technik
Cu	99.9	5-25	Sandvik
Nb	99.8	<45	ABCR
V	99.9	<45	Nmd

The FESEM images of the Al, Ti, Cu, Nb and V raw elemental powders reported in Figure 92 revealed that the precursor elemental powders had different morphologies. Al powder had an elongated shape; Ti and Cu powder particles were spherical and Nb and V powder particles are characterized by plate-like morphology and sharp edges. It is worth to note that it is industrially difficult to produce spherical particles of refractory Nb and V elements as well as of pure Al.

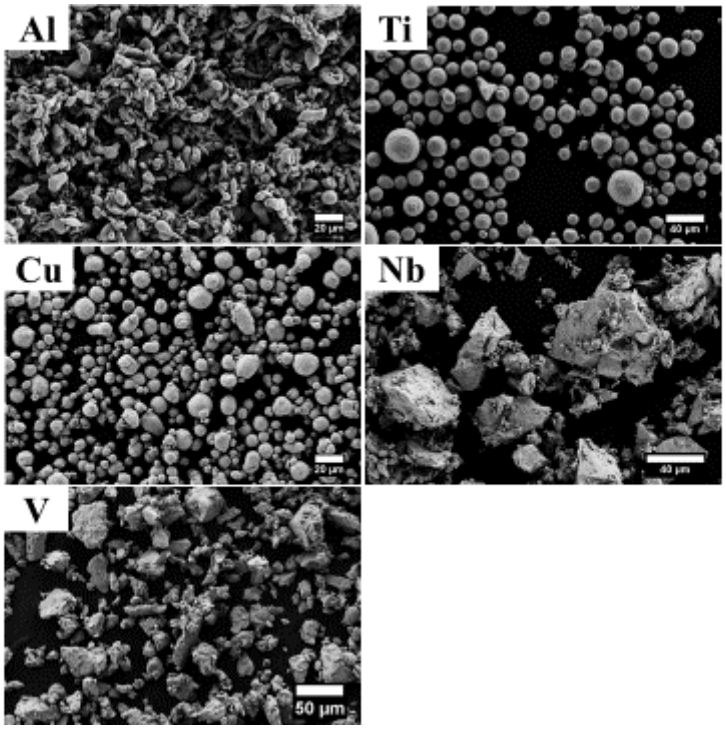

Figure 92. FESEM images of the elemental powders used in this work.

The elemental powders mixtures of AlTiCuNb and AlTiVNb corresponding to the equiatomic compositions were obtained by weighting the individual elemental powders and then by mixing them together. The weight percentages of each elements required to have an equiatomic proportion among the species is reported in Table 34.

Table 34. Weight percentage of each element (wt.%) necessary to produce equiatomic alloy compositions.

Alloy system	Al (wt.%)	Ti (wt.%)	Cu (wt.%)	V (wt.%)	Nb (wt.%)
AlTiCuNb	11.75	20.75	27.50	-	40
AlTiVNb	12.35	21.90	-	23.25	42.5

Figure 93 and Figure 94 show the equiatomic mixtures of elemental powders constituting the AlTiCuNb and the AlTiVNb systems, respectively. The row elemental particles can be easily recognized by their morphologies and/or sizes.

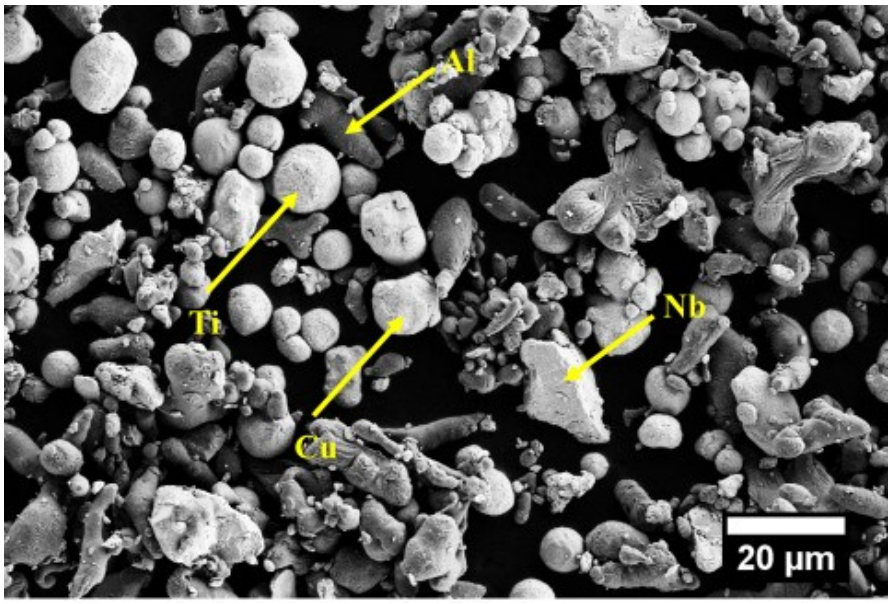

Figure 93. FESEM image of the AlTiCuNb equiatomic raw powder mixture.

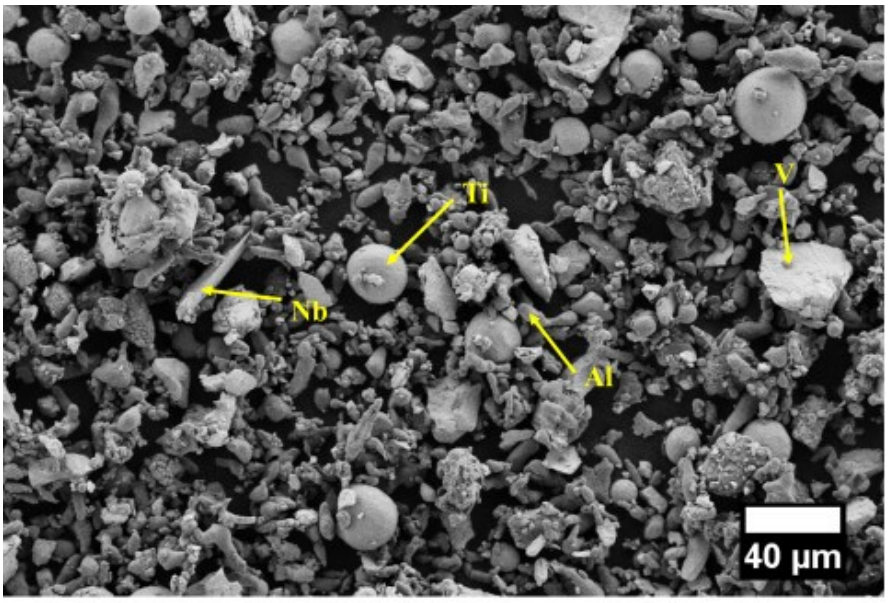

Figure 94. FESEM image of the AlTiVNb equiatomic raw powder mixture.

5.2.1.2 High Energy Mechanical Alloying (HEMA) system

Mechanical alloying was conducted using a Pulverisette 7 (Fritsch, Germany) planetary high-energy ball mill, working with two stations and few grams of powder at a time (Figure 95a). In the planetary ball mills, the vials rotate with a planet-like movement. The vials are placed on a rotating support disk and then a drive mechanism allows them to rotate around their own axes. The combination of the centrifugal forces produced by the rotation of the vials around their own axes and by the rotation of the support disk produces a resulting force acting on the vials content, constituted of the grinding balls and the powder to be ground. Since the supporting disk and the vials rotate in opposite directions, the centrifugal forces alternatively act in opposite directions. As consequence, the grinding balls run down the inner wall of the vials and then the grinding balls and the powder to be ground lift off and travel freely through the inner chamber of the vials, colliding against the opposite wall, as schematically shown in Figure 95b. The force of impact plastically deforms the powder particles trapped between the ball and the wall or between two balls (Figure 95c) yielding work hardening and fracture. During the process the powder particles cyclically flatten, cold weld, fracture and reweld bringing to significant variation into their size and/or morphology [103].

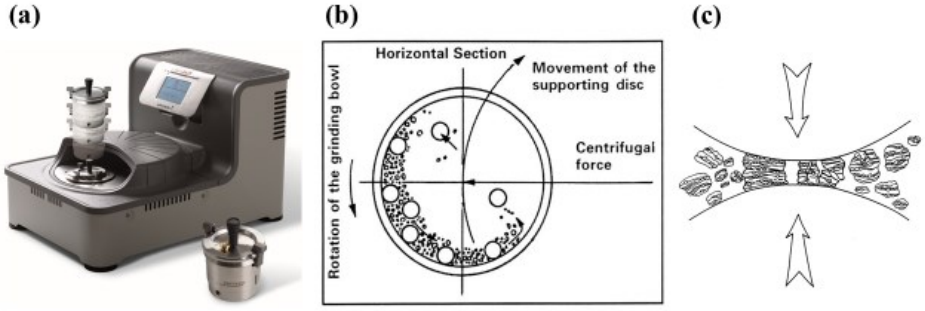

Figure 95. (a) Pulverisette 7 ball milling equipment used for the synthesis of HEAs, (b) schematic of the ball motion within the mill and (c) collision between two balls and the powder mixture during HEMA [103].

Mechanical alloying is a complex process involving the optimization of a large number of variables in order to achieve the desired product. The main variables are [103]:

- Milling container
- Milling speed
- Milling time
- Type, size and size distribution of the grinding medium
- Ball-to-powder weight ratio (BPR)
- Milling atmosphere
- Process control agent (PCA)

The material adopted for the *milling container* is important because it affects the extent of contamination of the grinded powders. Due to the impact of the grinding medium with the inner walls of the vials, indeed, some material may get incorporated into the powder. This occurs when the material of the vial is different from that of the powder. The most common type of materials used for grinding vials are hardened steel, hardened chromium steel, tempered steel, stainless steel and WC-Co.

The *milling speed* directly acts on the energy transferred to the powders: the higher the milling speed the higher the energy input. However, care must be taken in increasing excessively the milling speed, in order to limit the temperature rises within the vials, which may accelerate solid-state transformations and/or decomposition of supersatured solid solutions and may enhance powder contamination.

The *milling time* is by far the most important parameter and it is normally set so to reach a steady state between cold welding and fracturing of the powder particles. The time required needs to be optimized according to the intensity of milling, the BPR and the temperature of milling. It is worth to note that the extent of contamination of powder as well as the occurrence of undesirable phases increase when the powder is milled for times longer than required [103].

Materials used as the *grinding medium* are the same of those used for the milling container. The type of material of the grinding medium as well as its size affect the milling efficiency. In particular, the denser and the larger is the grinding medium, the higher will be the impact force on the powder and thus the energy transferred. The collision energy can also be increased by using balls with different diameters, which increase the shearing forces among the powder and the grinding medium.

The *ratio of the weight of balls to the powder* (BPR) is an important milling variable. The BPR value affects the amount of energy transferred by the balls to the powder, so that the higher is the BPR the shorter will be the time required to a powder for achieving a particular phase. A ratio of 10:1 is commonly used.

The main effect of the *milling atmosphere* is to prevent contamination and/or oxidation of the powder. For these reasons, milling process usually occurs in vials either filled with an inert gas, such as high purity argon, or evacuated. Usually, loading and unloading of the powders into vials, as well as powder sampling, are carried out inside a glove box with a controlled atmosphere.

The *process control agent* (PCA), also referred as surfactant or lubricant, is usually added to the powder mixture with the major function of reducing the cold welding of ductile powders, which causes excessive agglomeration of powder particles and poor alloying among the different species. PCA, indeed, adorbs onto the powder particles surface contributing in reducing the adhesion of powders on balls and inner surface of the vials as well as in minimizing the contamination and oxidation of powder particles, especially in the early stages of milling. Most of the PCAs are organic compounds (i.e. stearic acid) and are added in quantity of 1-5 wt.% of the powder charge.

5.2.1.3 Experimental condition for HEMA

For the AlTiCuNb and AlTiVNb compositions to synthesize, 40 g of equiatomic powder mixture of each composition were prepared.

At once, two batches of 20 g of each elemental powder mixture were added into the stainless steel vials of 80 ml, containing 24 and 11 stainless steel balls as the balling media with a diameter of 10 and 11 mm, respectively. The BPR was 6:1. 1.5 wt. % of 12-hydroxystearic acid ($C_{18}H_{36}O_3$), a modification of the most common stearic acid, was loaded in the vial as PCA.

The mixtures were subjected to dry milling in the Pulverisette 7 (Fritsch) planetary ball mill at the constant speed of 450 rpm up to 24 hours, with 10 minutes resting intervals after every 15 minutes of active milling, in order to let the system cools down. Powders mixtures were initially milled with no interruption and then samplings of powders were taken for characterization. Handling, loading and sampling of powders were conducted inside an argon-filled glove box in which the oxygen concentration was kept below 600 ppm.

The structure and qualitative phase analysis of powders before and after HEMA were investigated by conventional XRD analysis. The evolution into the morphology of powders during HEMA was assessed by means of FESEM equipped EDX for elemental analysis. EDX mappings were carried out in order to assess the alloying progress as well as the distribution of the elements in the powder particles during HEMA. The detailed description of the experimental equipment as well as the testing conditions were included in Appendix A.2.1 Powder characterization.

5.2.2 HEMA of AlTiCuNb

5.2.2.1 XRD and compositional analyses of AlTiCuNb milled powders

The XRD spectra reported in Figure 96 visualize the transformations that occurred during milling in the starting AlTiCuNb powder mixture.

The XRD pattern of the raw powder mixture (0 h) displayed the superimposition of the pure component reflections. Peaks were sharp and aligned to the PDF reference positions, as expected for highly crystalline elemental powders.

After the powder was grinded for 8 h, the intensities of the diffraction peaks of all the components dramatically decreased, peaks broadened and weakest reflections became so diffuse that they were no longer visible. After 8 h of milling, the individual lines of Al were the first to disappear, designating the beginning of the alloying process. To be more precise, the second reflection belonging to Al merged to the first reflection of Cu and formed a single peak at around 44°, which remained visible up to 16 h of milling. This peak was indexed as F_{Cu} and it represents a Cu-rich phase. There have been many studies reporting the formation of such Cu-rich phase in Cu-containing multi-principal element alloys. Praveen *et al.* [412] and Maulik *et al.* [428] observed the formation of a major bcc phase with minor content of fcc Cu-rich phase on the quinary AlCoCrCuFe and quaternary AlCrCuFe alloy synthesized by HEMA, respectively. The formation of such Cu-

rich phase in many HEAs compositions is generally rationalized by referring to the strong repulsive interaction of Cu with many 3-d transition metals, not surprisingly described by the positive enthalpy of mixing of the atomic pairs based on Cu. For instance, in the AlTiCuNb system, the Cu-Nb atomic pairs has an enthalpy of mixing of 3 KJ mol^{-1} [316], designating thus a low tendency to solid-state solubility. In fact, from a thermodynamic point of view, the only atomic pairs with high tendency to solid-state solubility are those with mixing enthalpy around zero or slightly negative [315]. This thermodynamic effect might account for the formation of the F_{Cu} phase since the beginning of the alloying process.

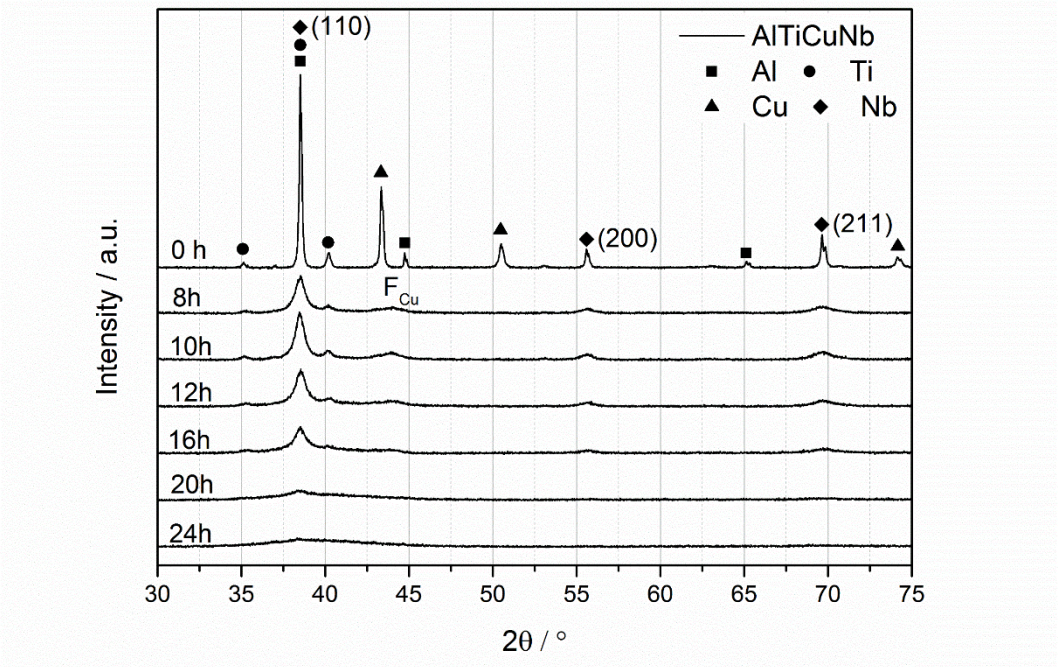

Figure 96. The X-ray diffraction (XRD) patterns of the raw elemental AlTiCuNb powder mixture and milled AlTiCuNb powders at increasing milling time (t = 8-24 h).

A closer look at the enlargement of the XRD profiles of milled powders presented below in Figure 97 revealed that after 8 h of milling there were residual diffraction peaks belonging to hcp Ti at approximately 35° and 40°. When the grinding time increased to 10, 12 and 16 h, the phase constitution of the alloy did not change but the structure further refined, as it was clear from the peaks broadening. With further milling up to 20 h, the reflections belonging to Ti disappeared as well as that belonging to F_{Cu}, whilst it is very difficult to state if they either disappeared or could no longer be distinguished because of the abnormal broadening of the (110) reflection of Nb.

However, it can be stated that after 20 h of milling, the AlTiCuNb powder consisted of a bcc solid solution based on Nb as main phase (β phase in Figure 97). The preferential dissolution of the elements into Nb structure could be rationalized by considering that the bcc structure is more open (packing factor 0.68) with respect to the close-packed fcc and hcp crystal structures of Al, Cu and Ti (packing factor 0.74) and hence it may accommodate other elements easier and without significant expansion of the crystal structure [429]. As consequence, elements were observed

to dissolve preferentially into Nb yielding the formation of a bcc HEA powder after 20 h of milling.

After 24 h, powder apparently turned into an amorphous structure (α phase in Figure 97). It is well reported in literature that the severe plastic deformation achieved during HEMA might facilitate the formation of amorphous phase after prolonged milling times [430].

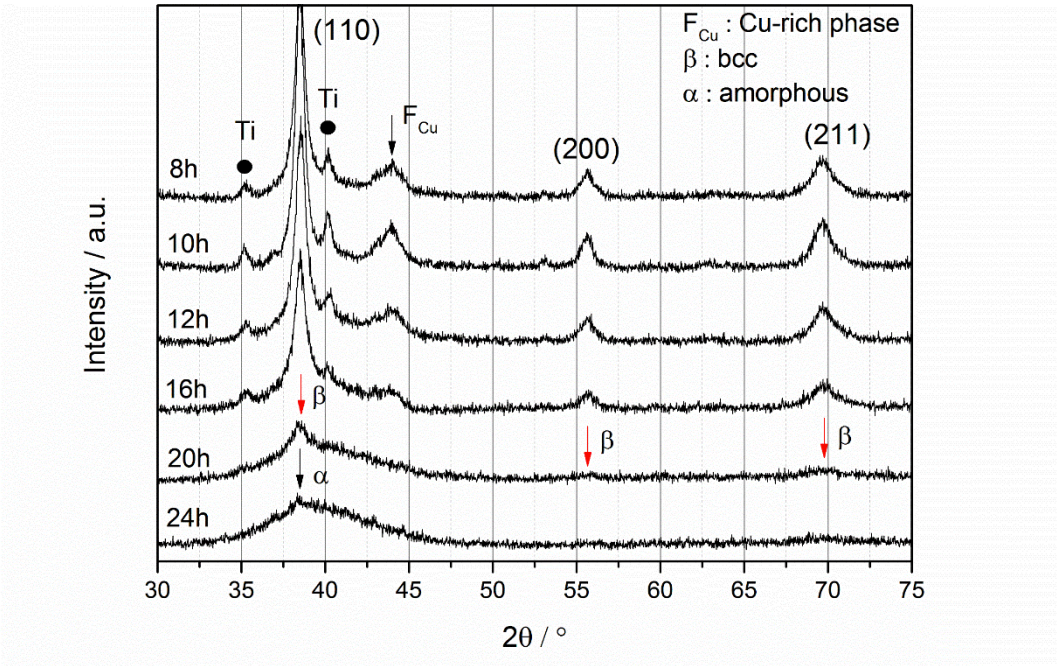

Figure 97. Enlargement of the XRD profiles of the AlTiCuNb milled powders.

The detailed XRD analysis at different milling times above-reported allows to speculate about the alloying behaviour of the AlTiCuNb system during mechanical alloying.

The first elements to disappear were Al and Cu, followed by Ti. By a kinetic standpoint, Al and Cu are the elements with the lowest melting point in the AlTiCuNb system and thus they should preferentially dissolve during the process. In conventional alloy systems, in fact, for a given crystal structure, the melting temperature of the element is a measure of its bonding strength and it is closely related to its self-diffusion coefficient. In a solution matrix, an element with lower melting point would have lower bonding strength and higher intrinsic diffusion coefficient than an element with high melting point [431]. Chen *et al.* [432] found that this empirical relation among the diffusion of different species in the same matrix and their melting points could be extended to the diffusion of elements in a matrix with multi-principal elements processed by HEMA. The alloying sequence in the octonary AlCuCoNiFeTiCrMo multi-principal element alloy investigated by the authors [432], in fact, correlated with the melting point of the elements. According to this theory and basing on the physical properties of the constitutive elements of the AlTiCuNb system listed in Table 35, the early disappearance of Al and Cu might be right account for the higher diffusion mobility of these elements in the forming solid solution matrix, because of their lower melting point.

The following element dissolved during the process in the host lattice of Nb was Ti. The retard in dissolving Ti need be ascribed both to kinetics (higher melting point) and probably also to thermodynamics, because the enthalpy of mixing of the binary Ti-Nb systems was slightly positive, corresponding to 2 KJ mol^{-1}. Furthermore, Wang *et al.* [433] found that the alloying ability of the elements in HEA produced by HEMA was also controlled by the crystal structure so that elements with similar crystal structure tended to easily form solid solutions. In the present system, hcp Ti has different crystal structure as compared to the final bcc structure of the host Nb. All these factors might have contributed in retarding the solutioning of Ti.

In the AlTiCuNb system here studied, combining both kinetics and thermodynamics, the alloying sequence conducting to the formation of the solid solution could be then determined as follows: Al → Cu → Ti → Nb.

Table 35. Fundamental properties of elements of the AlTiCuNb system listed following the anti-alloying ability [431].

	Al	**Cu**	**Ti**	**Nb**
Melting point [°C]	660	1085	1668	2477
Self-diffusion coefficient @ 400 K [mm^2 s^{-1}]	10^{-17}	10^{-25}	10^{-31}	10^{-55}
Crystal Structure @ 400 K	fcc	fcc	hcp	bcc

The bcc solid solution formed after 20 h of milling is supposed to be supersaturated since most of the components in equilibrium state have limited mutual miscibility. According to literature, the severe non-equilibrium synthesis conditions achieved during HEMA, in fact, allows to extend the solid solubility of the elements [103].

During HEMA of AlTiCuNb, diffraction peaks underwent continuous broadening and tremendous weakening, induced by a combination of severe lattice distortion, refined crystallite size and decreased crystallinity [305,434]. As reported in 4.1.2 Core effects of HEAs paragraph, the severe lattice distortion is one of the *core effects* of HEA, in general. It arises from the large difference in atomic sizes among the constitutive elements, which induces a significant loss of crystallization perfection as well as severe X-ray scattering in the material, the broadening of the XRD reflections and the decrease in their intensities [305]. Nevertheless, in HEAs synthesized by HEMA, many authors attributed most of the peak broadening observed in the XRD spectra to the formation of nanocrystalline structures during the strong non-equilibrium synthesis, with crystallite sizes as small as 10 nm [434–437]. The energy accumulated in the large volume fractions of grain boundaries at increasing milling times represents a driving force for the forming solid solution. The high density of structure defects and interfaces together with the high lattice strain was reported, in fact, to enhance the diffusion of atoms at the atomic scale,

extending the range of solid–state solubility [407,438]. The extension of the solubility range of the components at the solid state, which could account for the formation of the bcc solid solution in AlTiCuNb after 20 h of milling, should be then rigorously ascribed to the refinement of the crystallite size during the process after prolonged milling times.

The low temperatures DTA curves of AlTiCuNb powders mechanically alloyed at low (8 h) and high (24 h) milling time reported in Figure 98 provided evidences of the energy accumulated during the milling process as consequence of the refinement of the crystallite size.

The long exothermic line between approximately 150 and 500 °C, in fact, is generally attributed to the release of the internal stresses induced by the severe lattice deformation during the milling process [103,437,439]. Moreover, the lower peak temperature of the AlTiCuNb powder milled for 24 hours (388 °C) as compared to that of the powder milled for 8 h (450 °C) might be related to the higher amount of energy stored in the nanocrystalline grain boundaries of the powder milled for longer time, since the recovery occurred before [440].

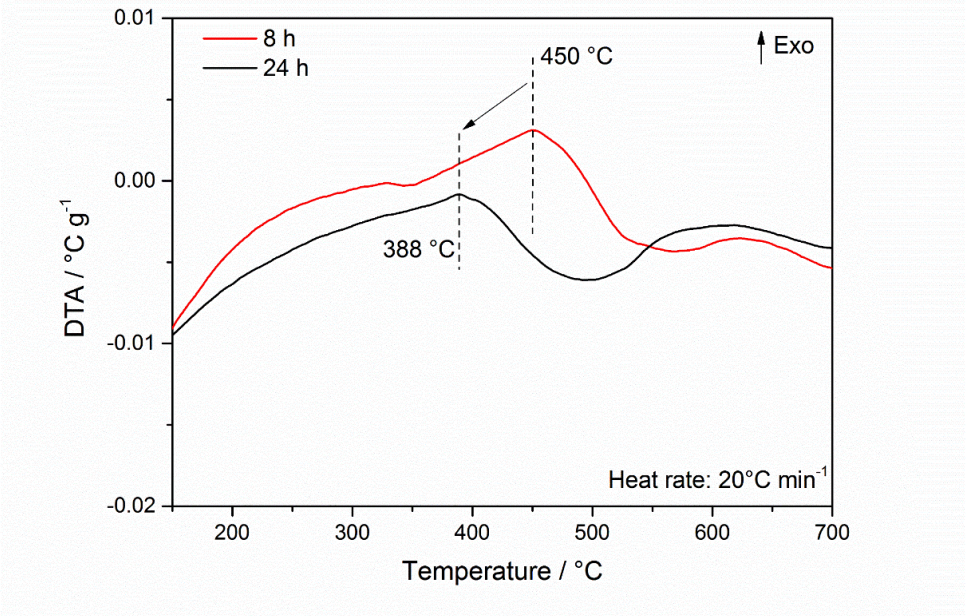

Figure 98. DTA curves for the AlTiCuNb powders by HEMA milled for 8 and 24 h.

Figure 99 shows the EDX images of AlTiCuNb powders including the elemental distribution of Al, Ti, Cu and Nb after HEMA at different milling times.

The distribution of the elements supported the outcomes from the above-reported XRD analysis confirming that it is necessary to mill the powder mixture for a certain amount of time before assessing the formation of a homogenous alloy structure. Powders milled for 8, 10, 12 and 16 h, in fact, exhibited the presence of residual quantities of unalloyed elements (Figure 99 a-d). The concentrated bright spots of Ti and Nb indicated that the grinding time was still not enough to incorporate all the elements into the forming solid solution. Finally, after 20 h of milling, powders exhibited high chemical composition homogeneity, as highlighted in Figure 99e.

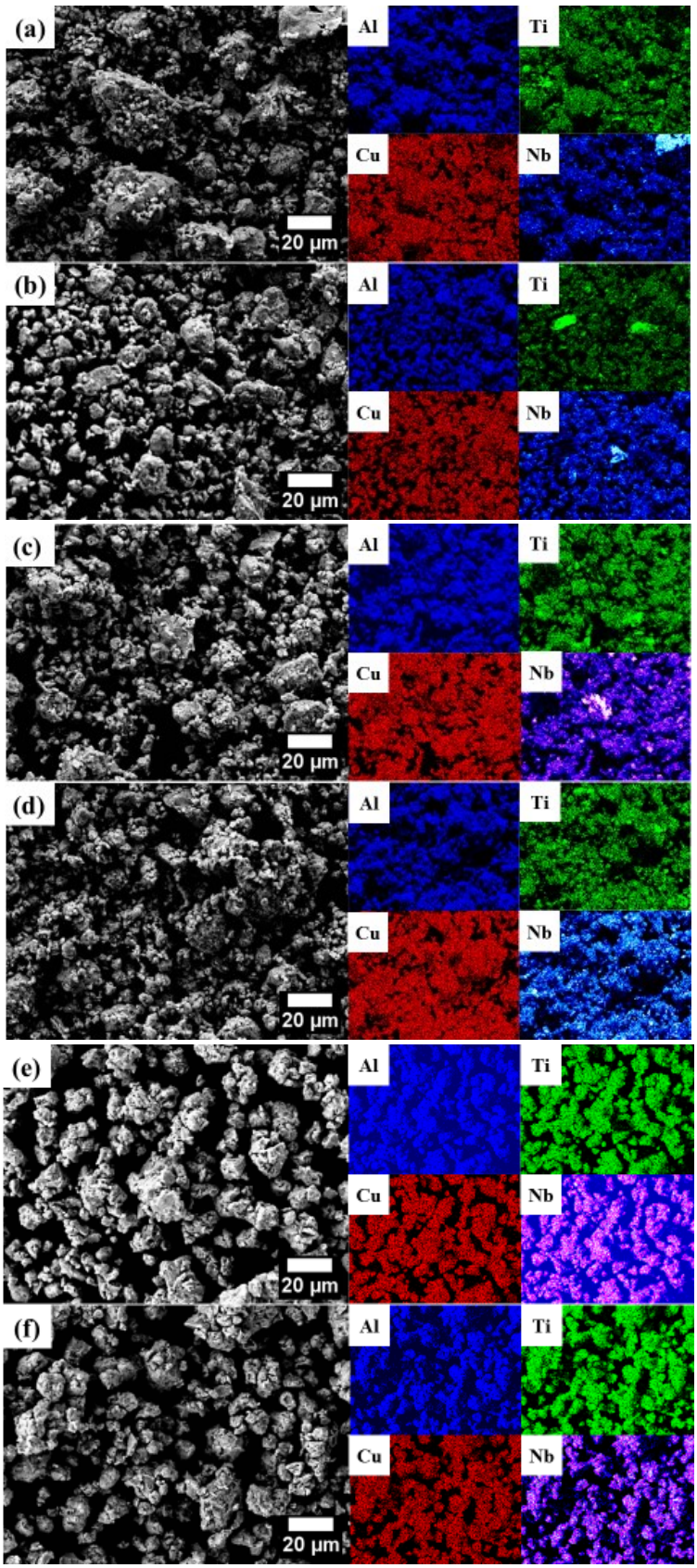

Figure 99. The EDX mapping images of AlTiCuNb powders including the elemental distribution of Al, Ti, Cu and Nb at different milling times: (a) 8 h, (b) 10 h; (c) 12 h; (d) 16 h, (e) 20 h and (f) 24 h. Powders milled for 20 h exhibit high chemical composition homogeneity.

The quantitative EDX analysis (expressed both in wt. % and at.%) of AlTiCuNb powder milled for 20 h is presented in Table 36 and the results are compared to the nominal chemical composition of the elemental powder mixture (wt. %). The analysis revealed that the chemical composition of the AlTiCuNb milled powder exhibited acceptable differences in the Al and Ti concentration with respect to the nominal chemical composition of the AlTiCuNb powder mixture but did not match for Nb and Cu amounts, whose experimental concentrations deviated by 4.6 wt.% and 4 wt.% with respect to the nominal values, respectively.

Table 36. Nominal chemical composition of the AlTiCuNb elemental powder mixture (wt.%) as compared to the experimental chemical composition (wt.% and at.%) from quantitative EDX analysis of the AlTiCuNb powder milled for 20 h. In bold the most significant deviations into the chemical composition of milled powders.

Element	Al	Ti	Cu	Nb
Nominal composition (wt.%)	11.8	20.7	**27.5**	**40**
Experimental composition (wt.%)	11.8 ± 0.08	21.3 ± 0.12	**31.5 ± 0.19**	**35.4 ± 0.22**
Experimental composition (at.%)	25.0	25.3	28.1	21.6

The lower amount of Nb in milled powders could be rationalized by considering the high thermodynamic affinity between Nb and the Fe constituting the milling media and the jars. The enthalpy of mixing of the Nb-Fe binary system, in fact, is as low as -16 KJ mol^{-1} [316] so that some Nb preferably adhered to the jars and/or balls and probably got lost. On the contrary, Cu has a very low affinity with Fe (the enthalpy of mixing of the Cu-Fe binary system is +13 KJ mol^{-1} [316]), which on the other hand could rationalize the positive deviation assessed into the chemical composition, due to its low affinity with the milling equipment. It is worth to mention here that mechanical alloying has major concerns of contamination, due to the cross-contamination between the powder and the milling media [103]. Due to the close contact between the powder and the milling equipment during the process, some material can be lost and/or incorporated. As expected, in fact, the AlTiCuNb powder milled for 20 h was found to be contaminated by Fe (< 0.7 ± 0.06 wt.%), most probably as consequence of the wear of the milling media. It goes without saying that the contamination included also the oxidation. Although the milling process was conducted in inert atmosphere (O_2 < 600 ppm), in fact, some oxygen picks up by powders during the milling process occurred, probably due to residual oxygen and humidity within the glove box as well as to the partial oxidation of the precursor powders. The extent of contamination, both due to wear and oxidation, was found to increase with the milling time, as shows the EDX analyses of AlTiCuNb powders milled for 8 and 20 h reported in Figure 100. Due to the higher wear and refinement of the microstructure after prolonged milling, powders become more sensitive to contamination with the increase of the milling time [441].

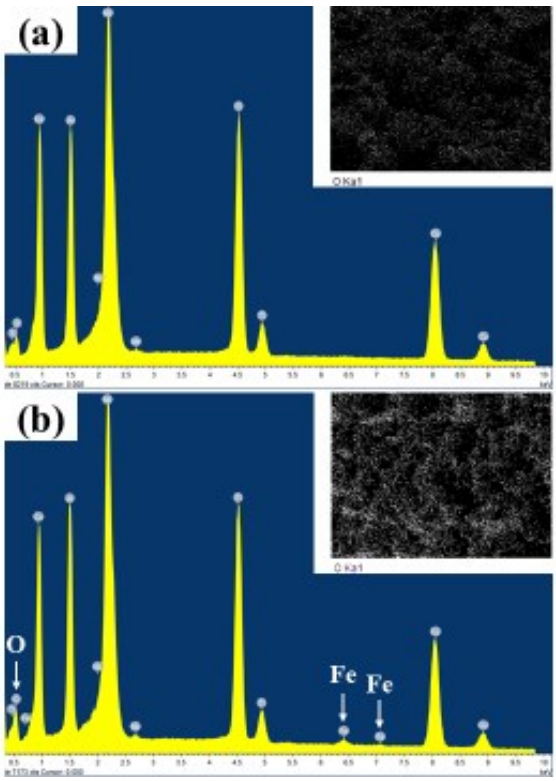

Figure 100. EDX sum spectrum of AlTiCuNb powders milled for (a) 8 h and (b) 20 h, showing the peaks Fe and O designating contamination. The insets indicate the elemental distribution of O in the milled powders. The extent Fe as well as O contamination increased with the milling time. Both the spectra and the insets refer to SEM-EDX images in Figure 99a and Figure 99e, respectively.

5.2.2.2 Morphological analysis of AlTiCuNb milled powders

During mechanical alloying, particles experience repeated deformation, cold welding, fracturing and rewelding [103]. The force transferred by the impact of the balls, in fact, plastically deforms the powder particles, which firstly work-harden, then fracture and weld again so that the final product consists of powder particles with shapes and sizes significantly different to that of the initial ones. Many authors [442–449] found that after a certain milling time, a steady-state equilibrium is reached during mechanical alloying when the rate of welding, which tents to increase the average size of powder particles, is equal to the rate of fracturing, which tends to decrease the average particle size.

Figure 101(a-f) show FESEM images for AlTiCuNb powders at increasing milling time (8, 10, 12, 16, 20 and 24 h). After 8 h of uninterrupted milling, the starting powder particles were agglomerated and formed irregular aggregates as large as 40 μm, as shown in Figure 101 (a, A). Increasing the milling time to 12 h (Figure 101 c, C), the cold welded agglomerates were crushed down to smaller particles, the powder gradually refined but significant differences into the dimension of particles existed. After 12 h of milling, the calculated average particle size was around 16 μm and the size of the powder particles spanned over the range ~10-37 μm. Here, the average as well as the range of particles sizes were calculated by image analysis by measuring the dimension of 50 powder particles in the SEM

micrograph. In the 20 h mechanically alloyed powder (Figure 101 e, E), the equilibrium between welding and fracturing was probably achieved. The powder overall refined and exhibited a narrow range of particles size. The calculated average particle size was around 15 μm and the particles size spanned over the range ~7-21 μm. At this point, the powder mainly consisted of equiaxed particles with a roundish morphology and a smooth surface with few aggregates as compared to the early stages of milling. Differently to gas-atomization process, which leads to spherically shaped powder particles, mechanical alloying generally yields powder particles with irregular shapes. Nevertheless, mechanical alloying was effective in reducing the differences existing into the shape and size among elemental particles in the original AlTiCuNb powders mixture.

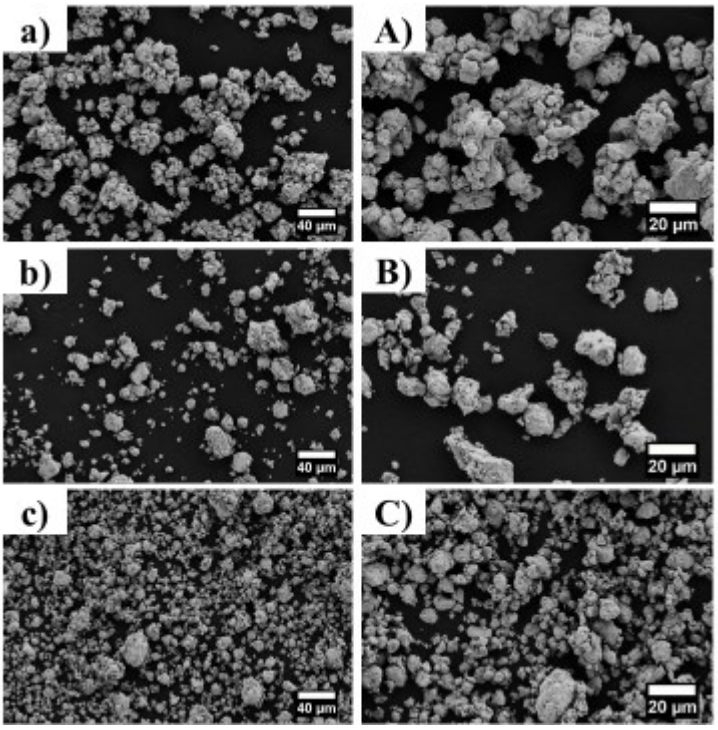

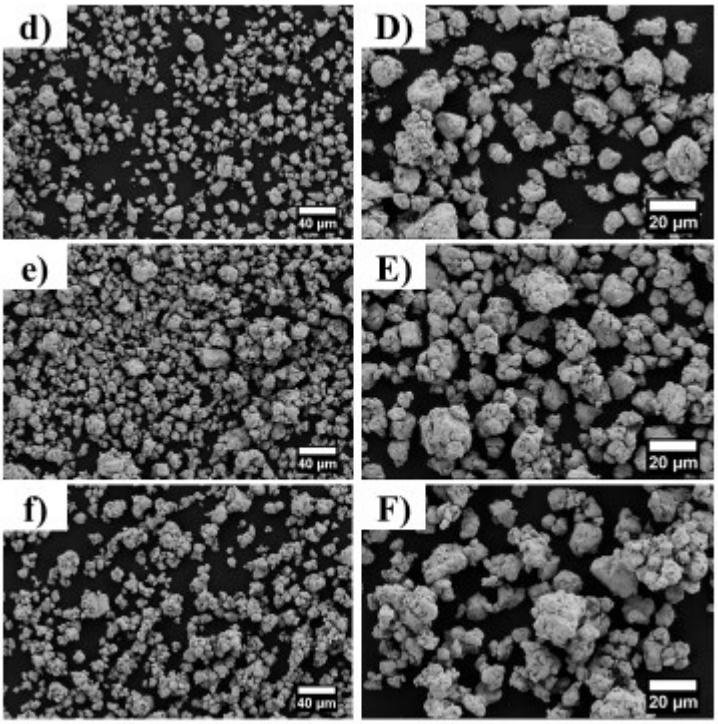

Figure 101. FESEM images of AlTiCuNb powders at different magnifications after HEMA for different milling times: (a, A) 8 h, (b, B) 10 h, (c, C) 12 h, (d, D) 16 h, (e, E) 20 h and (f, F) 24 h. Images on the left were taken at 1 kX and figures on the right were taken at 2 kX.

5.2.3 HEMA of AlTiVNb

The experimental milling conditions adopted during HEMA of the AlTiVNb powders mixture were kept the same with respect to the previous study (5.2.1.3 Experimental condition for HEMA paragraph) with the exception of the milling time, which was reduced. In order to investigate the alloying behaviour of the powder mixture during the early stages of milling and to reduce the extent of the contamination of the powders during the process, samplings for characterization were taken after 3, 5 and 10 h of milling.

5.2.3.1 XRD and compositional analyses of AlTiVNb milled powders

The structure of AlTiVNb powders at different milling time was firstly examined by means of XRD analysis and the corresponding spectra are reported in Figure 102.

The diffraction pattern corresponding to the AlTiVNb elemental powder mixture (0 h) showed the separated, sharp and obvious reflections of the crystalline precursor Al, Ti, V and Nb powders.

After 3 h of continuous milling, the peaks intensities of the elemental powders decreased, the peaks broadened and the peaks density decreased. The reflections of Al and Ti at high diffraction angles, in fact, became so diffuse and weak that they were no longer visible. As reported by Tariq *et al.* [439], these features designate the beginning of the alloy formation. The severe lattice distortion caused by the gradual dissolution of the elements together with the refinement of the crystallite

size during HEMA [407,438] produce a significant loss of crystallinity perfection as well as X-ray scattering effect, accountable for the anomalous peak intensity reduction and for the simplified XRD pattern assessed.

After 5 h of milling, peaks at low angles belonging to Al completely disappeared, suggesting its complete solutioning into the forming alloy. The microstructure of the AlTiVNb powder consisted of a bcc solid solution (β) based on Nb as main phase and residual quantities of Ti and V, as suggested by the peaks observed at approximately 35°, 40° and 42.5° in Figure 102.

As the milling time increased to 10 h, more peaks were found to decrease their intensities and to broaden but phase constitution of the alloy slightly changed. The V peak at around 42.5° was still weakly visible and the peak at around 40° belonging to Ti was most probably covered by the abnormal broadening of the (110) reflection of Nb, as suggests its non-symmetricity. The tremendous peak broadening is most probably due to the formation of a nanocrystalline structure [103]. These observations suggest that a bcc solid solution based on Nb only partially formed after 10 h of milling. This is reasonable, because of the relatively short milling time but mostly because of the low kinetics of solid-state dissolution of refractory Ti and V in the forming matrix, due to their high melting points and low self-diffusion coefficients (Table 37). On the other hand, phase constitution of AlTiVNb would probably slightly change with further milling and - on the contrary – high powder cross-contamination would occur. In a study, Tan *et al.* [450] reported the presence of residual diffraction peaks belonging to Ti, V and Zr in $Al_2Ti_3V_2NbZr$ with similar composition even after more than 12 hours of milling under more severe synthesis conditions, confirming the difficulties in fully dissolving these refractory elements.

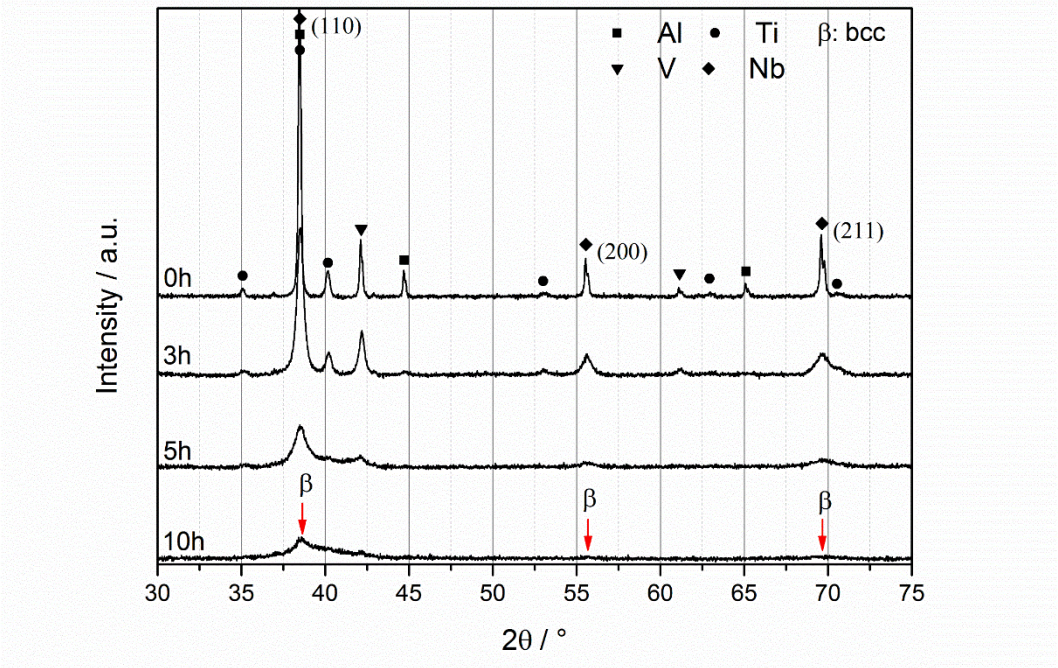

Figure 102. The X-ray diffraction patterns of the raw elemental AlTiVNb powder mixture (0 h) and the AlTiVNb milled powders produced by HEMA at increased milling time (t = 3, 5 and 10 h).

Table 37. Fundamental properties of components of the AlTiVNb system listed following the sequence of anti-alloying ability [431].

	Al	**Ti**	**V**	**Nb**
Melting point [°C]	660	1668	1910	2477
Self-diffusion coefficient @ 400 K [mm^2 s^{-1}]	10^{-17}	10^{-31}	10^{-39}	10^{-55}

The EDX analyses conducted on the AlTiVNb powders milled for 3, 5 and 10 h (Figure 103a-c) supported the outcomes of the XRD characterization.

The EDX maps of the powder milled for 3 h (Figure 103a) clearly revealed the incomplete alloying among the elements at the early stages of milling. The powder particles formed coarse aggregates constituted by fragments of Ti, V and Nb, as suggests the bright spot of the corresponding elemental maps.

By extended milling for 5 h, the spatial distribution of Ti, V and Nb improved, whilst bright spots representing fragments of elemental particles still existed (Figure 103b). In AlTiVNb powder milled for 10 h (Figure 103c), the density and the dimension of bright spots decreased and the spatial distribution of the elements significantly improved, resulting overall in a homogenous alloy powder. The pronounced non-equilibrium conditions and the formation of nanocrystalline structures during HEMA could rightly account for the enhanced distribution of the elements in the AlTiVNb powder milled for 10 h. The large volume fraction of grain boundaries in nanocrystalline MPEAs powders, in fact, enhances the diffusion of atoms at the atomic scale and from one grain into the other, leading to the homogenization of the alloy composition and to the increase of the solid solubility levels of the elements [407]. According to the characteristic alloying mechanism during HEMA, the main bcc solid solution based on Nb, which starts to form after 5 h (β phase in Figure 102), is supposed to be supersaturated.

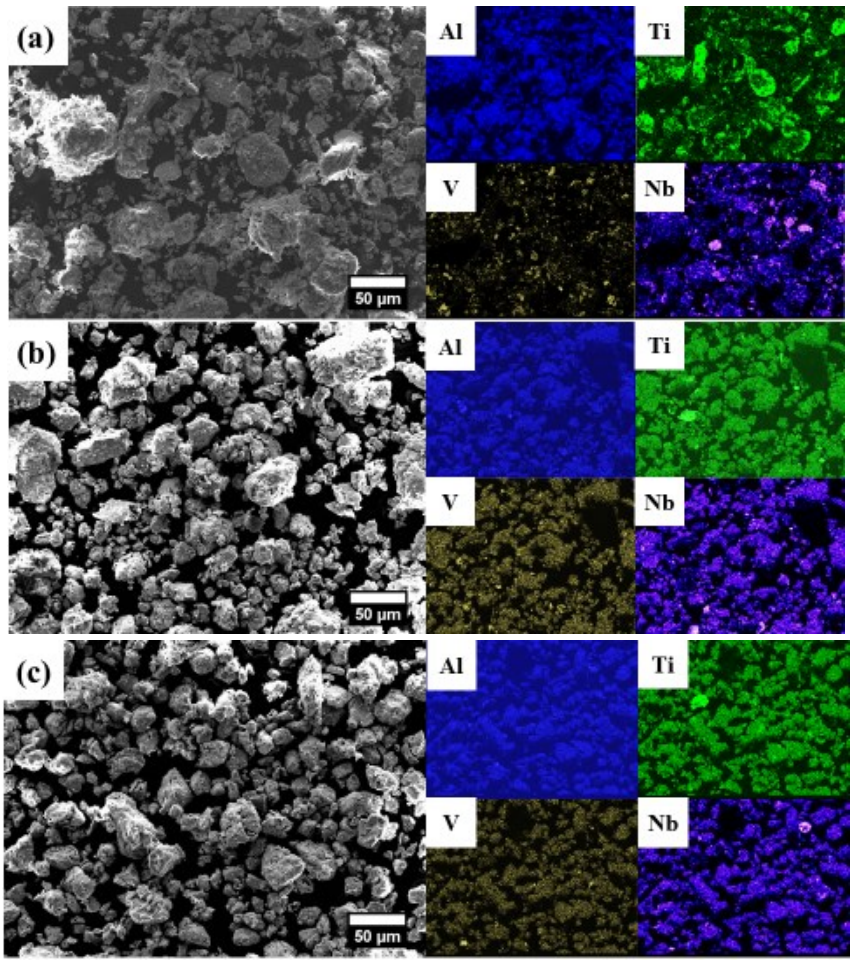

Figure 103. EDX maps of AlTiVNb powders including the elemental distribution of Al, Ti, V and Nb produced by HEMA at different milling times: (a) 3 h, (b) 5 h and (c) 10 h.

The low temperature DTA curve of the AlTiVNb powder milled for 10 h reported in Figure 104 supported the formation of a nanocrystalline structure and of energy stored in the grain boundaries of powder particles during the milling process. The long exothermic lines between 150 and 500 °C, in fact, accounts for the relieve of the internal stresses induced by the severe lattice deformation during the milling process [103,437,439].

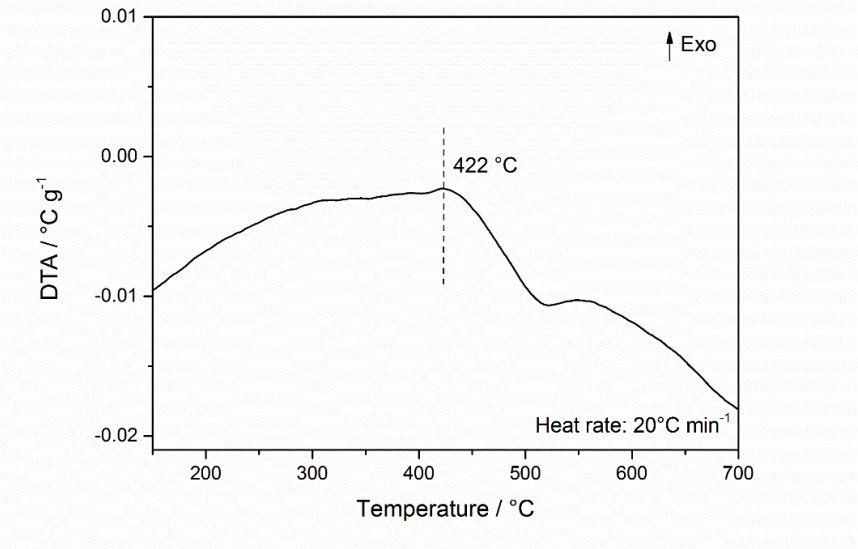

Figure 104. DTA curve for the AlTiVNb powder after 10 h of milling. The exothermic line between 150 and 500 °C, with a peak temperature at 422 °C, is attributed to the relief of internal stresses accumulated during the non-equilibrium HEMA process.

The quantitative EDX analysis (expressed in both wt. % and at.%) of AlTiVNb powder milled for 10 h is detailed in Table 38. The experimental chemical composition (at.%) of the milled powder matched pretty well with the nominal chemical composition of AlTiVNb powder mixture, whilst a major negative deviations of 5 wt.% was assessed in the Nb concentration of the milled powder. This deviation could be again ascribed to some cross-contamination between the powder and the milling equipment. Minor contaminations of Fe, as low as 0.5 ± 0.05 wt.%, and of O were found in the AlTiVNb powders milled for 10 h, due to the low milling time (Figure 105).

Table 38. Nominal chemical composition of the AlTiVNb powder mixture (wt.%) as compared to the experimental chemical composition (wt.% and at.%) from quantitative EDX analysis of the AlTiVNb powder milled for 10 h. In bold the most significant deviation into the chemical composition.

Element	Al	Ti	V	Nb
Nominal composition (wt.%)	12.3	21.9	23.3	**42.5**
Experimental composition (wt.%)	12.4 ± 0.06	24.4 ± 0.1	25.2 ± 0.1	**37.5 ± 0.15**
Experimental composition (at.%)	24.5	27.1	26.4	21.5

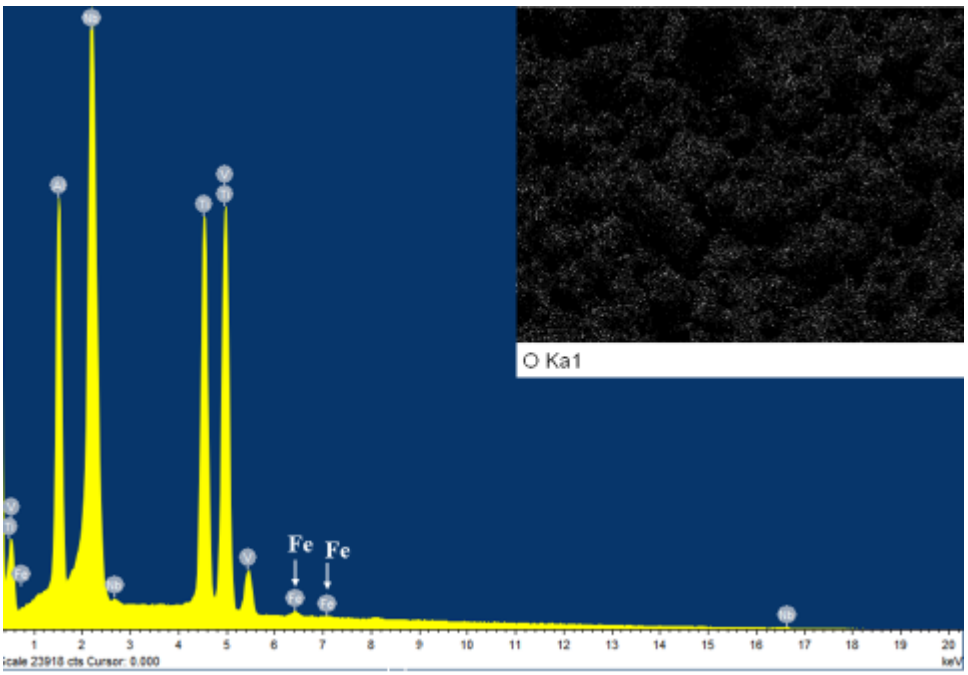

Figure 105. EDX sum spectrum of AlTiVNb powder milled for 10 h, showing a minor cross-contamination with Fe during milling. The inset indicates the elemental distribution of O in the milled powders. Both the spectrum and the inset refer to SEM-EDX image in Figure 103c

5.2.3.2 Morphological analysis of AlTiVNb milled powders

As already discussed for the previous alloy system, HEMA of AlTiVNb elemental powders mixture causes the change of both the particles morphology and size (Figure 106a-c).

After 3 h of milling, powder particles exhibited a faceted-flattened morphology (Figure 106 a, A). Generally, in the very early stage of milling, the tendency of powder particles is that of flattening and cold-welding, producing large and irregular aggregates of composite particles with a typical rugged surface because of the fine size of the welded particles that had been crushed to pieces during the process [103]. A characteristic aggregate with a composite-like structure is indicated in Figure 106 A. The aggregate seemed to be composed by fragments of elemental particles, as suggested the EDX maps of the powder milled for the same time (Figure 103a).

By increasing the milling time to 5 and 10 h (Figure 106b,B and 116c,C), the powder particles were gradually refined, because of the cold-welding and fracturing cycles. Cold welded agglomerates were crushed down to smaller particles and - whilst large aggregates could be still statistically found in the powder milled for 5 h - the tendency apparently was that of continuously refining the dimension of particles and of reducing the size differences existing among different powder particles. In the powder milled for 5 h the average particle size was 27 μm and the sizes of particles spanned over the range ~15-65 μm. After 10 h of milling, the average particle size of AlTiVNb powder decreased down to 20 μm and the sizes of particles spanned over a narrower range of ~10-37 μm. In addition, as consequence of the extended milling time, the morphology of the particles turned

to equiaxed with a smooth surface as compared to the rugged one of particles milled for 3 h.

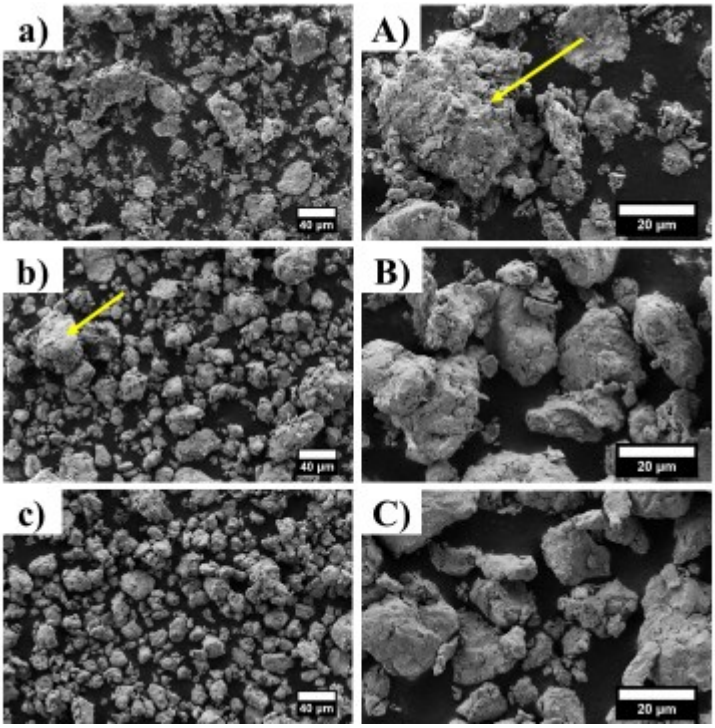

Figure 106. FESEM images of the AlTiVNb powder particles after different milling times and magnifications: (a, A) 3 h, (b, B) 5 h and (c, C) 10 h. Here, the yellow arrows point at composite aggregates. Images on the left were taken at 1 kX and figures on the right were taken at 2 kX.

5.2.4 Conclusion

In this paragraph the microstructural and morphological evolutions underwent by the AlTiCuNb and AlTiVNb elemental powder mixtures during HEMA for producing chemically and morphologically homogenous HEA powders were investigated.

The present investigation provided evidences that HEMA of the equiatomic AlTiCuNb powders mixture leads to the formation of a supersatured bcc solid solution based on Nb after 20 h of milling. The detailed XRD analysis allowed to determine the alloying sequence which conducts to the formation of the supersatured solid solution as follow Al → Cu → Ti → Nb.

The EDX analysis conducted on the powders milled for 20 h reveals the exceptionally homogenous and fine distribution of the alloying elements of the powder particles, obtained as consequence of the refinement of the crystallite size. Cross-contamination between the powders and the milling media occurs during the milling process and probably accounts for the slightly lower amount of Nb in the powders after mechanical alloying and for the minors Fe and O contaminations, whose extent increases with the milling time.

On the other hand, in the case of HEMA of the AlTiVNb powder mixture, a supersatured bcc solid solution based on Nb as main phase is obtained after 10 h of milling, with a fine and homogenous distribution of the alloying elements.

Nevertheless, for this composition residual amounts of elemental Ti and V were found probably due to the low kinetics of dissolution of these refractory elements under the experimental condition adopted (lower milling time). Cross-contamination resulted into slightly lower amount of Nb in the AlTiVNb powder milled for 10 h as compared to the nominal concentration in the powders mixture and minor Fe and O contaminations were also assessed.

On the other hand, morphological analyses confirm that mechanical alloying was effective in flattening differences existing into the shape and size among the elemental powder particles. In fact, after 20 h of milling AlTiCuNb particles with an equiaxed morphology and smooth surface were observed, having an average particle dimension of ~15 μm and sizes spanned over the range ~7-21 μm. Also, AlTiVNb particles, after 10 h of milling, exhibited homogenous morphology and equiaxed shape and smooth surface. Due to the lower milling time, the average particle dimension was ~20 μm and the particle size distribution spanned over the range ~10-37 μm.

Concluding, chemically homogenous AlTiCuNb and AlTiVNb HEA powders were successfully synthesized by mechanical alloying.

On the basis of the present results, due to the high chemical homogeneity, the fine distribution of the alloying elements in the powder particles and the absence of coarse aggregates, the AlTiCuNb HEA powder milled for 20 h and the AlTiVNb powder milled for 10 h were selected for conducting the single scan track experiment of the AlTiCuNb and AlTiVNb powder system prealloyed by HEMA.

5.3 Comparative analysis of the alloying behaviour of elemental powders mixtures and milled HEAs powders through SST experiments

SST experiments were conducted on AlTiCuNb and AlTiVNb MPEA powders obtained by both mixing the constitutive elemental powders and prealloying through HEMA.

From now on, the AlTiCuNb and AlTiVNb powders corresponding to the elemental powders mixtures will be referred as $AlTiCuNb_{mix}$ and $AlTiVNb_{mix}$, respectively. On the contrary, the prealloyed AlTiCuNb HEA powder milled for 20 h and the AlTiVNb HEA powder milled for 10 h will be referred as $AlTiCuNb_{mill}$ and $AlTiVNb_{mill}$, respectively. Figure 107 reports the FESEM images of the powders used for the SST experiments. The elemental powders mixtures (Figure 107a,c) exhibit broad variability in the size and morphology of the different species, being constituted by spherical powders with smooth surfaces (Cu and/or Ti), elongated particles (Al) and irregular ceramic-like powder particles with sharp edges and occasional coarse size (Nb and/or V). The resulting powder blends are highly heterogeneous and they are expected to have a rather restricted flowing ability and poor packing density over the building plate. Irregular powder particles (especially ceramic-like ones), in fact, may not flow easily, interlocking

mechanically and entangling with other particles. Ideally, powder particles for powder-bed AM processes should be highly spherical and with smooth surfaces and with particle size distribution optimized for having a good compromise between spreading and melting behaviours [107]. On the contrary, the milled powders look by far more homogenous than the mixed ones as concerns the particle size and morphology (Figure 107b,d). Although mechanical alloying generally lead to irregularly shaped powder particles with rough surfaces, the variability into the morphologies among the different powder particles significantly reduces and, overall, powders exhibit a uniform roundish morphology. This is expected to enhance the flowing ability with respect to the mixed compositions and to improve the homogeneity of the deposited layer.

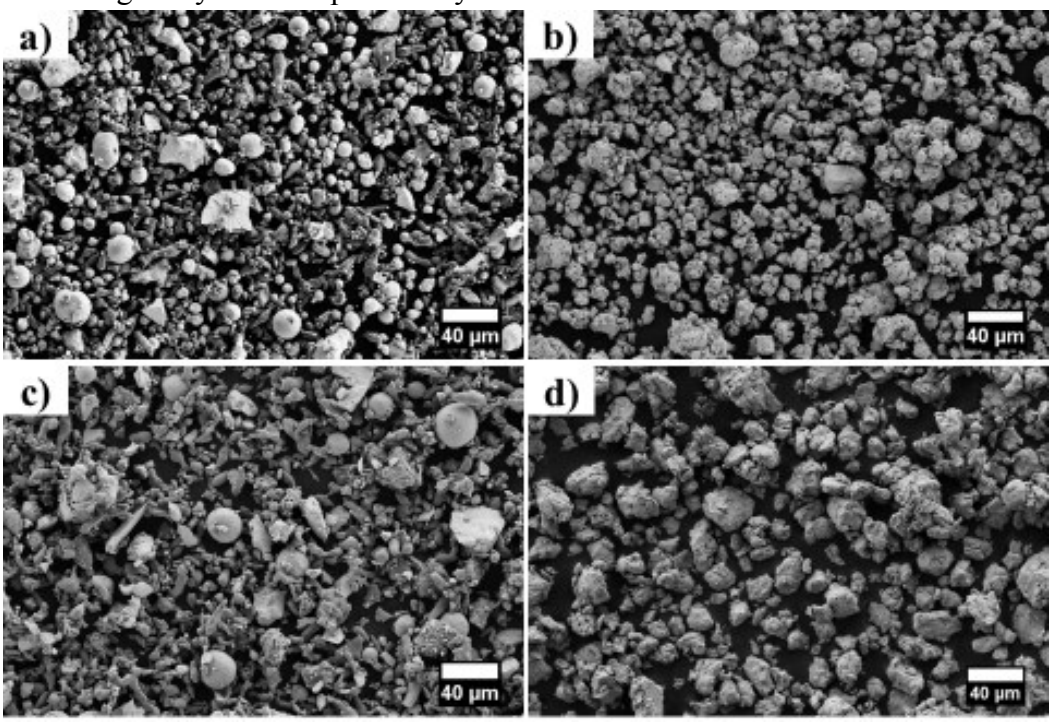

Figure 107. FESEM images of (a) $AlTiCuNb_{mix}$, (b) $AlTiCuNb_{mill}$, (c) $AlTiVNb_{mix}$ and (d) $AlTiVNb_{mill}$ powders used for conducting the SST experiments. The images are taken at 1 kX.

5.3.1 Experimental technique

SSTs of $AlTiCuNb_{mix}$, $AlTiCuNb_{mill}$, $AlTiVNb_{mix}$ and $AlTiVNb_{mill}$ were produced by LPBF using the EOS M270 machine, whose main features were already reported in 3.1.1 LPBF system and powder properties paragraph. A modified EOS Aluminium building platform was used for the experiments and consisted of nine holes occupied by disks, able to be removed for the subsequent characterizations (Figure 108a).

Rigorously, the material to use for the disks should have a chemical composition as close as possible to that of the powders to be processed. In this way, in fact, the modification of the material chemical composition due to the dilution by the substrate can be limited. Moreover, the molten powders certainly weld to the substrate/disk because of the compositional similarity.

However, due to the compositional complexity of the MPEAs systems here investigated and due also to the different type of powders used, just mixed or prealloyed, the issue on which material to adopt for the supporting disk was tricky. For the $AlTiCuNb_{mill}$ and $AlTiVNb_{mill}$ powders obtained by HEMA, the use of two different substrate disks - with compositions corresponding to that of the prealloyed powders - would be the best option. However, for $AlTiCuNb_{mix}$ and $AlTiVNb_{mix}$ consisting of pure Al, Ti, Cu and Nb and pure Al, Ti, V and Nb, respectively, the issue on which material would be best to use as substrate in order to ensure good wettability between the disks and the molten powders is not obvious. Would it be best to use pure Al, or pure Ti, Cu, V, Nb? Or would it be best to use a disk with same composition of the corresponding powder mixture?

The solution was readily available as follows. With the aim of preliminarily assessing (1) the processing behaviour during LPBF for different alloy compositions, whose constitutive powders had been in turn prepared by different processing routes (mixing and mechanical alloying), and (2) the alloying behaviour of the mixed and milled powders within the melt pool so to assess the feasibility of using non-atomized alloy powders for conducting SSTs experiments, it was decided to use the same substrate for all the powders systems. In particular, cast AlSi10 disks readily available in the laboratory were used for this experiments. By using the same substrate for all the powder systems, in fact, firstly, it would be easy to properly assess comparisons among the different powder systems, excluding in a way the substrate contribute from the interaction mechanism between the laser and the powder material and secondly it would actually make this preliminary analysis rapid, because it would not require the production of compositionally complex disks of customized composition, hard to obtain. The candidate is aware that the inevitable dilution of the powder material by the Al-Si substrate disk during SST would modify the chemical composition of the powder, making the processed material no longer a HEA. Nevertheless, this was not the first aim - at the moment - which was rather that of conducting a feasibility study into the processability by SST technique of complex HEAs powders prepared with two different processing routes, mixing and mechanical alloying.

Figure 108b represent the geometry used for the SST, consisting of an inner track (*scan*) and an outer *contour*. The *scan* can be processed with customized laser power P and scanning speed v. The *contour* by default is laser scanned by the LPBF machine system with a set of standard parameters, corresponding to $P = 150$ W and $v = 1250$ mm s^{-1}.

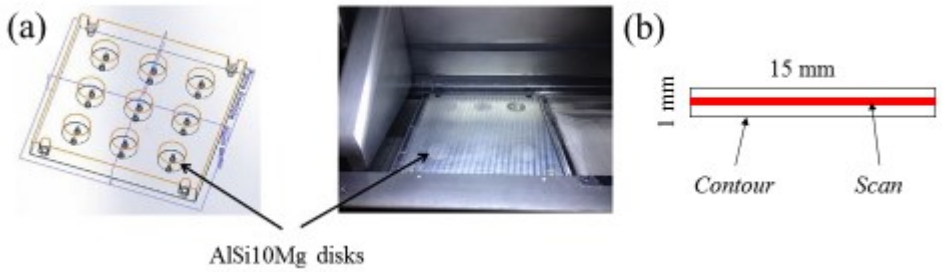

Figure 108. (a) Schematic representation and experimental building platform used in this work and (b) schematic representation of the geometry of the laser scan track, consisting of the *contour* and the infill *scan*.

A starting powder layer thickness of 50 μm was set for all the experiments and the layer of powders was spread over the disks using the film depositor in Figure 109a, with a fixed gap width of 50 μm. For each experiment, the $AlTiCuNb_{mix}$, $AlTiCuNb_{mill}$, $AlTiVNb_{mix}$ and $AlTiVNb_{mill}$ powders were mixed with ethanol, producing a thick slurry which made easier the spreading of the powders over the disks, according to the procedure set up by Aversa *et al.* [194] on different Aluminium based powders. In fact, as previously shown in Figure 107, both mixed and milled powders consisted of irregular particles inducing poor flowing ability, especially if dried. The wet-method allowed to deposit a dense layer of powder of constant thickness, as shown in Figure 109b.

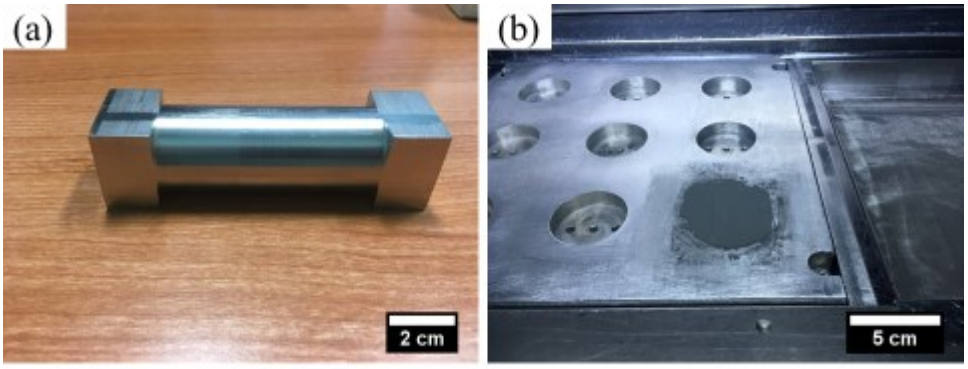

Figure 109. (a) Film depositor tool used in the present work for spreading a constant layer of powder of 50 μm over the disk and (b) uniform layer of powder achieved with the system in (a).

At the end, the chamber was filled with argon until the residual oxygen content was below 0.1% and the building platform was heated up to the temperature of 100 °C, in order to allow the evaporation of residual ethanol.

For single scan track experiment, the most important process parameters are the laser power *P* and the scanning speed *v*. Regardless the MPEA system, the powders were laser scanned at the constant power of 195 W and at four different scanning speeds (300, 400, 500 and 600 mm s^{-1}) (Figure 110). Due to the presence of elements with high melting point (1910 and 2477 °C for V and Nb, respectively) and high laser reflectivity (0.91 and 0.98 at 1076 nm wavelength for Al and Cu, respectively), it was decided to process powders at the maximum laser power and at low scan speeds, in order to provide to the material high amount of linear energy

input for melting. Four different scanning speeds were used in order to investigate a broad process window. In addition, due to the limited laser power in the LPBF machine system adopted, in order to be sure to melt all the constitutive elements, especially refractory elements in the powder mixtures, each track was laser scanned three times, consecutively. Others authors adopted a similar scanning strategy when laser-processing complex mixtures of powders constituted by refractory species, reporting an enhancement of the alloy homogeneity within the melt pool [426].

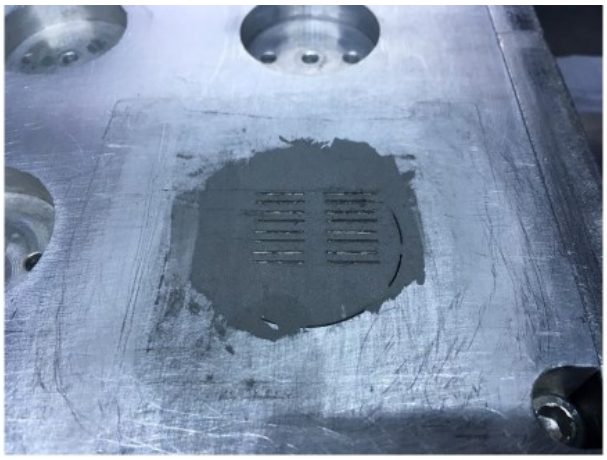

Figure 110. Image of a single scan experiment showing the single scan tracks at different parameters.

5.3.2 Analysis of the geometrical features of the SSTs

The cross sections of the SSTs were first observed at the OM in order to assess the geometrical features of the melt pool, namely the width (W) and the penetration depth (D) (Figure 111) (Appendix A.2.2 SSTs characterisation). The geometry of the SSTs could provide information on the processability of the different alloy systems within a process window as well as on some physical phenomena occurring in the exposed layer of powder, such as the wetting and melting behaviours [194,195]. This information could be helpful when developing materials by LPBF.

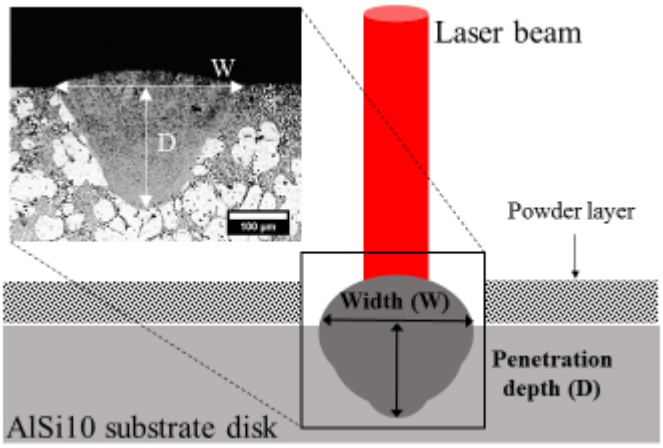

Figure 111. Schematic representation of the geometrical features of the SST calculated (W and D), together with the OM image of the typical cross section of a SST.

In Figure 112 the cross sections of SSTs of $AlTiCuNb_{mix}$, $AlTiCuNb_{mill}$, $AlTiVNb_{mix}$ and $AlTiVNb_{mill}$ processed at different scanning speeds are illustrated.

The melt pools could be easily distinguished from the substrate, due to the different microstructure. In fact, the supporting disk exhibits the characteristic microstructure of cast AlSi10, with α-Al dendrite (white grains) and the Al-Si eutectic (grey matrix).

The melts pool were cracks-free and dense and they exhibited a good bond with the AlSi10 substrate. This result is not obvious. The choice of an unappropriated substrate could lead to poor wetting and/or bonding between the SSTs and the disk and to balled SSTs hard to characterize. The choice of using AlSi10 disks for conducting the SSTs experiments on the novel MPEAs powders compositions was then appropriate. Occasionally, some pores were found in the vertical cross sections of SSTs (yellow arrows in Figure 112), probably due to instability phenomena within the melt pool, such as keyholing or to residual porosities in the disks obtained by casting.

The visual inspection of the SSTs cross sections reported in Figure 112 shows that, regardless the powder system processed, the melt pools had a characteristic conical shape, which deeply penetrated down within the substrate. The shape is similar with that indicating a keyhole mode melting in laser welding [451]. Moreover, the depth to width aspect ratio was greater than 0.5. These features designate a melting mechanism of the powders where keyholing dominated, probably due to excessive energy input [47,195]. Then, increasing the scanning speed, the geometrical features of the melt pool, namely the penetration depth (D) and the width (W), decreased for any powder system. This is reasonable, because when the scanning speed increases the energy transferred to the material decreased, resulting in a lower dimension of the melt pool [452].

From Figure 112 it can be also noticed that, regardless the laser scanning speed used, the width of the SSTs was much larger than the laser spot diameter of the LPBF system adopted (~ 100 μm). This is a consequence of the wetting of the alloy at the molten state and of the heat transferred to the substrate, which contributed in creating a melt pool wider than the laser-beam diameter [24].

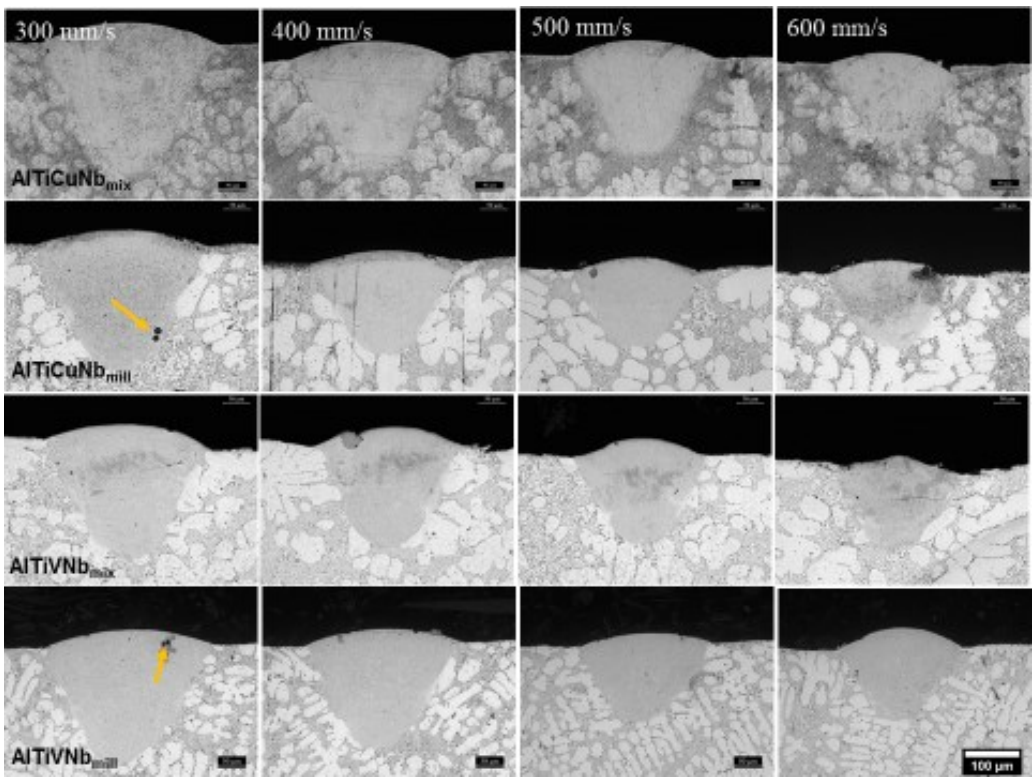

Figure 112. Cross sections of SSTs of $AlTiCuNb_{mix}$ (first row), $AlTiCuNb_{mill}$ (second row), $AlTiVNb_{mix}$ (third row) and $AlTiVNb_{mill}$ (forth row) at different scanning speeds (300, 400, 500 and 600 mm/s). Laser power is constant at 195 W. Yellow arrows point at porosities within the melt pool.

The summary plots of Figure 113, which report the values of the geometrical features of the SSTs calculated by image analysis for each powder system, revealed that, under the experimental conditions adopted in the present study, slight differences into the W and D values of the melt pool were found among the different powders systems. In fact, regardless the powder system processed the width of the melt pools always ranged approximately between 310 and 225 µm when the scanning speed increased from 300 to 600 mm s^{-1} and the penetration depth ranged approximately between 222 and 140 µm, within the same scanning speed range.

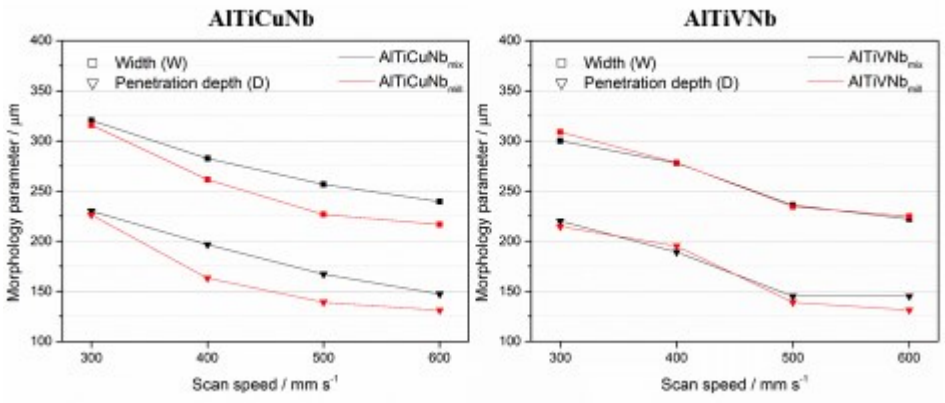

Figure 113. Influence of the scanning speed on the width and penetration depth of the melt pool of the SSTs of AlTiCuNb (left) and AlTiVNb (right). The black and the red lines refer to the mixed and milled powders, respectively.

The analysis of the geometrical features of the SSTs, thus, suggested that for both the compositions the powder preparation route (mixing and mechanical alloying) slightly affected the SST morphology. The differences, in fact, were mostly affected by the scanning speed rather than the powder system processed. To be more precise, the AlTiVNb composition showed the same values of W and D for both $AlTiVNb_{mix}$ and $AlTiVNb_{mill}$ (right chart in Figure 113) while the AlTiCuNb composition exhibited W and D values just slightly different between $AlTiCuNb_{mix}$ and $AlTiCuNb_{mill}$ (left chart in Figure 113). It is hard to rationalize these small differences taking into account a different type of interaction between the powder system and the laser beam. Due to the triple laser scan, in fact, only during the first scanning the laser actually interacted with the powders, while during the subsequent scans the laser interacted with already consolidated material, which is remelted.

These geometrical analyses of the SSTs suggest that, under the experimental condition adopted, the mixed and milled compositions behave pretty much the same.

5.3.3 Nanoindentation and chemical composition mappings

Nanoindentation tests were conducted along the cross section of SSTs for both mixed and milled compositions by using a standard nanoindentation grid for all the SSTs (Figure 114) (Appendix A.2.2 SSTs characterisation). As easily visible, the indentation array spans across the individual melt pool and the cast substrate.

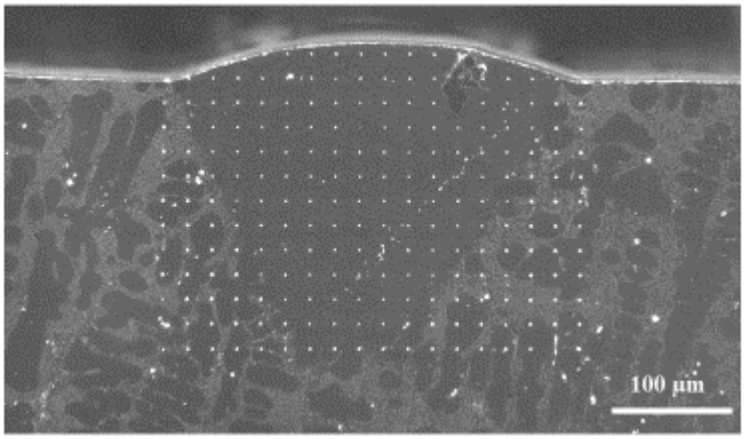

Figure 114. Experimental nanoindentation grid on a SST. The white dots represent the single indentations.

Nanoindentation test is an automated characterization technique for assessing the local mechanical properties of the material, i.e. hardness. However, regardless the local indentation value, the representation of the indentation grids through maps could be a useful tool for rapidly gaining information on the homogeneity of the microstructure within the melt pool as well as on the alloying behaviour of powders prepared by different methods.

The results were summarized in Figure 115, which reports the nanoindentation maps for $AlTiCuNb_{mix}$, $AlTiCuNb_{mill}$, $AlTiVNb_{mix}$ and $AlTiVNb_{mill}$ processed at different scanning speeds. The occasional blue dots within the melt pools represent points of low hardness were defects, such as pores, were found while the grey/red areas represent regions with high hardness an green/light-blue regions areas represent region of intermediate hardness.

The coloured maps helped in capturing substantial differences between the mixed (first and third rows in Figure 115) and the milled (second and fourth rows in Figure 115) compositions, being the nanohardness maps of the former less homogenous than that of the latter, at any scanning speed. Such dishomogeneities were particularly evident in SSTs of $AlTiVNb_{mix}$ but existed also in $AlTiCuNb_{mix,}$ suggesting the presence of microstructural features within the melt pool of mixed powders, which resulted into products with low homogeneity.

Under the experimental condition adopted, the scanning speed was found to not significantly affect the distribution of the mechanical properties within the melt pool. According to this observation, additional SEM-EDX characterizations were conducted on selected SSTs processed only at 500 mm s^{-1}, as a representative example of all the SSTs.

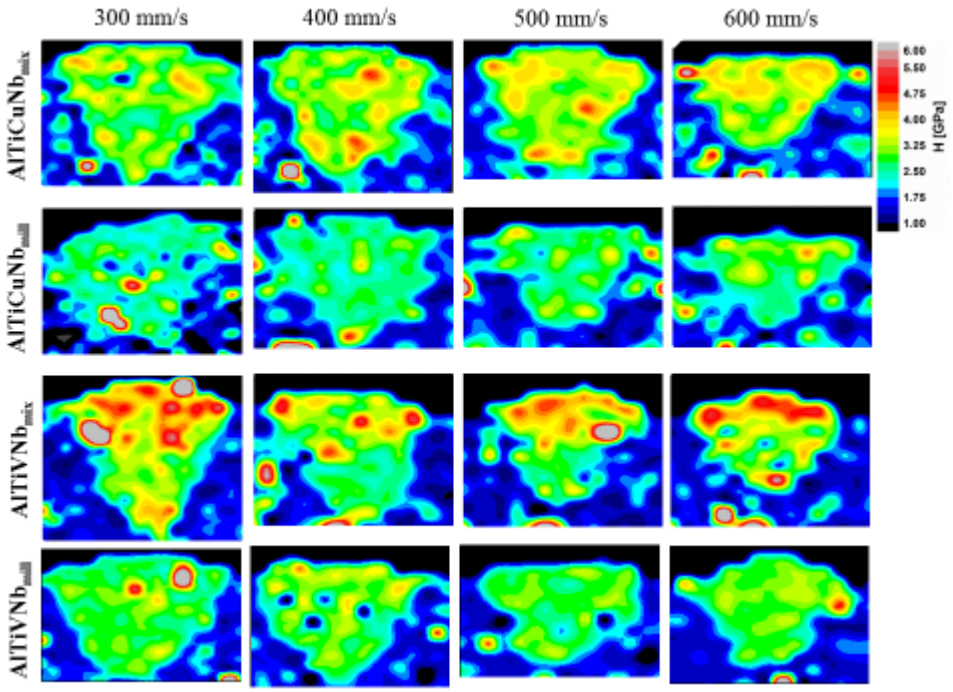

Figure 115. Nanoindentation maps conducted on the cross sections of SSTs of AlTiCuNb$_{mix}$ (first row), AlTiCuNb$_{mill}$ (second row), AlTiVNb$_{mix}$ (third row) and AlTiVNb$_{mill}$ (forth row) at different scanning speeds (300, 400, 500 and 600 mm s^{-1}). Laser power is constant at 195 W. The nanohardness scale is reported on the top right corner of the figure.

The EDX mappings performed on SSTs of AlTiCuNb$_{mix}$ and AlTiCuNb$_{mill}$ including the elemental distribution of Al, Ti, Cu and Nb are reports in Figure 116. In AlTiCuNb$_{mix,}$ a not homogenous distribution of the constitutive elements was clearly evident in the maps of Al and also in that of Cu (Figure 116a), as opposed to AlTiCuNb$_{mill}$ where a fine and homogenous distribution of the alloying elements was found (Figure 116b). EDX mapping on AlTiCuNb$_{mix}$ further reveals the presence of bright spots in the elemental maps of Ti and Nb, which most probably represented unmelted particles (yellow arrows in Figure 116a). These features were not found AlTiCuNb$_{mill}$.

Similar microstructural dishomogeneities but even more evident were found in the AlTiVNb system. Figure 117 shows the FESEM images and the EDX mappings including the elemental distribution of Al, Ti, V and Nb in SSTs of AlTiVNb$_{mix}$ and AlTiVNb$_{mill}$. In AlTiVNb$_{mix}$, the mixing efficiency of the different species within the melt pool was very low, as evident in the Al, V and Nb maps (Figure 117a). The elements were not homogenously distributed and higher concentrations of V and Nb were preferably located in the upper part of the melt pool. In addition, throughout the melt pool of AlTiVNb$_{mix}$, coarse V and Nb particles supposedly not molten during the triple laser scan, were also found (yellow arrows in Figure 117a). On the contrary, a fine and homogenous distribution of the alloying species was found again in the melt pool of AlTiVNb$_{mill}$ (Figure 117b), even if small bright spots in the elemental map of Ti, V and Nb were found also in the SST of AlTiVNb$_{mill}$ (yellow arrows in Figure 117b). The presence of these supposedly

unmelted particles should be ascribed to the phase constitution of the $AlTiVNb_{mill}$ powders after 10 h of milling, which contained residual amount of elemental Ti, V and Nb particles due to the low kinetics of dissolution of these refractory elements during mechanical alloying. This observation suggests that the use of fully alloyed MPEAs powders is necessary for enhancing the microstructural homogeneity within the melt pool when processing alloy compositions containing refractory species.

The results of the EDX analyses conducted on SSTs of AlTiCuNb and AlTiVNb suggests that the fine alloying of the elements achieved by mechanical alloying was effective in ensuring high compositional homogeneity within the melt pool, improving the processability of alloy compositions constituted by many different species. The more homogenous distribution of the mechanical properties of the milled compositions, so as assessed through the nanoindentation maps in Figure 115, could rightly account for the enhanced compositional homogeneity within the melt pool.

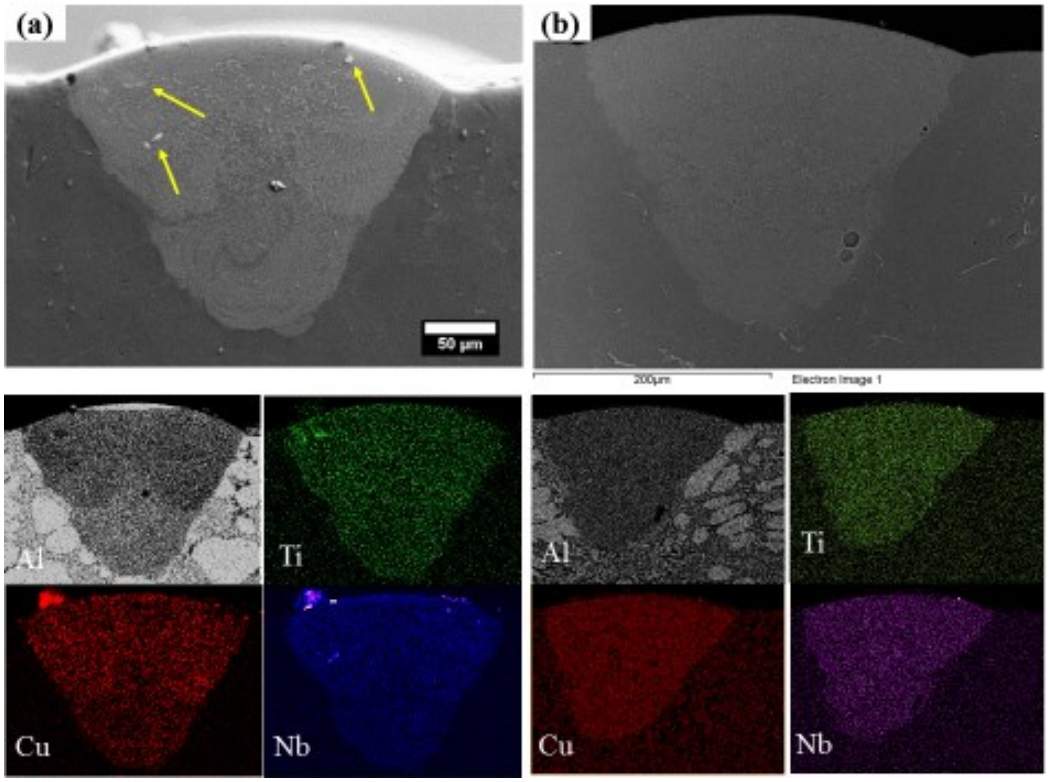

Figure 116. FESEM images and the EDX mapping of the SSTs and substrate disk of (a) $AlTiCuNb_{mix}$ and (b) $AlTiCuNb_{mill}$, respectively, including the elemental distribution of Al, Ti, Cu and Nb. SSTs were processed at 500 mm s^{-1}. Yellow arrows point at Ti and Nb unmelted particles.

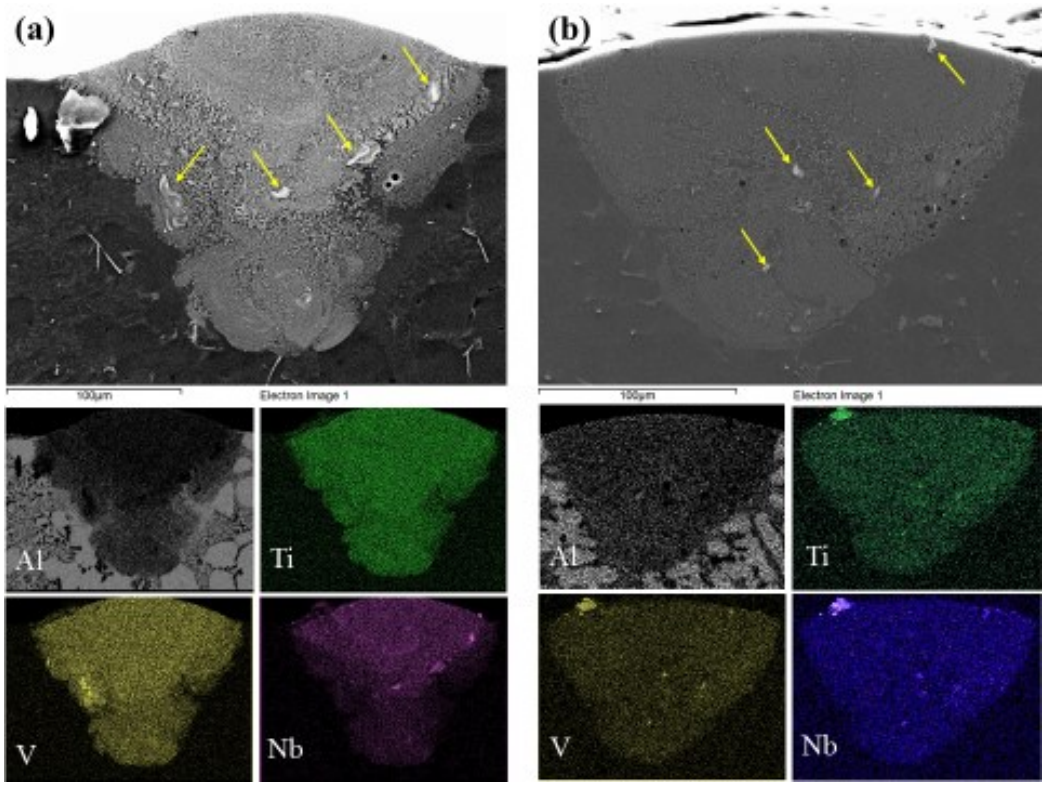

Figure 117. FESEM images and the EDX mapping of the SST and substrate disk of (a) $AlTiVNb_{mix}$ and (b) $AlTiVNb_{mill}$ including the elemental distribution of Al, Ti, V and Nb. SSTs were processed at 500 mm s^{-1}. Yellow arrows point at V and/or Nb unmelted particles.

The quantitative EDX analysis conducted within the melt pools of the AlTiCuNb and AlTiVNb powder systems further highlighted the advantages related to the use of prealloyed powders in terms of compositional homogeneity within the melt pool when conducting SSTs experiments on MPEAs.

The results for $AlTiCuNb_{mix}$ and $AlTiCuNb_{mill}$ SSTs are reported in Table 39. The at.% of Al (including also the Si fraction) within the melt pools was significantly higher than that of the other constitutive elements. During SST, in fact, the Al-Si disk was remelted and a strong dilution effect by the disk was thus expected. Nevertheless, while a near-equiatomic proportion among Ti, Cu and Nb - closely related to that of the prealloyed powders - was found within the melt pool of $AlTiCuNb_{mill}$ (first and second rows in Table 39), in the SSTs of $AlTiCuNb_{mix}$ the melt pool was found to be rich in Cu, slightly depleted in Nb and strongly depleted in Ti (third and fourth rows in Table 39), designating overall a composition where the proportion among the elements was different from that of the equiatomic elemental powder mixture. Similar deviations in the chemical composition were assessed in the SST of $AlTiVNb_{mix}$, as revealed the quantitative EDX analysis reported in Table 40.

Table 39. Quantitative EDX analyses of the SSTs of $AlTiCuNb_{mill}$ and $AlTiCuNb_{mix}$ reporting the at.% of the elements within the melt pool as compared to the experimental and nominal compositions of the powders used for the experiment, respectively. The concentrations of Ti, Cu

and Nb within the SSTs are in bold. In the SST of $AlTiCuNb_{mix}$, deviations from a near-equiatomic proportion among the species are found.

Alloy system	Al (at.%)	Ti (at.%)	Cu (at.%)	Nb (at.%)
SST $AlTiCuNb_{mill}$	96.7	1.1	1.2	1.0
Experimental composition of $AlTiCuNb_{mill}$ powder	25.0	25.2	28.2	21.6
SST $AlTiCuNb_{mix}$	92.4	1.6	3.7	2.3
Nominal composition of $AlTiCuNb_{mix}$ powder	25.0	25.0	25.0	25.0

Table 40. Quantitative EDX analyses of the SSTs of $AlTiVNb_{mill}$ and $AlTiVNb_{mix}$ reporting the at.% of the elements within the melt pool as compared to the experimental and nominal compositions of the powders used for the experiment, respectively.

Alloy system	Al (at.%)	Ti (at.%)	V (at.%)	Nb (at.%)
SST $AlTiVNb_{mill}$	96.0	1.4	1.4	1.2
Experimental composition of $AlTiVNb_{mill}$ powder	24.6	27.2	26.5	21.7
SST $AlTiVNb_{mix}$	94.3	1.2	2.5	2.0
Nominal composition of $AlTiVNb_{mix}$ powder	25.0	25.0	25.0	25.0

The underlying reason for the compositional deviations found in the SST of mixed compositions could be related to issues during the deposition of the powder layer. As already said, the procedure adopted for spreading the powder layer above the disk included the mixing of the equiatomic blend of elemental powders, the production of a thick slurry with ethanol and the spreading of the slurry with the film depositor illustrated in Figure 109. However, starting from a slurry with an equiatomic composition does not necessary imply that the composition of the deposited layer would be the same. Due to the differences into densities, sizes and morphologies among the species, the probability of depositing a powder layer with an equiatomic composition, in fact, could be very low. For instance, Ti has density as low as 4.50 g cm^{-3} while that of Nb and Cu is 8.57 and 8.94 g cm^{-3}, respectively. In the $AlTiCuNb_{mix}$ system, these densities differences probably created segregation effects in the slurry, which altered the chemical composition of the deposited powder layer, contributing in enriching this latter in Cu and Nb. In addition, preferential mutual interaction among elemental particles of different species might have further contributed in affecting the final composition of the

powder layer. As observable in Figure 118, Nb platles were found to preferentially adhere onto Cu particles while they did not exhibit any kind of interaction with the Ti particles (Figure 118 II-III). Together with the differences into physical properties as well as particle sizes and morphologies, the existence of preferential mutual interactions among the different powder particles might contributed in making more difficult the deposition of an equiatomic powder layer.

These observations suggest that many factors should be considered when processing equiatomic mixtures of different elemental powders and that some technological limitations may exist when applying the SST technique to highly heterogeneous powder systems constituted by many different species into equiatomic proportion. The use of prealloyed powder synthesized by mechanical alloying with homogenous composition and morphology, can avoid these issues, as confirmed by the homogenous chemical composition within the melt pool as assessed through quantitative EDX analysis.

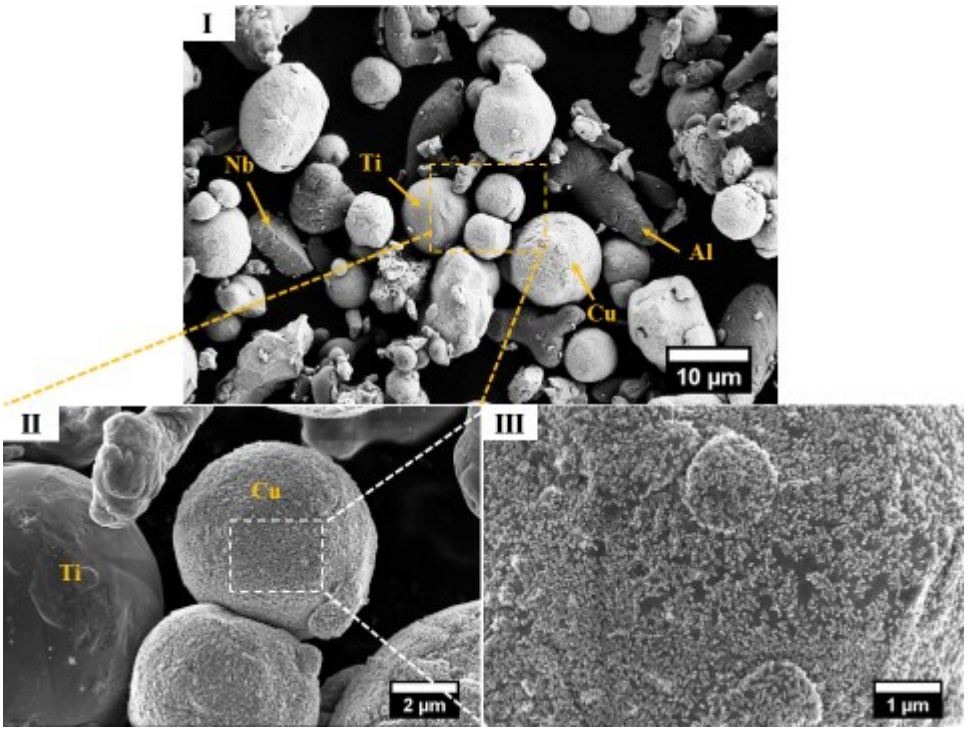

Figure 118. FESEM images of the equiatomic powder mixtures of $AlTiCuNb_{mix}$ at different magnifications: (I) 5kX, (II) 25 kX and (III) 50 kX. (I) The elemental powders particles exhibit different sizes, shapes and morphologies. (II) Cu particles are covered by fine platles, differently to Ti particles. (III) Sub-micrometric Nb platles are observed to adhere preferably onto the surface of Cu particles.

5.3.4 Conclusion

In the present work, SSTs of two customized MPEA compositions (AlTiCuNb and AlTiVNb) containing refractory elements were produced without resorting to gas-atomized alloy powders but by using both mixtures of elemental powders and alloy powders synthesized by mechanical alloying. The cross section of the SSTs

of the following powders systems, namely $AlTiCuNb_{mix}$, $AlTiCuNb_{mill}$, $AlTiVNb_{mix}$ and $AlTiVNb_{mill}$, were characterized.

The results reveals that SSTs of both elemental powders mixtures and alloy powders synthesized by mechanical alloying can be successfully produced and characterized by adopting Al-Si disks.

The compositional and mechanical characterization of the SSTs suggest that the alloy powders preparation route significantly influences the alloying behaviour of the different powder systems within the melt pool. In particular, the results show that *in-situ* alloying of MPEAs compositions containing refractory elements results into a not homogenous distribution of the alloying elements within the melt pool with residual Ti, V and/or Nb supposedly unmelted particles. This behaviour could be related to the broad differences into physical properties among the constitutive elements as well as the high melting point of refractory elements, which are not easily melted by the laser beam.

The processability by LPBF of MPEAs containing refractory elements is improved by the use of alloy powders synthesized by mechanical alloying, providing fine and uniform distribution of the elements within the melt pool as well as homogenous mechanical properties. High-quality milled powders, with low amounts of residual unalloyed elements, are fundamental for obtaining a homogenous microstructure within the melt pool.

The results further show that the use of alloy powders synthesized by mechanical alloying is preferred when conducting SST experiments on MPEAs because it prevents from bias into the chemical composition of the deposited powder layer. The large differences into the densities, sizes and shapes among the different powder particles constituting the complex powders mixtures, in fact, could hinder the deposition of a powder layer with well-defined composition. Consequently, the success of processing chemically homogenous SSTs from complex elemental powder mixtures is affected not only by the broad differences into the melting temperature, particles shape and size but also by the method specifically adopted for spreading the powder layer.

Concluding, a cost-effective method for preliminarily assessing the behaviour during LPBF of novel MPEAs could be represented by SSTs of chemically and morphologically homogenous MPEA powders synthesized by mechanical alloying.

Chapter 6

Conclusions

6.1 Development of two Aluminium alloys through LPBF of different powders mixtures

The aim of these studies was to investigate the feasibility of improving the mechanical properties of AlSi10Mg, the most widely processed Aluminium alloy by LPBF through the adoption of an *in-situ* alloying strategy based on the introduction of small quantities of transition metals (TM) from different powders, namely pure Ni powder, and Ni-, Cr- and Fe-rich nickel-base superalloy Hastelloy X powder. The alloying and densification behaviour, microstructures and properties of the corresponding Al-Si-Ni and Al-Si-Ni-Cr-Fe alloys were then investigated.

Firstly, the main results for the Al-Si-Ni alloy, processed in a LPBF system with a 200 W Yb fiber laser, can be summarized as follows:

- Dense and crack-free Al-Si-Ni samples can be manufactured by LPBF from a powder mixture of AlSi10Mg and pure Ni powders by selecting an alloy composition close to the eutectic one of the corresponding Al-Si-Ni ternary system. The alloy composition suffers of high residual stresses, which can deform the samples during manufacturing. This problem requires an *ad-hoc* technological solution, i.e. customized support structures.

- Within the melt pool, the thermophysical phenomena driven by temperature and surface tension gradients allow to finely mix the powders so that the chemical composition of the alloy is close to the nominal one. The high mixing efficiency of the powders within the melt pool is most probably obtained thanks to the fine size of Ni particles, whose d_{50} is 12 μm, with respect to the d_{50} value of 27.1 μm of AlSi10Mg powder. However, Ni-rich precipitates, probably representative of poorly melted spare large Ni powder particles, are randomly distributed throughout the matrix, designating overall a heterogeneous microstructure.

- The microhardness mean value of Al-Si-Ni alloys is 179 HV ± 3. It can be stated that the modification of the AlSi10Mg composition by pure Ni powders is effective in improving by more than 33 % the hardness with respect to the base material, due to the precipitation of sub-

micrometric Al_3Ni particles. Most of precipitates form at the melt pool border, where the material undergoes multiple liquid and/or solid solid-state transformations driving to the precipitation of stable phases.

On the other hand, the main results for the Al-Si-Ni-Cr-Fe, processed in a LPBF system with a 100 W Yb fiber laser, can be summarized as follows:

- Crack-free Al-Si-Ni-Cr-Fe samples can be manufactured from powder mixture of AlSi10Mg and Hastelloy X powders by selecting an alloy composition with narrow solidification range, so as calculated by Pandat-assisted Scheil simulations. Samples do not warp and delaminate during the manufacturing but they exhibit a residual porosity of around 11 %, most probably due to the selection of a starting powder layer thickness not adequate to the other processing parameters, mainly the laser power. The alloy composition developed is promising for LPBF but a further investigation for density optimization is required.

- Overall, the combined effect of the Marangoni flow within the melt pool and of the continuous remelting of the material due to the LPBF scanning strategy are not effective in fully mixing the alloy powders. The microstructure of the as-built alloy is strongly inhomogeneous, consisting of large TM-clusters randomly distributed throughout the material and solute-rich and solute-poor bands within the melt pool. The large size of Hastelloy X powder particles, whose d_{50} is 28.9 μm, with respect to the d_{50} value of 29.5 μm of AlSi10Mg powder, decreases the homogeneity of the powder mixture and the alloying efficiency during the process; moreover, the short melt pool lifetime hinders the effective homogenization of the composition at the molten state.

- Locally, the thermocapillary effect dominating the dynamics within the melt pool is effective in mixing the alloy powders. The α-Al cells are supersatured with Si and Fe and contain Cr and Mg into solid solution, due to the fast cooling. Upon solidification, the excess of solutes into the concentrated liquid is rejected along the α-Al cells boundaries, which are enriched by Si, Mg and Ni.

- During LPBF, the scanning speed is effective in controlling the extent of the reaction between the alloy powders as well as in influencing the hardness of the material. In particular, low laser scanning speed promotes both the nucleation of high fraction of α-Al(Fe,Cr)Si intermetallics and the segregation of Si, due to the increased energy input and reduced cooling rate.

- The microhardness mean value of Al-Si-Ni-Cr-Fe is 182 HV ± 12. The high material strength can be ascribed to a combination of solid solution and Orowan strengthening effects induced by the formation of

supersatured Al cells and the precipitation of intermetallics, respectively.

6.2 Development of two HEAs through SST experiments on different powders systems

The aim of this study was that of investigating the feasibility of producing compositionally homogenous SSTs of two selected HEA containing refractory species using different powders systems, namely powder mixtures of the elemental constitutive species or alloy powders synthesized by mechanical alloying.

The main results of the study, conducted in a LPBF system with a 200 W Yb fiber laser, can be summarized as follows:

- SSTs of both powder mixtures and alloy powders synthesized by mechanical alloying can be successfully produced by using Al-Si disks as substrate, whilst a considerable dilution effect by them can be observed.
- The compositional and mechanical characterizations of the AlTiCuNb and AlTiVNb SSTs reveal that the alloy powder preparation route weakly affects the geometrical features of the SSTs but significantly influences the alloying behaviour of the different powder systems within the melt pool.
- Even using a triple laser exposure for the SSTs, refractory particles constituting the AlTiCuNb and AlTiVNb powder mixtures are hard to fully melt. The melt pool microstructure is inhomogeneous as well as the chemical composition and difficulties exist in depositing a compositionally homogenous layer of powder over the substrate, most probably because of the physical as well as powder-related properties differences among the elemental powders.
- On the other hand, a fine and uniform distribution of the elements as well as homogenous mechanical properties can be achieved within the melt pool of SSTs of HEAs powders synthesized by mechanical alloying, improving the alloying behaviour of compositionally complex alloy systems.

6.3 Closing remarks

At the end of these studies, the final consideration that can be drown is that processing of powder mixtures can be a valuable strategy for having an insight into the processability, microstructure development as well as mechanical properties of novel alloys by LPBF. Nevertheless, concerns of truly *in-situ* homogenization of the composition as well as full melting of some of its constitutive elements exist due to the fast heating and cooling of the material and the high melting points of

refractory elements - if present - which hinder from obtaining a complete alloy homogeneity and a material with uniform properties.

Low scanning speed can promote the mixing among powders within the melt pool, due to the longer exposition of the material to the laser beam as well as to the longer melt pool lifetime. It is reasonable to conclude then that the manufacturing of alloy samples from powder mixture should look at sets of process parameters guaranteeing the best consolidation behaviour with the lowest scanning speed. At the end, at least three observations it is worth to mention here.

Firstly, the use of an alloy powder, i.e. Hastelloy X, with many chemical species for modifying the chemical composition of a base Aluminium alloy strongly limits the freedom in tailoring the final alloy composition, because of the fixed stoichiometric ratios among the elements in the alloy powder. This poses additional challenges to the design of the proper powder batch composition to process. On the contrary, the use of a pure element powder is preferred, allowing much higher flexibility in tailoring the powder batch composition so to reach an alloy composition with optimal processability and/or desired properties.

Secondly, the use of alloy powders specifically produced for the LPBF process, i.e. Hastelloy X, for *in-situ* tailoring the chemical composition of a base alloy does not represent the best option for obtaining a homogenous alloy. Its particle size distribution, in fact, would be mainly optimized for exhibiting good flowing properties during LPBF, generally spreading across the range 20-63 μm. Right for this reason, it would not contain high fraction of fine particles, which on the other hand would enhance the compositional homogeneity of the powder mixture. It is therefore preferred to tailor the alloy composition by using powders with a small average diameter, high fraction of "fines" and low quantity of large particles so to enhance the powder mixture as well as the alloy compositional homogeneity.

Lastly, the application of SSTs technique to powder mixtures containing refectory elements is not recommended as a tool to develop this novel multi principal element alloys (MPEAs) by LPBF because of the broad variability into the physical as well as powder related properties of the elements constituting such compositionally complex systems. These differences hinder from the obtainment of homogenous products of desired composition. On the contrary, SSTs technique on HEA powders synthesized by mechanical alloying could represent a cost-effective method for preliminarily assessing the behaviour of MPEAs during LPBF, without resorting to expensive and/or difficult to produce gas-atomized alloy powders. Although concerns of minor cross contamination between the powders and the milling media, which can be limited through proper optimization of the synthesis parameters, mechanical alloying is effective for synthesizing chemically and morphologically homogenous HEAs powders to be evaluated for LPBF processing by SSTs technique. Further developments of this work should be addressed to optimize the SSTs technique for HEAs powders and to limit the dilution effect by the substrate.

Appendix – Experimental equipment and characterization methods

In this chapter, the experimental equipment and characterization methods used to study samples produced within this thesis will be provided.

The chapter is divided in two sections. The first section is related to characterization techniques used to analyse powders and LPBF bulk samples in the Al-Si-Ni and Al-Si-Ni-Cr-Fe studies. The second section is related to characterization techniques used to analyse powders and SSTs produced in the HEA study.

A.1 Al-Si-Ni and Al-Si-Ni-Cr-Fe-Ni studies

A.1.1 Powder Characterization

A.1.1.1 Electron microscopy

The morphology of the metal powders was observed by means of electron microscopy using Zeiss SupraTM 40 Field Emission Scanning Electron Microscope (FESEM, SEM-FEG Assing SUPRA 25, Zeiss, Jena, Germany).

A.1.1.2 Laser granulometry

The diameter distribution of the metal powders were measured by means of laser granulometry using Fritsch Analysette 22 Compact instrument, with measuring range between 0.3 μm and 300 μm. The mean size distribution and the frequency distribution were based on a volumetric assumption. In addition, the d_{10}, d_{50} and d_{90}, which represent the diameters values of the 10, 50 and 90% of the cumulative size distribution, were found and reported.

A.1.2 Porosity evaluation

Residual porosity within the as-built LPBF samples was investigated adopting two different measurement techniques: Archimedes method was used for Al-Si-Ni samples while image analysis was used for porosity measurement of highly porous Al-Si-Ni-Cr-Fe samples.

A.1.2.1 Archimedes method

Porosity levels of the Al-Si-Ni samples were estimated by Archimedes method on 10 mm × 10 mm × 10 mm cubes. Before the measurements, the specimen surfaces were grinded by using SiC papers, in order to remove the external skin inducing surface roughness. The density of the samples was measured according to the ASTM B962-14 standard by weighting the samples in the air and in the deionized water adopting an ORMA BCA200S balance (accuracy ± 0.1 mg).

The density ρ_p of the samples was calculated using the following equation:

$$\boldsymbol{\rho_p \left[\frac{g}{cm^3}\right] = \frac{m_a}{m_a - m_{fl}} \times \rho_{fl}}$$

Where m_a is the mass of the sample measured in air, m_{fl} is the mass of the sample when immersed in the fluid and ρ_{fl} is the density of the deionized water. The porosity was then evaluated from the ratio between ρ_p and ρ_{th} representing the theoretical density of the material.

Due to the *in-situ* alloying of powder mixture and the reactions that arise during the laser LPBF process, the theoretical density of the material takes into account also the density of the precipitates. Assuming that all the Ni reacts forming Al_3Ni, the theoretical density of the Al-Si-Ni alloy was assumed 2.77 g cm^{-3}.

A.1.2.2 Image analysis

Porosity of the highly porous Al-Si-Ni-Cr-Fe samples was estimated by means of image analysis [453]. Five micrographs of the vertical (XZ) and horizontal (XY) cross sections were captured for each sample by using an Olympus GX51 optical microscope at 50X magnification from locations in the central areas of the surfaces. The total area analysed amounted to approximately 46 mm^2. Before taking the micrographs, the specimens were grinded up to 4000 SiC paper. The images were converted into black-and-white micrographs and processed through ImageJ software. For each cross micrograph, the porosity was expressed as fraction of blacks (pores) over whites (bulk). The average porosity and the standard deviation of each sample were then calculated conducting the analysis in five different regions of the same sample.

A.1.3 X-ray diffraction analysis

X-Ray diffraction (XRD) analysis was used to characterize phases in the feedstock powders as well as LPBFed samples.

On the Al-Si-Ni samples, XRD analysis was carried out on the surface grinded up to 1200 SiC paper by means of a X-pert Philips diffractometer in a Bragg Brentano configuration operated at 40 kV and 40 mA, working with a Cu cathode ray tube ($\lambda_{K\alpha 1}$ = 1.5406 Å). The analysis was conducted in the 2θ range between 10° and 110°, with a step size of 0.013° and 25 s per step.

On the Al-Si-Ni-Cr-Fe samples, the XRD analysis was performed on OP-S end-polished specimens using a Bruker D8 Advance diffractometer in a Bragg-Brentano geometry. A Cu cathode ($\lambda_{K\alpha1}$ = 1.5406 Å) ray tube was used at a tube voltage of 40 kV and a tube current of 40 mA. A step size of 0.021° with a dwell time of 7 seconds at each step was used to obtain good quality diffraction patterns for phase identification in the 2θ scan range between 15° and 90°. Phase identification was then performed by manual search-match procedure. Powder diffraction file (PDF) reference cards of possible phases were obtained from International Centre for Diffraction data (ICDD) and their peak position and intensity were compared to those observed experimentally. A step size of 0.0164° with a dwell time of 1 second was used to obtain higher spatial resolution diffraction data for precise lattice parameter determination. In this case, a 2θ scan range from 20° to 120° was adopted. The data were plotted using OriginPro software and curves were smoothed by Savitzky-Golay filtering method with 20 points per window and a polynomial order of 5. A Nelson-Riley procedure was used to obtain the lattice parameters from the position of the diffraction peaks, by using the following extrapolation function:

$$\frac{\cos^2\theta}{\sin\theta} + \frac{\cos^2\theta}{\theta}$$

A.1.4 Microstructure analysis

Microstructure of samples after LPBF was investigated by means of optical microscopy (OM), electronic microscopy, energy-dispersive X-ray spectroscopy (EDS) and transmission electron microscopy (TEM).

The vertical (XZ) cross sections were prepared for the microstructure analyses by hand grinding with SiC abrasive papers, polishing with diamond paste up to 1 μm and then end-polishing the surface with silica oxide suspension (OP-S) down to 0.25 μm.

A.1.4.1 Optical microscopy

OM on Al-Si-Ni samples was carried out before and after chemical etching by using Keller's reagent for 10 seconds (95 ml H_2O, 2.5 ml HNO_3, 1.5 ml HCl, 1 ml HF). Samples were observed at Leica DMI 5000 M optical microscope.

OM microscopy on Al-Si-Ni-Cr-Fe samples was carried out before and after electro-chemical etching conducted by using Barker's reagent (2 vol.% HBF4 in H2O) at 20 V and 25 °C for 10 seconds with a Lectrupol5 instrument. Samples were observed at Olympus GX51 optical microscope.

A.1.4.2 Electronic microscopy

Microstructures of etched Al-Si-Ni and Al-Si-Ni-Cr-Fe samples were studied by means of Zeiss SupraTM 40 Field Emission Scanning Electron Microscope (FESEM, SEM-FEG Assing SUPRA 25, Zeiss, Jena, Germany) equipped with energy-dispersive X-Ray spectroscopy (EDS) probe.

Microstructure of as-built Al-Si-Ni-Cr-Fe samples was further studied by means of JEOL JSM-7001F Scanning Electron Microscope (SEM, FEGSEM at 15KV) in both secondary electron (SE) and back-scattered electron (BSE) modes. The instrument was equipped with an Oxford Instrument Aztec X-ray system for energy-dispersive X-ray spectroscopy (EDXS) analysis.

A.1.4.3 Transmission electronic microscopy

Selected Al-Si-Ni-Cr-Fe samples were further studied by means of TEM. A thin lamella was sectioned using a Ga focused ion beam using the FIB lift-out procedure (FEI Quanta® 3D FEG, equipped with a Pegasus Hikari® EBSD system).

Bright-field (BF-STEM) and high-angle annular dark-field (HAADF-STEM) scanning transmission electron microscopy (STEM) were performed on FEI Tecnai G2 F20 S-TWIN FEG operated at 200 kV. Energy-dispersive X-ray spectroscopy (EDXS) was performed using a Bruker X-flash X-ray detector on the F20, and the EDXS data was analysed using the Bruker Esprit X-ray software.

A.1.5 Thermal analyses

Phase transformations on the as-built Al-Si-Ni and Al-Si-Ni-Fe-Cr LPBF samples were studied by means of Differential Thermal Analysis (DTA).

The coefficient of thermal expansion (CTE) of Al-Si-Ni samples was evaluated by Thermo-Mechanical Analysis (TMA).

A.1.5.1 DTA

For Differential Thermal Analysis (DTA), a TGA-SDTA METTLER Toledo 1600 system working in argon atmosphere was used.

For Al-Si-Ni and Al-Si-Ni-Cr-Fe samples, a heating ramp of 10 °C min^{-1} between 50 and 450 °C and of 2 °C min^{-1} between 450 and 650 °C was adopted.

A.1.5.2 TMA

For Thermo-Mechanical Analysis (TMA) a SETSYS Evolution system was used. The analysis was carried out on 10 mm × 5 mm × 5 mm samples adopting a heating ramp of 5 °C min^{-1} from 50 to 400 °C.

A.1.6 Micro-hardness evaluation

In order to preliminary assess mechanical properties of samples Vickers hardness of LPBF samples was evaluated.

On Al-Si-Ni samples, micro-hardness was evaluated on cubes of 10 mm × 10 mm × 10 mm size using a Leica VMHT micro-indenter, with a load of 100 g applied for 15 s ($HV_{0.1}$). The Brinnel hardness was also evaluated in agreement with the Standard ASTM E10 using a load of 62.5 Kg for 15 s ($HBW_{2.5/62.5}$).

On Al-Si-Ni-Fe-Cr samples, micro-hardness was evaluated on cubes of 12 mm ×12 mm × 12 mm size using a Duramin A300 hardness test machine at a load of 500 gf and a loading time of 10 seconds ($HV_{0.5}$). Measurements were taken at

twenty different locations along the vertical and horizontal cross sections and the average hardness value was calculated; the typical standard deviation was 12 HV. One-way analysis of variance (one-way ANOVA) with a significance threshold for p-value of 0.05 was conducted using Minitab software in order to assess the significance of difference between hardness means for selected samples.

A.1.7 Nano-hardness evaluation

In order to characterize the hardness of the samples at the small scale typically found in fine LPBF microstructures, nanohardness was evaluated by nanoindentation testing.

Nanoindentation testing was carried out using a TI950 nanoindenter (Hysitron) equipped with a diamond Berkovich tip indenter. A controlled load was applied to the specimens and then removed, producing traditional force versus displacement curves. The analysis of the curves, then, provides information regarding the mechanical properties of the specimen. The Oliver-Pharr method was used to analyse the hardness of modulus curves [454]. This method does not require imaging of the indentation since it is based on a contact mechanics solution developed by Sneddon [455]. The Berkovich tip indenter consists of a 3-side diamond pyramid with an included angle of 142° and an angle from the normal to the face of 65.35°.

For Al-Si-Ni, the load was increased at 65 $\mu N\ s^{-1}$ up to a maximum load of 1000 μN and then decreased at the same rate. The load was applied for 5 sec. A grid of 11 × 11 with 121 indentations, distant 2 μm from each other, was realized.

For Al-Si-Ni-Cr-Fe, a grid of 11 × 11 with 121 indentations, distant 5 μm from each other, was realized. Then the nanohardness indentations were analysed by means of FESEM observation.

A.2 HEAs study

This section goes through the description of the characterization and testing techniques used within the work on HEAs.

A.2.1 Powder characterization

The morphologies of mixed powders as well as the evolution in the morphology of milled powders during the HEMA process were assessed by means of electron microscopy using Zeiss SupraTM 40 Field Emission Scanning Electron Microscope (FESEM, SEM-FEG Assing SUPRA 25, Zeiss, Jena, Germany) equipped with energy-dispersive X-ray (EDX) for elemental analysis.

EDX mappings were carried out in order to assess the alloying of elemental powders and the element distribution during the HEMA process.

The structure and qualitative phase analysis of powders before and after HEMA were investigated by conventional X-Ray diffraction (XRD). The analyses were performed using a Philips PW3040 diffractometer in a Bragg Brentano

configuration, working with Cu-Kα radiation operated at 40 KV and 30 mA and scanning angle (2ϑ) from 30° to 75°, with 0.02° step size and 1 sec per step. The International Centre for Diffraction Data's Powder Diffraction File (PDF) database was used for peak identification.

The thermal behaviour of the milled powders was investigated by thermo-gravimetric and simultaneously differential thermal analysis (TGA-SDTA, METTLER Toledo 1600) at a heating rate of 20 °C min^{-1} from 25 to 700 °C in flowing argon atmosphere.

A.2.2 SSTs characterisation

The microstructure of SSTs was investigated by means of optical microscopy (OM) and electron microscopy while the distribution of the elements over the cross section of SSTs was assessed by means of energy-dispersive X-ray spectroscopy (EDX). Before conducting the analysis, the SSTs were cut, mounted and polished.

The cross sections of SSTs were prepared for the microstructure analyses by hand grinding with SiC abrasive papers, polishing with diamond paste up to 1 μm and then end-polishing the surface with silica oxide suspension (OP-S) down to 0.25 μm. No etchant was used.

The microstructure of SSTs was observed at Leica DMI 5000 M optical microscope and at Zeiss SupraTM 40 Field Emission Scanning Electron Microscope (FESEM) equipped with energy-dispersive X-ray (EDX) for elemental analysis.

Nanoindentation testing was carried out on end-polished cross sections of SSTs by using a TI950 nanoindenter (Hysitron) equipped with a diamond Berkovich tip. The details on the instrument can be found in in A.1.7 Nano-hardness evaluation. The load was increased at 125 μN s^{-1} up to a maximum load of 2500 μN and then decreased at the same rate. The load was applied for 5 sec. A grid of 16 × 13 with 208 indentations, distant 20 μm from each other, was realized. For our experiment, the local hardness values, expressed in GPa, were plotted using coloured maps.

References

[1] S.A.M. Tofail, E.P. Koumoulos, A. Bandyopadhyay, S. Bose, L. O'Donoghue, C. Charitidis, Additive manufacturing: Scientific and technological challenges, market uptake and opportunities, *Materials Today*. 21 (2017) 22–37. doi:10.1016/j.mattod.2017.07.001.

[2] ASTM International, ASTM F2792-12a: Standard Terminology for Additive Manufacturing Technologies, (2012). doi:10.1520/F2792-12A.

[3] I. Gibson, D.W. Rosem, B. Stucker, Additive Manufacturing Technologies: rapid prototyping to direct digital manufacturing, Berlin, 2009.

[4] L. Yang, K. Hsu, B. Baughman, D. Godfrey, F. Medina, M. Menon, S. Wiener, Additive Manufacturing Process Chain, in: Addit. Manuf. Met. Technol. Mater. Des. Prod., Springer, 2017: pp. 33–44. doi:10.1007/978-3-319-55128-9.

[5] D.L. Bourell, D.W. Rosen, M.C. Leu, The Roadmap for Additive Manufacturing and Its Impact, *3D Printing and Additive Manufacturing*. 1 (2014) 1–4. doi:http://doi.org/10.1089/3dp.2013.0002.

[6] V. Matilainen, H. Piili, A. Salminen, T. Syvänen, O. Nyrhilä, Characterization of Process Efficiency Improvement in Laser Additive Manufacturing, *Physics Procedia*. 56 (2014) 317–326. doi:10.1016/j.phpro.2014.08.177.

[7] Additive Manufacturing : stategic research agenda, (2014). http://www.rm-platform.com/linkdoc/AM SRA - February 2014.pdf.

[8] B.N. Turner, S.A. Gold, A review of melt extrusion additive manufacturing processes: II. Materials, dimensional accuracy, and surface roughness, *Rapid Prototyping Journal*. 21 (2015) 250–261. doi:10.1108/RPJ-02-2013-0017.

[9] N. Guo, M.C. Leu, Additive manufacturing: Technology, applications and research needs, *Frontiers of Mechanical Engineering*. 8 (2013) 215–243. doi:10.1007/s11465-013-0248-8.

[10] Wholers, Wohlers Report 2015, *Wholers*. (2015) 1–33. doi:10.1002/ejoc.201200111.

[11] B.P. Conner, G.P. Manogharan, A.N. Martof, L.M. Rodomsky, C.M. Rodomsky, D.C. Jordan, J.W. Limperos, Making sense of 3-D printing: Creating a map of additive manufacturing products and services, *Additive Manufacturing*. 1 (2014) 64–76. doi:10.1016/j.addma.2014.08.005.

[12] W.E. Frazier, Metal additive manufacturing: A review, *Journal of Materials Engineering and Performance*. 23 (2014) 1917–1928. doi:10.1007/s11665-014-0958-z.

[13] Roland Berger, Additive Manufacturing: A game changer for the manufacturing industry?, *Roland Berger Strategy Consultants*. (2013) 33. http://www.rolandberger.com/media/pdf/Roland_Berger_Additive_Manufacturing_20131129.pdf.

[14] Arcam EBM, Arcam brochure, (2017) 1–20.

doi:10.1080/03632415.2015.1027159.
[15] SLM Solutions GmbH, SLM Solutions increases revenue by 2.2 percent in challenging 2017 fiscal year, (n.d.). https://slm-solutions.com/en/investor-relations/announcements/corporate-news/slm-solutions-increases-revenue-22-percent-0/.
[16] A. Digital, Digital Alloys' Guide to Metal Additive Manufacturing – Part 2, (2018). https://www.digitalalloys.com/blog/application-criteria-metal-additive-manufacturing/.
[17] J. Van Humbeeck, B. Vrancken, Re-viewing alloy compositions for selective laser melting, (2017) 1–21.
[18] I.J. Polmear, Light Alloys: From Traditional Alloys to Nanocrystals, Fourth Edi, Oxford, 2006. http://linkinghub.elsevier.com/retrieve/pii/S1044580306002099.
[19] F. Trevisan, F. Calignano, M. Lorusso, J. Pakkanen, A. Aversa, E.P. Ambrosio, M. Lombardi, P. Fino, D. Manfredi, On the Selective Laser Melting (SLM) of the AlSi10Mg Alloy: Process, Microstructure, and Mechanical Properties, (n.d.). doi:10.3390/ma10010076.
[20] F. Calignano, Design optimization of supports for overhanging structures in aluminum and titanium alloys by selective laser melting, *Materials and Design*. 64 (2014) 203–213. doi:10.1016/j.matdes.2014.07.043.
[21] H. Attar, M. Calin, L.C. Zhang, S. Scudino, J. Eckert, Manufacture by selective laser melting and mechanical behavior of commercially pure titanium, *Materials Science and Engineering A*. 593 (2014) 170–177. doi:10.1016/j.msea.2013.11.038.
[22] D. Herzog, V. Seyda, E. Wycisk, C. Emmelmann, Additive manufacturing of metals, *Acta Materialia*. 117 (2016) 371–392. doi:10.1016/j.actamat.2016.07.019.
[23] Renishaw, Our Technology, (n.d.). https://www.renishaw.com/en/our-technology--27362.
[24] F. Calignano, G. Cattano, D. Manfredi, Manufacturing of thin wall structures in AlSi10Mg alloy by laser powder bed fusion through process parameters, *Journal of Materials Processing Technology*. 255 (2018) 773–783. doi:10.1016/j.jmatprotec.2018.01.029.
[25] I. Yadroitsev, P. Bertrand, I. Smurov, Parametric analysis of the selective laser melting process, *Applied Surface Science*. 253 (2007) 8064–8069. doi:10.1016/j.apsusc.2007.02.088.
[26] S.A. Khairallah, A.T. Anderson, A. Rubenchik, W.E. King, Laser powder-bed fusion additive manufacturing: Physics of complex melt flow and formation mechanisms of pores, spatter, and denudation zones, *Acta Materialia*. 108 (2016) 36–45. doi:10.1016/j.actamat.2016.02.014.
[27] I. Yadroitsev, P. Bertrand, G. Antonenkova, S. Grigoriev, I. Smurov, Use of track/layer morphology to develop functional parts by selective laser melting, *Journal of Laser Applications*. 25 (2013) 052003. doi:10.2351/1.4811838.
[28] C. Meier, R.W. Penny, Y. Zou, J.S. Gibbs, A.J. Hart, Thermophysical Phenomena in Metal Additive Manufacturing by Selective Laser Melting: Fundamentals, Modeling, Simulation and Experimentation, *Annual Review of Heat Transfer*. (2017). doi:DOI: 10.1615/AnnualRevHeatTransfer.2018019042.
[29] I. Yadroitsev, Selective laser melting: Direct manufacturing of 3D-objects by selective laser melting of metal powders, LAP LAMBERT, 2009.

doi:10.1007/s13398-014-0173-7.2.
[30] C.D. Boley, S.A. Khairallah, A.M. Rubenchik, Calculation of laser absorption by metal powders in additive manufacturing, *Additive Manufacturing Handbook: Product Development for the Defense Industry*. (2017) 507–517. doi:10.1201/9781315119106.
[31] D. Dai, D. Gu, R. Poprawe, M. Xia, Influence of additive multilayer feature on thermodynamics , stress and microstructure development during laser 3D printing of aluminum-based material, *Science Bulletin*. 62 (2017) 779–787. doi:10.1016/j.scib.2017.05.007.
[32] S. Das, Physical Aspects of Process Control in Selective Laser Sintering of Metals, *Advanced Engineering Materials*. 5 (2003) 701–711. doi:10.1002/adem.200310099.
[33] S.A. Khairallah, A. Anderson, Mesoscopic simulation model of selective laser melting of stainless steel powder, *Journal of Materials Processing Technology*. 214 (2014) 2627–2636. doi:10.1016/j.jmatprotec.2014.06.001.
[34] J. Trapp, A.M. Rubenchik, G. Guss, M.J. Matthews, In situ absorptivity measurements of metallic powders during laser powder-bed fusion additive manufacturing, *Applied Materials Today*. 9 (2017) 341–349. doi:10.1016/j.apmt.2017.08.006.
[35] A. V. Gusarov, J.P. Kruth, Modelling of radiation transfer in metallic powders at laser treatment, *International Journal of Heat and Mass Transfer*. 48 (2005) 3423–3434. doi:10.1016/j.ijheatmasstransfer.2005.01.044.
[36] M. Rombouts, L. Froyen, A. V Gusarov, E.H. Bentefour, C. Glorieux, Photopyroelectric measurement of thermal conductivity of metallic powders, *Journal of Applied Physics*. 97 (2005).
[37] C. Körner, A. Bauereiß, E. Attar, Fundamental consolidation mechanisms during selective beam melting of powders, *Modelling and Simulation in Materials Science and Engineering*. 21 (2013) 085011. doi:10.1088/0965-0393/21/8/085011.
[38] C.J. Ion, Laser Processing of Engineering Materials - Principles, Procedure and Industrial Application, Butterworth-Heinemann, 2005.
[39] T. Zacharia, S.A. David, Computer modeling of arc welds to predict effects of criticalvariables on weld penetration, in: Annu. North Am. Weld. Res. Conf., Columbus, OH (U.S.), 1991.
[40] W.E. King, A.T. Anderson, R.M. Ferencz, N.E. Hodge, C. Kamath, S.A. Khairallah, A.M. Rubenchik, Laser powder bed fusion additive manufacturing of metals; physics, computational, and materials challenges, *Applied Physics Reviews*. 2 (2015) 041304. doi:10.1063/1.4937809.
[41] A. V. Gusarov, I. Yadroitsev, P. Bertrand, I. Smurov, Heat transfer modelling and stability analysis of selective laser melting, *Applied Surface Science*. 254 (2007) 975–979. doi:10.1016/j.apsusc.2007.08.074.
[42] Y.P. Lei, H. Murakawa, Y.W. Shi, X.Y. Li, Numerical analysis of the competitive influence of Marangoni flow and evaporation on heat surface temperature and molten pool shape in laser surface remelting, *Computational Materials Science*. 21 (2001) 276–290. doi:10.1016/S0022-0000(71)80011-9.
[43] N.T. Aboulkhair, N.M. Everitt, I. Ashcroft, C. Tuck, Reducing porosity in AlSi10Mg parts processed by selective laser melting, *Additive Manufacturing*. 1 (2014) 77–86. doi:10.1016/j.addma.2014.08.001.
[44] S.I. Anisimov, V.A. Khokhlov, Instabilities in Laser-matter Interaction, CRC press, Boca Raton, Florida, 1995.

[45] R. Rai, J.W. Elmer, T.A. Palmer, T. DebRoy, Heat transfer and fluid flow during keyhole mode laser welding of tantalum, Ti–6Al–4V, 304L stainless steel and vanadium, *Journal of Physics D: Applied Physics*. 40 (2007) 5753. http://stacks.iop.org/0022-3727/40/i=18/a=037.

[46] Y.J. Liu, S.J. Li, H.L. Wang, W.T. Hou, Y.L. Hao, R. Yang, T.B. Sercombe, L.C. Zhang, Microstructure, defects and mechanical behavior of beta-type titanium porous structures manufactured by electron beam melting and selective laser melting, *Acta Materialia*. 113 (2016) 56–67. doi:10.1016/j.actamat.2016.04.029.

[47] W.E. King, H.D. Barth, V.M. Castillo, G.F. Gallegos, J.W. Gibbs, D.E. Hahn, C. Kamath, A.M. Rubenchik, Observation of keyhole-mode laser melting in laser powder-bed fusion additive manufacturing, *Journal of Materials Processing Technology*. 214 (2014) 2915–2925. doi:10.1016/j.jmatprotec.2014.06.005.

[48] M. Simonelli, C. Tuck, N.T. Aboulkhair, I. Maskery, I. Ashcroft, R.D. Wildman, R. Hague, A Study on the Laser Spatter and the Oxidation Reactions During Selective Laser Melting of 316L Stainless Steel, Al-Si10-Mg, and Ti-6Al-4V, *Metallurgical and Materials Transactions A: Physical Metallurgy and Materials Science*. 46 (2015) 3842–3851. doi:10.1007/s11661-015-2882-8.

[49] D. Wang, S. Wu, F. Fu, S. Mai, Y. Yang, Y. Liu, C. Song, Mechanisms and characteristics of spatter generation in SLM processing and its effect on the properties, *Materials and Design*. 117 (2017) 121–130. doi:10.1016/j.matdes.2016.12.060.

[50] D.S. Nguyen, H.S. Park, C.M. Lee, Effect of cleaning gas stream on products in selective laser melting, *Materials and Manufacturing Processes*. 00 (2018) 1–7. doi:10.1080/10426914.2018.1512132.

[51] Y. Liu, Y. Yang, S. Mai, D. Wang, C. Song, Investigation into spatter behavior during selective laser melting of AISI 316L stainless steel powder, *Materials and Design*. 87 (2015) 797–806. doi:10.1016/j.matdes.2015.08.086.

[52] J.P. Kruth, G. Levy, F. Klocke, T.H.C. Childs, Consolidation phenomena in laser and powder-bed based layered manufacturing, *CIRP Annals - Manufacturing Technology*. 56 (2007) 730–759. doi:10.1016/j.cirp.2007.10.004.

[53] A. V. Gusarov, I. Smurov, Modeling the interaction of laser radiation with powder bed at selective laser melting, *Physics Procedia*. 5 (2010) 381–394. doi:10.1016/j.phpro.2010.08.065.

[54] E. Louvis, P. Fox, C.J. Sutcliffe, Selective laser melting of aluminium components, *Journal of Materials Processing Technology*. 211 (2011) 275–284. doi:10.1016/j.jmatprotec.2010.09.019.

[55] M.E. Glicksman, Principles of Solidification: An Introduction to Modern Casting and Crystal Growth Concepts, Springer New York, 2010. https://books.google.it/books?id=Df7PjwEACAAJ.

[56] J.N. DuPont, Fundamentals of Weld Solidification, *ASM Handbook Vol 6, Welding, Brazing and Soldering*. 6 (2011) 96–114. doi:10.1361/asmhba000.

[57] D. Gu, Y.C. Hagedorn, W. Meiners, G. Meng, R.J.S. Batista, K. Wissenbach, R. Poprawe, Densification behavior, microstructure evolution, and wear performance of selective laser melting processed commercially pure titanium, *Acta Materialia*. 60 (2012) 3849–3860. doi:10.1016/j.actamat.2012.04.006.

[58] T. DebRoy, H.L. Wei, J.S. Zuback, T. Mukherjee, J.W. Elmer, J.O. Milewski, A.M. Beese, A. Wilson-Heid, A. De, W. Zhang, Additive manufacturing of metallic components – Process, structure and properties, *Progress in Materials Science*. 92 (2018) 112–224. doi:10.1016/j.pmatsci.2017.10.001.

[59] H.L. Wei, J.W. Elmer, T. Debroy, Origin of grain orientation during solidification of an aluminum alloy, *Acta Materialia*. 115 (2016) 123–131. doi:10.1016/j.actamat.2016.05.057.

[60] L. Thijs, K. Kempen, J.P. Kruth, J. Van Humbeeck, Fine-structured aluminium products with controllable texture by selective laser melting of pre-alloyed AlSi10Mg powder, *Acta Materialia*. 61 (2013) 1809–1819. doi:10.1016/j.actamat.2012.11.052.

[61] K.G. Prashanth, J. Eckert, Formation of metastable cellular microstructures in selective laser melted alloys, *Journal of Alloys and Compounds*. 707 (2017) 27–34. doi:10.1016/j.jallcom.2016.12.209.

[62] T. KIMURA, T. NAKAMOTO, Microstructures and Mechanical Properties of Al–10%Si–0.4%Mg Fabricated by Selective Laser Melting, *Journal of the Japan Society of Powder and Powder Metallurgy*. 61 (2014) 531–537. doi:10.2497/jjspm.61.531.

[63] I.A. Roberts, C.J. Wang, R. Esterlein, M. Stanford, D.J. Mynors, A three-dimensional finite element analysis of the temperature field during laser melting of metal powders in additive layer manufacturing, *International Journal of Machine Tools and Manufacture*. 49 (2009) 916–923. doi:10.1016/j.ijmachtools.2009.07.004.

[64] Y. Li, D. Gu, Parametric analysis of thermal behavior during selective laser melting additive manufacturing of aluminum alloy powder, *Materials and Design*. 63 (2014) 856–867. doi:10.1016/j.matdes.2014.07.006.

[65] E.J. Lavernia, T.S. Srivatsan, The rapid solidification processing of materials: Science, principles, technology, advances, and applications, *Journal of Materials Science*. 45 (2010) 287–325. doi:10.1007/s10853-009-3995-5.

[66] E.A. Jägle, P.-P. Choi, J. Van Humbeeck, D. Raabe, Precipitation and austenite reversion behavior of a maraging steel produced by selective laser melting, *Journal of Material Research*. 29 (2014) 2072–2079. doi:10.1557/jmr.2014.204.

[67] L. Thijs, F. Verhaeghe, T. Craeghs, J. Van Humbeeck, J.P. Kruth, A study of the microstructural evolution during selective laser melting of Ti-6Al-4V, *Acta Materialia*. 58 (2010) 3303–3312. doi:10.1016/j.actamat.2010.02.004.

[68] B. Vrancken, L. Thijs, J.P. Kruth, J. Van Humbeeck, Heat treatment of Ti6Al4V produced by Selective Laser Melting: Microstructure and mechanical properties, *Journal of Alloys and Compounds*. 541 (2012) 177–185. doi:10.1016/j.jallcom.2012.07.022.

[69] E.O. Olakanmi, R.F. Cochrane, K.W. Dalgarno, A review on selective laser sintering/melting (SLS/SLM) of aluminium alloy powders: Processing, microstructure, and properties, *Progress in Materials Science*. 74 (2015) 401–477. doi:10.1016/j.pmatsci.2015.03.002.

[70] D. Manfredi, F. Calignano, M. Krishnan, R. Canali, E.P. Ambrosio, E. Atzeni, From powders to dense metal parts: Characterization of a commercial alsimg alloy processed through direct metal laser sintering, *Materials*. 6 (2013) 856–869. doi:10.3390/ma6030856.

[71] W. Xu, M. Brandt, S. Sun, J. Elambasseril, Q. Liu, K. Latham, K. Xia, M.

Qian, Additive manufacturing of strong and ductile Ti-6Al-4V by selective laser melting via in situ martensite decomposition, *Acta Materialia*. 85 (2015) 74–84. doi:10.1016/j.actamat.2014.11.028.

[72] T.B. Sercombe, X. Li, Selective laser melting of aluminium and aluminium metal matrix composites: review, *Materials Technology*. 00 (2015) 1753555715Y.000. doi:10.1179/1753555715Y.0000000078.

[73] A. Hussein, L. Hao, C. Yan, R. Everson, Finite element simulation of the temperature and stress fields in single layers built without-support in selective laser melting, *Materials and Design*. 52 (2013) 638–647. doi:10.1016/j.matdes.2013.05.070.

[74] J. Günther, F. Brenne, M. Droste, M. Wendler, O. Volkova, H. Biermann, T. Niendorf, Design of novel materials for additive manufacturing - Isotropic microstructure and high defect tolerance, *Scientific Reports*. 8 (2018) 1–14. doi:10.1038/s41598-018-19376-0.

[75] E.A. Jägle, Z. Sheng, L. Wu, L. Lu, J. Risse, A. Weisheit, D. Raabe, Precipitation Reactions in Age-Hardenable Alloys During Laser Additive Manufacturing, *Jom*. 68 (2016) 943–949. doi:10.1007/s11837-015-1764-2.

[76] L. Zheng, Y. Liu, S. Sun, H. Zhang, Selective laser melting of Al-8.5Fe-1.3V-1.7Si alloy: Investigation on the resultant microstructure and hardness, *Chinese Journal of Aeronautics*. 28 (2015) 564–569. doi:10.1016/j.cja.2015.01.013.

[77] L. Thijs, F. Verhaeghe, T. Craeghs, J. Van Humbeeck, J.P. Kruth, A study of the microstructural evolution during selective laser melting of Ti-6Al-4V, *Acta Materialia*. 58 (2010) 3303–3312. doi:10.1016/j.actamat.2010.02.004.

[78] J.P. Kruth, J. Deckers, E. Yasa, R. Wauthlé, Assessing and comparing influencing factors of residual stresses in selective laser melting using a novel analysis method, *Proceedings of the Institution of Mechanical Engineers, Part B: Journal of Engineering Manufacture*. 226 (2012) 980–991. doi:10.1177/0954405412437085.

[79] P. Mercelis, J.P. Kruth, Residual stresses in selective laser sintering and selective laser melting, *Rapid Prototyping Journal*. 12 (2006) 254–265. doi:10.1108/13552540610707013.

[80] K. Kempen, B. Vrancken, S. Buls, L. Thijs, J. Van Humbeeck, J.-P. Kruth, Selective Laser Melting of Crack-Free High Density M2 High Speed Steel Parts by Baseplate Preheating, *Journal of Manufacturing Science and Engineering*. 136 (2014) 061026. doi:10.1115/1.4028513.

[81] S. Suresh, A.E. Giannakopoulos, A new method for estimating residual stresses by instrumented sharp indentation, *Acta Materialia*. 46 (1998) 5755–5767. doi:10.1016/S1359-6454(98)00226-2.

[82] M.B. Prime, Cross-Sectional Mapping of Residual Stresses by Measuring the Surface Contour After a Cut, *Journal of Engineering Materials and Technology*. 123 (2001) 162. doi:10.1115/1.1345526.

[83] T. Watkins, H. Bilheux, K. An, A. Payzant, R. Dehoff, C. Duty, W. Peter, C. Blue, C. Brice, Neutron Characterization for Additive Manufacturing, *Advanced Materials & Processes*. (n.d.) 23–27.

[84] ASTM E837-13a, Standard Test Method for Determining Residual Stresses by the Hole-Drilling Strain-Gage Method, *ASTM Int*. (2013). doi:10.1520/E0837.

[85] M.F. Zaeh, G. Branner, Investigations on residual stresses and deformations in selective laser melting, *Production Engineering*. 4 (2010) 35–45. doi:10.1007/s11740-009-0192-y.

[86] S. Kou, Solidification and liquation cracking issues in welding, *Jom*. 55 (2003) 37–42. doi:10.1007/s11837-003-0137-4.
[87] F.M. Ghaini, M. Sheikhi, M.J. Torkamany, J. Sabbaghzadeh, The relation between liquation and solidification cracks in pulsed laser welding of 2024 aluminium alloy, *Materials Science and Engineering A*. 519 (2009) 167–171. doi:10.1016/j.msea.2009.04.056.
[88] J.H. Martin, B.D. Yahata, J.M. Hundley, J.A. Mayer, T.A. Schaedler, T.M. Pollock, 3D printing of high-strength aluminium alloys, *Nature*. 549 (2017) 365–369. doi:10.1038/nature23894.
[89] H. Zhang, H. Zhu, X. Nie, J. Yin, Z. Hu, X. Zeng, Effect of Zirconium addition on crack, microstructure and mechanical behavior of selective laser melted Al-Cu-Mg alloy, *Scripta Materialia*. 134 (2017) 6–10. doi:10.1016/j.scriptamat.2017.02.036.
[90] S.Z. Uddin, L.E. Murr, C.A. Terrazas, P. Morton, D.A. Roberson, R.B. Wicker, Processing and characterization of crack-free aluminum 6061 using high-temperature heating in laser powder bed fusion additive manufacturing, *Additive Manufacturing*. 22 (2018) 405–415. doi:10.1016/j.addma.2018.05.047.
[91] N. Kaufmann, M. Imran, T.M. Wischeropp, C. Emmelmann, S. Siddique, F. Walther, Influence of process parameters on the quality of aluminium alloy en AW 7075 using Selective Laser Melting (SLM), *Physics Procedia*. 83 (2016) 918–926. doi:10.1016/j.phpro.2016.08.096.
[92] G. Marchese, E. Bassini, A. Aversa, Study of the Microstructure and Cracking Mechanisms of Hastelloy X Produced by Laser Powder Bed Fusion, *Materials*. 11 (2018) 106. doi:10.3390/ma11010106.
[93] M. Cloots, P.J. Uggowitzer, K. Wegener, Investigations on the microstructure and crack formation of IN738LC samples processed by selective laser melting using Gaussian and doughnut profiles, *Materials and Design*. 89 (2016) 770–784. doi:10.1016/j.matdes.2015.10.027.
[94] M.L. Montero, R. Mertens, B. Vrancken, X. Wang, B. Van Hooreweder, J. Kruth, J. Van Humbeeck, Changing the alloy composition of Al7075 for better processability by selective laser melting, *Journal of Materials Processing Tech.* 238 (2016) 437–445. doi:10.1016/j.jmatprotec.2016.08.003.
[95] J. Dawes, R. Bowerman, R. Trepleton, Introduction to the Additive Manufacturing Powder Metallurgy Supply Chain, *Johnson Matthey Technology Review*. 59 (2015) 243–256. doi:10.1595/205651315X688686.
[96] R. Li, Y. Shi, Z. Wang, L. Wang, J. Liu, W. Jiang, Densification behavior of gas and water atomized 316L stainless steel powder during selective laser melting, *Applied Surface Science*. 256 (2010) 4350–4356. doi:10.1016/j.apsusc.2010.02.030.
[97] E. Louvis, P. Fox, C.J. Sutcliffe, Selective laser melting of aluminium components, *Journal of Materials Processing Technology*. 211 (2011) 275–284. doi:10.1016/j.jmatprotec.2010.09.019.
[98] S. Hoeges, A. Zwiren, C. Schade, Additive manufacturing using water atomized steel powders, *Metal Powder Report*. 72 (2017) 111–117. doi:10.1016/j.mprp.2017.01.004.
[99] D. Gu, Z. Wang, Y. Shen, Q. Li, Y. Li, In-situ TiC particle reinforced Ti-Al matrix composites: Powder preparation by mechanical alloying and Selective Laser Melting behavior, *Applied Surface Science*. 255 (2009) 9230–9240. doi:10.1016/j.apsusc.2009.07.008.

[100] F. Deirmina, B. AlMangour, D. Grzesiak, M. Pellizzari, H13–partially stabilized zirconia nanocomposites fabricated by high-energy mechanical milling and selective laser melting, *Materials and Design*. 146 (2018) 286–297. doi:10.1016/j.matdes.2018.03.017.
[101] B. AlMangour, D. Grzesiak, J.M. Yang, Nanocrystalline TiC-reinforced H13 steel matrix nanocomposites fabricated by selective laser melting, *Materials and Design*. 96 (2016) 150–161. doi:10.1016/j.matdes.2016.02.022.
[102] H. Attar, K.G. Prashanth, L.C. Zhang, M. Calin, I. V. Okulov, S. Scudino, C. Yang, J. Eckert, Effect of powder particle shape on the properties of in situ Ti-TiB composite materials produced by selective laser melting, *Journal of Materials Science and Technology*. 31 (2015) 1001–1005. doi:10.1016/j.jmst.2015.08.007.
[103] C. Suryanarayana, Mechanical alloying and milling, *Progress in Materials Science*. 46 (2001) 1–184. doi:10.1016/S0079-6425(99)00010-9.
[104] P. Sun, Z.Z. Fang, Y. Zhang, Y. Xia, Review of the Methods for Production of Spherical Ti and Ti Alloy Powder, *Jom*. 69 (2017) 1853–1860. doi:10.1007/s11837-017-2513-5.
[105] A.B. Spierings, N. Herres, G. Levy, Influence of the particle size distribution on surface quality and mechanical properties in AM steel parts, *Rapid Prototyping Journal*. 17 (2011) 195–202. doi:10.1108/13552541111124770.
[106] B. Liu, R. Wildman, C. Tuck, I. Ashcroft, R. Hague, Investigation the Effect of Particle Size Distribution on Processing Parameters Optimisation in Selective Laser Melting Process, *International Solid Feeform Fabrication Symposium*. (2011) 227–238. doi:10.1017/CBO9781107415324.004.
[107] M.L. Günther, F. Schwer, C. Seidel, G. Reinhart, Effects on Properties of Metal Powders for Laser Beam Melting Along the Powder Process Chain, *Frauhofer Direct Digital Manufacturing Conference*. (2016) 1–8.
[108] W.J. Sames, F.A. List, S. Pannala, R.R. Dehoff, S.S. Babu, The metallurgy and processing science of metal additive manufacturing, *International Materials Reviews*. 61 (2016) 315–360. doi:10.1080/09506608.2015.1116649.
[109] K.J.P. Kempen K., Thijs L., Yasa E., Badrossamay M., Verheecke W., Process Optimization and Microstructural Analysis for Selective Laser Melting of AlSi10Mg, in: Proc. 26th Int. Solid Free. Fabr. Symp., 2011: pp. 484–495.
[110] C. Weingarten, D. Buchbinder, N. Pirch, W. Meiners, K. Wissenbach, R. Poprawe, Formation and reduction of hydrogen porosity during selective laser melting of AlSi10Mg, *Journal of Materials Processing Technology*. 221 (2015) 112–120. doi:10.1016/j.jmatprotec.2015.02.013.
[111] X.P. Li, K.M. O'Donnell, T.B. Sercombe, Selective laser melting of Al-12Si alloy: Enhanced densification via powder drying, *Additive Manufacturing*. 10 (2016) 10–14. doi:10.1016/j.addma.2016.01.003.
[112] I. Yadroitsev, P. Krakhmalev, I. Yadroitsava, S. Johansson, I. Smurov, Energy input effect on morphology and microstructure of selective laser melting single track from metallic powder, *Journal of Materials Processing Technology*. 213 (2013) 606–613. doi:10.1016/j.jmatprotec.2012.11.014.
[113] C. Kamath, B. El-dasher, G.F. Gallegos, W.E. King, A. Sisto, Density of Additively-Manufactured, 316L SS Parts Using Laser Powder-Bed Fusion at Powers Up to 400W, *International Journal of Additive Manufacturing Techologies*. (2013). doi:10.2172/1116929.
[114] N.K. Tolochko, Y. V. Khlopkov, S.E. Mozzharov, M.B. Ignatiev, T. Laoui,

V.I. Titov, Absorptance of powder materials suitable for laser sintering, *Rapid Prototyping Journal*. 6 (2000) 155–161. doi:10.1108/13552540010337029.
[115] A. Bauereiß, T. Scharowsky, C. Körner, Defect generation and propagation mechanism during additive manufacturing by selective beam melting, *Journal of Materials Processing Tech.* 214 (2014) 2522–2528. doi:10.1016/j.jmatprotec.2014.05.002.
[116] Conceptlaser, Mlab cusing R Metal laser melting system, (2016). https://www.concept-laser.de/fileadmin/Machine_brochures/CL_Mlab_cusing_R_DS_EN_A4_2_v1.pdf.
[117] Eosint, M270 DMLS system, (2017). https://dmlstechnology.com/images/pdf/EOSINT_M_270.pdf.
[118] D. Buchbinder, H. Schleifenbaum, S. Heidrich, W. Meiners, J. Bültmann, High power Selective Laser Melting (HP SLM) of aluminum parts, *Physics Procedia*. 12 (2011) 271–278. doi:10.1016/j.phpro.2011.03.035.
[119] L.E. Loh, Z.H. Liu, D.Q. Zhang, M. Mapar, S.L. Sing, C.K. Chua, W.Y. Yeong, Selective Laser Melting of aluminium alloy using a uniform beam profile, *Virtual and Physical Prototyping*. 9 (2014) 11–16. doi:10.1080/17452759.2013.869608.
[120] F. Calignano, D. Manfredi, E.P. Ambrosio, L. Iuliano, P. Fino, Influence of process parameters on surface roughness of aluminum parts produced by DMLS, *International Journal of Advanced Manufacturing Technology*. 67 (2013) 2743–2751. doi:10.1007/s00170-012-4688-9.
[121] N. Read, W. Wang, K. Essa, M.M. Attallah, Selective laser melting of AlSi10Mg alloy: Process optimisation and mechanical properties development, *Materials and Design*. 65 (2015) 417–424. doi:10.1016/j.matdes.2014.09.044.
[122] X. Su, Y. Yang, Research on track overlapping during Selective Laser Melting of powders, *Journal of Materials Processing Tech.* 212 (2012) 2074–2079. doi:10.1016/j.jmatprotec.2012.05.012.
[123] N. Read, W. Wang, K. Essa, M.M. Attallah, Selective laser melting of AlSi10Mg alloy: Process optimisation and mechanical properties development, *Materials and Design*. 65 (2015) 417–424. doi:10.1016/j.matdes.2014.09.044.
[124] I. Yadroitsev, I. Smurov, Selective laser melting technology : from the single laser melted track stability to 3D parts of complex shape, *Physics Procedia*. 5 (2010) 551–560. doi:10.1016/j.phpro.2010.08.083.
[125] W.J. Sames, F. Medina, W.H. Peter, S.S. Babu, R.R. Dehoff, Effect of process control and powder quality on inconel 718 produced using electron beam melting, *8th International Symposium on Superalloy 718 and Derivatives 2014*. (2014) 409–423. doi:10.1002/9781119016854.ch32.
[126] E.O. Olakanmi, R.F. Cochrane, K.W. Dalgarno, Densification mechanism and microstructural evolution in selective laser sintering of Al-12Si powders, *Journal of Materials Processing Technology*. 211 (2011) 113–121. doi:10.1016/j.jmatprotec.2010.09.003.
[127] A. Simchi, Direct laser sintering of metal powders: Mechanism, kinetics and microstructural features, *Materials Science and Engineering A*. 428 (2006) 148–158. doi:10.1016/j.msea.2006.04.117.
[128] H. Gu, H. Gong, P. Deepankar, R. Khalid, S. Thomas, B. Stucker, Influences of Energy Density on Porosity and Microstructure of Selective Laser Melted

17-4PH Stainless Steel, *Journal of Chemical Information and Modeling*. 53 (2013) 1689–1699. doi:10.1017/CBO9781107415324.004.
[129] H. Gong, K. Rafi, H. Gu, T. Starr, B. Stucker, Analysis of defect generation in Ti – 6Al – 4V parts made using powder bed fusion additive manufacturing processes, *Additive Manufacturing*. 1–4 (2014) 87–98. doi:10.1016/j.addma.2014.08.002.
[130] H. Meier, C. Haberland, Experimental studies on selective laser melting of metallic parts, *Materialwissenschaft Und Werkstofftechnik*. 39 (2008) 665–670. doi:10.1002/mawe.200800327.
[131] E.O. Olakanmi, Selective laser sintering/melting (SLS/SLM) of pure Al, Al-Mg, and Al-Si powders: Effect of processing conditions and powder properties, *Journal of Materials Processing Technology*. 213 (2013) 1387–1405. doi:10.1016/j.jmatprotec.2013.03.009.
[132] L. Wang, Q.S. Wei, Y.S. Shi, J.H. Liu, W.T. He, Experimental Investigation into the Single-Track of Selective Laser Melting of IN625, *Advanced Materials Research*. 233–235 (2011) 2844–2848. doi:10.4028/www.scientific.net/AMR.233-235.2844.
[133] I. Yadroitsev, I. Yadroitsava, P. Bertrand, I. Smurov, Factor analysis of selective laser melting process parameters and geometrical characteristics of synthesized single tracks, *Rapid Prototyping Journal*. 18 (2012) 201–208. doi:10.1108/13552541211218117.
[134] U. Scipioni Bertoli, A.J. Wolfer, M.J. Matthews, J.P.R. Delplanque, J.M. Schoenung, On the limitations of Volumetric Energy Density as a design parameter for Selective Laser Melting, *Materials and Design*. 113 (2017) 331–340. doi:10.1016/j.matdes.2016.10.037.
[135] B. Cheng, S. Shrestha, K. Chou, Stress and deformation evaluations of scanning strategy effect in selective laser melting, *Additive Manufacturing*. 12 (2016) 240–251. doi:10.1016/j.addma.2016.05.007.
[136] H. Ali, H. Ghadbeigi, K. Mumtaz, Effect of scanning strategies on residual stress and mechanical properties of Selective Laser Melted Ti6Al4V, *Materials Science and Engineering A*. 712 (2018) 175–187. doi:10.1016/j.msea.2017.11.103.
[137] J. Song, W. Wu, L. Zhang, B. He, L. Lu, X. Ni, Q. Long, G. Zhu, Role of scanning strategy on residual stress distribution in Ti-6Al-4V alloy prepared by selective laser melting, *Optik*. 170 (2018) 342–352. doi:10.1016/j.ijleo.2018.05.128.
[138] K. Guan, Z. Wang, M. Gao, X. Li, X. Zeng, Effects of processing parameters on tensile properties of selective laser melted 304 stainless steel, *Materials and Design*. 50 (2013) 581–586. doi:10.1016/j.matdes.2013.03.056.
[139] P.C. Collins, D.A. Brice, P. Samimi, I. Ghamarian, H.L. Fraser, Microstructural Control of Additively Manufactured Metallic Materials, *Annual Review of Materials Research*. 46 (2016) 63–91. doi:10.1146/annurev-matsci-070115-031816.
[140] D. Buchbinder, W. Meiners, K. Wissenbach, R. Poprawe, Selective laser melting of aluminum die-cast alloy—Correlations between process parameters, solidification conditions, and resulting mechanical properties, *Journal of Laser Applications*. 27 (2015) S29205. doi:10.2351/1.4906389.
[141] Y. Shi, K. Yang, S.K. Kairy, F. Palm, X. Wu, P.A. Rometsch, Effect of platform temperature on the porosity, microstructure and mechanical properties of an Al–Mg–Sc–Zr alloy fabricated by selective laser melting, *Materials Science and Engineering A*. 732 (2018) 41–52.

doi:10.1016/j.msea.2018.06.049.
[142] X.J. Wang, L.C. Zhang, M.H. Fang, T.B. Sercombe, The effect of atmosphere on the structure and properties of a selective laser melted Al-12Si alloy, *Materials Science and Engineering A*. 597 (2014) 370–375. doi:10.1016/j.msea.2014.01.012.
[143] B. Zhang, L. Dembinski, C. Coddet, The study of the laser parameters and environment variables effect on mechanical properties of high compact parts elaborated by selective laser melting 316L powder, *Materials Science and Engineering A*. 584 (2013) 21–31. doi:10.1016/j.msea.2013.06.055.
[144] B. Ferrar, L. Mullen, E. Jones, R. Stamp, C.J. Sutcliffe, Gas flow effects on selective laser melting (SLM) manufacturing performance, *Journal of Materials Processing Technology*. 212 (2012) 355–364. doi:10.1016/j.jmatprotec.2011.09.020.
[145] E.O. Olakanmi, R.F. Cochrane, K.W. Dalgarno, A review on selective laser sintering/melting (SLS/SLM) of aluminium alloy powders: Processing, microstructure, and properties, *Progress in Materials Science*. 74 (2015) 401–477. doi:10.1016/j.pmatsci.2015.03.002.
[146] S. Gorsse, C. Hutchinson, M. Gouné, R. Banerjee, Additive manufacturing of metals: a brief review of the characteristic microstructures and properties of steels, Ti-6Al-4V and high-entropy alloys, *Science and Technology of Advanced Materials*. 18 (2017) 584–610. doi:10.1080/14686996.2017.1361305.
[147] EOS GmbH - Electro Optical Systems, Materials for Metal Additive Manufacturing LPBF, 49 (2014) 1–5. https://cdn0.scrvt.com/eos/public/8837de942d78d3b3/4e099c3a857fdddca4be9d59fbb1cd74/EOS_Aluminium_AlSi10Mg_en.pdf.
[148] LPW, Metal powders from LPW, (n.d.). https://www.lpwtechnology.com/wp-content/uploads/2016/11/LPW_Powders_Brochure.pdf.
[149] APWorks, Scalmalloy® - Aluminum powder at its best, (n.d.). https://apworks.de/en/scalmalloy-3/.
[150] A20X, A20X^{TM} POWDER, (n.d.). http://a20x.com/powder/.
[151] Progold3D, Precious metals, (2019). https://www.progol3d.com/servicebureau#hollow.
[152] D. Zito, V. Allodi, F. Trevisan, Potential and innovation of Selective Laser Melting technique in platinum jewelry production, in: St. Fe Symp., 2018: pp. 625–684. https://www.dropbox.com/s/pxdp4l03d9osoxo/Zito_Damiano.pdf?dl=0.
[153] Wolfmet, Case Study Wolfmet 3D Printed Tungsten Collimator, (2017). https://www.wolfmet.com/news/wolfmet-announces-new-3d-additive-manufacturing-capability-for-tungsten-alloy-products/%0Ahttp://www.wolfmet.com/wp-content/uploads/2017/07/Wolfmet-3D-and-DEPICT-Case-Study-1.pdf.
[154] MaterialsToday, Tantalum powder success for biomedical applications, (2016). doi:10.1007/978-981-13-2724-7.
[155] 3D metal Printing, Green-Laser Printing of Pure Copper and Other Precious Metals, (n.d.). https://www.3dmpmag.com/magazine/article/?/2018/12/3/Green-Laser_Printing_of_Pure_Copper_and_Other_Precious_Metals.
[156] Concept Laser, CL 80CU Copper alloy, (n.d.). https://www.ge.com/additive/sites/default/files/2018-

12/CLMAT_80CU_DS_EN_US_2_v1.pdf.
[157] P. Bordeenithikasem, M. Stolpe, A. Elsen, D.C. Hofmann, Glass forming ability, flexural strength, and wear properties of additively manufactured Zr-based bulk metallic glasses produced through laser powder bed fusion, *Additive Manufacturing*. 21 (2018) 312–317. doi:10.1016/j.addma.2018.03.023.
[158] Exmet, Additive manufacturing of bulk mettalic glass. Any thickness. Any shape. Any alloy, (n.d.). http://www.exmet.se/.
[159] Meterialise, Titanium Inserts for Spacecraft: 66% Lighter with Metal 3D Printing, (n.d.). https://www.materialise.com/en/cases/titanium-inserts-for-spacecraft-66-lighter-metal-3d-printing.
[160] Concept Laser, CL 30AL - AlSi12 Aluminum alloy, (n.d.). https://www.ge.com/additive/sites/default/files/2018-12/CLMAT_30_31AL_DS_EN_US_2_v1.pdf.
[161] K.G. Prashanth, S. Scudino, H.J. Klauss, K.B. Surreddi, L. Lober, Z. Wang, A.K. Chaubey, U. Kuhn, J. Eckert, Microstructure and mechanical properties of Al-12Si produced by selective laser melting: Effect of heat treatment, *Materials Science and Engineering A*. 590 (2014) 153–160. doi:10.1016/j.msea.2013.10.023.
[162] Oerlicon, Additive Manufacturing Solutions, (n.d.). https://www.oerlikon.com/am/en/offerings/additive-manufacturing/design-application-engineering/.
[163] J.H. Rao, Y. Zhang, X. Fang, Y. Chen, X. Wu, C.H.J. Davies, The origins for tensile properties of selective laser melted aluminium alloy A357, *Additive Manufacturing*. 17 (2017) 113–122. doi:10.1016/j.addma.2017.08.007.
[164] H. Rao, S. Giet, K. Yang, X. Wu, C.H.J. Davies, The influence of processing parameters on aluminium alloy A357 manufactured by Selective Laser Melting, *Materials and Design*. 109 (2016) 334–346. doi:10.1016/j.matdes.2016.07.009.
[165] K. Kempen, L. Thijs, J. Van Humbeeck, J.-P. Kruth, Processing AlSi10Mg by selective laser melting: parameter optimisation and material characterisation, *Materials Science and Technology*. 31 (2015) 917–923. doi:10.1179/1743284714Y.0000000702.
[166] M. Krishnan, E. Atzeni, R. Canali, D. Manfredi, F. Calignano, E.P. Ambrosio, L. Iuliano, On the effect of process parameters on properties of AlSi10Mg parts produced by DMLS, *Rapid Prototyping Journal*. (2014) manuscript accepted. doi:10.1108/RPJ-03-2013-0028.
[167] M. Liu, N. Takata, A. Suzuki, M. Kobashi, Microstructural characterization of cellular AlSi10Mg alloy fabricated by selective laser melting, *Materials and Design*. 157 (2018) 478–491. doi:10.1016/j.matdes.2018.08.005.
[168] N.T. Aboulkhair, I. Maskery, C. Tuck, I. Ashcroft, N.M. Everitt, The microstructure and mechanical properties of selectively laser melted AlSi10Mg: the effect of a conventional T6-like heat treatment, *Materials Science and Engineering: A*. (2016). doi:10.1016/j.msea.2016.04.092.
[169] N.T. Aboulkhair, I. Maskery, C. Tuck, I. Ashcroft, N.M. Everitt, Improving the fatigue behaviour of a selectively laser melted aluminium alloy: Influence of heat treatment and surface quality, *Materials Science and Engineering: A*. 104 (2016) 174–182. doi:10.1016/j.msea.2016.04.092.
[170] K. Kempen, L. Thijs, J. Van Humbeeck, J.P. Kruth, Mechanical Properties of AlSi10Mg Produced by Selective Laser Melting, *Physics Procedia*. 39

(2012) 439–446. doi:10.1016/j.phpro.2012.10.059.
[171] K. Kempen, L. Thijs, J. Van Humbeeck, J.-P. Kruth, Mechanical Properties of AlSi10Mg Produced by Selective Laser Melting, *Physics Procedia*. 39 (2012) 439–446. doi:10.1016/j.phpro.2012.10.059.
[172] W. Li, S. Li, J. Liu, A. Zhang, Y. Zhou, Q. Wei, C. Yan, Y. Shi, Effect of heat treatment on AlSi10Mg alloy fabricated by selective laser melting: Microstructure evolution, mechanical properties and fracture mechanism, *Materials Science and Engineering A*. 663 (2016) 116–125. doi:10.1016/j.msea.2016.03.088.
[173] M. Cabrini, S. Lorenzi, T. Pastore, S. Pellegrini, C. Testa, D. Manfredi, F. Calignano, P. Fino, G. Cattano, Evaluation of corrosion resistance of aluminum silicon alloys manufactured by LPBF, *La Metallurgia Italiana*. 109 (2017) 123–126.
[174] M. Cabrini, S. Lorenzi, T. Pastore, S. Pellegrini, D. Manfredi, P. Fino, S. Biamino, C. Badini, Evaluation of corrosion resistance of Al – 10Si – Mg alloy obtained by means of Direct Metal Laser Sintering, *Journal of Materials Processing Tech.* 231 (2016) 326–335. doi:10.1016/j.jmatprotec.2015.12.033.
[175] Y. Ding, J.A. Muñiz-Lerma, M. Trask, S. Chou, A. Walker, M. Brochu, Microstructure and mechanical property considerations in additive manufacturing of aluminum alloys, *MRS Bulletin*. 41 (2016) 745–751. doi:10.1557/mrs.2016.214.
[176] J.J. Lewandowski, M. Seifi, Metal Additive Manufacturing: A Review of Mechanical Properties, *Annual Review of Materials Research*. 46 (2016) 151–186. doi:10.1146/annurev-matsci-070115-032024.
[177] L. Denti, Additive Manufactured A357.0 Samples Using the Laser Powder Bed Fusion Technique: Shear and Tensile Performance, *Metals*. 8 (2018) 670. doi:10.3390/met8090670.
[178] J. Royset, Scandium in Aluminium alloys overview: Physical Metallurgy, Properties and applications, *Metallurgical Science AndTechnology*. 25 (2007) 11–21.
[179] Y. Zhang, T.T. Zuo, Z. Tang, M.C. Gao, K.A. Dahmen, P.K. Liaw, Z.P. Lu, Microstructures and properties of high-entropy alloys, *Progress in Materials Science*. 61 (2014) 1–93. doi:10.1016/j.pmatsci.2013.10.001.
[180] Y.D. Wu, Y.H. Cai, T. Wang, J.J. Si, J. Zhu, Y.D. Wang, X.D. Hui, A refractory Hf25Nb25Ti25Zr25high-entropy alloy with excellent structural stability and tensile properties, *Materials Letters*. 130 (2014) 277–280. doi:10.1016/j.matlet.2014.05.134.
[181] Y. Brif, M. Thomas, I. Todd, The use of high-entropy alloys in additive manufacturing, *Scripta Materialia*. 99 (2015) 93–96. doi:10.1016/j.scriptamat.2014.11.037.
[182] F. Palm, R. Leuschner, T. Schubert, B. Kieback, Scalmalloy ® = A Unique High Strength AlMgSc Type Material Concept Processed b y Innovative Technologies f or Aerospace Applications, in: PM2010 World Congr., 2010: pp. 0–7.
[183] A.B. Spierings, K. Dawson, M. Voegtlin, F. Palm, P.J. Uggowitzer, Microstructure and mechanical properties of as-processed scandium-modified aluminium using selective laser melting, *CIRP Annals - Manufacturing Technology*. 65 (2016) 213–216. doi:10.1016/j.cirp.2016.04.057.
[184] S.L. Sing, W.Y. Yeong, F.E. Wiria, Selective laser melting of titanium alloy

with 50 wt% tantalum: Microstructure and mechanical properties, *Journal of Alloys and Compounds*. 660 (2016) 461–470. doi:10.1016/j.jallcom.2015.11.141.

[185] B. Vrancken, L. Thijs, J.P. Kruth, J. Van Humbeeck, Microstructure and mechanical properties of a novel β titanium metallic composite by selective laser melting, *Acta Materialia*. 68 (2014) 150–158. doi:10.1016/j.actamat.2014.01.018.

[186] S.L. Sing, F.E. Wiria, W.Y. Yeong, Selective laser melting of titanium alloy with 50 wt% tantalum: Effect of laser process parameters on part quality, *International Journal of Refractory Metals and Hard Materials*. 77 (2018) 120–127. doi:10.1016/j.ijrmhm.2018.08.006.

[187] D. Gu, Y.C. Hagedorn, W. Meiners, K. Wissenbach, R. Poprawe, Selective Laser Melting of in-situ TiC/Ti5Si3 composites with novel reinforcement architecture and elevated performance, *Surface and Coatings Technology*. 205 (2011) 3285–3292. doi:10.1016/j.surfcoat.2010.11.051.

[188] D. Gu, H. Wang, D. Dai, F. Chang, W. Meiners, Y.-C. Hagedorn, K. Wissenbach, I. Kelbassa, R. Poprawe, Densification behavior, microstructure evolution, and wear property of TiC nanoparticle reinforced AlSi10Mg bulk-form nanocomposites prepared by selective laser melting, *Journal of Laser Applications*. 27 (2015) S17003. doi:10.2351/1.4870877.

[189] F. Chang, D. Gu, D. Dai, P. Yuan, Selective laser melting of in-situ Al4SiC4 + SiC hybrid reinforced Al matrix composites: Influence of starting SiC particle size, *Surface and Coatings Technology*. 272 (2015) 15–24. doi:10.1016/j.surfcoat.2015.04.029.

[190] N. Kang, M. El Mansori, X. Lin, F. Guittonneau, H.L. Liao, W.D. Huang, C. Coddet, In-situ synthesis of aluminum/nano-quasicrystalline Al-Fe-Cr composite by using selective laser melting, *Composites Part B: Engineering*. 155 (2018) 382–390. doi:10.1016/j.compositesb.2018.08.108.

[191] Y. Lu, L. Ren, X. Xu, Y. Yang, S. Wu, J. Luo, M. Yang, L. Liu, D. Zhuang, K. Yang, J. Lin, Effect of Cu on microstructure, mechanical properties, corrosion resistance and cytotoxicity of CoCrW alloy fabricated by selective laser melting, *Journal of the Mechanical Behavior of Biomedical Materials*. 81 (2018) 130–141. doi:10.1016/j.jmbbm.2018.02.026.

[192] P. Wang, L. Deng, K.G. Prashanth, S. Pauly, J. Eckert, S. Scudino, Microstructure and mechanical properties of Al-Cu alloys fabricated by selective laser melting of powder mixtures, *Journal of Alloys and Compounds*. 735 (2018) 2263–2266. doi:10.1016/j.jallcom.2017.10.168.

[193] X. Nie, H. Zhang, H. Zhu, Z. Hu, L. Ke, X. Zeng, Analysis of processing parameters and characteristics of selective laser melted high strength Al-Cu-Mg alloys: From single tracks to cubic samples, *Journal of Materials Processing Technology*. 256 (2018) 69–77. doi:10.1016/j.jmatprotec.2018.01.030.

[194] A. Aversa, M. Moshiri, E. Librera, M. Hadi, G. Marchese, D. Manfredi, M. Lorusso, F. Calignano, S. Biamino, M. Lombardi, M. Pavese, Single scan track analyses on aluminium based powders, *Journal of Materials Processing Technology*. 255 (2018) 17–25. doi:10.1016/j.jmatprotec.2017.11.055.

[195] T. Qi, H. Zhu, H. Zhang, J. Yin, L. Ke, X. Zeng, Selective laser melting of Al7050 powder : Melting mode transition and comparison of the characteristics between the keyhole and conduction mode, *Materials & Design*. 135 (2017) 257–266. doi:10.1016/j.matdes.2017.09.014.

[196] X.P. Li, C.W. Kang, H. Huang, L.C. Zhang, T.B. Sercombe, Selective laser melting of an Al86Ni6Y4.5Co2La1.5 metallic glass: Processing, microstructure evolution and mechanical properties, *Materials Science and Engineering A*. 606 (2014) 370–379. doi:10.1016/j.msea.2014.03.097.
[197] A. Piglione, B. Dovgyy, C. Liu, C.M. Gourlay, P.A. Hooper, M.S. Pham, Printability and microstructure of the CoCrFeMnNi high-entropy alloy fabricated by laser powder bed fusion, *Materials Letters*. 224 (2018) 22–25. doi:10.1016/j.matlet.2018.04.052.
[198] J.D. Embury, D.J. Lloyd, T.R. Ramachandran, Strengthening Mechanisms in Aluminum Alloys, in: Treatise Mater. Sci. Technol., 1989: pp. 579–599. doi:10.1016/B978-0-12-341831-9.50027-9.
[199] T. Sato, Chapter 9 - Nanostructure Control for High-Strength and High-Ductility Aluminum Alloys, 2006. doi:https://doi.org/10.1016/B978-008044964-7/50011-X.
[200] A.K. Gupta, D.J. Lloyd, S.A. Court, Precipitation hardening in Al – Mg – Si alloys with and without excess Si, *Materials Science and Engineering A*. 316 (2001) 11–17.
[201] C.D. Marioara, H. Nordmark, S.J. Andersen, Post- β phases and their influence on microstructure and hardness in 6xxx Al-Mg-Si alloys, *Journal of Material Science*. 41 (2006) 471–478. doi:10.1007/s10853-005-2470-1.
[202] L. Katgerman, F. Dom, Rapidly solidified aluminium alloys by meltspinning, *Materials Science & Engineering A*. 377 (2004) 1212–1216. doi:10.1016/j.msea.2003.10.094.
[203] Y. Barbaux, G. Pons, New rapidly solidified aluminium alloys for elevated temperature applications on aerospace structures, *Journal de Physique IV*. 3 (1993) 191–196.
[204] G.H. Li, S.P. Pan, J.Y. Qin, Z.H. Zhang, W.M. Wang, Insight into thermodynamics and corrosion behavior of Al – Ni – Gd glassy alloys from atomic structure, *Corrosion Science*. 66 (2013) 360–368. doi:10.1016/j.corsci.2012.09.043.
[205] A.V. Krainikov, O.D. Neikov, Rapidly solidified high-temperatuare aluminium alloys. I. structure, *Powder Metallurgy and Metal Ceramics*. 51 (2012) 399–411.
[206] E. Karakose, T. Karaaslan, M. Keskin, O. Uzun, Microstructural evolution and microhardness of a melt-spun Al – 6Ni – 2Cu – 1Si (in wt .%) alloy, 5 (2007) 58–62. doi:10.1016/j.jmatprotec.2007.04.115.
[207] K. Saksl, Structural evolution of rapidly solidified Al – Mn and Al – Mn – Sr alloys, *Materials Science and Engineering A*. 428 (2006) 188–195. doi:10.1016/j.msea.2006.05.017.
[208] N.L. Tawfik, Mechanical properties of rapidly solidified ribbons of some AI – Si based alloys, *Journal of Materials Science*. 32 (1997) 2997–3000.
[209] S.E.E. Profile, S.E.E. Profile, Crystallization behavior of amorphous alloys in the Al-Ce-Ni system, *Reviews on Advanced Materials Science*. 18 (2008) 469–475.
[210] N. Unlu, A. Genc, N. Eruslu, F.H. Froes, N. Unlu, M.L. Ovec, Characterization investigations of melt-spun ternary Al– x Si–3.3Fe (x 5 10, 20 wt.%) alloys, *Journal of Alloys and Compounds*. 322 (2001) 249–256.
[211] T. Hirano, T. Fujita, Properties of Al-Si-X P / M alloys using rapidly solidified powders, in: Proc. Powder Metall. World Congr., 1987: pp. 563–566.
[212] P. Todeschini, G. Champier, F.H. Samuel, Production of Al-(12-25) wt % Si

alloys by rapid soldification: melt spnning versus centrifugal atomization, *Journal of Material Science*. 27 (1992) 3539–3551.
[213] L.S. Toropova, D.G. Eskin, M.L. Kharakterova, T. V Dobatkina, Advanced Aluminum Alloys Containing Scandium, Taylor & Francis, London, 1998.
[214] R. Delhez, L. Katgerman, Characterization of Al-Si-alloys rapidly quenched from the melt, *Journal of Materials Science*. 15 (1980) 2803–2810. doi:10.1007/BF00550549.
[215] A.G. Escorial, B. Sánchez, M.C. Cristina, G. Caruana, M. Torralba, Rapidly solidified Al3CrX (Ni, Mo) ribbons: structure and decomposition behaviour, *Materials Science and Engineering A*. 134 (1991) 1204–1207. doi:10.1016/0921-5093(91)90956-N.
[216] W.C. Moshier, G.D. Davis, G.O. Cote, Surface Chemistry of Sputter-Deposited Al-Mo and Al-Cr Alloys Polarized in 0.1N KCl, *Electrochemical Science and Technology*. 136 (1989) 356–362.
[217] R.K. Gupta, D. Fabijanic, T. Dorin, Y. Qiu, J.T. Wang, N. Birbilis, Simultaneous improvement in the strength and corrosion resistance of Al via high-energy ball milling and Cr alloying, *Materials and Design*. 84 (2015) 270–276. doi:10.1016/j.matdes.2015.06.120.
[218] J. Esquivel, H.A. Murdoch, K.A. Darling, R.K. Gupta, Excellent corrosion resistance and hardness in Al alloys by extended solid solubility and nanocrystalline structure, *Materials Research Letters*. 6 (2018) 79–83. doi:10.1080/21663831.2017.1396262.
[219] D.J. Skinner, R.L. Bye, D. Raybould, A.M. Brown, A. Corporation, Dispersion strengthened Al–Fe–V–Si alloys, *Scripta Metallurgica*. 20 (1986) 867–872.
[220] A. Kalkanli, S. Angi, Effect of cooling rate on microstructure and high temperature stability of rapidly solidified Al–Fe–V–Si alloys, *Powder Metallurgy*. 42 (1999) 359–365. doi:10.1179/003258999665710.
[221] A. Fabrizi, G. Timelli, The influence of cooling rate and Fe/Cr content on the evolution of Fe-rich compounds in a secondary Al-Si-Cu diecasting alloy, *IOP Conference Series: Materials Science and Engineering*. 117 (2016). doi:10.1088/1757-899X/117/1/012017.
[222] Y. Yang, S.Y. Zhong, Z. Chen, M. Wang, N. Ma, H. Wang, Effect of Cr content and heat-treatment on the high temperature strength of eutectic Al-Si alloys, *Journal of Alloys and Compounds*. 647 (2015) 63–69. doi:10.1016/j.jallcom.2015.05.167.
[223] E.M. Ahmed, M.R. Ebrahim, Microstructure and Microhardness Evolutions of High Fe Containing Near-Eutectic Al-Si Rapidly Solidified Alloy, *Journal of Metallurgy*. 2014 (2014) 1–8. doi:http://dx.doi.org/10.1155/2014/587265.
[224] Y. Cai, R. Liang, L. Hou, J. Zhang, Effect of Cr and Mn on the microstructure of spray-formed Al – 25Si – 5Fe – 3Cu alloy, *Materials Science & Engineering A*. 528 (2011) 4248–4254. doi:10.1016/j.msea.2011.02.029.
[225] G. Gonzalez, G.A. Lara-Rodriguez, A. Sandoval-Jiménez, W. Saikaly, A. Charai, The influence of cooling rate on the microstructure of an Al-Ni hypereutectic alloy, *Materials Characterization*. 59 (2008) 1607–1612. doi:10.1016/j.matchar.2008.02.006.
[226] T.H. Lee, S.J. Hong, Microstructure and mechanical properties of Al-Si-X alloys fabricated by gas atomization and extrusion process, *Journal of Alloys and Compounds*. 487 (2009) 218–224. doi:10.1016/j.jallcom.2009.07.108.
[227] E.R. Wang, X.D. Hui, S.S. Wang, Y.F. Zhao, G.L. Chen, Microstructure and

mechanical properties of Al-Si-Ni-Ce alloys prepared by gas-atomization spark plasma sintering and hot-extrusion, *Materials Science and Engineering A*. 528 (2011) 5764–5771. doi:10.1016/j.msea.2011.03.102.
[228] R. González, A. González, J. Talamantes-Silva, S. Valtierra, R.D. Mercado-Solís, N.F. Garza-Montes-De-Oca, R. Colás, Fatigue of an aluminium cast alloy used in the manufacture of automotive engine blocks, *International Journal of Fatigue*. 54 (2013) 118–126. doi:10.1016/j.ijfatigue.2013.03.018.
[229] Greenteam, Additive manufacturing helps racing team finish first, *Metal Powder Report*. 68 (2013) 32–33. doi:10.1016/S0026-0657(13)70216-9.
[230] Greenteam, Race Car with Water-Cooled Electric Motors Brings Students a Place on the Podium Improved Cooling Thanks to Aluminum Jacket with Internal Helix-Structure Produced with Additive Manufacturing, (n.d.). https://cdn0.scrvt.com/eos/5615eec790a69bb1/5e516575b5e9/CS_M_Automotive_GreenTeamUniStuttgart_en_WEB.pdf.
[231] T.B. Massalski, H. Okamoto, P.R. Subramanian, L. Kacprzak, Binary Alloy Phase Diagrams, 2nd Edition, 1990.
[232] D. Manfredi, F. Calignano, M. Krishnan, R. Canali, E.P. Ambrosio, S. Biamino, D. Ugues, M. Pavese, P. Fino, Additive Manufacturing of Al Alloys and Aluminium Matrix Composites (AMCs), *Light Metal Alloys Applications*. (2014) 3–34. doi:10.5772/57069.
[233] D. Manfredi, R. Bidulský, Laser powder bed fusion of aluminum alloys, *Acta Metallurgica Slovaca*. 23 (2017) 276–282. doi:10.12776/ams.v23i3.988.
[234] J. Wu, X.Q. Wang, W. Wang, M.M. Attallah, M.H. Loretto, Microstructure and strength of selectively laser melted AlSi10Mg, *Acta Materialia*. 117 (2016) 311–320. doi:10.1016/j.actamat.2016.07.012.
[235] S. Marola, D. Manfredi, G. Fiore, M.G. Poletti, M. Lombardi, P. Fino, L. Battezzati, A comparison of Selective Laser Melting with bulk rapid solidification of AlSi10Mg alloy, *Journal of Alloys and Compounds*. 742 (2018) 271–279. doi:10.1016/j.jallcom.2018.01.309.
[236] M. Tang, P.C. Pistorius, S. Narra, J.L. Beuth, Rapid Solidification: Selective Laser Melting of AlSi10Mg, *Jom*. 68 (2016) 960–966. doi:10.1007/s11837-015-1763-3.
[237] A. Mertens, O. Dedry, M.M. Science, R.B. St-jean, Thermal Treatments of AlSi10Mg Processed By Laser Beam Melting, in: Proc. 26th Int. Solid Free. Fabr. Symp., 2015: pp. 1007–1016.
[238] M. Cabrini, D. Manfredi, S. Lorenzi, C. Testa, Corrosion resistance in chloride solution of the AlSi10Mg alloy obtained by means of LPBF, *Surface and Interface Analysis*. (2018) 1–6. doi:10.1002/sia.6601.
[239] A. Manufacturing, I. Counterpart, Corrosion Behavior of AlSi10Mg Alloy Produced by Additive Manufacturing (AM) vs. Its Counterpart Gravity Cast Alloy, (2016). doi:10.3390/met6070148.
[240] K. Schmidtke, F. Palm, A. Hawkins, C. Emmelmann, Process and Mechanical Properties : Applicability of a Scandium modified Al-alloy for Laser Additive Manufacturing, *Physics ProcediaProcedia*. 12 (2011) 369–374. doi:10.1016/j.phpro.2011.03.047.
[241] D.N. Seidman, E.A. Marquis, D.C. Dunand, Precipitation strengthening at ambient and elevated temperatures of heat-treatable Al (Sc) alloys, *Acta Materialia*. 50 (2002) 4021–4035.
[242] E. Clouet, L. Laé, T. Épicier, W. Lefebvre, A. Deschamps, E. Clouet, L. Laé, T. Épicier, W. Lefebvre, M. Nastar, Complex Precipitation Pathways in Multi-Component Alloys To cite this version : Complex precipitation

pathways in multi-component alloys, *Nature Materials*. 5 (2006) 482–488.
[243] A.B. Spierings, K. Dawson, T. Heeling, P.J. Uggowitzer, R. Schäublin, F. Palm, K. Wegener, Microstructural features of Sc- and Zr-modi fi ed Al-Mg alloys processed by selective laser melting, *Materials & Design*. 115 (2017) 52–63. doi:10.1016/j.matdes.2016.11.040.
[244] K. V Yang, Y. Shi, F. Palm, X. Wu, P. Rometsch, Columnar to equiaxed transition in Al-Mg (-Sc) -Zr alloys produced by selective laser melting, *Scripta Materialia*. 145 (2018) 113–117. doi:10.1016/j.scriptamat.2017.10.021.
[245] A.B. Spierings, K. Dawson, P.J. Uggowitzer, K. Wegener, Influence of SLM scan-speed on microstructure , precipitation of Al3Sc particles and mechanical properties in Sc- and Zr-modi fi ed Al-Mg alloys, *Materials & Design*. 140 (2018) 134–143. doi:10.1016/j.matdes.2017.11.053.
[246] P. Ma, Y. Jia, K. Gokuldoss, S. Scudino, Z. Yu, Microstructure and phase formation in Al-20Si-5Fe-3Cu-1Mg synthesized by selective laser melting, *Journal of Alloys and Compounds*. 657 (2016) 430–435. doi:10.1016/j.jallcom.2015.10.119.
[247] S.-B. Sun, L.-J. Zheng, J.-H. Liu, H. Zhang, Selective Laser Melting of an Al–Fe–V–Si Alloy: Microstructural Evolution and Thermal Stability, *Journal of Materials Science & Technology*. 33 (2016) 389–396. doi:10.1016/j.jmst.2016.09.015.
[248] S. Sun, L. Zheng, Y. Liu, J. Liu, H. Zhang, Characterization of Al–Fe–V–Si heat-resistant aluminum alloy components fabricated by selective laser melting, *Journal of Materials Research*. 30 (2015) 1661–1669. doi:10.1557/jmr.2015.110.
[249] S. Sun, L. Zheng, Y. Liu, J. Liu, H. Zhang, Characterization of Al–Fe–V–Si heat-resistant aluminum alloy components fabricated by selective laser melting, *Journal of Materials Research*. (2015) 1–9. doi:10.1557/jmr.2015.110.
[250] A. Simchi, M. Mansouri, E.S. Park, N. Varahram, Melt Spinning of Amorphous Aluminum Alloys Containing Transition (Ni , Fe , Cu) and Mish Metals : Thermal Stability and Nano-crystallization World PM2016 – Lightweight MMCs, in: World PM2016, 2016: pp. 7–11.
[251] K.G. Prashanth, H.S. Shahabi, H. Attar, V.C. Srivastava, N. Ellendt, V. Uhlenwinkel, J. Eckert, S. Scudino, Production of high strength Al 85 Nd 8 Ni 5 Co 2 alloy by selective laser melting, *Additive Manufacturing*. 6 (2015) 1–5. doi:10.1016/j.addma.2015.01.001.
[252] H. Zhang, H. Zhu, T. Qi, Z. Hu, X. Zeng, Selective laser melting of high strength Al – Cu – Mg alloys : Processing , microstructure and mechanical properties, *Materials Science & Engineering A*. 656 (2016) 47–54. doi:10.1016/j.msea.2015.12.101.
[253] H. Zhang, H. Zhu, X. Nie, T. Qi, Z. Hu, X. Zeng, Fabrication and heat treatment of high strength Al-Cu-Mg alloy processed using selective laser melting, in: Proc. Vol. 9738, Laser 3D Manuf. III, 2016. doi:doi: 10.1117/12.2211362.
[254] L. Zhou, H. Pan, H. Hyer, S. Park, Y. Bai, B. Mcwilliams, K. Cho, Y. Sohn, Microstructure and tensile property of a novel AlZnMgScZr alloy additively manufactured by gas atomization and laser powder bed fusion, *Scripta Materialia*. 158 (2019) 24–28. doi:10.1016/j.scriptamat.2018.08.025.
[255] X. Nie, H. Zhang, H. Zhu, Z. Hu, L. Ke, X. Zeng, Effect of Zr content on formability, microstructure and mecahanical pracoperties of selective laser

melted Zr modified Al-4.24Cu-1.97Mg-0.56Mn alloys, *Journal of Alloys and Compounds*. 764 (2018) 977–986. doi:10.1016/j.jallcom.2018.06.032.
[256] D. Gu, H. Wang, D. Dai, P. Yuan, Rapid fabrication of Al-based bulk-form nanocomposites with novel reinforcement and enhanced performance by selective laser melting, *Scripta Materialia*. 96 (2015) 25–28. doi:10.1016/j.scriptamat.2014.10.011.
[257] H. Attar, M. Bo, M. Calin, L. Zhang, Selective laser melting of in situ titanium – titanium boride composites : Processing , microstructure and mechanical properties, *Acta Materialia*. 76 (2014) 13–22. doi:10.1016/j.actamat.2014.05.022.
[258] N. Kang, P. Coddet, H. Liao, T. Baur, C. Coddet, Wear behavior and microstructure of hypereutectic Al-Si alloys prepared by selective laser melting, *Applied Surface Science*. 378 (2016) 142–149. doi:10.1016/j.apsusc.2016.03.221.
[259] C.E. Roberts, D. Bourell, T. Watt, J. Cohen, A novel processing approach for additive manifacturing of commercial aluminium alloys, *Physics Procedia*. 83 (2016) 909–917. doi:10.1016/j.phpro.2016.08.095.
[260] K. Bartkowiak, S. Ullrich, T. Frick, M. Schmidt, New developments of laser processing aluminium alloys via additive manufacturing technique, *Physics Procedia*. 12 (2011) 393–401. doi:10.1016/j.phpro.2011.03.050.
[261] N. Kang, Y. Fu, P. Coddet, B. Guelorget, H. Liao, C. Coddet, On the microstructure, hardness and wear behavior of Al-Fe-Cr quasicrystal reinforced Al matrix composite prepared by selective laser melting, *Materials and Design*. 132 (2017) 105–111. doi:10.1016/j.matdes.2017.06.060.
[262] F. Stadler, H. Antrekowitsch, W. Fragner, H. Kaufmann, E.R. Pinatel, P.J. Uggowitzer, The effect of main alloying elements on the physical properties of Al-Si foundry alloys, *Materials Science and Engineering A*. 560 (2013) 481–491. doi:10.1016/j.msea.2012.09.093.
[263] A. Aversa, M. Lorusso, G. Cattano, D. Manfredi, F. Calignano, E.P. Ambrosio, S. Biamino, P. Fino, M. Lombardi, M. Pavese, A study of the microstructure and the mechanical properties of an AlSiNi alloy produced via selective laser melting, *Journal of Alloys and Compounds*. (2016) 1–9. doi:10.1016/j.jallcom.2016.10.285.
[264] P.K. Rohatgi, R.C. Sharma, K. V Prabhakar, Microstructure and mechanical properties of unidirectionally solidified Al-Si-Ni ternary eutectic, *Metallurgical Transactions A*. 6 (1975) 569. doi:10.1007/BF02658416.
[265] U. Boyuk, S. Engin, N. Mara??li, Microstructural characterization of unidirectional solidified eutectic Al-Si-Ni alloy, *Materials Characterization*. 62 (2011) 844–851. doi:10.1016/j.matchar.2011.05.010.
[266] J. Fiocchi, a. Tuissi, P. Bassani, C. a. Biffi, Low temperature annealing dedicated to AlSi10Mg selective laser melting products, *Journal of Alloys and Compounds*. 695 (2016) 3402–3409. doi:10.1016/j.jallcom.2016.12.019.
[267] P. Ma, Y. Jia, K.G. Prashanth, S. Scudino, Z. Yu, J. Eckert, Microstructure and phase formation in Al-20Si-5Fe-3Cu-1Mg synthesized by selective laser melting, *Journal of Alloys and Compounds*. 657 (2016) 430–435. doi:10.1016/j.jallcom.2015.10.119.
[268] L.A. Godlewski, X. Su, T.M. Pollock, J.E. Allison, The Effect of Aging on the Relaxation of Residual Stress in Cast Aluminum, *Metallurgical and Material Transcations A*. 44 (2013) 4809–4818. doi:10.1007/s11661-013-

1800-1.
[269] J. Zhang, B. Song, Q. Wei, D. Bourell, Y. Shi, A review of selective laser melting of aluminum alloys : Processing, microstructure, property and developing trends, *Journal of Materials Science & Technology*. 35 (2019) 270–284. doi:10.1016/j.jmst.2018.09.004.
[270] G. Marchese, A. Aversa, M. Lorusso, D. Manfredi, F. Calignano, M. Lombardi, S. Biamino, M. Pavese, Development and Characterisation of Aluminium Matrix Nanocomposites AlSi10Mg/MgAl2O4 by Laser Powder Bed Fusion, *Metals*. 8 (2018) 175. doi:10.3390/met8030175.
[271] Y. Fukui, K. Takashima, C.B. Ponton, Measurement of Young's modulus and internal friction of an in situ Al-Al3Ni functionally gradient material, *Journal of Materials Science*. 29 (1994) 2281–2288. doi:10.1007/BF00363415.
[272] Computherm Llc, Pandat CompuTherm Database User 's Guide, 2016.
[273] P. Schaffnit, C. Stallybrass, J. Konrad, F. Stein, M. Weinberg, A Scheil – Gulliver model dedicated to the solidi fi cation of steel, *Calphad*. 48 (2015) 184–188. doi:10.1016/j.calphad.2015.01.002.
[274] C. Qiu, C. Panwisawas, M. Ward, H.C. Basoalto, J.W. Brooks, M.M. Attallah, On the role of melt flow into the surface structure and porosity development during selective laser melting, *Acta Materialia*. 96 (2015) 72–79. doi:10.1016/j.actamat.2015.06.004.
[275] O. Gharbi, D. Jiang, D.R. Feenstra, S.K. Kairy, Y. Wu, C.R. Hutchinson, N. Birbilis, On the corrosion of additively manufactured aluminium alloy AA2024 prepared by selective laser melting, 143 (2018) 93–106. doi:10.1016/j.corsci.2018.08.019.
[276] Y. Li, Y. Yang, Y. Wu, Z. Wei, X. Liu, Supportive strengthening role of Cr-rich phase on Al-Si multicomponent piston alloy at elevated temperature, *Materials Science and Engineering A*. 528 (2011) 4427–4430. doi:10.1016/j.msea.2011.02.047.
[277] Y. Fu, N. Kang, H. Liao, Y. Gao, C. Coddet, An investigation on selective laser melting of Al-Cu-Fe-Cr quasicrystal : From single layer to multilayers, *Intermetallics*. 86 (2017) 51–58. doi:10.1016/j.intermet.2017.03.012.
[278] M.H. Farshidianfar, A. Khajepour, A.P. Gerlich, Effect of real-time cooling rate on microstructure in Laser Additive Manufacturing, *Journal of Materials Processing Technology*. 231 (2016) 468–478. doi:10.1016/j.jmatprotec.2016.01.017.
[279] W.B. Pearson, A handbook of lattice spacings and structures of metals and alloys, Pergamon Press, London, 1959. doi:https://doi.org/10.1016/0001-6160(59)90040-9.
[280] T. Maeshima, K. Oh-ishi, Solute clustering and supersaturated solid solution of AlSi10Mg alloy fabricated by selective laser melting, *Heliyon*. (2019) e01186. doi:10.1016/j.heliyon.2019.e01186.
[281] L. Loh, C. Chua, W. Yeong, J. Song, M. Mapar, S. Sing, Z. Liu, D. Zhang, Numerical investigation and an effective modelling on the Selective Laser Melting (SLM) process with aluminium alloy 6061, *International Journal of Heat and Mass Transfer*. 80 (2015) 288–300. doi:10.1016/j.ijheatmasstransfer.2014.09.014.
[282] B. Cantor, Multicomponent and high entropy alloys, *Entropy*. 16 (2014) 4749–4768. doi:10.3390/e16094749.
[283] A.J.B. Vincent, A study of three multicomponet alloys, *PhD Thesis, University of Sussex*. (1981).

[284] P. Knight, Multicomponent alloys, *Bsc Part 2, Univeristy of Oxford*. (1995).
[285] B. Cantor, I.T.H. Chang, P. Knight, A.J.B. Vincent, Microstructural development in equiatomic multicomponent alloys, *Materials Science and Engineering A*. 375–377 (2004) 213–218. doi:10.1016/j.msea.2003.10.257.
[286] J.W. Yeh, S.K. Chen, S.J. Lin, J.Y. Gan, T.S. Chin, T.T. Shun, C.H. Tsau, S.Y. Chang, Nanostructured high-entropy alloys with multiple principal elements: Novel alloy design concepts and outcomes, *Advanced Engineering Materials*. 6 (2004) 299-303+274. doi:10.1002/adem.200300567.
[287] J.W. Yeh, US Patent - High-entropy multielement alloys, 2002. doi:10.1037/t24245-000.
[288] Y.Y. Chen, T. Duval, U.D. Hung, J.W. Yeh, H.C. Shih, Microstructure and electrochemical properties of high entropy alloys-a comparison with type-304 stainless steel, *Corrosion Science*. 47 (2005) 2257–2279. doi:10.1016/j.corsci.2004.11.008.
[289] O.N. Senkov, G.B. Wilks, D.B. Miracle, C.P. Chuang, P.K. Liaw, Refractory high-entropy alloys, *Intermetallics*. 18 (2010) 1758–1765. doi:10.1016/j.intermet.2010.05.014.
[290] D.B. Miracle, J.D. Miller, O.N. Senkov, C. Woodward, M.D. Uchic, J. Tiley, Exploration and development of high entropy alloys for structural applications, *Entropy*. 16 (2014) 494–525. doi:10.3390/e16010494.
[291] Y.J. Zhou, Y. Zhang, Y.L. Wang, G.L. Chen, Microstructure and compressive properties of multicomponent Alx(TiVCrMnFeCoNiCu)100-xhigh-entropy alloys, *Materials Science and Engineering A*. 454–455 (2007) 260–265. doi:10.1016/j.msea.2006.11.049.
[292] B.S. Li, Y.P. Wang, M.X. Ren, C. Yang, H.Z. Fu, Effects of Mn, Ti and V on the microstructure and properties of AlCrFeCoNiCu high entropy alloy, *Materials Science and Engineering A*. 498 (2008) 482–486. doi:10.1016/j.msea.2008.08.025.
[293] N.D. Stepanov, D.G. Shaysultanov, G.A. Salishchev, M.A. Tikhonovsky, Structure and mechanical properties of a light-weight AlNbTiV high entropy alloy, *Materials Letters*. 142 (2015) 153–155. doi:10.1016/j.matlet.2014.11.162.
[294] O.N. Senkov, D.B. Miracle, A new thermodynamic parameter to predict formation of solid solution or intermetallic phases in high entropy alloys, *Journal of Alloys and Compounds*. 658 (2016) 603–607. doi:10.1016/j.jallcom.2015.10.279.
[295] J.K. Jensen, B.A. Welk, R.E.A. Williams, J.M. Sosa, D.E. Huber, O.N. Senkov, G.B. Viswanathan, H.L. Fraser, Characterization of the microstructure of the compositionally complex alloy Al1Mo0.5Nb1Ta0.5Ti1Zr1, *Scripta Materialia*. 121 (2016) 1–4. doi:10.1016/j.scriptamat.2016.04.017.
[296] Y. Qiu, Y.J. Hu, A. Taylor, M.J. Styles, R.K.W. Marceau, A. V Ceguerra, M.A. Gibson, Z.K. Liu, H.L. Fraser, N. Birbilis, A lightweight single-phase AlTiVCr compositionally complex alloy, 123 (2017). doi:10.1016/j.actamat.2016.10.037.
[297] R.A. Swaling, Thermodynamics of Solids, 2nd ed, Wiley, NY, 1991.
[298] A. Benisek, E. Dachs, The vibrational and configurational entropy of disordering in Cu3Au, *Journal of Alloys and Compounds*. 632 (2015) 585–590. doi:10.1016/j.jallcom.2014.12.215.
[299] Y.F. Ye, Q. Wang, J. Lu, C.T. Liu, Y. Yang, The generalized thermodynamic rule for phase selection in multicomponent alloys, *Intermetallics*. 59 (2015)

75–80. doi:10.1016/j.intermet.2014.12.011.
[300] J.H. Hildebran, A quantitative treatment of deviations from Raoult's low, in: Proc. Natl. Acad. Sci. U. S. A., 1927: pp. 267–272. http://www.ncbi.nlm.nih.gov/pubmed/17739576.
[301] H.K. Hardy, A "sub-regular" solution model and its application to some binary alloy systems, *Acta Metallurgica*. 1 (1953) 202–209. doi:10.1016/0001-6160(53)90059-5.
[302] J.W. Yeh, Recent progress in high-entropy alloys, *Annales de Chimie: Science Des Materiaux*. 31 (2006) 633–648. doi:10.3166/acsm.31.633-648.
[303] M.S. Lucas, G.B. Wilks, L. Mauger, J.A. Muñoz, O.N. Senkov, E. Michel, J. Horwath, S.L. Semiatin, M.B. Stone, D.L. Abernathy, E. Karapetrova, Absence of long-range chemical ordering in equimolar FeCoCrNi, *Applied Physics Letters*. 100 (2012) 1–5. doi:10.1063/1.4730327.
[304] C. Ng, G. Sheng, J. Luan, S. Shi, C.T. Liu, Entropy-driven phase stability and slow diffusion kinetics in an Al0.5CoCrCuFeNi high entropy alloy, *Intermetallics*. 31 (2012) 165–172. doi:10.1016/j.intermet.2012.07.001.
[305] J.W. Yeh, S.Y. Chang, Y. Der Hong, S.K. Chen, S.J. Lin, Anomalous decrease in X-ray diffraction intensities of Cu-Ni-Al-Co-Cr-Fe-Si alloy systems with multi-principal elements, *Materials Chemistry and Physics*. 103 (2007) 41–46. doi:10.1016/j.matchemphys.2007.01.003.
[306] J. Yeh, S. Chen, J. Gan, S. Lin, Formation of simple crystal structures in Cu-Co-Ni-Cr-Al-Fe-Ti-V alloys with multiprincipal metallic elements, *Metallurgical and Materials Transactions*. 35 (2004) 2004.
[307] Y. Zhang, X. Yang, P.K. Liaw, Alloy design and properties optimization of high-entropy alloys, *Jom*. 64 (2012) 830–838. doi:10.1007/s11837-012-0366-5.
[308] Y.J. Zhou, Y. Zhang, Y.L. Wang, G.L. Chen, Solid solution alloys of AlCoCrFeNi Tix with excellent room-temperature mechanical properties, *Applied Physics Letters*. 90 (2007). doi:10.1063/1.2734517.
[309] H.W. Chang, P.K. Huang, J.W. Yeh, A. Davison, C.H. Tsau, C.C. Yang, Influence of substrate bias, deposition temperature and post-deposition annealing on the structure and properties of multi-principal-component (AlCrMoSiTi)N coatings, *Surface and Coatings Technology*. 202 (2008) 3360–3366. doi:10.1016/j.surfcoat.2007.12.014.
[310] K.Y. Tsai, M.H. Tsai, J.W. Yeh, Sluggish diffusion in Co-Cr-Fe-Mn-Ni high-entropy alloys, *Acta Materialia*. 61 (2013) 4887–4897. doi:10.1016/j.actamat.2013.04.058.
[311] S. Ranganathan, Alloyed pleasures: Multimetallic cocktails, *Current Science*. 85 (2003) 1404–1406.
[312] Y.F. Kao, T.J. Chen, S.K. Chen, J.W. Yeh, Microstructure and mechanical property of as-cast, -homogenized, and -deformed AlxCoCrFeNi ($0 < x < 2$) high-entropy alloys, *Journal of Alloys and Compounds*. 488 (2009) 57–64. doi:10.1016/j.jallcom.2009.08.090.
[313] Y.F. Ye, Q. Wang, J. Lu, C.T. Liu, Y. Yang, High-entropy alloy: Challenges and prospects, *Materials Today*. 00 (2015). doi:10.1016/j.mattod.2015.11.026.
[314] W. Hume-Rothery, H.M. Powell, Zeit schrift Fur Kristallographie, 91 (1935) 23–47.
[315] A. Takeuchi, A. Inoue, Quantitative evaluation of critical cooling rate for metallic glasses, *Materials Science and Engineering A*. 304–306 (2001) 446–451. doi:10.1016/S0921-5093(00)01446-5.

[316] A. Takeuchi, A. Inoue, Metallic Glasses By Atomic Size Difference, Heat of Mixing and Period of Constituent Elements and Its Application To Characterization of the Main Alloying Element, *Materials Transactions*. 46 (2005) 2817–2829. doi:10.2320/matertrans.46.2817.
[317] B.Y. Zhang, Y.J. Zhou, J.P. Lin, G.L. Chen, P.K. Liaw, Solid-Solution Phase Formation Rules for Multi-component Alloys, *Advanced Engineering Materials*. (2008) 534–538. doi:10.1002/adem.200700240.
[318] S. Guo, C.T. Liu, Phase stability in high entropy alloys: Formation of solid-solution phase or amorphous phase, *Progress in Natural Science: Materials International*. 21 (2011) 433–446. doi:10.1016/S1002-0071(12)60080-X.
[319] S. Guo, Q. Hu, C. Ng, C.T. Liu, More than entropy in high-entropy alloys: Forming solid solutions or amorphous phase, *Intermetallics*. 41 (2013) 96–103. doi:10.1016/j.intermet.2013.05.002.
[320] M.H. Tsai, J.H. Li, A.C. Fan, P.H. Tsai, Incorrect predictions of simple solid solution high entropy alloys: Cause and possible solution, *Scripta Materialia*. 127 (2017) 6–9. doi:10.1016/j.scriptamat.2016.08.024.
[321] X. Yang, Y. Zhang, Prediction of high-entropy stabilized solid-solution in multi-component alloys, 2012. doi:10.1016/j.matchemphys.2011.11.021.
[322] A.R. Miedema, P.F. de Châtel, F.R. de Boer, Cohesion in alloys - fundamentals of a semi-empirical model, *Physica B+C*. 100 (1980) 1–28. doi:10.1016/0378-4363(80)90054-6.
[323] A.K. Singh, N. Kumar, A. Dwivedi, A. Subramaniam, A geometrical parameter for the formation of disordered solid solutions in multi-component alloys, *Intermetallics*. 53 (2014) 112–119. doi:10.1016/j.intermet.2014.04.019.
[324] Z. Wang, Y. Huang, Y. Yang, J. Wang, C.T. Liu, Atomic-size effect and solid solubility of multicomponent alloys, *Scripta Materialia*. 94 (2015) 28–31. doi:10.1016/j.scriptamat.2014.09.010.
[325] Y.F. Ye, Q. Wang, J. Lu, C.T. Liu, Y. Yang, Design of high entropy alloys: A single-parameter thermodynamic rule, *Scripta Materialia*. 104 (2015) 53–55. doi:10.1016/j.scriptamat.2015.03.023.
[326] M.G. Poletti, G. Fiore, B.A. Szost, L. Battezzati, Search for high entropy alloys in the X-NbTaTiZr systems (X = Al, Cr, V, Sn), *Journal of Alloys and Compounds*. 620 (2015) 283–288. doi:10.1016/j.jallcom.2014.09.145.
[327] F.G. Coury, T. Butler, K. Chaput, A. Saville, J. Copley, J. Foltz, P. Mason, K. Clarke, M. Kaufman, A. Clarke, Phase equilibria, mechanical properties and design of quaternary refractory high entropy alloys, *Materials and Design*. 155 (2018) 244–256. doi:10.1016/j.matdes.2018.06.003.
[328] S. Guo, C. Ng, J. Lu, C.T. Liu, Effect of valence electron concentration on stability of fcc or bcc phase in high entropy alloys, *Journal of Applied Physics*. 109 (2011) 0–5. doi:10.1063/1.3587228.
[329] M.H. Tsai, K.Y. Tsai, C.W. Tsai, C. Lee, C.C. Juan, J.W. Yeh, Criterion for sigma phase formation in Cr- and V-Containing high-entropy alloys, *Materials Research Letters*. 1 (2013) 207–212. doi:10.1080/21663831.2013.831382.
[330] M.G. Poletti, L. Battezzati, Electronic and thermodynamic criteria for the occurrence of high entropy alloys in metallic systems, *Acta Materialia*. 75 (2014) 297–306. doi:10.1016/j.actamat.2014.04.033.
[331] F. Zhang, C. Zhang, S.L. Chen, J. Zhu, W.S. Cao, U.R. Kattner, An understanding of high entropy alloys from phase diagram calculations, *Calphad: Computer Coupling of Phase Diagrams and Thermochemistry*. 45

(2014) 1–10. doi:10.1016/j.calphad.2013.10.006.
[332] A.M. Manzoni, U. Glatzel, New multiphase compositionally complex alloys driven by the high entropy alloy approach, *Materials Characterization*. (2018) 0–1. doi:10.1016/j.matchar.2018.06.036.
[333] D.B. Miracle, O.N. Senkov, A critical review of high entropy alloys and related concepts, *Acta Materialia*. (2016). doi:10.1016/j.actamat.2016.08.081.
[334] A. Takeuchi, K. Amiya, T. Wada, K. Yubuta, W. Zhang, High-Entropy Alloys with a Hexagonal Close-Packed Structure Designed by Equi-Atomic Alloy Strategy and Binary Phase Diagrams, *Jom*. 66 (2014) 1984–1992. doi:10.1007/s11837-014-1085-x.
[335] K.J. Laws, C. Crosby, A. Sridhar, P. Conway, L.S. Koloadin, M. Zhao, S. Aron-Dine, L.C. Bassman, High entropy brasses and bronzes - Microstructure, phase evolution and properties, *Journal of Alloys and Compounds*. 650 (2015) 949–961. doi:10.1016/j.jallcom.2015.07.285.
[336] S. Sohn, Y. Liu, J. Liu, P. Gong, S. Prades-Rodel, A. Blatter, B.E. Scanley, C.C. Broadbridge, J. Schroers, Noble metal high entropy alloys, *Scripta Materialia*. 126 (2017) 29–32. doi:10.1016/j.scriptamat.2016.08.017.
[337] M. Winter, The periodic table, (2011) 2011. https://www.webelements.com/.
[338] Y.J. Hsu, W.C. Chiang, J.K. Wu, Corrosion behavior of FeCoNiCrCux high-entropy alloys in 3.5% sodium chloride solution, *Materials Chemistry and Physics*. 92 (2005) 112–117. doi:10.1016/j.matchemphys.2005.01.001.
[339] S. Singh, N. Wanderka, B.S. Murty, U. Glatzel, J. Banhart, Decomposition in multi-component AlCoCrCuFeNi high-entropy alloy, *Acta Materialia*. 59 (2011) 182–190. doi:10.1016/j.actamat.2010.09.023.
[340] H.-Y. Chen, C.-W. Tsai, C.-C. Tung, J.-W. Yeh, T.-T. Shun, C.-C. Yang, S.-K. Chen, Effect of the substitution of Co by Mn in Al-Cr-Cu-Fe-Co-Ni high-entropy alloys, *Annales de Chimie - Science Des Matériaux*. 31 (2006) 685–698. doi:doi:10.3166.
[341] C.-J. Tong, Y.-L. Chen, J.-W. Yeh, S.-J. Lin, S.-K. Chen, T.-T. Shun, C.-H. Tsau, S.-Y. Chang, Microstructure characterization of Al x CoCrCuFeNi high-entropy alloy system with multiprincipal elements, *Metallurgical and Materials Transactions A*. 36 (2005) 881–893. doi:10.1007/s11661-005-0283-0.
[342] F.J. Wang, Y. Zhang, G.L. Chen, Atomic packing efficiency and phase transition in a high entropy alloy, *Journal of Alloys and Compounds*. 478 (2009) 321–324. doi:10.1016/j.jallcom.2008.11.059.
[343] X. Liu, W. Lei, L. Ma, J. Liu, J. Liu, J. Cui, On the microstructures, phase assemblages and properties of Al0.5CoCrCuFeNiSixhigh-entropy alloys, *Journal of Alloys and Compounds*. 630 (2015) 151–157. doi:10.1016/j.jallcom.2014.11.085.
[344] C. Li, M. Zhao, J.C. Li, Q. Jiang, B2 structure of high-entropy alloys with addition of Al, *Journal of Applied Physics*. 104 (2008). doi:10.1063/1.3032900.
[345] Z. Tang, M.C. Gao, H. Diao, T. Yang, J. Liu, T. Zuo, Y. Zhang, Z. Lu, Y. Cheng, Y. Zhang, K.A. Dahmen, P.K. Liaw, T. Egami, Aluminum alloying effects on lattice types, microstructures, and mechanical behavior of high-entropy alloys systems, *Jom*. 65 (2013) 1848–1858. doi:10.1007/s11837-013-0776-z.
[346] M.-R. Chen, S.-J. Lin, J.-W. Yeh, S.-K. Chen, Y.-S. Huang, C.-P. Tu, Microstructure and Properties of Al0.5CoCrCuFeNiTix (x= 0-2.0) High-

Entropy Alloys, *Materials Transactions*. 47 (2006) 1395–1401. doi:10.2320/matertrans.47.1395.
[347] S.G. Ma, Y. Zhang, Effect of Nb addition on the microstructure and properties of AlCoCrFeNi high-entropy alloy, *Materials Science and Engineering A*. 532 (2012) 480–486. doi:10.1016/j.msea.2011.10.110.
[348] T.T. Shun, L.Y. Chang, M.H. Shiu, Microstructures and mechanical properties of multiprincipal component CoCrFeNiTi x alloys, *Materials Science and Engineering A*. 556 (2012) 170–174. doi:10.1016/j.msea.2012.06.075.
[349] U. Sydney, A. Hohenwarter, A Fracture-Resistant High-Entropy Alloy for Cryogenic Applications, *Science*. 345 (2014) 1153–1159. doi:10.1126/science.1254581.
[350] F. Otto, A. Dlouhý, C. Somsen, H. Bei, G. Eggeler, E.P. George, The influences of temperature and microstructure on the tensile properties of a CoCrFeMnNi high-entropy alloy, *Acta Materialia*. 61 (2013) 5743–5755. doi:10.1016/j.actamat.2013.06.018.
[351] F. Wang, Y. Zhang, G. Chen, H.A. Davies, Tensile and compressive mechanical behaviour of a CoCrCuFeNiAl0.5 high entropy alloy, *International Journal of Modern Physics B*. 23 (2009) 1254–1259. doi:10.1142/S0217979209060774.
[352] A. V. Kuznetsov, D.G. Shaysultanov, N.D. Stepanov, G.A. Salishchev, O.N. Senkov, Tensile properties of an AlCrCuNiFeCo high-entropy alloy in as-cast and wrought conditions, *Materials Science and Engineering A*. 533 (2012) 107–118. doi:10.1016/j.msea.2011.11.045.
[353] M.P. Ryan, D.E. Williams, R.J. Chater, B.M. Hutton, D.S. McPhail, Why stainless steel corrodes, *Nature*. 415 (2002) 770–774. doi:10.1038/415770a.
[354] F.H. Stott, G.C. Wood, T. Stringer, The influence of alloying elements on the development and maintenance of protective scales, *Oxidation of Metals*. 44 (1995). doi:10.1007/BF01046725.
[355] G. Laplanche, U.F. Volkert, G. Eggeler, E.P. George, Oxidation Behavior of the CrMnFeCoNi High-Entropy Alloy, *Oxidation of Metals*. 85 (2016) 629–645. doi:10.1007/s11085-016-9616-1.
[356] W. Kai, C.C. Li, F.P. Cheng, K.P. Chu, R.T. Huang, L.W. Tsay, J.J. Kai, Air-oxidation of FeCoNiCr-based quinary high-entropy alloys at 700–900 °C, *Corrosion Science*. 121 (2017) 116–125. doi:10.1016/j.corsci.2017.02.008.
[357] N.K. Adomako, J.H. Kim, Y.T. Hyun, High-temperature oxidation behaviour of low-entropy alloy to medium- and high-entropy alloys, *Journal of Thermal Analysis and Calorimetry*. 133 (2018) 13–26. doi:10.1007/s10973-018-6963-y.
[358] S.T. Chen, W.Y. Tang, Y.F. Kuo, S.Y. Chen, C.H. Tsau, T.T. Shun, J.W. Yeh, Microstructure and properties of age-hardenable AlxCrFe1.5MnNi0.5alloys, *Materials Science and Engineering A*. 527 (2010) 5818–5825. doi:10.1016/j.msea.2010.05.052.
[359] M.H. Chuang, M.H. Tsai, W.R. Wang, S.J. Lin, J.W. Yeh, Microstructure and wear behavior of AlxCo1.5CrFeNi1.5Tiyhigh-entropy alloys, *Acta Materialia*. 59 (2011) 6308–6317. doi:10.1016/j.actamat.2011.06.041.
[360] C. Huang, Y. Zhang, J. Shen, R. Vilar, Thermal stability and oxidation resistance of laser clad TiVCrAlSi high entropy alloy coatings on Ti-6Al-4V alloy, *Surface and Coatings Technology*. 206 (2011) 1389–1395. doi:10.1016/j.surfcoat.2011.08.063.

[361] J.H. Devan, P.F. Tortorelli, The oxidation-sulfidation behaviour of iron alloys containing 16-40 at% Aluminium, 35 (1993) 1065–1071.
[362] M.D. Merz, The oxidation resistance of fine-grained sputter-deposited 304 stainless steel, *Metallurgical Transactions A*. 10 (1979) 71–77. doi:10.1007/BF02686409.
[363] Y.K. Kim, Y.A. Joo, H.S. Kim, K.A. Lee, High temperature oxidation behavior of Cr-Mn-Fe-Co-Ni high entropy alloy, *Intermetallics*. 98 (2018) 45–53. doi:10.1016/j.intermet.2018.04.006.
[364] H.P. Chou, Y.S. Chang, S.K. Chen, J.W. Yeh, Microstructure, thermophysical and electrical properties in AlxCoCrFeNi ($0 < x < 2$) high-entropy alloys, *Materials Science and Engineering B: Solid-State Materials for Advanced Technology*. 163 (2009) 184–189. doi:10.1016/j.mseb.2009.05.024.
[365] M.H. Tsai, Physical properties of high entropy alloys, *Entropy*. 15 (2013) 5338–5345. doi:10.3390/e15125338.
[366] O.N. Senkov, S.L. Semiatin, Microstructure and properties of a refractory high-entropy alloy after cold working, *Journal of Alloys and Compounds*. 649 (2015) 1110–1123. doi:10.1016/j.jallcom.2015.07.209.
[367] B. Dutta, F.H. (Sam. Froes, The Additive Manufacturing (AM) of titanium alloys, *Metal Powder Report*. 72 (2017) 96–106. doi:10.1016/j.mprp.2016.12.062.
[368] Haynes 230 Alloy, (n.d.). http://haynesintl.com/docs/default-source/pdfs/new-alloy-brochures/high-temperature-alloys/brochures/230-brochure.pdf.
[369] Inconel Alloy 718, (n.d.). http://www.specialmetals.com/assets/smc/documents/inconel_alloy_718.pdf.
[370] O.N. Senkov, G.B. Wilks, J.M. Scott, D.B. Miracle, Mechanical properties of Nb25Mo25Ta25W25 and V20Nb20Mo20Ta20W20 refractory high entropy alloys, *Intermetallics*. 19 (2011) 698–706. doi:10.1016/j.intermet.2011.01.004.
[371] Z.D. Han, N. Chen, S.F. Zhao, L.W. Fan, G.N. Yang, Y. Shao, K.F. Yao, Effect of Ti additions on mechanical properties of NbMoTaW and VNbMoTaW refractory high entropy alloys, *Intermetallics*. 84 (2017) 153–157. doi:10.1016/j.intermet.2017.01.007.
[372] H. Chen, A. Kauffmann, S. Laube, I.C. Choi, R. Schwaiger, Y. Huang, K. Lichtenberg, F. Müller, B. Gorr, H.J. Christ, M. Heilmaier, Contribution of Lattice Distortion to Solid Solution Strengthening in a Series of Refractory High Entropy Alloys, *Metallurgical and Materials Transactions A: Physical Metallurgy and Materials Science*. 49 (2018) 772–781. doi:10.1007/s11661-017-4386-1.
[373] N.D. Stepanov, N.Y. Yurchenko, D.G. Shaysultanov, G.A. Salishchev, M.A. Tikhonovsky, Effect of Al on structure and mechanical properties of Al_xNbTiVZr ($x = 0, 0.5, 1, 1.5$) high entropy alloys, *Materials Science and Technology*. 31 (2015) 1184–1193. doi:10.1179/1743284715Y.0000000032.
[374] N.Y. Yurchenko, N.D. Stepanov, D.G. Shaysultanov, M.A. Tikhonovsky, G.A. Salishchev, Effect of Al content on structure and mechanical properties of the AlxCrNbTiVZr (x=0; 0.25; 0.5; 1) high-entropy alloys, *Materials Characterization*. 121 (2016) 125–134. doi:10.1016/j.matchar.2016.09.039.
[375] N.Y. Yurchenko, N.D. Stepanov, S. V Zherebtsov, M.A. Tikhonovsky, G.A. Salishchev, Structure and mechanical properties of B2 ordered refractory

AlNbTiVZr x (x = 0 – 1 . 5) high-entropy alloys, *Materials Science & Engineering A*. 704 (2017) 82–90. doi:10.1016/j.msea.2017.08.019.
[376] T. Wang, Z. Jin, J.C. Zhao, Thermodynamic assessment of the Al-Zr binary system, *Journal of Phase Equilibria*. 22 (2001) 544–551. doi:10.1361/105497101770332695.
[377] O.N. Senkov, S. V. Senkova, C. Woodward, D.B. Miracle, Low-density, refractory multi-principal element alloys of the Cr-Nb-Ti-V-Zr system: Microstructure and phase analysis, *Acta Materialia*. 61 (2013) 1545–1557. doi:10.1016/j.actamat.2012.11.032.
[378] O.N. Senkov, S.V. Senkova, D.B. Miracle, C. Woodward, Mechanical properties of low-density, refractory multi-principal element alloys of the Cr–Nb–Ti–V–Zr system, *Materials Science and Engineering: A*. 565 (2013) 51–62. doi:10.1016/j.msea.2012.12.018.
[379] O.N. Senkov, S. V. Senkova, C. Woodward, Effect of aluminum on the microstructure and properties of two refractory high-entropy alloys, *Acta Materialia*. 68 (2014) 214–228. doi:10.1016/j.actamat.2014.01.029.
[380] N.D. Stepanov, N.Y. Yurchenko, D. V. Skibin, M.A. Tikhonovsky, G.A. Salishchev, Structure and mechanical properties of the AlCr<inf>x</inf>NbTiV (x = 0, 0.5, 1, 1.5) high entropy alloys, *Journal of Alloys and Compounds*. 652 (2015) 266–280. doi:10.1016/j.jallcom.2015.08.224.
[381] O.N. Senkov, C. Woodward, D.B. Miracle, Microstructure and Properties of Aluminum-Containing Refractory High-Entropy Alloys, *Jom*. 66 (2014) 2030–2042. doi:10.1007/s11837-014-1066-0.
[382] C.M. Liu, H.M. Wang, S.Q. Zhang, H.B. Tang, A.L. Zhang, Microstructure and oxidation behavior of new refractory high entropy alloys, *Journal of Alloys and Compounds*. 583 (2014) 162–169. doi:10.1016/j.jallcom.2013.08.102.
[383] E.M. Savitskii, G.S. Burkhanov, Physical Metallurgy of Refractory Metals and Alloys, Boston, 1995.
[384] M.R. Jackson, B.P. Bewlay, R.G. Rowe, D.W. Skelly, H.A. Lipsitt, High temperature refractory metal-intermetallic material composites, *Metal Powder Report*. 48 (1996) 39–44. doi:10.1016/S0026-0657(96)93566-3.
[385] K.S. Chan, Alloying effects on fracture mechanisms in Nb-based intermetallic in-situ composites, *Materials Science and Engineering A*. 329–331 (2002) 513–522. doi:10.1016/S0921-5093(01)01502-7.
[386] B. Gorr, F. Müller, M. Azim, H.J. Christ, T. Müller, H. Chen, A. Kauffmann, M. Heilmaier, High-Temperature Oxidation Behavior of Refractory High-Entropy Alloys: Effect of Alloy Composition, *Oxidation of Metals*. 88 (2017) 339–349. doi:10.1007/s11085-016-9696-y.
[387] O.N. Senkov, S. V. Senkova, D.M. Dimiduk, C. Woodward, D.B. Miracle, Oxidation behavior of a refractory NbCrMo0.5Ta0.5TiZr alloy, *Journal of Materials Science*. 47 (2012) 6522–6534. doi:10.1007/s10853-012-6582-0.
[388] Y. Murayama, S. Hanada, High temperature strength, fracture toughness and oxidation resistance of Nb–Si–Al–Ti multiphase alloys, *Science and Technology of Advanced Materials*. 3 (2002) 145–156.
[389] R.A. Perkins, R.A. Padgett, Oxygen diffusion in niobium and NbZr alloys, *Acta Metallurgica*. 25 (1977) 1221–1230. doi:10.1016/0001-6160(77)90211-5.
[390] S. Sheikh, S. Shafeie, Q. Hu, J. Ahlström, C. Persson, J. Veselý, J. Zýka, U. Klement, S. Guo, Alloy design for intrinsically ductile refractory high-

entropy alloys, *Journal of Applied Physics*. 120 (2016) 1–5. doi:10.1063/1.4966659.
[391] S. Sheikh, M.K. Bijaksana, A. Motallebzadeh, S. Shafeie, A. Lozinko, L. Gan, T.-K. Tsao, U. Klement, D. Canadinc, H. Murakami, S. Guo, Accelerated oxidation in ductile refractory high-entropy alloys, *Intermetallics*. 97 (2018) 58–66. doi:10.1016/j.intermet.2018.04.001.
[392] O.N. Senkov, C.F. Woodward, Microstructure and properties of a refractory NbCrMo0.5Ta0.5TiZr alloy, *Materials Science and Engineering A*. 529 (2011) 311–320. doi:10.1016/j.msea.2011.09.033.
[393] B. Gorr, F. Mueller, H.J. Christ, T. Mueller, H. Chen, A. Kauffmann, M. Heilmaier, High temperature oxidation behavior of an equimolar refractory metal-based alloy 20Nb-20Mo-20Cr-20Ti-20Al with and without Si addition, *Journal of Alloys and Compounds*. 688 (2016) 468–477. doi:10.1016/j.jallcom.2016.07.219.
[394] H. Chen, A. Kauffmann, B. Gorr, D. Schliephake, C. Seemüller, J.N. Wagner, H.J. Christ, M. Heilmaier, Microstructure and mechanical properties at elevated temperatures of a new Al-containing refractory high-entropy alloy Nb-Mo-Cr-Ti-Al, *Journal of Alloys and Compounds*. 661 (2016) 206–215. doi:10.1016/j.jallcom.2015.11.050.
[395] R. Li, J.C. Gao, K. Fan, Study to Microstructure and Mechanical Properties of Mg Containing High Entropy Alloys, *Materials Science Forum*. 650 (2010) 265–271. doi:10.4028/www.scientific.net/MSF.650.265.
[396] X. Yang, S.Y. Chen, J.D. Cotton, Y. Zhang, Phase Stability of Low-Density, Multiprincipal Component Alloys Containing Aluminum, Magnesium, and Lithium, *Jom*. 66 (2014) 2009–2020. doi:10.1007/s11837-014-1059-z.
[397] T. Kokai, Y. Yachu, J. Chienchang, C. Tsungshune, T. Chewei, Y. Jienwei, A light-weight high-entropy alloy Al 20 Be 20 Fe 10 Si 15 Ti 35, *Sci China Tech Sci*. 61 (2018) 184–188. doi:10.1007/s11431-017-9073-0.
[398] K.M. Youssef, A.J. Zaddach, C. Niu, D.L. Irving, C.C. Koch, A Novel Low-Density, High-Hardness, High-entropy Alloy with Close-packed Single-phase Nanocrystalline Structures, *Materials Research Letters*. 3 (2015) 95–99. doi:10.1080/21663831.2014.985855.
[399] J.P. Couzinié, G. Dirras, L. Perrière, T. Chauveau, E. Leroy, Y. Champion, I. Guillot, Microstructure of a near-equimolar refractory high-entropy alloy, *Materials Letters*. 126 (2014) 285–287. doi:10.1016/j.matlet.2014.04.062.
[400] W.H. Liu, Y. Wu, J.Y. He, Y. Zhang, C.T. Liu, Z.P. Lu, The Phase Competition and Stability of High-Entropy Alloys, *Jom*. 66 (2014) 1973–1983. doi:10.1007/s11837-014-1119-4.
[401] X. Ye, M. Ma, W. Liu, L. Li, M. Zhong, Y. Liu, Q. Wu, Synthesis and Characterization of High-Entropy Alloy AlFeCoNiCuCr by Laser Cladding, *Advances in Materials Science and Engineering*. 2011 (2011) 1–7. doi:10.1155/2011/485942.
[402] B.R. Braeckman, F. Boydens, H. Hidalgo, P. Dutheil, M. Jullien, A. Thomann, D. Depla, High entropy alloy thin fi lms deposited by magnetron sputtering of powder targets, *Thin Solid Films*. 580 (2015) 71–76. doi:10.1016/j.tsf.2015.02.070.
[403] S. Chang, S. Lin, Y. Huang, C. Wu, Mechanical properties , deformation behaviors and interface adhesion of (AlCrTaTiZr) N x multi-component coatings, *Surface & Coatings Technology*. 204 (2010) 3307–3314. doi:10.1016/j.surfcoat.2010.03.041.
[404] A. Siao, M. Ang, C.C. Berndt, A. Anupam, P. Sathiyamoorthi, Plasma-

Sprayed High Entropy Alloys : Microstructure and Properties of AlCoCrFeNi and MnCoCrFeNi, *Metallurgical and Material Transcations A*. (2014). doi:10.1007/s11661-014-2644-z.
[405] W. Huo, H. Shi, X. Ren, J. Zhang, Microstructure and Wear Behavior of CoCrFeMnNbNi High-Entropy Alloy Coating by TIG Cladding, *Advances in Materials Science and Engineering*. 2015 (2015) 1–6.
[406] X. Ye, M. Ma, Y. Cao, W. Liu, X. Ye, Y. Gu, The property research on high-entropy alloy AlxFeCoNiCuCr coating by laser cladding, *Physics Procedia*. 12 (2011) 303–312. doi:10.1016/j.phpro.2011.03.039.
[407] B.L. Huang, R.J. Perez, E.J. Lavernia, M.J. Luton, Formation of Supersaturated Solid Solutions by Mechanical Alloying, *Nonostructured Materials*. 7 (1996) 67–79. doi:10.1016/0965-9773(95)00299-5.
[408] V.H. Hammond, M.A. Atwater, K.A. Darling, H.Q. Nguyen, L.J. Kecskes, Equal-Channel Angular Extrusion of a Low-Density High-Entropy Alloy Produced by High-Energy Cryogenic Mechanical Alloying, *Jom*. 66 (2014) 2021–2029. doi:10.1007/s11837-014-1113-x.
[409] G. Zepon, D.R. Leiva, R.B. Strozi, A. Bedoch, S.J.A. Figueroa, T.T. Ishikawa, W.J. Botta, Hydrogen-induced phase transition of MgZrTiFe0.5Co0.5Ni0.5high entropy alloy, *International Journal of Hydrogen Energy*. 43 (2018) 1702–1708. doi:10.1016/j.ijhydene.2017.11.106.
[410] W. Guo, B. Liu, Y. Liu, T. Li, A. Fu, Q. Fang, Y. Nie, Microstructures and mechanical properties of ductile NbTaTiV refractory high entropy alloy prepared by powder metallurgy, *Journal of Alloys and Compounds*. 776 (2019) 428–436. doi:10.1016/j.jallcom.2018.10.230.
[411] Y. Tong, P. Qi, X. Liang, Y. Chen, Y. Hu, Different-Shaped Ultrafine MoNbTaW HEA Powders, *Materials*. (2018) 1–8. doi:10.3390/ma11071250.
[412] S. Praveen, B.S. Murty, R.S. Kottada, Alloying behavior in multi-component AlCoCrCuFe and NiCoCrCuFe high entropy alloys, *Materials Science and Engineering: A*. 534 (2012) 83–89. doi:10.1016/j.msea.2011.11.044.
[413] H. Zhang, Y.Z. He, Y. Pan, L.Z. Pei, Phase selection, microstructure and properties of laser rapidly solidified FeCoNiCrAl2Si coating, *Intermetallics*. 19 (2011) 1130–1135. doi:10.1016/j.intermet.2011.03.017.
[414] M. Baricco, M. Palumbo, D. Baldissin, E. Bosco, L. Battezzati, Metastable phases and phase diagrams, *Metalurgia Fisica*. (2004) 1. doi:10.1088/0953-8984/18/42/010.
[415] X. Li, Additive Manufacturing of Advanced Multi-Component Alloys: Bulk Metallic Glasses and High Entropy Alloys, *Advanced Engineering Materials*. 20 (2018) 1–18. doi:10.1002/adem.201700874.
[416] T. Fujieda, H. Shiratori, K. Kuwabara, T. Kato, K. Yamanaka, Y. Koizumi, A. Chiba, First demonstration of promising selective electron beam melting method for utilizing high-entropy alloys as engineering materials, *Materials Letters*. 159 (2015) 12–15. doi:10.1016/j.matlet.2015.06.046.
[417] I. Kunce, M. Polanski, K. Karczewski, T. Plocinski, K.J. Kurzydlowski, Microstructural characterisation of high-entropy alloy AlCoCrFeNi fabricated by laser engineered net shaping, *Journal of Alloys and Compounds*. 648 (2015) 751–758. doi:10.1016/j.jallcom.2015.05.144.
[418] D. Yim, M.J. Jang, J.W. Bae, J. Moon, C.H. Lee, S.J. Hong, S.I. Hong, H.S. Kim, Compaction behavior of water-atomized CoCrFeMnNi high-entropy alloy powders, *Materials Chemistry and Physics*. 210 (2018) 95–102.

doi:10.1016/j.matchemphys.2017.06.013.
[419] J. Guo, M. Goh, Z. Zhu, X. Lee, M.L.S. Nai, J. Wei, On the machining of selective laser melting CoCrFeMnNi high-entropy alloy, *Materials and Design*. 153 (2018) 211–220. doi:10.1016/j.matdes.2018.05.012.
[420] K. Kuwabara, H. Shiratori, T. Fujieda, K. Yamanaka, Y. Koizumi, A. Chiba, Mechanical and Corrosion Properties of AlCoCrFeNi High-Entropy Alloy Fabricated with Selective Electron Beam Melting, *Additive Manufacturing*. 23 (2018) 264–271. doi:10.1016/j.addma.2018.06.006.
[421] R. Li, P. Niu, T. Yuan, P. Cao, C. Chen, K. Zhou, Selective laser melting of an equiatomic CoCrFeMnNi high-entropy alloy: Processability, non-equilibrium microstructure and mechanical property, *Journal of Alloys and Compounds*. 746 (2019) 125–134. doi:10.1016/j.jallcom.2018.02.298.
[422] Z.G. Zhu, Q.B. Nguyen, F.L. Ng, X.H. An, X.Z. Liao, P.K. Liaw, S.M.L. Nai, J. Wei, Hierarchical microstructure and strengthening mechanisms of a CoCrFeNiMn high entropy alloy additively manufactured by selective laser melting, *Scripta Materialia*. 154 (2018) 20–24. doi:10.1016/j.scriptamat.2018.05.015.
[423] V. V Popov, A. Katz-demyanetz, A. Koptyug, Selective electron beam melting entropy alloys using elemental powder blend, *Heliyon*. (2019) e01188. doi:10.1016/j.heliyon.2019.e01188.
[424] N. Eißmann, B. Klöden, T. Weißgärber, B. Kieback, High-entropy alloy CoCrFeMnNi produced by powder metallurgy, *Powder Metallurgy*. 60 (2017) 184–197. doi:10.1080/00325899.2017.1318480.
[425] V. Ocelík, N. Janssen, S.N. Smith, J.T.M. De Hosson, Additive Manufacturing of High-Entropy Alloys by Laser Processing, *Jom*. 68 (2016) 15–18. doi:10.1007/s11837-016-1888-z.
[426] H. Dobbelstein, M. Thiele, E.L. Gurevich, E.P. George, A. Ostendorf, Direct metal deposition of refractory high entropy alloy MoNbTaW, *Physics Procedia*. 83 (2016) 624–633. doi:10.1016/j.phpro.2016.08.065.
[427] H. Zhang, W. Xu, Y. Xu, Z. Lu, D. Li, The thermal-mechanical behavior of WTaMoNb high-entropy alloy via selective laser melting (SLM): experiment and simulation, *International Journal of Advanced Manufacturing Technology*. 96 (2018) 461–474. doi:10.1007/s00170-017-1331-9.
[428] O. Maulik, V. Kumar, Synthesis of AlFeCuCrMg x (x = 0, 0.5, 1, 1.7) alloy powders by mechanical alloying, *Materials Characterization*. 110 (2015) 116–125. doi:10.1016/j.matchar.2015.10.025.
[429] Z. Fu, W. Chen, S. Fang, D. Zhang, H. Xiao, D. Zhu, Alloying behavior and deformation twinning in a CoNiFeCrAl0.6Ti0.4high entropy alloy processed by spark plasma sintering, *Journal of Alloys and Compounds*. 553 (2013) 316–323. doi:10.1016/j.jallcom.2012.11.146.
[430] N. Al-Aqeeli, C. Suryanarayana, M.A. Hussein, Formation of an amorphous phase and its crystallization in the immiscible Nb-Zr system by mechanical alloying, *Journal of Applied Physics*. 114 (2013) 0–4. doi:10.1063/1.4825325.
[431] D.A. Porter, K.E. Easterling, Phase Transformations in Metals and Alloys, 2nd Ed., Chapman & Hall, London, 1992. doi:10.1007/978-1-4899-3051-4.
[432] Y.L. Chen, Y.H. Hu, C.A. Hsieh, J.W. Yeh, S.K. Chen, Competition between elements during mechanical alloying in an octonary multi-principal-element alloy system, *Journal of Alloys and Compounds*. 481 (2009) 768–775. doi:10.1016/j.jallcom.2009.03.087.

[433] P. Wang, H. Cai, X. Cheng, Effect of Ni/Cr ratio on phase, microstructure and mechanical properties of NixCoCuFeCr2-x(x = 1.0, 1.2, 1.5, 1.8 mol) high entropy alloys, *Journal of Alloys and Compounds*. 662 (2016) 20–31. doi:10.1016/j.jallcom.2015.11.205.
[434] S. Varalakshmi, M. Kamaraj, B.S. Murty, Synthesis and characterization of nanocrystalline AlFeTiCrZnCu high entropy solid solution by mechanical alloying, *Journal of Alloys and Compounds*. 460 (2008) 253–257. doi:10.1016/j.jallcom.2007.05.104.
[435] S. Varalakshmi, M. Kamaraj, B.S. Murty, Formation and stability of equiatomic and nonequiatomic nanocrystalline CuNiCoZnAlTi high-entropy alloys by mechanical alloying, *Metallurgical and Materials Transactions A: Physical Metallurgy and Materials Science*. 41 (2010) 2703–2709. doi:10.1007/s11661-010-0344-x.
[436] N.T.B.N. Koundinya, C. Sajith Babu, K. Sivaprasad, P. Susila, N. Kishore Babu, J. Baburao, Phase evolution and thermal analysis of nanocrystalline AlCrCuFeNiZn high entropy alloy produced by mechanical alloying, *Journal of Materials Engineering and Performance*. 22 (2013) 3077–3084. doi:10.1007/s11665-013-0580-5.
[437] P. Wang, H. Cai, S. Zhou, L. Xu, Processing, microstructure and properties of Ni1.5CoCuFeCr(0.5-x)Vx high entropy alloys with carbon introduced from process control agent, *Journal of Alloys and Compounds*. 695 (2017) 462–475. doi:10.1016/j.jallcom.2016.10.288.
[438] H.X. Sui, M. Zhu, M. Qi, G.B. Li, D.Z. Yang, The enhancement of solid solubility limits of AlCo intermetallic compound by high-energy ball milling, *Journal of Applied Physics*. 71 (1992) 2945–2949. doi:10.1063/1.351028.
[439] N.H. Tariq, M. Naeem, B.A. Hasan, J.I. Akhter, M. Siddique, Effect of W and Zr on structural, thermal and magnetic properties of AlCoCrCuFeNi high entropy alloy, *Journal of Alloys and Compounds*. 556 (2013) 79–85. doi:10.1016/j.jallcom.2012.12.095.
[440] Z. Fu, W. Chen, H. Wen, S. Morgan, F. Chen, B. Zheng, Y. Zhou, L. Zhang, E.J. Lavernia, Microstructure and mechanical behavior of a novel Co20Ni20Fe20Al20Ti20 alloy fabricated by mechanical alloying and spark plasma sintering, *Materials Science and Engineering: A*. 644 (2015) 10–16. doi:10.1016/j.msea.2015.07.052.
[441] B. Kang, J. Lee, H. Jin, S. Hyung, Microstructure, mechanical property and Hall-Petch relationship of a light-weight refractory Al0.1CrNbVMo high entropy alloy fabricated by powder metallurgical process, *Journal of Alloys and Compounds*. 767 (2018) 1012–1021. doi:10.1016/j.jallcom.2018.07.145.
[442] P.-Y. Lee, J.-L. Yang, H.-M. Lin, Amorphization behaviour in mechanically alloyed Ni – Ta powders, *Journal of Materials Science*. 33 (1998) 235–239. doi:10.1023/A:1004334805505.
[443] C.K. Lin, S.W. Liu, P.Y. Lee, Preparation and Thermal Stability of Zr-Ti-Al-Ni-Cu Amorphous Powders by Mechanical Alloying Technique, 32 (2001).
[444] J.. Fogagnolo, F. Velasco, M.. Robert, J.. Torralba, Effect of mechanical alloying on the morphology, microstructure and properties of aluminium matrix composite powders, *Materials Science and Engineering: A*. 342 (2003) 131–143. doi:10.1016/S0921-5093(02)00246-0.
[445] K.B. Zhang, Z.Y. Fu, J.Y. Zhang, W.M. Wang, S.W. Lee, K. Niihara,

Characterization of nanocrystalline CoCrFeNiTiAl high-entropy solid solution processed by mechanical alloying, *Journal of Alloys and Compounds*. 495 (2010) 33–38. doi:10.1016/j.jallcom.2009.12.010.

[446] M. Murali, S.P.K. Babu, B.J. Krishna, A. Vallimanalan, Materials International Synthesis and characterization of AlCoCrCuFeZn x high-entropy alloy by mechanical alloying, *Progress in Natural Science: Materials International*. 26 (2016) 1–5. doi:10.1016/j.pnsc.2016.06.008.

[447] F. Salemi, M.H. Abbasi, F. Karimzadeh, Synthesis and thermodynamic analysis of nanostructured CuNiCoZnAl high entropy alloy produced by mechanical alloying, *Journal of Alloys and Compounds*. 685 (2016) 278–286. doi:10.1016/j.jallcom.2016.05.274.

[448] A.I. Yurkova, V. V. Chernyavskii, V.F. Gorban', Structure and Mechanical Properties of High-Entropy AlCuNiFeTi and AlCuNiFeCr Alloys Produced by Mechanical Activation Followed by Pressure Sintering, *Powder Metallurgy and Metal Ceramics*. 55 (2016) 1–12. doi:10.1007/s11106-016-9790-3.

[449] Y. Liu, J. Wang, Q. Fang, B. Liu, Y. Wu, S. Chen, Preparation of superfine-grained high entropy alloy by spark plasma sintering gas atomized powder, *Intermetallics*. 68 (2016) 16–22. doi:10.1016/j.intermet.2015.08.012.

[450] X.R. Tan, G.P. Zhang, Q. Zhi, Z.X. Liu, Effects of milling on the microstructure and hardness of Al2NbTi3V2Zr high-entropy alloy, *Materials and Design*. 109 (2016) 27–36. doi:10.1016/j.matdes.2016.07.066.

[451] I. Egry, E. Ricci, R. Novakovic, S. Ozawa, Surface tension of liquid metals and alloys-Recent developments, *Advances in Colloid and Interface Science*. 159 (2010) 198–212. doi:10.1016/j.cis.2010.06.009.

[452] N.W. Makoana, H. Moller, H. Burger, M. Tlotleng, I. Yadroitsev, Evaluation of Single Tracks of 17-4Ph Steel Manufactured At Different Power Densities and Scanning Speeds By Selective Laser Melting, *South African Journal of Industrial Engineering*. 27 (2016) 210–218. doi:10.7166/27-3-1668.

[453] J.C. Grande, Principles of Image Analysis, *Metallography, Microstructure, and Analysis*. 1 (2012) 227–243. doi:10.1007/s13632-012-0037-5.

[454] Y. Huang, J. Shen, Y. Sun, J. Sun, Indentation size effect of hardness of metallic glasses, *Materials and Design*. 31 (2010) 1563–1566. doi:10.1016/j.matdes.2009.09.046.

[455] I.A.N.N. Sneddon, The relation between load and penetration in the axisymmetric boussinesq problem for a punch of arbitrary profile, *International Journal of Engineering Science*. 3 (1965) 47–57.